Synthesis and Characterization of Bimetallic Nickel Nanoparticles for the Reverse Water Gas Shift Reaction

Dissertation

zur Erlangung des akademischen Grades

doctor rerum naturalium

(Dr. rer. nat.)

im Fach: Chemie

Spezialisierung: Analytische Chemie

eingereicht an der

Mathematisch-Naturwissenschaftlichen Fakultät

der Humboldt-Universität zu Berlin

von

M. Sc. Maria Theresia Heilmann

Präsidentin der Humboldt-Universität zu Berlin

Prof. Dr.-Ing. Dr. Sabine Kunst

Dekan der Mathematisch-Naturwissenschaftlichen Fakultät

Prof. Dr. Elmar Kulke

Gutachter/innen:

1. PD habil. Franziska Emmerling
2. Prof. Dr. Klaus Rademann
3. Prof. Dr. Wolfgang Tremel

Tag der mündlichen Prüfung: 08.12.2021

Contents

List of Abbreviations

abbreviation	explanation
Å	Ångström
AFM	atomic force microscopy
AF4	asymmetric flow field flow fractionation
API	active pharmaceutical ingredient
(A)SAXS	(anomalous) small-angle X-ray scattering
ATR	autothermal reforming
BF	bright field
BtL	biomass-to-liquid
CO	carbon monoxide
CO_2	carbon dioxide
CCS	CO_2 capturing and storing
CCU	CO_2 capturing and utilization
CNT	classical nucleation theory
$Cu(acac)_2$	copper acetylacetonate
$Co(acac)_2$	cobalt acetylacetonate
CtL	coal-to-liquid
DBE	dibenzylether
DFT	density functional theory
DLS	dynamic light scattering
DRM	dry reforming of methane
EDX	energy dispersive X-ray spectroscopy
EED	effective electron density
(E)SEM	(environmental) scanning electron microscopy
EtOAc	ethyl acetate
EtOH	ethanol
EXAFS	extended X-ray absorption fine structure
FAT	fixed analyzer transmission
fcc	face centered cubic
FCM	four crystal monochromator

Table 0.1: Continued from previous page.

abbreviation	explanation
FTS	Fischer-Tropsch synthesis
GtL	gas-to-liquid
HAADF	high-angle annular dark field
HPLC	high pressure liquid chromatography
ICP	inductively coupled plasma
K	Kelvin
keV	kilo electron Volt
LDL	low density lipopropein cholesterol
MIP	mercury intrusion porosimetry
MOF	metal organic frameworks
MS	mass spectrometry
$Ni(acac)_2$	nickel acetylacetonate
$Ni(COD)_2$	bis(1,5-cyclooctadiene)nickel
NMR	nuclear magnetic resonance spectroscopy
NP	nanoparticle
NiNPs	nickel nanoparicles
OAm	oleylamine
PD	polydispersity
PDF	pari distribution function
POX	partial oxidation
PTFE	polytetrafluoroethylene
PXRD	powder X-ray diffraction
RED	relative effective electron density
(R)WGS	(reverse) water gas shift reaction
SiO_2	silicon dioxide
SRM	steam reforming of methane
STEM	scanning transmission electron microscopy
TEM	transmission electron mikroscopy
TOP	trioctylphosphine
VSM	vibrating sample magnetometers
XANES	X-ray absorption near-edge structure
XAS	X-ray absorption spectroscopy
XRD	X-ray diffraction
XPS	X-ray photoelectron spectroscopy

Kurzzusammenfassung

Eine zentrale Herausforderung des 21. Jahrhunderts ist die Reduktion von Treibhausgasen wie beispielsweise Kohlenstoffdioxid (CO_2). Ein vielversprechender Ansatz hierfür ist die katalytische Umsetzung von CO_2 zu Synthesegas (CO + H_2) über die umgekehrte Wassergas-Shift-Reaktion. Nanopartikel sind ein wichtiges Forschungsgebiet aufgrund ihrer einzigartigen Eigenschaften und vielfältigen Anwendungsmöglichkeiten, einschließlich als Katalysatoren für die umgekehrte Wassergas-Shift-Reaktion.
Im Fokus dieser Arbeit steht die Synthese von mono- und bimetallischen Nickel-Nanopartikeln und deren Aktivität für die umgekehrte Wassergas-Shift-Reaktion. Im ersten Teil dieser Arbeit wird das weithin bekannte thermische Reduktionsverfahren zur Herstellung von Nickel-Nanopartikeln vereinfacht und modifiziert. Die monometallischen Nickel-Nanopartikel werden eingehend charakterisiert und der Einfluss der Synthesebedingungen auf die finalen Nanopartikel sowie deren katalytische Aktivität für die Umwandlung von CO_2 zu Synthesegas untersucht. In einem zweiten Teil wird das modifizierte Syntheseverfahren auf bimetallische Nickel-Nanopartikel durch Co-Reduktion von Nickel mit entweder Kupfer oder Kobalt übertragen. Die Nanopartikel werden eingehend untersucht und die Kern-Schale-Struktur der Nickel-Kupfer-Nanopartikel wird identifiziert und detailliert charakterisiert. Der Einfluss der Reaktionsparameter auf die finalen Nanopartikel und die Korrelation von Größe, Form und Kupfergehalt der Nanopartikel auf die Aktivität für die umgekehrte Wasser-Gas-Shift-Reaktion werden untersucht.

Abstract

A great challenge of the 21^{st} century is the minimization of greenhouse gases such as CO_2. A promising approach is the catalytic conversion of CO_2 to synthesis gas (CO + H_2) via the reverse water gas shift reaction. Nanoparticles are an important field of research due to their unique properties and variety of applications including catalysts for the reverse water gas shift reaction.
This work focusses on the synthesis of mono- and bimetallic nickel nanoparticles and their activity for the reverse water gas shift reaction. In the first part of this work the well-known thermal reduction procedure for the preparation of nickel nanoparticles is adapted and simplified. The monometallic nickel nanoparticles are characterized thoroughly and the impact of the synthesis conditions on the final nanoparticles and their catalytic activity for the conversion of CO_2 to CO are investigated. In a second part the adapted synthesis procedure is transferred to bimetallic nickel nanoparticles by co-reduction of nickel with either copper or cobalt. The nanoparticles are investigated thoroughly and the core-shell structure of nickel copper nanoparticles is identified and characterized in detail. The impact of the reaction parameters on the final nanoparticles as well as the correlation of size, shape and copper content of the nanoparticles on the activity for the reverse water gas shift reaction is investigated.

1 Introduction

Nanoparticles have been the focus of intense research for over half a century due to their outstanding properties which open a broad field of research and offer broad range of applications. Nanoparticles are defined as nano-objects that lie in the range of 1 to 100 nm in all three external dimensions (ISO/TS 27687:2008).[1] Depending on their size, shape, composition and crystallinity, the electrical, magnetic, optical and chemical properties of nanoparticles change in comparison to the bulk material.[2]

Nanoparticles (NPs) are already used today as catalysts, in analytical assays and in antimicrobial applications.[3–5] In particular, metal NPs such as Au, Ag, Ru, Pt, Rh, Pd, and Ni NPs are important for biomedical applications[6] and antimicrobial applications,[7] as well as for the transport of active substances,[8] sensor/biosensor technology,[9] and catalysis.[10,11] Metallic NPs are used for the electrocatalytic hydrogen evolution reaction,[12] acidic oxygen evolution,[13] and the reverse water gas shift reaction.[14] Ni NPs can be used for further catalytic applications such as the hydrogenation of olefins,[15] chemoselective oxidative coupling of thiols[16] or alkaline hydrogen evolution reaction.[17]

One of the greatest challenges of the 21^{st} century is the minimization of greenhouse gases. Greenhouse gases such as carbon dioxide (CO_2), methane (CH_4), and nitrous oxide (N_2O), originating from anthropogenic sources, are the main cause of global warming, climate change, rising sea level, and ocean acidification, with CO_2 accounting for about 66%.[18,19] Research has focused on solving these problems through CO_2 capture and storage (CCS) and CO_2 capture and utilization (CCU). The catalytic conversion of CO_2 to carbon monoxide (CO) and further higher alkanes and alkanoles using hydrogen, known as the Reverse Water Gas Shift reaction (RWGS), is a promising approach here. This conversion can close an energy-saving cycle in the overall power-to-syngas process.[20]

Over the past decades, there has been extensive research to develop catalysts that are both highly active and stable for the RWGS reaction. Supported Pt,[21] Rh,[22] Cu,[23,24] and Ni[23,25] have been found to be suitable catalyst materials. Ni is a promising alternative to expensive noble and precious metals because it shows high selectivity at sufficiently high activity, comparably low price and high availability.[26] Compared to pure metal, Ni NPs offer the advantage of a much larger surface-to-volume ratio, which means that greater effect can be achieved with less mass and therefore lower material costs.

The aim of this work is to synthesize monometallic and bimetallic Ni NPs in defined shape and size in a targeted manner. For this purpose a simplifying modification of the thermal reduction pathway is applied. In the first part of the work the influence of the reaction parameters on the final monometallic Ni NPs, the NPs themselves, and their activity for the RWGS reaction are extensively studied. In a second part, bimetallic NP systems are considered, with the main focus on Ni-Cu and its size control in addition to Ni-Co. The characteristics of the NPs in dependence of the synthesis conditions and their catalytic performance in the RWGS reaction are investigated. The composition and element distribution of the bimetallic NiCu NPs and the impact on the catalytic activity should be determined.

2 Literature Review

In the following chapter a brief description of the important aspects including nanoparticles, their synthesis and analytics, and the RWGS reaction.

2.1 Brief Introduction to Nanoparticles

Richard Feynman gave prospect into the nanotechnology we achieved nowadays in his famous lecture "There's Plenty of Room at the Bottom" in 1959.[27] Nanomaterials bridge the gap between atomic or molecular structures and bulk materials. Nanomaterials are defined as nano-objects with at least one external dimension in the nanoscale, which ranges from 1 to 100 nm (ISO/TS 27687:2008).[1]
In contrast with size independent chemical and physical properties in bulk material, nanomaterials often show size-dependent optical, magnetic, chemical and catalytical properties.[28,29] The band gap between the valence and the conduction band increases with decreasing size, the melting point is decreased in very small particles, the mechanical strength in nanomaterials is high due to a lower probability of defects, the optical properties and colour highly depend on the particle size, ferromagnetism shifts to supermagnetism, and NPs show high catalytic efficiency compared to bulk material.[30] In solids in the nanometer size range, quantum effects can dominate the behaviour of materials such as electric/conducting, magnetic and optical properties, described by the quantum size effect.
Another stark difference between bulk and nanomaterials is the surface-to-volume-ratio. The ratio increases with decreasing particle size leading to an increasing number of surface atoms. These atoms on the surface exhibit a higher potential energy due to the surface tension and are less strongly bound. Due to the high surface-to-volume-ratio and the resulting reactivity, NPs have great potential as catalysts.[31]
Ni NPs are used to catalyze various organic reactions including the hydrogenation of olefins,[15] the reduction of aldehydes and ketones,[32] the chemoselective oxidative coupling of thiols,[16] and α-alkylation of methyl ketone.[33] They can also be employed as catalyst for the hydrogen oxidation at the anode in the field of platinum-group-metal-free hydrogen exchange membrane fuel cells[34] or as catalyst for the fabrication of carbon nanotubes.[35] They are furthermore used in biomedicine due to their good antibacterial and anti-

inflammatory activities[36,37] and their cytotoxicity against cancerous cells.[38,39] They can be used for the adsorption of hazardous dyes or inorganic pollutants,[40] in photovoltaics[41] and in smart windows.[42] The ferromagnetic behaviour of Ni NPs can furthermore be used to realize memory applications for long-term data storage[43] and various magnetic applications.[44]

2.1.1 Nanoparticle Synthesis and Formation Mechanisms

There are numerous physical and chemical ways for the preparation of NPs. Physical methods often rely on a "top down" approach using laser ablation, ion sputtering, or mechanical subdivision of bulk material into smaller units. This approach comes with several disadvantages as limited particle size, broad size distribution and possible chemical and physical changes due to local heat and force formations.[45] Chemical methods for NPs in general use a "bottom up" approach based on solid state, gas phase, or liquid state methods such as wet chemical or thermal reduction of metal precursors, vapour deposition, hydrothermal synthesis, sol-gel processes, and spray or laser pyrolysis.[46] Gas phase processes are conducted at elevated temperatures up to over 1000°C in complex setups. Solid state methods generate low volumes of material and are expensive.[46] The wet chemical approach instead is simple, fast and versatile and offers the opportunity to control the reaction process.[47] It includes the reduction of dissolved metal precursors in aqueous or non-aqueous solvents with organic or inorganic reducing agents followed by their nucleation and growth to particles.[48,49] A number of methods have been adapted for the preparation of metal NPs, including photolytic reduction,[50] radiolytic reduction,[51] sonochemical method,[52,53] solvent extraction reduction,[54] microemulsion technique,[53] polyol process,[55] and thermal reduction.[49,56–58] The production of Ni NPs requires more drastic conditions compared to noble metal NPs. The redox potential of Ni ($E_0(Ni^{2+}/Ni^0) = -0.23V$) is significantly lower than gold ($E_0(Au^{3+}/Au^0) = 1.5V$) and silver ($E_0(Ag^+/Ag^0) = 0.8V$). Therefore, strong reducing agents such as hydrazine (N_2H_4), sodium borohydride ($NaBH_4$), or oleylamine at higher temperatures are necessary for the reduction of Ni.

In wet chemical approaches in water mostly Ni chloride ($NiCl_2 \cdot 6\,H_2O$) is reduced by N_2H_4 under basic conditions. Moderate reaction temperatures of room temperature up to around 60°C are used and the NPs are stabilized by surfactants like cetyltrimethylammonium bromide/tetradodecylammonium bromide (CTAB/$TC_{12}AB$).[59,60] Alternative approaches in water use $Ni(NO_3)_2$ with $NaBH_4$ as reducing agent.[61,62] In general it is difficult to synthesize Ni NPs due to their sensitivity to oxidation. An alternative route are microemulsions, such as Kumar *et al.*[63] used, or changing to an organic solvent such as ethanol or ethylene glycol.[64] Polymers are often used as stabilizers, such as

PVP or glycoles.[55,65] In the polyol method glycoles are both solvent and stabilizer enabling the synthesis of mono- and bimetallic Ni NPs.[66,67] The nucleation with hydrazine and sodium borohydride as reducing agents is often swift and thus hard to control and monodisperse NPs in a broad range of size is often not achieved.

The thermal reduction at elevated temperatures uses long-chain amines and phosphines as stabilizers. Most commonly used are oleylamine (OAm) and trioctylphosphine (TOP). Ni complexes such as nickel(II) acetate (Ni(acac)), nickel(II) acetylacetonate ($Ni(acac)_2$) and bis(1,5-cyclooctadiene)nickel(0) $Ni(COD)_2$ serve as precursors. The latter decomposes already at 60 °C providing the necessary nucleation seeds. However, $Ni(COD)_2$ is extremely sensitive to oxidation and is therefore less commonly used than $Ni(acac)_2$.[68] For Ni(II) acetate and $Ni(acac)_2$, the temperature applied for the formation of Ni NPs is mostly above 200°C.[69] However, by using a mild reducing agent such as tributylamineborane, Metin *et al.* succeeded in preparing Ni NPs even at 90 °C.[70] And Wang *et al.* were able to prepare triangular and hexagonal Ni nanosheets at 160°C with the aid of tungsten hexacarbonal.[48] Most commonly OAm is used in large excess, since it serves both as solvent and as reducing agent. Carenco *et al.* were able to prove, using $Ni(acac)_2$, that at least three equivalents of the amine are necessary for the formation of Ni NPs.[71]

Various preparation methods are utilized for bimetallic Ni NPs. Pd-Ni core-shell NPs could be prepared via hydrothermal synthesis,[72] Ag@Ni and Au@Ni NPs were achieved by a two step thermal reduction.[73,74] Ni-Co core-shell NPs were achieved via microwave assisted synthesis[75] and two step thermal reduction.[76] Bimetallic Ni Co NPs for catalytic purposes are used for dry reformation of methane[77,78] and the Fischer-Tropsch reaction.[79] Bimetallic NiCu NPs could be prepared via hydrothermal reduction[80] and thermal reduction adaptations using standard air-free methods,[81] with borane tributylamine as reducing agent in OAm under Argon,[82] and pure OAm as solvent.[83]

Most theoretical descriptions of nucleation processes are based on the classical nucleation theory (CNT), which was developed by Becker and Döring in 1935.[84] Therein they described the condensation of liquid droplets from a supersaturated vapor phase in a thermodynamic manner.[85] This approach was further modified and extended to other types of phase transitions,[86,87] allowing the description of precipitation and crystallization of solids from solution. The CNT is based on the macroscopic Gibbs capillary effect, which means that the macroscopic surface energy is taken to develop mathematical expressions for the nucleation rate.[84,88–90] It can be distinguished between homogeneous and heterogeneous nucleation in this context. Homogeneous nucleation occurs spontaneously, randomly and uniformly throughout the parent phase, but requires a supercritical state such as a supersaturation. In contrast, heterogeneous nucleation oc-

curs at nucleation sites on solid surfaces contacting the liquid or vapour phase. This thermodynamic theory was transferred to nucleation and growth processes of NPs by LaMer in the 1950s[91,92](Figure 2.1). Since the CNT only describes the nucleation, the particle growth is separated and can be described via different growth processes such as reaction-limited or diffusion-limited growth, aggregation or Ostwald ripening.

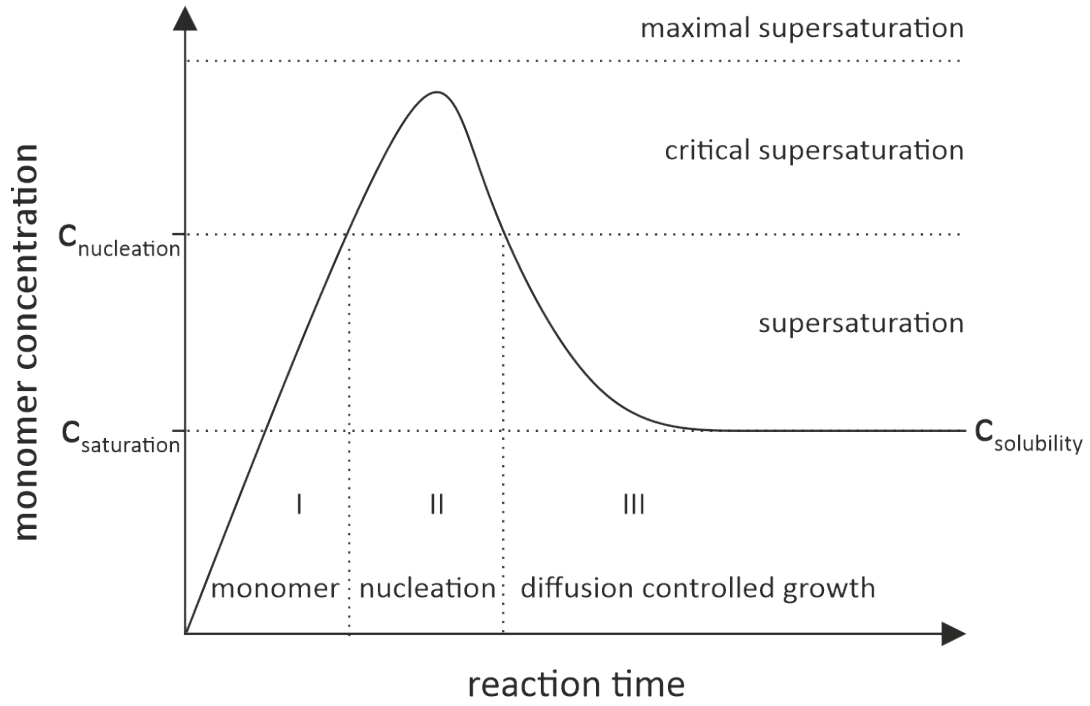

Figure 2.1: LaMer mechanism for nucleation and growth.[91,92]

In the monomer phase (phase I) the steady reduction of metal ions to atoms leads to an increasing monomer concentration and homogeneous nucleation after supersaturation ($C_{saturation}$) of the solution. In the nucleation phase (II) homogeneous "burst-nucleation" occurs as soon as the critical supersaturation level ($C_{nucleation}$) is reached. This level marks the activation energy barrier for nucleation causing rapid self-nucleation as soon as it is overcome. By this burst-nucleation the supersaturation decreases to ($C_{nucleation}$) thus ending the nucleation period. During the final phase (III) particle growth by monomer diffusion to the particle surface occurs, which can be interpreted as heterogeneous nucleation/growth. Regarding the time scale phases I and II show a fast increasing and decreasing monomer concentration, whereas it is approximately constant during final growth (III). Nanoparticle growth is dependent on the number of particles, the concentration of metal atoms and the diffusion coefficient.[91,92] To obtain small NPs with a narrow size distribution, fast nucleation and slow growth is favoured. This leads to a high concentration of nuclei, which grow to particles. In contrast a slow nucleation

leads to fewer nuclei, which grow to larger NPs. Besides the nucleation rate also the concentration and type of stabilizing agents influence the final particle size.[93]

2.1.2 Important Interactions and Processes

Particles in the nanometer-scale are unstable and tend to aggregate due to attraction via van-der-Waals, electrostatic, or magnetic interactions at short interparticle distances. These particles can be stabilized by counteractive repulsive forces such as steric and electrostatic stabilization.[94]
Although agglomeration and aggregation both characterize an accumulation of objects, they differ in their interparticle interactions. Both describe a process that is mass-conserving, but numberreducing and thus shifting the particle distribution towards larger sizes.[95] Both processes are defined by the ISO/TS 8004-2:2015[95] and depicted in Figure 2.2 a-b. During agglomeration, particles interact weakly thus retaining the total surface of the initial particles in the agglomerate. In contrast aggregates exhibit a significantly smaller external surface compared to the individual particles, which aggregated, due to a strong bond or fusion.

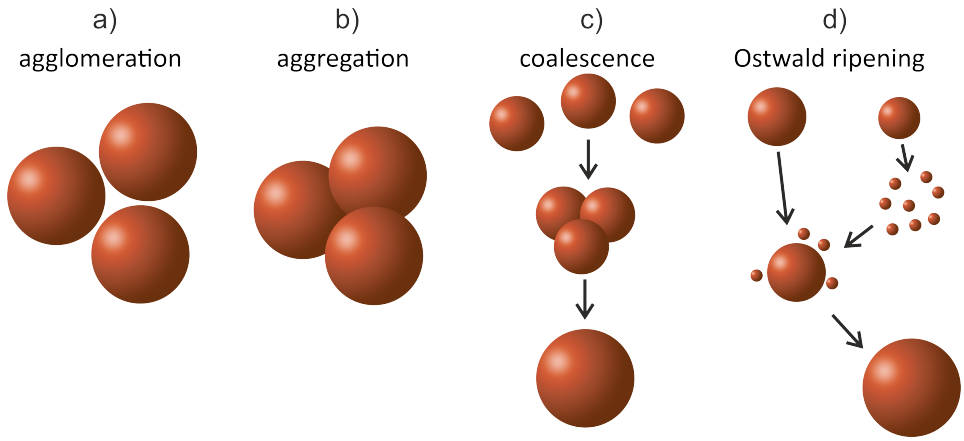

Figure 2.2: Important nanoparticle interactions and processes; such as a) agglomeration, b) aggregation, c) coalescence, and d) Ostwald ripening.

Coalescence is defined as a "process in which two phase domains of essentially identical composition in contact with one another form a larger phase domain. Coalescence reduces the total interfacial area" in the IUPAC Compendium of Chemical Terminology.[96] Thus, coalescence describes a merging of formed aggregates forming a larger particle with strongly reduced total surface energy, as depicted schematically in Figure 2.2 c.
Ostwald ripening (first described by Wilhelm Ostwald more than 100 years ago)[97] occurs during particle formation when the monomers are almost consumed for particles growth. It describes the dissolution of small particles into smaller units (like monomers) due to

their high chemical potential, and their subsequent redeposition on the surfaces of larger particles as schematically depicted Figure 2.2 d. Normally Ostwald ripening does not occur for metallic NPs,[98] which indicates that the bond of monomers to the metallic crystals is to strong or irreversible.

2.1.3 Nanoparticle analytics

A variety of advanced analytical methods are needed to investigate and characterize NPs concerning size, shape, material, surface properties, and structure.[99,100] Quantitative techniques such as mass spectrometry (MS) or spectrophotometry provide mass- or particle number concentrations.[101,102] Also the chemical composition can be determined by MS, nuclear magnetic resonance spectroscopy (NMR), and energy dispersive X-ray spectroscopy (EDX).[103,104] High pressure liquid chromatography combined with inductively coupled plasma MS (HPLC-ICP MS) was used for the quantification of silver NPs as well as asymmetric flow field flow fractionation (AF4) combined with ICP MS for the quantification of functional groups on the surface of polystyrene NPs.[101,105] While MS offers high accuracy and precision it requires expensive equipment. NMR spectroscopy is a non-destructive, but time-consuming and expensive method and limited to certain nuclei. The structure of NPs can be investigated using for example NMR and X-ray diffraction (XRD), while NMR gives insights in the local environment, XRD provides information about the crystal structure.[58,106,107] XRD is well-established but it is limited to crystalline materials while NMR can also be applied to amorphous materials. With X-ray absorption spectroscopy (XAS) element specific information of electronic structure and local geometry can be achieved. The amount of sample needed and the averaging over a longer time period is a drawback for NP analysis. Surface properties such as composition, structure, and charge can be determined by X-ray photoelectron spectroscopy (XPS), atomic force microscopy (AFM), and zeta potential measurements. XPS offers an atomic composition profile of the nanoparticle surface,[108] AFM results in a 3D surface map revealing the structural features of the surface,[109] and the surface charge can be determined using zeta potential measurements.[110] Magnetic properties of NPs are investigated by vibrating sample magnetometers (VSM).[111] Imaging techniques such as transmission electron microscopy (TEM), scanning electron microscopy (SEM) and AFM are used to determine shape, size, and its distribution. AFM uses a cantilver, which is moved over the sample surface, while TEM and SEM use electrons, which are backscattered or transmitted resulting in contrast images depending on the density of the sample. TEM and AFM offer a very high spatial resolution, which is limited in SEM. Mean size and size distribution can also be identified by scattering methods like dynamic light scattering (DLS) and small angle X-ray scattering (SAXS). DLS gives

the hydrodynamic size distribution while it is limited by an intensive impact of small numbers of large particles. SAXS is also a non-destructive method with a simple sample preparation. A main difference between the microscopic imaging approaches like TEM and the scattering approaches like SAXS for size determination is the amount of sample investigated. TEM gives insights into microscopic volumes of a sample while SAXS takes a vastly larger sample volume into account, which is more representative of the bulk material.[112] The limitation of microscopy on a small area is compensated by the real space image which is gained in contrast to SAXS, where a large volume is taken into account while hte ambiguity of the data is a drawback. A multitude of solutions might be valid for a set of collected scattering intensities. By knowing or assuming the shape and packing of a sample solution the size and its distribution can be obtained. This knowledge can be achieved by combining TEM and SAXS.[113] An example of the combination of techniques was reported for in situ nanoparticle growth and crystallization investigated by SAXS and XAS utilizing an acoustic levitator as shown by Kabelitz *et al.*[114]

2.2 Synthesis Gas and Reverse Water Gas Shift Reaction

The concentrations of green house gases like CO_2, CH_4, and N_2O in the earth's atmosphere have been increasing for decades. These gases are considered the main cause of global warming, climate change, rising sea level, increased frequency of extreme weather events and glacier melting. From anthropogenic sources approximately 66 % are ascribed to CO_2.[19] CO_2 is also the main reason for ocean acidification, which seriously threatens the survival of marine organisms.[115,116] This negative trend might be stopped through CO_2 capture and storage (CCS) and CO_2 capture and utilization (CCU). CO_2 CCS of industrially produced CO_2 in porous sediment layers in approx. 900 m depths[117] is discussed controversially. The environmental risks of a possible release of CO_2 cannot be assessed.[118] Since all carbon on earth is in a cycle, it is only a matter of time before the stored CO_2 is released back into the atmosphere. Furthermore, the storage of CO_2 involves considerable costs that are not matched by any added value, so that CCS technology must be considered a transitional solution, if at all. Alternative to the storage method is the usage of the pollutant CO_2 as energy source and carbon source. So far only urea, salicylic acid and carbonate are industrially produced from CO_2[119] due to the thermodynamic stability of CO_2 demanding harsh conditions such as thermal and electrical energy and catalyst. The improvement of catalysts may lead to CO_2 not only

being considered as a pollutant but also as a useful carbon source in the future. The conversion of CO_2 to synthesis gas (syngas), a mixture of CO and H_2, has been recognized as one of the most promising processes for CO_2 utilization.[120] In this case, the conversion of CO_2 to syngas plays a key role in the production of important industrial chemicals and synthetic fuels.
The CO_2 emission can be reduced by catalytic CO_2 conversion with renewable energy, such as wind power, solar energy, hydropower, and biomass.[121]
In the future it will be even more important to increase the efficiency of energy production since fossil resources are limited. One possibility for this is the conversion of conventional fuels such as coal and natural gas into syngas and hydrogen. Steam reforming of methane (SRM) from natural gas is the main reaction to produce syngas and it is mainly used for H_2 production. It is a strongly endothermic reaction and leads to volume expansion (see Equation 2.1). Due to the principle of Le Chatelier it is performed at high temperatures and low pressure.
In principle any solid, liquid of gaseous hydrocarbon and even biomass can be used as raw material, thus distinguishing between gas-to-liquid (GtL), coal-to-liquid (CtL), and biomass-to-liquid (BtL).[122] This variety of raw materials makes the production process very flexible and it can be adapted to local conditions. For cost and process reasons, only the GtL process is currently of interest, whereby mainly natural gas from sources that are currently not economically developed serves as raw material (stranded gas).[123]

$$SRM \qquad CH_4 + H_2O \rightleftharpoons CO + 3\ H_2 \qquad \Delta_R H = 206\ kJmol^{-1} \tag{2.1}$$

$$DRM \qquad CH_4 + CO_2 \rightleftharpoons 2\ CO + 2\ H_2 \qquad \Delta_R H = 247\ kJmol^{-1} \tag{2.2}$$

$$POX \qquad CH_4 + 0.5\ O_2 \rightleftharpoons CO + 2\ H_2 \qquad \Delta_R H = -36\ kJmol^{-1} \tag{2.3}$$

$$ATR \qquad CH_4 + 0.5\ O_2 \rightleftharpoons CO + 2\ H_2 \qquad \Delta_R H = -36\ kJmol^{-1} \tag{2.4}$$

$$CH_4 + H_2O \rightleftharpoons CO + 3\ H_2 \qquad \Delta_R H = 206\ kJmol^{-1} \tag{2.5}$$

Alternative technologies for the syngas production starting from methane include dry reforming of methane (DRM), partial oxidation (POX), and autothermal reforming (ATR). As shown in Equation 2.2 DRM is endothermic and volume expanding and requires thereby high temperatures and low pressures with for example Ni-based catalysts.[11] Compared to SRM, DRM produces a stoichiometric mixture of CO and H_2. POX is used for the conversion of biomass to syngas.[124] The partial oxidation of methane, as shown in Equation 2.3, is exothermic and therefore conducted without additional heating at atmospheric pressure. The ATR combines SRM and POX (see Equation 2.5). The exothermic POX of methane to CO and water delivers the reaction partner for further methane to be reformed to CO and hydrogen. Overall a 2:1 ratio of H_2 to CO

is achieved, which is an optimum for the further use of the product gas mixture for the Fischer-Tropsch synthesis (FTS).[125] A disadvantage of the POX and ATR is the use of oxygen for oxidation and the associated process costs. The production of oxygen accounts for up to 40% of the total costs for synthesis gas production. In principle, oxygen could be replaced by air, but the high nitrogen content in the synthesis gas mixture is a disadvantage.[126,127]

Syngas can also be synthesized starting from CO_2 using the RWGS reaction. CO_2 e.g from the atmosphere is split catalytically using hydrogen at elevated temperatures due to the endothermic reaction. The RWGS reaction was first observed by Wild and Bosch in 1914, when they attempted to produce H_2 from CO and steam on an iron oxide catalyst.[128] The RWGS reaction is currently a field of extensive studies[23,129] and it is important in the synthesis of methanol[120] and in adjusting the H_2/CO ration of syngas for various applications.

Different routes to transform CO_2 into liquid fuels using solar assisted processes and H_2 provided by electrolysis were compared by Mallapragada *et al.*[130] The investigated methods included biomass gasification, RWGS, algae-derived oils, and direct photosynthesis. The conversion of CO_2 to CO by RWGS reaction followed by CO conversion to fuels with FTS had the highest current and estimated potential efficiency when CO_2 is captured from a waste gas or from the atmosphere.[130]

$$CO_2 + H_2 \rightleftharpoons CO + H_2O \qquad \Delta_R H = 41\ kJmol^{-1} \tag{2.6}$$

CO_2 represents the most stable component of all carbon- and oxygen-based molecules and acts as inert in many reactions.[125] Therefore the price to induce reactivity has to be paid, but compared to DRM, SRM, and ATR the thermodynamics of the RWGS appear to be more favourable. If economical and stable conditions can be developed for RWGS reaction, it can be coupled with CO-based industry, making the existing processes overall carbon neutral.[131]

Supported noble metal catalysts, such as Au,[132,133] Pd,[134] Pt,[135] Rh,[136] and Ru[137] are the most active catalysts. They show high activity towards dissociation of H_2 and CO_2 conversions close to the equilibrium and are resistant to coking and corrosion. But their cost and limited availability as depicted in Figure 2.3 requires the development of cheaper and more abundant catalysts, mainly of 3d transition metals such as Cu,[23] Ni,[14,23–25,138] Fe,[139] and Co.[140]

The reaction mechanism of the RWGS reaction was studied by Roiaz *et al.* under near ambient pressure on pure Ni(110) stable surface. They resumed that CO_2 is chemisorbed on the Ni(110) surface and acts as precursor for the dissociation to CO and O, which is converted to water by the H_2. This chemisorbed activated CO_2-species was found to be

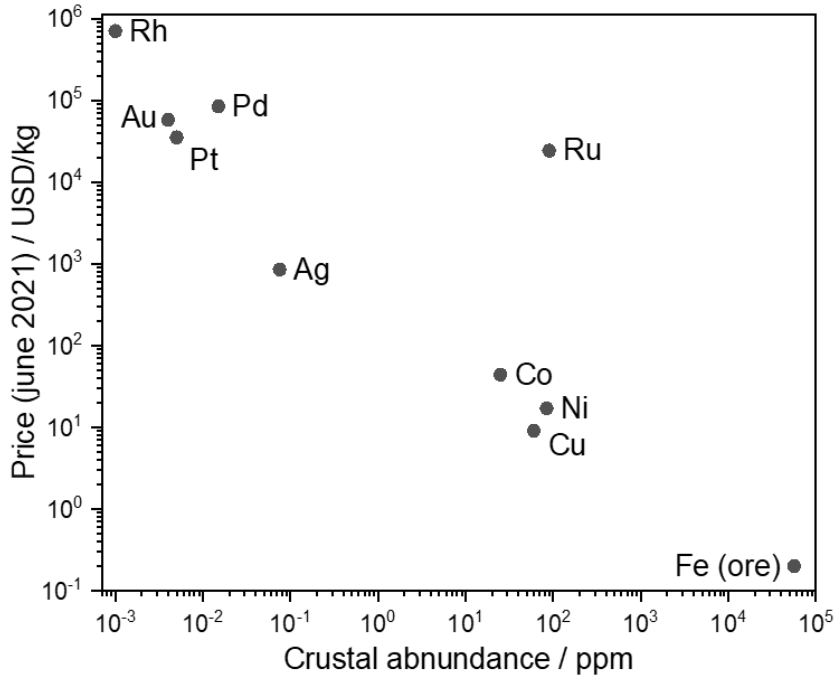

Figure 2.3: Price versus crustal abundance (in parts per million) for selected elements.[141,142]

also the reactive species for the full reduction of CO_2 to CH_4 within the Sabatier reaction.[143] Yang *et al.* investigated the mechanism on Rh/TiO_2 as part of the methanation using density functional theory calculations confirming the adsorption of CO_2 on the surface. But they found a preferred pathway via an adsorbed(*) COOH* species, which dissociates into CO* while forming water, which was identified as the rate-determining step.[144] Rodriguez *et al.* found both mechanisms named above for the RWGS reaction over $Cu_4/TiC(001)$, with HOCO being a key intermediate, as examined by density functional theory-based calculations.[145] The pathways of the CO_2 hydrogenation by NiCu/ZnO was investigated by Dziadyk with molecular dynamics simulations with the DFT methodology. They considered the CO_2 dissociation after adsorption via two different kinetically feasible pathways. Either by dissociating the C-O bond at the wall of the nanocluster consisting of Ni and Cu or with the cleaved oxygen forming a bridge between two Ni sites.[146] The RWGS reaction can be driven using excess energy from renewable energy sources. In a first step hydrogen and oxygen are generated via electrolysis of water driven by renewable energy. The hydrogen is converted with CO_2 from the atmosphere to syngas via the RWGS reaction. The syngas can be utilized in various processes as discussed earlier. These steps are summarized in the Power-to-Syngas concept depicted in Figure 2.4, which can become a cornerstone of a sustainable energy system.[147]

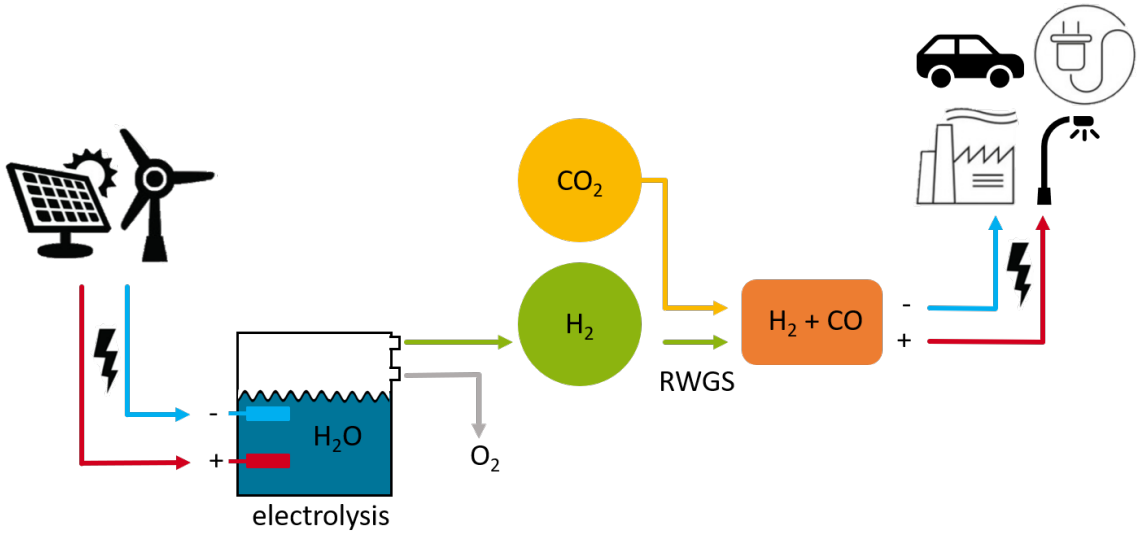

Figure 2.4: Schematic depiction of the Power-to-Syngas concept. Adapted from Rueter.[148]

In principle, syngas can be utilized in two different ways. Either by maximizing the hydrogen yield or by directly converting into synthetic fuels or industrial chemicals (see Figure 2.5). The purification of the hydrogen is achieved by e.g. using the WGS reaction to convert the CO to CO_2 or by cryogenic purification. The hydrogen is stored in various manners such as gaseous (compressed hydrogen), liquid, chemically (metal hydrides), or physically in metal organic frameworks (MOFs).[149] It is later used in fuel cells/ hydrogen engines, H_2-gas stations, gas distribution systems, methanation, higher hydrocarbons, or the Haber-Bosch-process producing ammonia used for e.g. fertilizers.[150] In Germany 55 TWh of hydrogen is used for industrial applications every year, mostly produced by DRM.[151] Syngas can be directly used for the direct reduction of iron ore to iron sponge[152] or in the FTS to produce diesel and other hydrocarbons. The FTS is a

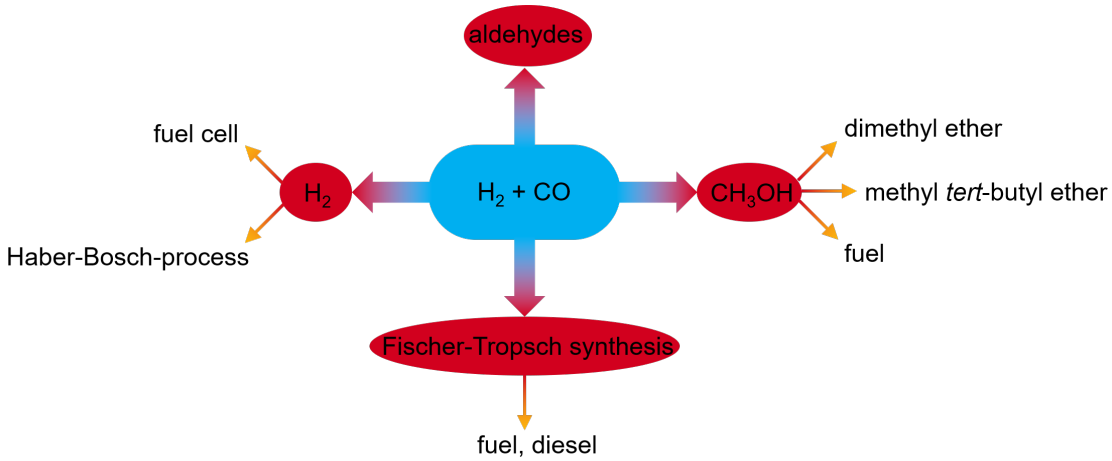

Figure 2.5: Different approaches for the utilization of synthesis gas.

reductive oligomerization process catalysed by Fe or Co taking place at low temperatures and pressures.[153] Saturated and unsaturated hydrocarbons are the main product, which can then be converted into fuels such as diesel, gasoline or heating oil via hydrocracking. Another important utilization of CO is the production of methanol. CO and hydrogen react to methanol over a catalyst, the most widely used catalyst nowadays is a mixture of Cu and ZnO, supported on alumina, as first used by Imperial Chemical Industries Ltd in 1966.[154] Besides its use as a solvent, it can also be used as a transportable fuel. Derivatives of methanol such as dimethyl ether and methyl *tert*-butyl ether are already used in fuels. Methanol is also an important starting material for the industrial production of formaldehyde, formic and acetic acid. A last significant use of synthesis gas is in hydroformylation, where olefins are converted to aliphatic aldehydes using Co and Rh complexes. These can be further hydrogenated to alcohols and then used for the production of fine chemicals.

3 Materials and Methods

3.1 Materials

All chemicals were used without further purification and are mentioned in Table 3.1 with purity and supplier.

Table 3.1: Used chemicals with purity and supplier.

chemical	**molecular formular**	**purity**	**supplier**
Oleylamine	$C_{18}H_{37}N$	C18-content 80 - 90%	Acros Organics
Trioctylphosphine	$C_{24}H_{51}P$	97 %	abcr GmbH
Trioctylphosphine	$C_{24}H_{51}P$	90 %	Sigma Aldrich
Nickel(II)acetylacetonate	$C_{10}H_{14}NiO_4$	96 %	Acros Organics
Copper(II)acetylacetonate	$C_{10}H_{14}CuO_4$	98 %	Acros Organics
Cobalt(II)acetylacetonate	$C_{10}H_{14}CoO_4$	99 %	Acros Organics
Dibenzylethene	$C_{16}H_{16}$	99 %	Acros Organics
n-Hexane	C_6H_{14}	99.0 %	CHEMSOLUTE
Acetone	C_3H_6O	99.5 %	CHEMSOLUTE
Ethanol	C_2H_6O	99.9 %	CHEMSOLUTE
2-Propanol	C_3H_8O	99.8 %	CHEMSOLUTE
Acetone dry	C_3H_6O	99 %, <0.01 % water	PanReac
Ethanol dry	C_2H_6O	99.5 %, <0.005 % water	Acros Organics
Ethyl acetate pure	$C_4H_8O_2$	99.95 %	CHEMSOLUTE
Ethyl acetate	$C_4H_8O_2$	99.5 %	CHEMSOLUTE
Simvastatin	$C_{25}H_{38}O_5$	99.3 %	Jubilant Organosys
Boron nitride	BN	99.5 %	Alfa Aesar
GRACE (porous SiO_2)	SiO_2		Grace GmbH

3.2 Nanoparticle Synthesis

All syntheses were performed under nitrogen atmosphere in 20 mL vials sealed with a septum (butyl/PTFE) in a screw cap. These vials were heated to reaction temperature in a dry heating block (IKA, Staufen, Germany, DB 5.6) on a heating plate (IKA, Staufen, Germany). In a typical synthesis of monometallic NiNPs, varying volumes (5 mL-10 mL) of oleylamine (OAm) were added to 0.25 mmol nickel acetylacetonate ($Ni(acac)_2$) at room temperature and the total volume was kept constant by adding dibenzyl ether (DBE). After degassing the reaction solution by flushing it with a stream of nitrogen for two minutes, the solution was heated to 100 °C and kept for 10 minutes. After the addition of trioctylphosphine (TOP), the solution was degassed again with a nitrogen stream for two minutes and heated to 220 °C reaction temperature for two hours. The temperature profile of the heating block and the reaction solution is shown in Figure 3.1. After cooling the solution to room temperature, an excess of acetone was added to the solution, the solution was centrifuged (4000 rpm, 4 min) and the supernatant was decanted. The nanoparticles were then redispersed in n-hexane. For analysis, 250 µL reaction solution was mixed with 750 µL acetone in an Eppendorf vessel, centrifuged in a benchtop centrifuge, decanted and then redispersed in 750 µL n-hexane. The synthesis of bimetallic NiCu- and NiCo-nanoparticles was carried out according to the synthesis of pure nickel nanoparticles with varying ratios of the metal salts $Ni(acac)_2$ and copper(II) acetylacetonate ($Cu(acac)_2$) respectively cobalt(II) acetylacetonate ($Co(acac)_2$).

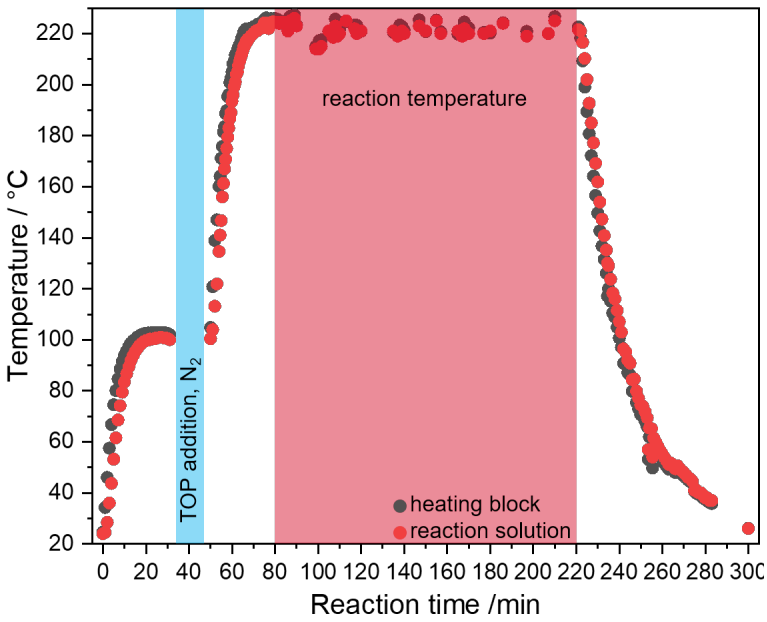

Figure 3.1: Temperature profile during the synthesis of nanoparticles of th aluminium heating block (black) and the reaction solution (red).

3.3 Methods

Various X-ray-based methods were used to characterize the mono- and bimetallic nanoparticles. X-rays are electromagnetic radiation in the wavelength range of 10^{-3} to 10^{1} nm or an energy range of 3 to 500 keV. In the used laboratory equipment, X-rays are generated in an X-ray tube under high vacuum. By applying a high voltage, electrons generated at a cathode are accelerated towards a high-purity metal anode. They expel inner electrons from the anode material. The holes in inner shells are filled up by electrons from outer shells, emitting X-ray radiation characteristic of each transition. These X-ray lines are designated by a capital letter (K, L, M, etc.), which stands for the shell into which the electron is transferred. In addition, a Greek letter indicates the difference between the principal quantum numbers n of the shells between which the transition takes place (α when $\Delta n = 1$, β when $\Delta n = 2$, etc.). The X-ray lines of these transitions further split up by the fine structure splitting. These result from the interaction of orbital angular moment (l) ($l \leq n\text{-}1$) and spin moment (s) ($+\frac{1}{2}$, $-\frac{1}{2}$) leading to the total angular moment (j) ($j = l \pm s$). These transitions are called $K_{\alpha 1}$ and $K_{\alpha 2}$. Since all characteristic X-rays are emitted simultaneously, a monochromator (e.g. metal filter, single crystal) is used to obtain monochromatic radiation of most often K_{α}.

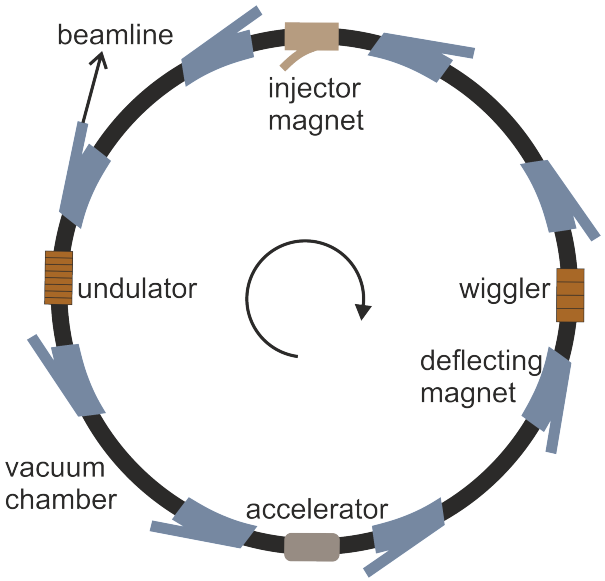

Figure 3.2: Schematic depiction of a synchrotron storage ring. The circular arrow indicates the direction of the electron beam current, after reference.[155]

An increased efficiency of the experiment can be achieved by using synchrotron radiation. The X-ray beam is very intense, has a high flux, and the radiation is precisely collimated, allowing a higher angular resolution. The wavelength can be adjusted to suit the sample for measurement.[155] Synchrotron radiation is produced when electrons are accelerated or

change direction. Electrons are accelerated to almost the speed of light in high vacuum tubes and guided along a circular path by magnets. These magnets can be bending magnets, wiggler, undulators, or wavelength shifter. The bending magnet keeps the electrons on their circular path. During the deflection process, the electrons emit a large part of their energy in form of Bremsstrahlung.[156] The wiggler and undulator (both insertion devices) consist of a series of magnets whose magnetic fields vary sinusoidal forcing the electrons to oscillate. The relatively large oscillation in a wiggler increases the intensity of the emitted radiation as a continuous spectra just like the bending magnets. In the undulator a higher number of smaller oscillations lead to the interference of the emitted radiation resulting in a more brilliant beam with a fundamental and its harmonic energies. By changing the vertical gap between the array of magnets in the insertion devices the wavelength of the X-rays in the beam can be tuned. The desired wavelength from the polychromatic synchrotron radiation can be selected using monochromators. Compared to laboratory devices short measuring times can be achieved as well as a better penetration of the material due to the high photon flux at the synchrotron.[155]

3.3.1 Small Angle X-ray Scattering

Small angle X-ray scattering (SAXS) is a powerful method to characterize size, size distribution and form of nanostructured systems in which the elastic scattering of X-rays of a sample is recorded at very small angles. The smallest accessible angle determines the largest resolvable feature size according to Bragg´s law. Compared to imaging techniques, based on electron microscopy, all particles in the system are investigated.[157]

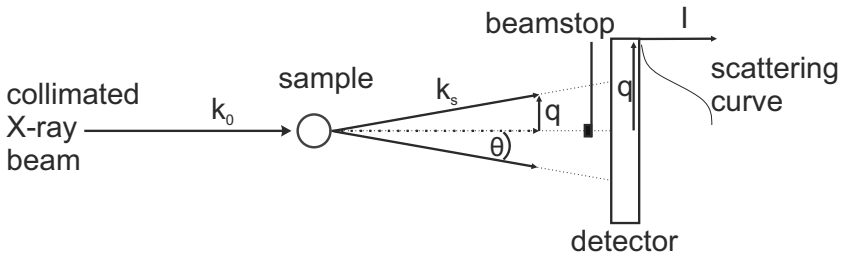

Figure 3.3: Depiction of a SAXS setup, consisting of a monochromated, collimated X-ray beam, the sample and the detector. A scattering curve as a function of the scattering vector q is shown behind the detector.

The scheme of a typical SAXS experiment is shown in Figure 3.3, in which a collimated and monochromatic X-ray beam with the wavelength λ hits the sample. The scattered photons at small angles are collected while the primary beam is blocked by a beamstop. X-ray scattering at small angles is assumed to be fully elastic and coherent,[158] hence, the scattered intensity is proportional to the number of electrons in the sample and the magnitude of the wave vectors of the incident and the scattered beam are equal:

$$|\boldsymbol{k}_0| = |\boldsymbol{k}_\mathrm{s}| = \frac{2\pi}{\lambda} \tag{3.1}$$

Assuming two scattering centers in a nanoparticle as depicted in Figure 3.4, the difference between the scattered beam is the optical path difference δ, which can be described by the vector $\boldsymbol{r}$

$$\delta = \boldsymbol{r}(\boldsymbol{k}_0 - \boldsymbol{k}_\mathrm{s}) \tag{3.2}$$

leading to a phase shift x of

$$x = \frac{2\pi}{\lambda}\delta = -(\frac{2\pi}{\lambda})\boldsymbol{r}(\boldsymbol{k}_\mathrm{s} - \boldsymbol{k}_0) \tag{3.3}$$

The scattering vector $\mathbf{q}$ is an important variable for SAXS and equals $\boldsymbol{q} = (\boldsymbol{k}_\mathrm{s} - \boldsymbol{k}_0)$, so the phase shift can be written as $x = -\boldsymbol{r} \cdot \boldsymbol{q}$. $(\boldsymbol{k}_\mathrm{s} - \boldsymbol{k}_0)$ has a magnitude of $2ksin(\theta)$ (see Figure 3.3) and $|\boldsymbol{q}|$ is given as Bragg´s law by

$$|\boldsymbol{q}| = q = 2 \cdot k \sin\theta = \frac{4\pi}{\lambda} \sin\theta \tag{3.4}$$

including λ as the wavelength and θ as half of the scattering angle, see Figure 3.3.

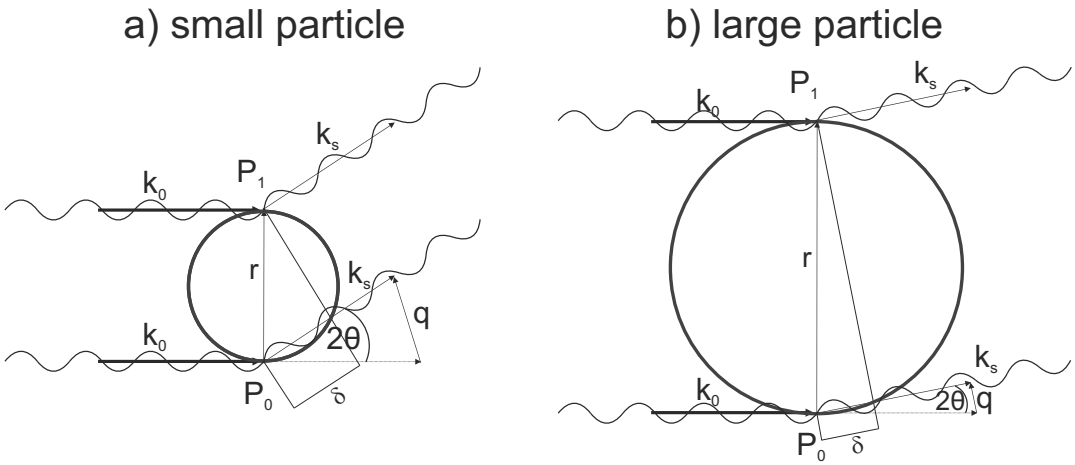

Figure 3.4: Illustration of the scattering process at two scattering centres P_1 and P_0 in a small a) and a large particle b). It highlights that for the same irradiated wavelength and the same path difference δ (phase difference), the scattering angle 2θ and the scattering vector q is larger for smaller particles than for large particles.[158] Thus, the scattering curve obtained on the detector for smaller particles shows a drop in intensity at larger q values.

The total scattered intensity I_{total} of colloidal systems is composed of the scattering of the colloidal particles $I_{particles}$, the solvent $I_{solvent}$, the capillary $I_{capillary}$, and the dark current I_{dc}.

$$I_{total} = I_{particles} + I_{solvent} + I_{capillary} + I_{dc} \tag{3.5}$$

$I_{particles}$ is the sum of all particles in the system. I_{total} can be calculated for a diluted colloidal solution, which is a system with non-interfering particles with a number distribution $N(r)$, a form factor $P(q)$ and the volume of the particle $V(r)$

$$I_{total} = \int_0^\infty N(r) \cdot (V(r)P(q))^2 dr \tag{3.6}$$

The SAXS measurements were performed with a Kratky type instrument (SAXSess, Anton Paar at 25 °C. An X-ray tube (40 kV / 40 mA) emitting Cu K_α radiation (λ = 0.1542 nm) was used as X-ray source. The scattered radiation was detected at a sample-detector distance of 303 mm with a microstrip X-ray detector (Mythen2 detector, Dectris, 8 mm x 50 mm. A flow capillary with a diameter of 1 mm served as sample holder. The measuring time was between 5 and 20 min, with an irradiation time of 10 s. For background correction n-hexane measurements with identical measurement conditions were performed. The used flow capillary was cleaned after each measurement with n-hexane, a 2 % Hellmanex solution, water and 30 % nitric acid. The successfull cleaning of the flow capillary was confirmed before each measurement by a reference measurement of water for about 2 min. The experimentally obtained scattering curves were background corrected and desmeared with the scattering curves of hexane and a beam profile using the program SAXSquant 4.2.4 (Anton Paar). Then the corrected scattering curves were approximated with a homogenenous sphere and a Schulz-Zimm distribution of the radius in the program SASfit 0.93.5.[159] In the Schulz-Zimm approximation the scattering intensity I(q, r) results from the form factor for a monodisperse sphere P(q, r, $\Delta\rho$)and the Schulz-Zimm distribution S(r) for the radius.

$$I(q,r) = S(r)P(q,r,\Delta\rho) \tag{3.7}$$

$$P(q,r,\Delta\rho) = \left(\frac{4}{3}\pi r^3 \Delta\rho \left(\frac{3(sin(qr)) - qrcos(qr)}{(qr)^3}\right)\right)^2 \tag{3.8}$$

$$S(R) = \frac{N}{r_a}\left(\frac{r}{r_a}\right)^{k-1} \frac{k^k e^- kr/r_a}{\Gamma(k)} \tag{3.9}$$

Where r is the mean radius and k is based on the polydispersity, $k = 1/\sigma^2$, where σ^2 corresponds to the valence. r_a is the scaling parameter that defines the size distribution for large k values, and N is the number of particles.[160] The scattering vector q is given by Bragg´s law (see Equation 3.15). As an alternative to the classical curve fitting approach using e.g. the Schulz-Zimm distribution, the Monte Carlo based regression package McSAS was applied.[161] It avoids any mathematical restrictions to the parameter distribution which analytical expressions typically imply. This method is based on a set of independent non-interacting contributions being defined by one or more fitting

parameters. For scattering data the method starts with a set of non-interacting scatterers of predefined shape (e.g. spheres), but with random values chosen for the fitting parameter(s). The total model scattering pattern is given by the (weighted) sum of the scattering patterns of each scatterer in the set. The optimization procedure progresses through replacement of contributions in the set. At the end, the spread of fitting parameter values of the contributions in this set defines the final parameter distribution. The detailed procedure is described elsewhere.[159,162] The corrected scattering curves were optimized using 300 contributions and 100 repetitions, respectively 1000 contributions and 10 repetitions.

3.3.2 Anomalous Small Angle X-ray Scattering

SAXS is based on the measurement of the differential scattering cross section $(\frac{d\sigma}{d\Omega})$ at a fixed X-ray energy, which is why the X-ray energy dependences are neglected in SAXS theory. Differences between the SAXS differential scattering cross sections are occurring in energy ranges near the X-ray absorption edges of an element present in the sample. Anomalous Small Angle X-ray Scattering (ASAXS) is based on that effect and utilizes the nonlinear energy dependence of the atomic scattering factor $f(E)$ of these elements (Equation 3.10) near their absorption edges. ASAXS consists of several SAXS measurements carried out at different energies near the absorption edge of an element and can be understand as a nanostructural and nanochemical characterization method, because the distinguished effect near the absorption edges makes the method element sensitive.[163] Therefore, ASAXS allows the determination of the spatial distribution of a specific element in or outside nanoobjects. The atomic scattering factor $f(E)$ equals the number of electrons of a given element (f_0) far from the absorption edge, but shows strong and nonlinear variations in the vicinity of an absorption edge. $f(E)$ is given near to an absorption edge of an element by:

$$f(E) = f_0 + f'(E) + i \cdot f''(E) \tag{3.10}$$

where E is the X-ray energy. The anomalous dispersion corrections $f'(E)$ and $f''(E)$ depend on the number of elements in the sample and the photon energy. They are both connected to each other by the Kramers-Kronig relation[164] and theoretically calculated and tabulated by Cromer and Liberman.[165] An example of $f'(E)$ and $f''(E)$ of the element Ni are shown in Figure 3.5a.

The total scattering intensity, $I(q, E)$, is in case of ASAXS a function of q and the X-ray energy, and can be written as linear combination of three independent scattering

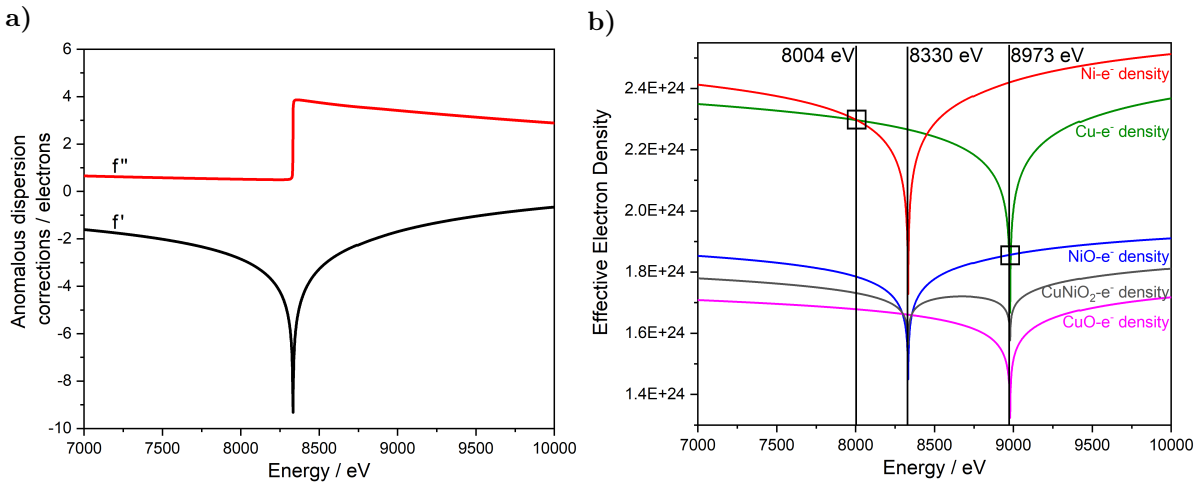

Figure 3.5: a) Variation of the real and imaginary part of the atomic scattering amplitude around the X-ray K-absorption edge of the element Ni at 8333 eV. The values are taken from Cromer and Libermann.[165] b) Energy dependences of the effective electron densities of Ni and Cu and some of their oxides calculated around their X-ray absorption edges of Ni (8333 eV) and Cu (8979 eV). Three energies (8004, 8330 and 8973eV), at which ASAXS was measured are marked with straight lines.

contributions after Stuhrmann[166]

$$I(q,E) = I_0(q) + f'(E)I_{sc}(q) + (f'(E)^2 + f''(E)^2)I_r(q) \tag{3.11}$$

where I_0 is the normal SAXS term, I_{sc} the scattering cross term, and I_r the pure resonant scattering.[166] By performing SAXS measurements on at least three X-ray energies near but below the absorption edge, I_r can be separated and information about the spatial distribution in nanosized structures of the resonant element can be achieved.[167]

The term b describes a background that is caused by the fluctuation scattering (density and composition) and near an absorption edge also by fluorescence and from resonant Raman scattering and needs to be added to the total scattering in Equation 3.6 giving:

$$I(q) = \int_0^\infty N(r) \cdot (Vp(r)P(q,r,\Delta\eta))^2 dr + b \tag{3.12}$$

The form factor, $P(q,r,\Delta\eta)$ depends on the shape and size r and on the electron density difference $\Delta\eta$. The contrast in SAXS depends on the electron density difference, $\Delta\eta$, between two nanosized regions. In case of a two phase system the differential scattering cross section is proportional to the squared electron density difference $(\Delta\rho(E))^2$ between the two phases:

$$I(q) = \frac{d\sigma}{d\Omega}(q,E) \propto (\Delta\rho(E))^2 = (\eta_{NP}(E) - \eta_s(E)) \cdot (\eta_{NP}(E) - \eta_s(E))^* \tag{3.13}$$

Here $\eta_{NP}(E)$ and $\eta_s(E)$ are the electron densities of the particle phase phase NP and the solution s. The star indicates a multiplication with its conjugate imaginary value, because in case of ASAXS the electron density becomes complex and will be assigned as an "effective" electron density (EED). The EED $\eta_i(E)$ of a phase i can be calculated with the composition and the macroscopic mass density ρ_i as shown in Equation 3.14.

$$\eta_i(E) = \rho_i \cdot N_A \cdot \sum_j \frac{f_i(E) \cdot c_j}{c_j \cdot M_j} \tag{3.14}$$

N_A is the Avogadro constant, j denotes the elements the phase consists of (e.g. Ni, Cu, O), c_j is the mole fraction of the element j and M_jMj denotes the molar mass. The effective electron densities of some relevant elements and compositions are calculated using these equations and are shown in Figure 3.5b.

ASAXS measurements were conducted at the FCM beamline (four-crystal monochromator) of the Physikalisch-Technische Bundesanstalt (PTB) (BESSY II, Helmholtz Zentrum, Berlin).[168] The scattering patterns were recorded with a 2D X-ray detector (Pilatus 1M). The incoming photon flux was permanently measured with a 8 micrometer thin Si-photodiode operated in transmission mode[169] and the transmitted beam intensity with a photodiode inside the beamstop. The samples are measured in 1 mm capillaries together with an empty capillary and the pure solution for a background subtraction. The scattering of glassy carbon was measured at every X-ray energy to scale the measured intensities to absolute units, which is necessary to derive the contrast variations with respect to the energies and $f'(E)$ and $f''(E)$. The magnitude of q was calibrated using the d-spacing of silver behenate measured with the samples at each energy. Ni and Cu have 28 and 29 electrons, respectively. Their X-ray K-absorption edges to be used for ASAXS are very close at 8333 eV and 8979 eV. Therefore, the anomalous behaviour of the two elements is not independent, but is overlapping as can be seen in Figure 3.5b. Moreover, the fluorescence appearing after the edges are increasing the angle independent scattering, which could cover scattering of smallest structural details. As a consequence and to avoid this negative effect, the ASAXS experiment was focused to the pre-edge region of Ni. SAXS was measured at 8 different X-ray energies, that are 7000 eV, 8004 eV, 8239 eV, 8304 eV, 8324 eV, 8330 eV, 8973 eV and 10000 eV. While 5 energies are near below the Ni-K edge, the 7 keV and 10 keV are chosen far from the edges and 8973 eV is near the Cu absorption edge. Ni and Cu exhibit the same EED at 8004 eV, as shown in Figure 3.5b, while being much higher than the oxides. Very close to the Ni K-edge at 8330 eV the EED of Cu is much higher than Ni, which turns around at 8973 eV, where Ni has the highest EED and Cu equals NiO. These matching points will be used in the interpretation of ASAXS and to derive the elemental composition of the bimetallic NPs.

The program SASfit 0.93.5[159] was used for the approximation of the scattering curves at the different incident energies. The nanostructure of the NPs must be identically at the three energies (8004, eV, 8330 eV, and 8973 eV) and only the EED of possible structural units can vary. Structural units could be a particle core or a surrounding shell of varying compositions. SASfit was used in a quasi-simultaneous manner: After a common structural model was identified, able to fit all three energies, the RED of the core was fixed to one. The approximation of the scattering curves at all energies with a homogeneous sphere and a core-shell model failed. Therefore an advanced model with a homogeneous core with a logarithmic size distribution and two shells with constant thickness and a relative electron density difference to the solution was applied as shown in Figure 3.6.

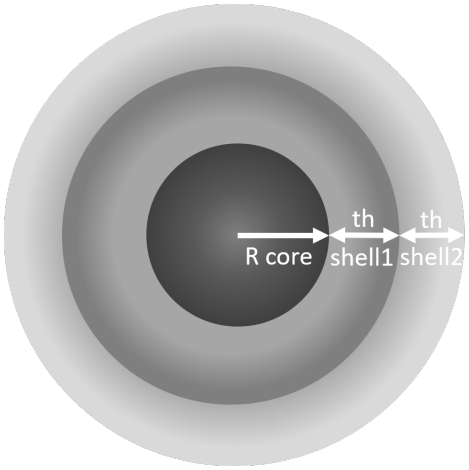

Figure 3.6: The applied fitting model consisting of a core, an inner shell 1, and an outer shell 2.

3.3.3 X-ray Diffraction

The most commonly used method to study crystalline materials is X-ray diffraction (XRD). Crystal structures of inorganic and organic compounds can be assigned. The interference of the X-rays with the crystal lattices[170] allows access to structural information via the Bragg's law (derived above), which was developed by William H. and William L. Bragg in 1912 as simplification of the models theorized by von Laue.[171,172]

$$2 \cdot d \cdot sin(\theta) = n \cdot \lambda \tag{3.15}$$

The interference of the elastically scattered X-rays is constructive, if the interplanar spacing of parallel diffracting planes d is an integer multiple n of the wavelength of the incoming X-ray beam λ with θ θ being the incident and exit angle. When it is a first order scattering, n subsumes into d.

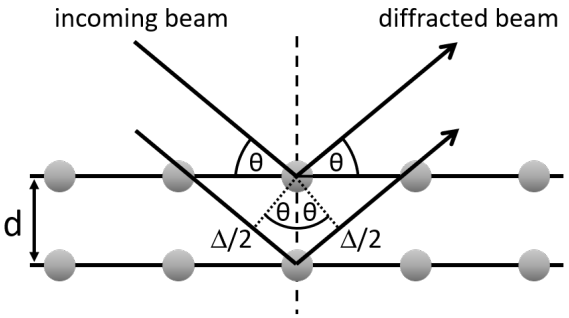

Figure 3.7: Schematic illustration of X-ray diffraction.

The XRD measurements were performed at the µSpot beamline (BESSY II, Helmholtz Zentrum, Berlin).[173] An acoustic levitator was used as sample holder(see

subsection 3.3.10).[174] With this, 10 µL of the colloidal hexane nanoparticle dispersion were levitated and a scattering image was recorded for 5 min after solvent evaporation in air. The synchrotron beam was focused by a pinhole, resulting in a beam diameter of 100 µm with a photon flux of $10^9\,s^{-1}$ at a ring current of 298 mA. The wavelength achieved by a double crystal monochromator was 0.729 29 Å (17 keV) and the X-rays were detected 213 mm behind the sample with a 2D X-ray detector (Eiger 9M, 3110 x 3269 pixels, pixel size 75 × 75 µm). This setup provided a q-max of $59\,nm^{-1}$. The diffraction images obtained were integrated and converted into diagrams of scattered intensities versus the scattering vector q using DPDAK[175] and compared with the COD[176] and the JCPDS/ICDD database.[177]

3.3.4 X-ray Photoelectron Spectroscopy

X-ray photoelectron spectroscopy (XPS) is the most popular method for surface analysis. It is based on the photoelectric effect described 1905 by Albert Einstein.[178] When solid matter is irradiated by light of sufficient energy, electrons can be ejected from the matter with a kinetic energy E_{kin}, which depends on the energy of the light $h{\cdot}\lambda$ and the binding energy of the electron in the matter E_b:

$$E_{kin} = h \cdot \lambda - E_b \tag{3.16}$$

In a relaxation process during the filling of an inner-shell vacancy of an atom Auger electrons are ejected from the same atom.[179] The detection of the amount of photoemmitted and Auger electrons as function of their kinetic energy in a suitable spectrometer leads to the typical X-ray photoelectron spectra. The following information can be obtained from the spectra: (a) elements which are present in the analysis volume and (b) their amount from the intensities of the peaks. A high energy resolution, which allows a determination of the binding energy with an uncertainty of ±0.2 eV, enables the identification of the valence states of the elements. The surface sensitivity of this methods is based on the low inelastic mean free path of the ejected electrons in matter of a few nanometers. Usually only 5 % of the ejected electrons can pass from the atom within the matter to the surface in a depth lower than 10 nm without interacting and loosing energy. Therefore, the information depth of XPS is often indicated with 10 nm. This inelastic mean free path depends on the energy of the electrons, on the density, and the valence electrons of the matter, which must be overcome by the electron on its way from the excited atom to the surface of the matter. Modern databases allow an estimation of this information depth with a relative uncertainty of around 15 %.[180] An estimation of the information depth with this database results in an information depth smaller than 5 nm for the nanoparticles investigated in this work.

Samples were prepared by dropping nanoparticle suspensions onto a cleaned silicon wafer, previously treated with an UV Ozone Cleaner UVC-1014 (185 nm and 354 nm wavelength UV radiation source; manufactured by NanoBioAnalytics, Berlin, Germany) for 20 min. The suspensions deposited on the wafer were dried in air. The XPS measurements were performed with an AXIS Ultra DLD photoelectron spectrometer manufactured by Kratos Analytical (Manchester, UK) with monochromatic Al K_α radiation ($h{\cdot}\lambda$ = 1486.6 eV) at a pressure of approximately 5×10^{-9} mbar. The electron emission angle was 0° and the source-to-analyzer angle was 60°. The binding energy scale of the instrument was calibrated following a Kratos Analytical procedure, which uses ISO 15472 binding energy data.[181] The XPS spectra were recorded by setting the instrument to the hybrid lens mode and the slot mode providing approximately a $300{\times}700\,\mu m^2$ analysis area. Furthermore, the charge neutralizer was used and all spectra were recorded in the fixed analyzer transmission (FAT) mode. Survey spectra used for the quantification, for the element identification, and the quantification were measured with a pass energy of 80 eV, high-resolution spectra used for the speciation were recorded with a pass energy of 20 eV. The intensities of the significant peaks were determined after subtraction of a modified Tougaard background using UNIFIT2022.[182] For quantification of the spectra, the intensities were normalized with Scofield cross sections,[183] an estimation of the inelastic mean free path[184] and the transmission function of the spectrometer which was determined by a protocol recently published.[185] It must be noted, that this quantitative approach is only valid for samples, which are homogeneous in the analysis volume. This is not the applicable for the core-shell nanoparticles, which were investigated herein. In the last years several approaches to determine the shell thicknesses of core-shell nanoparticles by XPS were developed,[186] but they assume monodisperse spherical particles with a homogeneous shell. The core-shell nanoparticles investigated here are nearly spherical, but the other two assumptions couldn't be ensured. The results were therefore considered in a semiquantitative manner. The Cu 2p and Ni 2p peaks were used for the determination of the Cu/Ni ratio, and for the Ni(0) to Ni(II) ratio the Ni$2p_{3/2}$ peak was considered. For Cu only metallic Cu or monovalent Cu was detected. Due to weakness of the Cu LMM Auger signal it was not possible to distinguish between both valence states without doubt.

3.3.5 X-ray Absorption Spectroscopy

X-ray near edge absorption structure spectroscopy (XANES) and extended X-ray absorption fine structure (EXAFS) are part of X-ray absorption spectroscopy (XAS), which is an element specific technique for the determination of electronic structure and local geometry of materials.[187] X-ray radiation is partially absorbed and transferred to an

electron close to the nucleus, when the incident energy is equal or greater than the binding energy of the inner-shell electrons of the probed atom. This electron is removed of its shell and replaced by an electron from a higher shell. By scanning the monochromatic incident energy an X-ray absorption spectrum is obtained. It can be divided into a pre-edge, near-edge (XANES), and extended (EXAFS) region. The height of the pre-edge peak depends on the coordination number, the oxidation state as well as the symmetry of the molecule. In 3d metal ions the pre-edge peak is higher the lower the coordination number, the higher the oxidation state as well as the assymmetry around the probing atom. XANES includes the absorption edge, which depends on the oxidation state and the near-edge region, which is a fingerprint of the atom species including the white line, which increases with increasing oxidation state. In this region, multiple scattering of the electron by neighbouring atoms occurs. The EXAFS region is about 50 to 1000 eV above the absorption edge and is dominated by single scattering processes, which are used for the analysis of the fine structure. Thus, the nature of the direct neighbours as well as their distances can be inferred.[188]
XANES and EXAFS investigations were performed at the BAMline beamline at BESSY II.[189] The samples were prepared by applying a colloidal NiCu NP dispersion to boron nitride to dilute it. The size of the resulting solid specimen was reduced with a mortar and pestle and the resulting specimen was pressed to a defined layer thickness of 1 mm. The pre- and post-edge normalization of the absorption, the transformation of the experimental EXAFS data into k-space (k = wave vector of the photoelectron), and the determination of the EXAFS oscillations $\chi(k)$ were performed with the program Athena.[190] The evaluation of the $\chi(k)$ function and the simulation of the scattering paths of the photoelectron were performed with the program Artemis using CIF files with model structures to simulate the first coordination sphere around Ni and Cu.

3.3.6 Electron Microscopy

Transmission Electron Microscopy

First microscopic images using electrons were taken by Knoll and Ruska in 1931 and reached higher resolutions than light microscopy from 1933 onwards.[191] Transmission electron microscopy (TEM) uses an accelerated and focused electron beam that is transmitted through a sample and then detected.

The electron beam created by an electron gun is focussed by several lenses in vacuum on the specimen plane. When the electrons hit the sample they pass through regions consisting of lighter materials, but they are rebound at regions with atoms possessing heavy nuclei. The image is formed on the underlying objective lens, greatly enlarged by the projector lens, and finally collected as contrasted image with a CCD camera as

depicted in Figure 3.8. Besides the transmission of the electrons, additional elastic and inelastic scattering occurs, when the electron hit the sample. This produces various signals such as secondary electrons, characteristic X-rays, Bremsstrahlung and Auger electrons.[192]

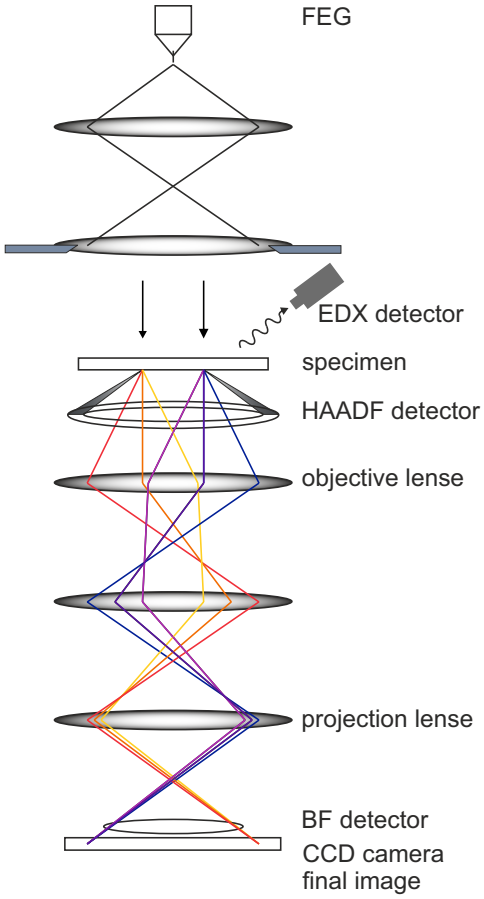

Figure 3.8: Schematic depiction of a transmission electron microscope.

In 1925 De Broglie defined the wave nature of electrons with the wavelength λ, the Plank's constant h, the mass of the particle m and the velocity of the particle as follows:[193]

$$\lambda = \frac{h}{mv} \tag{3.17}$$

Derived from this, Ernst Abbe showed that the resolution d depends directly on the wavelength and thus the speed of the electrons; with n·sinα= numerical aperture (NA):[194]

$$d = 0.61 \cdot \frac{\lambda}{n \cdot sin\alpha} = 0.61 \cdot \frac{\lambda}{NA} \tag{3.18}$$

The TEM images were acquired on a Talos F200S microscope (Thermo Scientific, 1.4 Å point resolution) at an acceleration voltage of 200 kV. For the measurement, a diluted nanoparticle hexane dispersion was dropped onto a lacey carbon coated copper or gold grid and dried in air. The samples were cleaned before the measurement using a plasma cleaner (Fischione Instruments, Model 1020) for 10 s under Ar atmosphere. The counting of the particles in the obtained images was done with the graphics program Image J 1.52e. For the size determination at least 200 particles were semi-automatically detected and the Ferret radius of each particle was determined.

Scanning Transmission Electron Microscopy

For scanning transmission electron microscopy (STEM) measurements a parallel beam set-up is chosen and an image is scanned pixel by pixel and row by row either via the direct beam as bright field image (BF), or as dark field image (DF) by only detecting the scattered electrons e.g. as HAADF image (high-angle annular dark field) very close underneath the specimen plane.

Scanning Transmission Electron Microscopy - Energy Dispersive X-ray Spectroscopy

STEM-EDX combines a STEM image with an informations of the elemental composition of the sample. The inelastic scattering of the primary electrons hitting the sample leads to the emission of characteristic X-rays, which is used for energy dispersive X-ray spectroscopy (EDX). A beam electron knocks an electron out of an inner shell of an atom and creates a hole, which is filled up with an electron from an outer shell with higher energy. The energy difference between the two shells is emitted as elemental specific X-rays and detected by an EDX detector positioned above the specimen plane. This specific X-ray radiation is detected at every point of the STEM image resulting in an EDX map of the investigated sample.

Scanning Electron Microscopy

Scanning electron microscopy is based on the same physics as TEM. The sample is gradually scanned in vacuum with a focused electron beam, while the image is generated by collecting the backscattered electrons. During environmental SEM (ESEM) measurements the vacuum in the sample chamber is not so high, decreasing solvent evaporation and allow the measurement of biological samples. SEM images of Au-sputtered samples were recorded in high vacuum, using a FEI XL30 ESEM apparatus, with a resolution of 50 nm. The electron beam voltage was set to 20 kV. The samples were fixed on a carbon tape and covered with a 15 nm gold layer.

3.3.7 Pore Structure Analysis

For the pore structure analysis gas sorption with nitrogen at 77 Kelvin with an ASAP 2020 (Micromimetics) was used to determine the specific surface area from a multipoint adsorption isotherm branch with the BET (Brunauer-Emmitt-Teller) calculation model (relative pressure range of $0.05 < p/p0 < 0.2$) according to DIN ISO 9277:2014.[195] Mercury intrusion porosimetry (MIP) was used for further characterization of the pore size distribution (most frequent), the specific pore volume and the porosity with an Autopore V (Micromeritics) according to ISO 15901-1: 2016-04.[196]

3.3.8 Mass Spectrometry

Inductively coupled plasma mass spectrometry (ICP-MS) measurements were performed with an iCAP Qc ICP-MS (Thermo Scientific GmbH), equipped with a Teflon nebulizer and quartz torch and spray chamber. Sample preparation was conducted by dissolving

5 mg catalyst in 2 mL chloric acid, separating the supporting material by centrifugation, after which 1:10 and 1:100 dilutions were measured.

3.3.9 Catalytic Testing

The catalytic testing of the bimetallic nanoparticles was conducted at Leibniz Institut für Katalyse e.V. (LIKAT) in Rostock in the group of Dr. Sebastian Wohlrab. In preparation nanoparticle dispersions were dry impregnated on a porous SiO_2 (from the supplier GRACE) in several steps until an approximate loading of 1 wt% nanoparticles was reached. This process includes the the addition of a small amount of nanoparticle dispersion (ca. 2 mL per 5 g GRACE) which diffuses into the pores and leaves the material still dry. The solvent was evaporated at 70 °C in an oven for 1 hour after which the process was repeated. After drying, the supported nanoparticles were washed several times with ethanol and dried finally. Small portions of the catalysts (5 to 10 mg) were dissolved in 2 mL chloric acid (s.b.), centrifuged and decanted. With ICP OES the metal loading was measured as well as the molar ratio of Ni and Cu. Catalyst dispersions in ethanol were sprayed in TEM grids for TEM measurements using pressurized argon.
The catalytic activities for the reverse water gas shift (RWGS) reaction were tested in a horizontal fixed bed plug flow reactor at atmospheric pressure and in the temperature range of 300 to 700 °C. Typically, 100 mg of catalyst was placed in the quartz tube with an inner diameter of 8 mm and fixed with quartz wool. Behind the catalyst bed the inner diameter of the reactor decreases to 4 mm. The temperature was controlled by a thermocouple in the middle of the catalyst bed and the activity was measured for 5 minutes after reaching steady state at each testing point. The premixed reactant gas consisted of 1:1 CO_2:H_2 and the gas flow passing the reactor was controlled by a mass flow controller (MKS-Instruments, Andover, MA, US) a total flow rate of 25 ml/min. The on-line gas analysis was carried out with a FT-IR spectrometer (Bruker Matrix-MG01, Ettlingen, Germany) and the Bruker software Opus GA which uses reference spectra of the single compounds and a non-linear fitting algorithm with a time resolution of 1 minute. The conversion of CO_2 (X_{CO_2}) and the yield of CO (Y_{CO}) as well as the selectivity (S_{CO}) were then calculated by the following equations:

$$X_{CO_2}(\%) = \frac{[CO_2]_{in} - [CO_2]_{out}}{[CO_2]_{in}} \cdot 100 \tag{3.19}$$

$$Y_{CO}(\%) = \frac{[CO]_{out} - [CO]_{in}}{[CO_2]_{in}} \cdot 100 \tag{3.20}$$

$$S_{CO}(\%) = \frac{Y_{CO}}{X_{CO_2}} \cdot 100 \tag{3.21}$$

3.3.10 Acoustic Levitation

A custom-made acoustic levitator[174] was used as a sample holder for XRD measurements of NPs and the time-resolved XRD, Raman and thermographic investigations of the crystallization of simvastatin. This device allows the handling of smallest sample quantities in an acoustic field with elimination of any surface[197] and it finds a wide range of application in analytical and material processing.[198–201] The acoustic levitator consists of a sonotrode and a concave reflector sharing the same axis of cylindrical symmetry. The sonotrode is an ultrasound transducer transforming alternating voltage into acoustic waves with a piezo-electric crystal working with an oscillating frequency of 58 kHz. These ultrasonic waves are reflected and focused by the concave reflector as shown in Figure 3.9. Adjusting the distance between sonotrode and reflector a standing wave with several pressure nodes emerges in a multiple of half the used wavelength. The superposition of the primary and reflected wave results in pressure minima and pressure maxima.[202] Solid and liquid materials can be levitated in the pressure minima between, which can reach a maximal diameter of half the used wavelength as the size is a function of the wavelength.

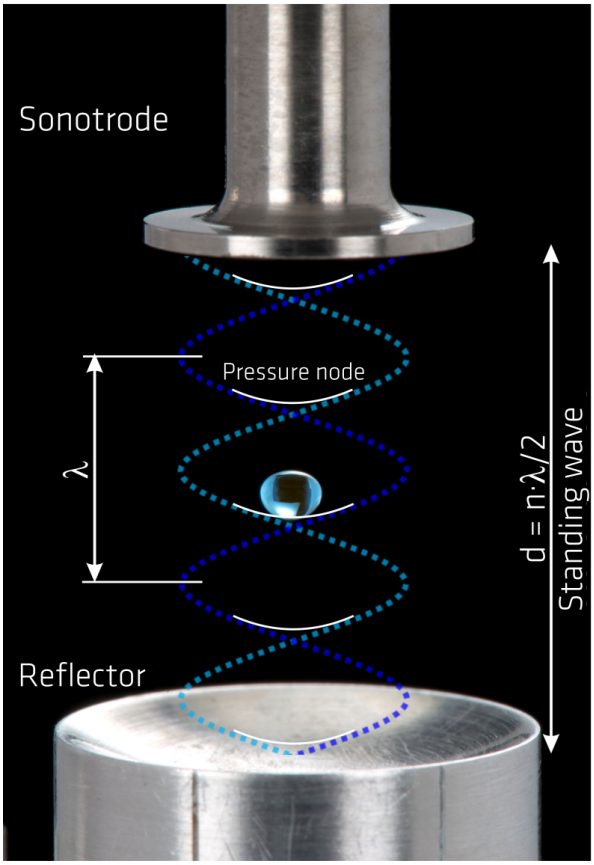

Figure 3.9: Depiction of the acoustic levitator including the sonotrode (top), the reflector (bottom), the standing acoustic wave in between, and a representative levitated droplet.

In situ Investigation of Crystallization Processes

The in situ X-ray diffraction experiments were performed at the µSpot beamline (BESSY II, Helmholtz Center Berlin for Materials and Energy). A beam with a wavelength of 1.001 Å (12.4 keV), a beam diameter of 100 µm, and a photon flux of 1×10^9 photons/s at a ring current of 100 mA was used in a typical experiment. Scattered intensities were recorded 214 mm behind the sample with a time resolution of 10 s with a two-dimensional X-ray detector (EIGER 9M, 3110 x 3269 pixels, pixel size 75 x 75 µm) providing a q-max of 43 nm^{-1}. The scattering images were integrated employing the software DPDAK[175]

and displayed using ORIGIN 9G. The in situ thermography measurements were performed with an infrared camera (Microbolometer FPA detector, spectral range 7.5-14 µm, 640 x 480 pixels). The temperature diagrams obtained from the thermal camera were normalized to the absolute temperature, which was determined with a temperature sensor (Klimalogg Pro 30.3039.IT, ± 1°C) positioned near by the droplet. In a typical experiment 10 µL of a simvastatin solution in ethyl acetate, acetone, or ethanol was transferred with a pipette in the levitator where an approximately spherical droplet was formed. The simvastatin solutions in these solvents had the following molal concentrations: $4.3 \times 10^{-2}\,\mathrm{mol\,kg^{-1}}$ in acetone, $3.8 \times 10^{-2}\,\mathrm{mol\,kg^{-1}}$ in ethyl acetate, and $4.1 \times 10^{-2}\,\mathrm{mol\,kg^{-1}}$ in ethanol. The moment of sample insertion was taken as the initial time (t_0) of solvent evaporation.

At the synchrotron the evaporation was followed by Raman spectroscopy and X-ray diffraction. Where the Raman spectra give an insight into the evaporation process of the solvent while the XRD pattern reveal the crystallization behaviour. In the lab Raman spectroscopy was combined with thermographic measurements following the temperature evolution over the evaporation and crystallization process. In both set ups the size of the shrinking droplet was detected by a camera and from the images the volume and concentration of simvastatin in the droplet was calculated as shown in Figure 3.11.

Raman Spectroscopy

The Raman effect was experimentally proven by Chandrasekhara Raman in 1928.[203] The effect describes the inelastic scattering of monochromatic light on materials based on vibration, which involve a change of polarizability. The irradiated light causes the energy state of a molecule to raise to an excited virtual state (see Figure 3.10). When the molecule subsequently returns to its old state light of the same wavelength is emitted, which is elastic scattering, also called Rayleigh scattering. However a part of the energy is transferred to the molecule, which leads to an increase of the vibrational energy. The scattered light has less energy and thus higher wavelengths, the so-called Stokes Raman scattering. If the molecule was already in an excited state before excitation, and returns to a lower level after light irradiation, light is emitted at a lower wavelength, also called anti-Stokes Raman scattering. The resulting Raman bands reflect the frequency shift of the scattered light relative to the irradiation wavelength and thus correspond to the oscillation frequencies of the molecules. Preferably, the Stokes shift is measured, since the probability of a molecule being in an excited vibrational state at room temperature is lower than in the ground state according to the Boltzmann distribution.[204] Raman spectroscopy allows the distinction between crystalline and amorphous phases due to changes in inter- and intramolecular interactions and conformational changes.

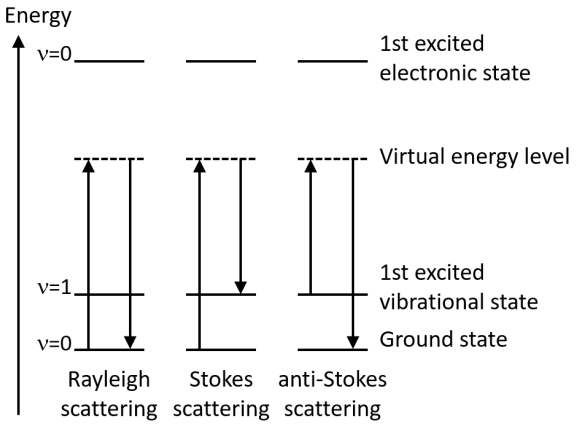

Figure 3.10: Excitation scheme with Rayleigh, Stokes, and anti-Stokes scattering.

The in situ Raman measurements were performed with a Raman RXN1TM Analyzer (Kaiser Optical Systems, Inc., Ecully, France) using NIR excitation at 785 nm, an irradiance of 6.4 W/cm^2 on the sample, and a CCD camera (1024 x 256 pixels). A non-contact probe head with a spot size of 1 mm diameter and a working distance of 1.5 cm was used for the experiments. An acquisition time of 5 x 5 s was chosen resulting in a time resolution of 30 s, respectively.

Volume Detection

Volume detection was used during the in situ crystallization to determine the concentration of simvastatin in t he droplet. The volume of the shrinking droplet was monitored based on the shadowgraph of the droplet using an USB-camera (UK1175, ABS GmbH, Jena) and the software Image Capture 1.20.17 with a time resolution of 5 seconds. By using a reference object with known size ($L_{ref} = 2mm$) the calibrated dimensions of the droplet ($L_{length,cal}$ and $L_{hight,cal}$) can be extracted from the images (Equation 3.22). The volume $V_{droplet}$ and concentration $c_{droplet}$ of the droplet are available at any time using Equation 3.23 and Equation 3.24.

$$L_{cal}[mm] = \frac{l_{droplet}[px]}{l_{ref}[px]} \cdot L_{ref}[mm] \tag{3.22}$$

$$V_{droplet}[mm^3] = \frac{4 \cdot \pi}{3} \cdot L_{length,cal}[mm]^2 \cdot L_{hight,cal}[mm] \tag{3.23}$$

$$c_{droplet}[mg/mL] = \frac{V_{droplet}[mm^3]}{V_0[mm^3]} \cdot c_0[mg/mL] \tag{3.24}$$

The supersaturation was calculated dividing the actual concentration in the droplet by the temperature dependent solubility determined as described in subsection 3.3.11.

3.3.11 Solubility Determination

The solubility determinations of simvastatin in aceton, ethanol and ethyl acetate were performed in an apparatus described by Gonçalves *et al.* over a temperature range from 10 to 30 °C (283 to 303 K) by the gravimetric method and UV Vis spectroscopy.[205] In a typical experiment suspension of simvastatin in around 10 mL of solvent was stirred for 24 h inside a jacketed glass cell whose temperature (± 0.01 °C) was controlled by circulating water from a thermostatic bath through the cell jacket. The temperature of the suspension was monitored with a resolution of ± 0.01 °C by a Pt100 sensor. After the equilibration period the stirring was stopped and four aliquots of 2 to 3 mL of the saturated solution were collected, using a preheated syringe adapted to a Whatman PuradiscTM 25 TF micro filter (0.2 µm with a PTFE membrane). The aliquots were transferred to pre-weighed glass vials. For the gravimetric method the mass of dissolved simvastatin was determined by weighing the glass vials before and after solvent evaporation to constant mass. The mole fraction of the simvastatin (χ_{Sim}) in the saturated solution was calculated from Equation 3.25

$$\chi_{Sim} = \frac{M_{solvent} \cdot (m_3 - m_1)}{M_{solvent} \cdot (m_3 - m_1) + M_{Sim} \cdot (m_2 - m_3)} \tag{3.25}$$

where m_1 is the mass of the empty vial, m_2 the mass of the vial containing the saturated solution, m_3 the mass of the vial with the dried residue, and M_{Sim} and $M_{solvent}$ the molar masses of simvastatin and the solvent, respectively.

The UV Vis measurements were conducted on a Shimadzu UV-1800 apparatus equipped with a TCC-240A cell holder. The quartz cell (1 cm optical path, covered by a Teflon cap) temperature was maintained constant at 25.0 ± 0.10 °C using a Shimadzu TCC-controller. For the measurements around 0.1 mL of the saturated simvastatin solution was diluted in a volumetric flask to obtain an absorbance of around 0.5. The masses of simvastatin solution and solvent used in the dilution process were both determined. The wavelength 238 nm was chosen for calibration and concentration determination, which corresponds to the absorbance maximum of simvastatin in ethanol. It was found to exhibit a linear correlation to the simvastatin concentration in all solvent mixtures used, exemplarily shown for the diluted simvastatin solutions examined at 20 °C.

Since the cutoff wavelengths of acetone (330 nm) and ethyl acetate (256 nm) are higher than 238 nm, the saturated simvastatin solutions in acetone and ethyl acetate were diluted with solvent mixtures of 1/100 acetone/ethanol and 1/200 ethyl acetate/ethanol (v/v) mixtures. Calibration curves were obtained from measurements of simvastatin solutions with known concentrations (see Table A.5).

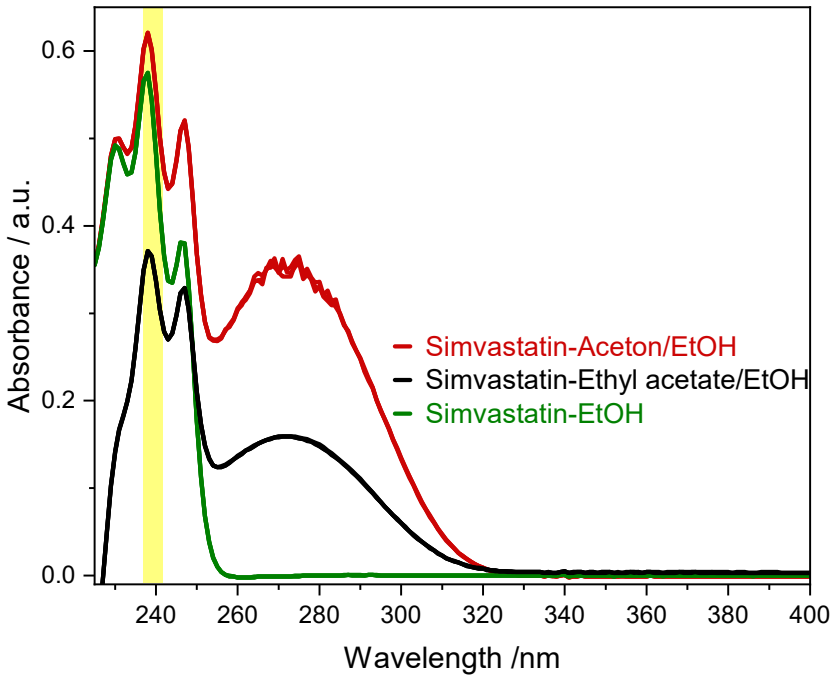

Figure 3.11: UV Vis spectra of saturated solutions at 20 °C of simvastatin in aceton (red) diluted to 1:50,000 (aceton:EtOH 1:100), in EtOH (green) diluted to 1:20,000, and in ethyl acetate (black) diluted to 1:33,000 (ethyl acetate:EtOH 1:200) with the chosen wavelength marked in yellow.

$$\chi_{Sim} = \frac{c \cdot M_{solvent}}{c \cdot (M_{solvent} - M_{Sim}) + 1000 \cdot M_{Sim}} \tag{3.26}$$

The mole fraction solubility of simvastatin, χ_{Sim}, was calculated from Equation 3.26 where M_{Sim} and $M_{solvent}$ are the molar masses and c ($\mathrm{g\,kg^{-1}}$) represents the simvastatin concentration in the saturated solution. The c values were obtained from the UV Vis absorbance measurements using the Lambert–Beer law and considering the dilutions applied.

4 Results and Discussion

In the following chapter an adapted approach for the synthesis of monometallic nickel nanoparticles via thermal reduction is investigated regarding the influence of reaction parameters such as the amount of reducing agent and stabilizing agent, as well as concentration and reaction volume on the final nanoparticles (NPs). The formed nickel nanoparticles (NiNPs) are investigated extensively by various analytical techniques resulting in information about size, shape, crystallinity and electronic structure. The catalytic activity for the reverse water gas shift reaction (RWGS) is confirmed. The adapted synthesis approach is extended to bimetallic Ni NPs with either Co or Cu and the influence of the reaction parameters on the final NPs is studied extensively. Besides the catalytic activity for the RWGS reaction, its relation to structural and surface properties of the NPs is revealed and the final NPs are investigated thoroughly.
First experiments in the acoustic levitator investigating the crystallization behaviour of the active pharmaceutical ingredient simvastatin were performed. Interesting solvent dependent behaviour was found and extensively studied as discussed in section 4.4 as well as in two publications.[206,207]

4.1 Size-tunable Synthesis of Monometallic Nickel Nanoparticles

A number of methods for the preparation of metal NPs have been developed, including photolytic reduction,[50] radiolytic reduction,[51] sonochemical method,[52,53] solvent extraction reduction,[54] microemulsion technique,[53] polyol process,[55] and thermal reduction.[49,56–58] The thermal reduction using amines as reducing agent and phosphines as stabilizer was studied by various research groups. Most syntheses of NiNPs described in the literature are conducted under standard air-free conditions using vacuum or inert gases like nitrogen[49,71,208] or argon[48,57,209] to remove air potentially trapped in solution and gas phase. The procedures take place in bulky equipment like Schlenk tubes,[71] three-necked flasks,[48,49,208] or, alternatively, in an autoclave.[111] A simpler and much more efficient approach for synthesizing NiNPs under thermal conditions is needed that must still prevent the oxidation of Ni. The typical synthesis procedure of the thermal

reduction of nickel(II) acetylacetonate ($Ni(acac)_2$) with oleylamine (OAm) as reducing agent and trioctylphosphine (TOP) as stabilizing agent is schematically shown in Figure 4.1 and described in detail in section 3.2. ($Ni(acac)_2$), OAm, and co-solvent dibenzyl ether (BDE) are mixed in 20 mL glass vials and flushed with N_2 at room temperature. The reaction mixture is heated up to 100 °C, TOP is added and flushed with N_2 again. After two hours at reaction temperature (220 °C) the NP dispersion is cooled down. The synthesis is conducted under near-air-free conditions purging the reaction solution with N_2 stream in 20 mL glass vials with a septum circumventing standard air-free conditions and space-consuming glassware.

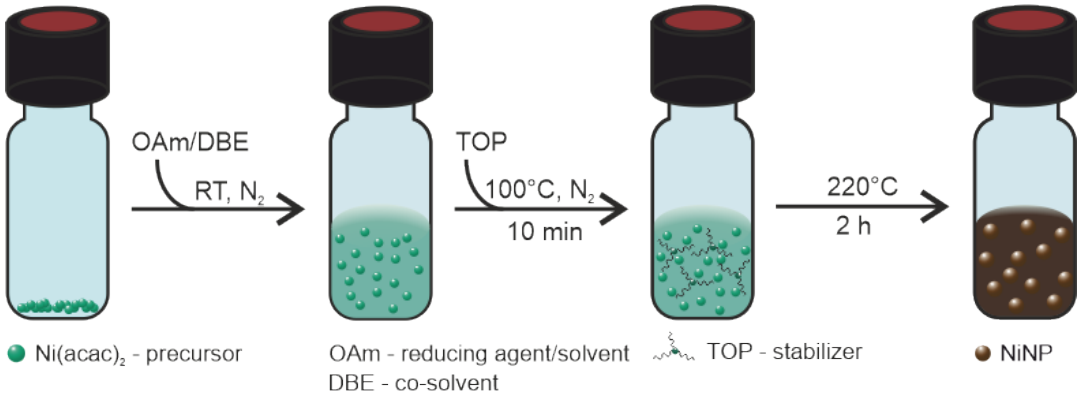

Figure 4.1: Schematic illustration of NiNP synthesis conditions using $Ni(acac)_2$ as precursor, OAm as reducing agent and solvent, DBE as co-solvent, and TOP as stabilizer.

This synthesis route leads to the formation of NiNPs with a narrow size distribution. To investigate size and shape of the NPs as well as the size distribution transmission electron microscopy (TEM) measurements were conducted. The TEM image in Figure 4.2a shows NiNPs prepared using the following representative conditions: 50 mmol L^{-1} $Ni(acac)_2$, two equivalents (eq) of stabilizer trioctylphosphine (TOP), ten eq oleylamine (OAm) as reducing agent and dibenzyl ether (DBE) as co-solvent, 220 °C, and a two-hour reaction time. Typical spherical 12.5 nm NiNPs in diameter are obtained. The narrow size distribution (±0.5 nm) of the NPs derived from the TEM images is shown in Figure 4.2c. High resolution TEM images of the NPs reveal polycrystalline domains in the NPs. The lattice fringes of 0.20 nm (Figure 4.2b) are an indication for the formation of face centered cubic (fcc) Ni (111). To analyse the structure and confirm the finding from high resolution TEM X-ray diffraction (XRD) was conducted. The XRD pattern of the NiNPs is shown in Figure 4.2d (inset) in comparison to fcc Ni (JCPDS database, PDF 04-0850).[210] The reflections at q = 30.6 and 35.6 nm^{-1} correspond to the Miller indices (111) and (200) and confirm the fcc structure of the Ni consistent with the TEM images. The width of the reflections in the XRD pattern result from the relatively small crystalline domain sizes in the NPs.

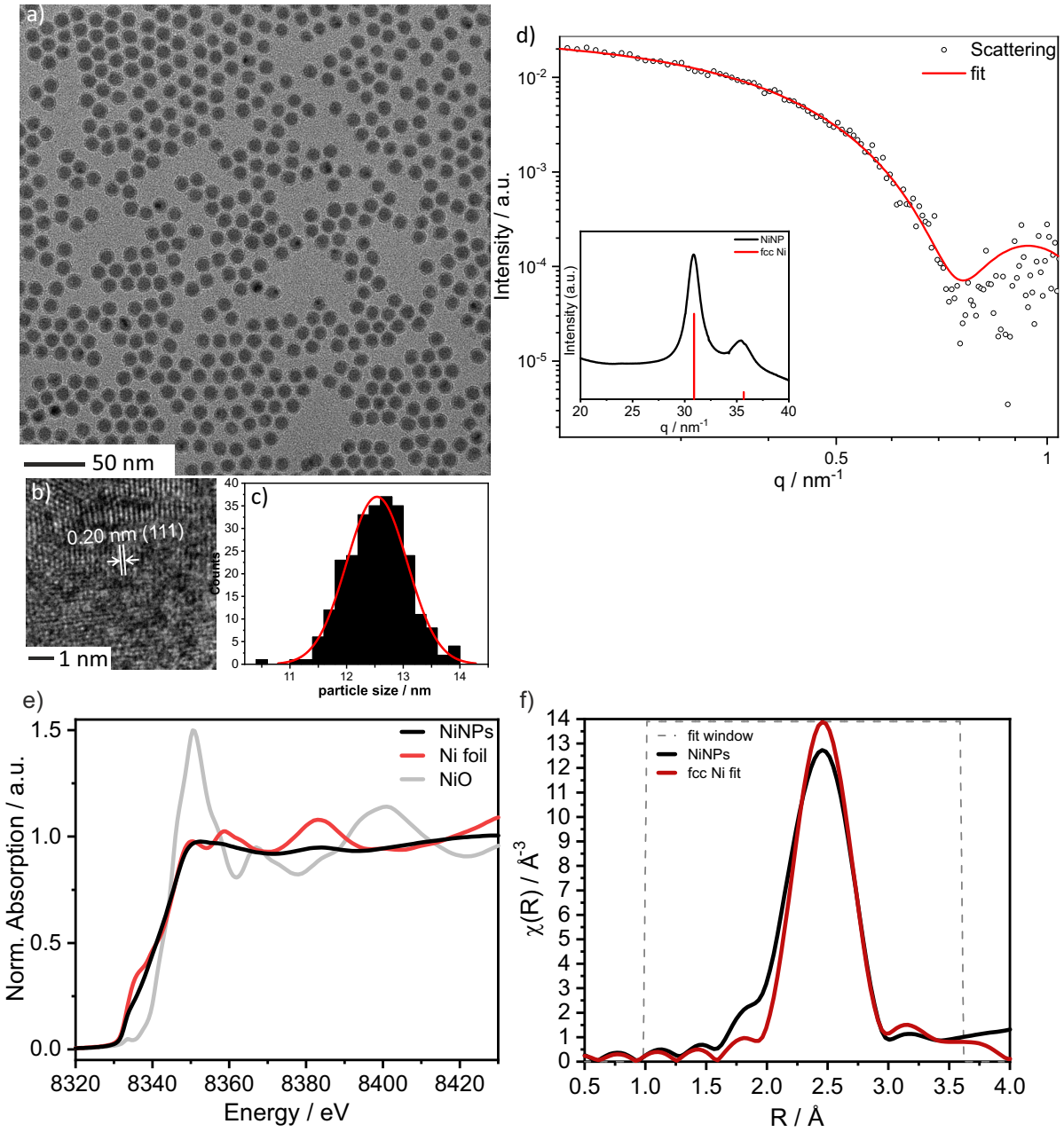

Figure 4.2: a) TEM image of NiNPs prepared with 50 mmol L^{-1} $Ni(acac)_2$, 2 eq TOP, 10 eq OAm, 2 h at 220 °C, with narrow size distribution (diameter = 12.5 ± 0.5 nm); (b) HR-TEM image revealing lattice fringes of 0.20 nm in NiNPs indicating fcc Ni (111); (c) particle size distribution of NiNPs; d) SAXS data of NiNPs dispersed in hexane with a curve fit according to a homogenous sphere with a Schulz–Zimm size distribution resulting in 11.8 nm and a polydispersity of 8%; (inset) XRD of NiNPs (black) as compared to the database entry JCPDS database PDF 04-0850 (red) for bulk Ni; e) normalized Ni K-edge XANES-spectra of NiNPs (black straight), a Ni foil (black dots), NiO (grey straight), and $Ni(acac)_2$ used as precursor (grey dots); f) EXAFS oscillations as a function of the interatomic distance R in real space obtained by Fourier transformation of NiNPs (black) and fcc Ni bulk fit (red).

TEM is a direct method providing real images of the NPs and gives a very good impression of size and shape. But due to its limitation on a microscopic volume of the sample being depicted, it is not able to give an information of the whole sample. Structural effects might appear during the drying process when preparing the NPs on the TEM grid. Small angle X-Ray scattering (SAXS) in contrast is an indirect and bulk method analysing the NPs in solution and taking the whole sample volume into account. SAXS lacks on the other hand any shape information, which has a major impact on the scattering curve and is necessary for the data evaluation. Thus a combination of TEM, giving insights into the shape of the NPs, and SAXS, giving a statistical size and its distribution across the NPs, is very powerful for NP characterization. Correspondingly the size of the NPs shown in Figure 4.2a were additionally evaluated as NP dispersed in solution using SAXS. The SAXS data shown in Figure 4.2d were fitted with a monodisperse sphere and a Schulz-Zimm distribution of the radius, which is described in subsection 3.3.1. This analysis resulted in a particle size (diameter) of 11.8 nm with a polydispersity of 8 %.
Borchert *et al.* compared the particle size measurements using TEM, SAXS and XRD using quasi-spherical, highly monodisperse and crystalline $CoPt_3$ NPs.[157] They found a good agreement between the sizes obtained from the three methods within a mean deviation of 5-7 %. The more homogenous the sample the more accurate and reliable was the particle size determination. The mean deviation of the mean NP size of the NiNPs determined by TEM and SAXS in the present work is about 6%, which is in good agreement, considering the study of Borchert *et al.*
After investigating size, shape and crystal structure of the NPs, the local structure and the oxidation state were examined by X-ray absorption near edge structure (XANES) spectroscopy and extended X-ray absorption fine structure (EXAFS) measurements. Figure 4.2e shows XANES spectra at the Ni K-edge of the NiNPs alongside $Ni(acac)_2$, NiO, and a metallic Ni foil. The intense white line observed in the spectra of NiO and $Ni(acac)_2$ (dotted and solid grey lines in Figure 4.2f) is an expression of the bivalent state of Ni compared to the absence in pure Ni (dotted black line) due to the valence difference. The absence of the intense white line in the spectrum of the NiNPs (solid black line) verifies the similarity to pure Ni(0) and the valence differences compared to NiO and $Ni(acac)_2$.[211] This strongly suggests the formation of pure non-oxidized NiNPs.

Table 4.1: Comparison of the fitted EXAFS data, including coordination number and Ni-Ni distance (R), of the NiNPs with the structural parameters of fcc Ni (RMSE = 0.05 Å).

	coordination number		**distance R/Å**	
	Ni fcc	**NiNPs**	**Ni fcc**	**NiNPs**
Ni fcc Ni1.1	12	6.55 ± 0.44	2.49	2.47
Ni fcc Ni1.2	6	2.85 ± 2.69	3.52	3.46

EXAFS measurements were carried out in addition to the XANES measurements, to gain an understanding of the local coordination geometry around Ni. In Figure 4.2f, the EXAFS spectrum is shown in real space with a fit for bulk fcc Ni. The good agreement of the simulated structure of fcc Ni with the experimental data indicates that the crystalline domains of the NiNPs form fcc Ni. The interatomic distances between the Ni atoms in real space (Figure 4.2f) in the NiNPs correlate with the bulk fcc Ni in the first and second coordination sphere as listed in Table 4.1. The number of Ni atoms is, however, lower than the bulk Ni. The EXAFS and XANES measurements confirm the structural finding derived from TEM and XRD (in Figure 4.2a and d), suggesting the formation of fcc Ni in the NPs. The short range interatomic distances correlating with bulk fcc Ni derived from EXAFS support the findings in the high resolution TEM images indicating polycrystalline domains inside the NiNPs which are limited in size and order, indicated by the lowered coordination numbers.

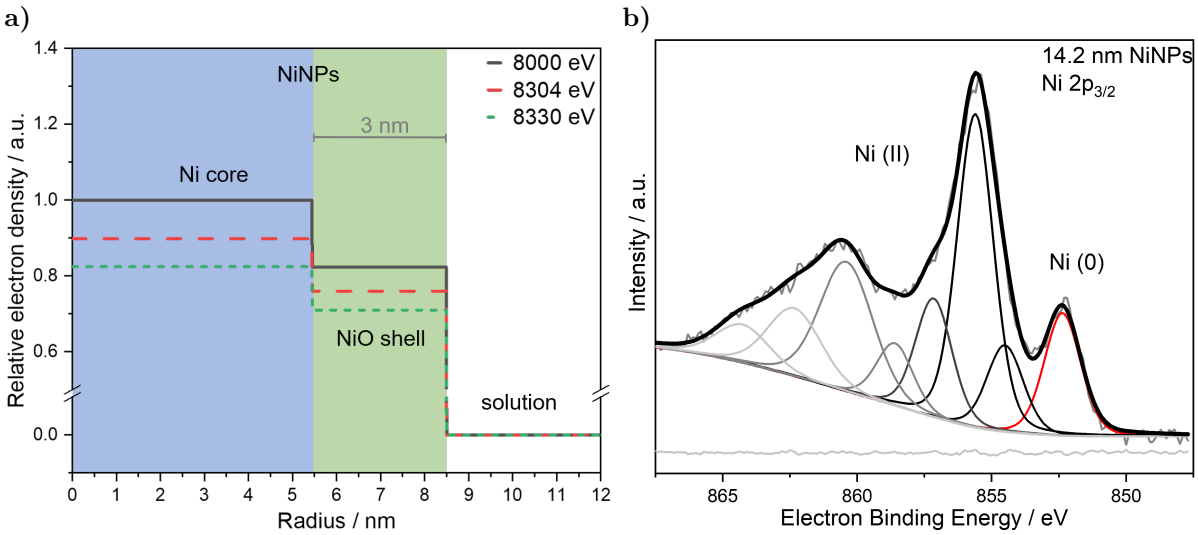

Figure 4.3: a) Relative radially averaged electron density of NiNPs derived from scattering curves obtained at energies of 8000, 8304, and 8330 eV. b) XPS spectra of NiNPs in the region of the Ni2p$_{3/2}$ states.

Surface analysis of the NiNPs with X-ray photoelectron spectroscopy (XPS) were conducted and the Ni2p$_{3/2}$ region given in Figure 4.3b was used to determine the Ni(0) to Ni(II) ratio. A Ni(0)/Ni(II) ratio of 0.13±0.02 was determined suggesting the formation of a passivation NiO layer on the NiNPs. To support the passivation of the NiNPs surface, anomalous SAXS (ASXAS) measurements were conducted at the FCM beamline at BESSY II at different energies around the Ni X-ray K-absorption edge (8333 eV), which are 8004, 8304, and 8330 eV. The effective electron density (EED) of Ni decreases strongly towards the Ni K-absorption edge as given in Figure 4.31, so does the EED of

NiO correspondingly. The relative effective electron density (RED) NiO/Ni is at around 0.8 constantly. A core-shell model was applied and the relative radial electron density profile is depicted in Figure 4.3a. It includes a core with a radius of 5.5 nm and a shell with a thickness of 3.0 nm resulting in a total NP size of 17 nm. The RED in the core decreases towards the Ni K-edge, which follows the trend of the EED of metallic Ni, confirming the presence of Ni in the core. The calculated RED of Ni given in Figure 4.3a is higher than in the shell at all energies, indicating the location of pure Ni in the core and NiO in the shell, since the EED of NiO is lower than of metallic Ni at all used energies. The ASAXS measurements confirm the formation of a passivation layer of NiO around a Ni(0) core. The applicability of a core-shell model vs a homogeneous sphere model on the SAXS data derived from the lab and the synchrotron is discussed in subsection 4.3.5.

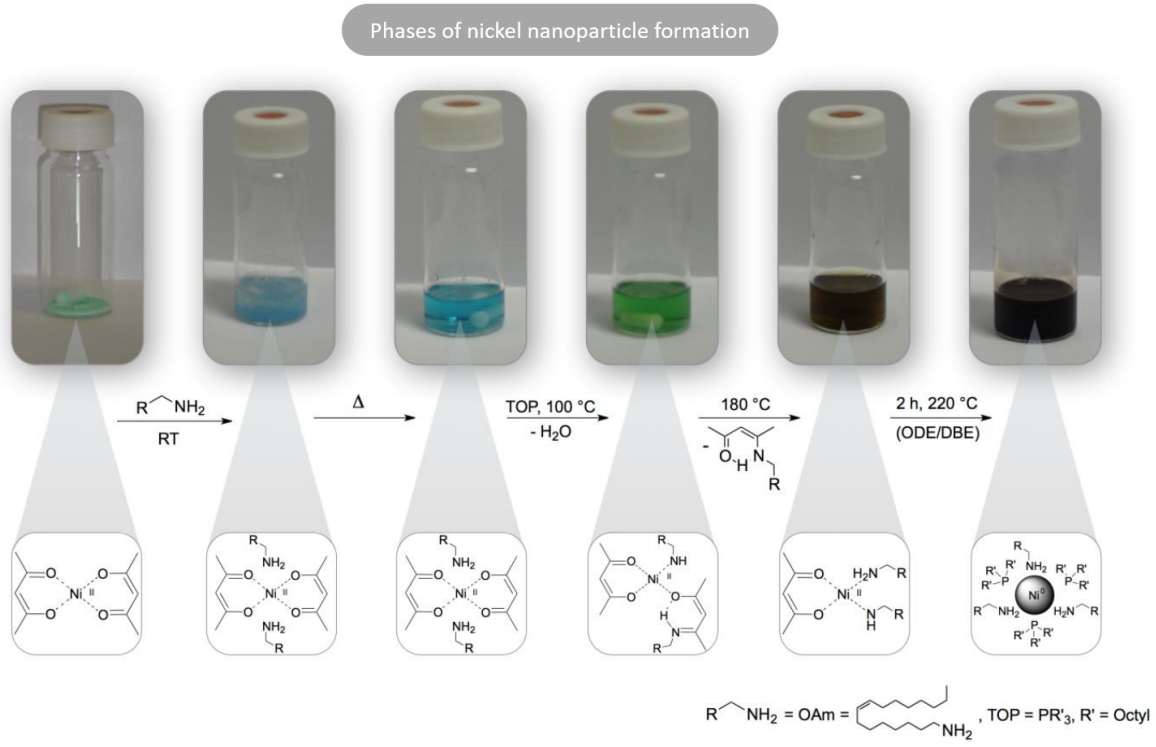

Figure 4.4: Formation of NiNPs using primary amines and TOP as stabilizer adapted from H. Kulla.[212]

A closer look was then taken at the reaction pathway of the NP formation. A generalized reaction pathway proposed by H. Kulla is shown in Figure 4.4.[212] At room temperature $Ni(acac)_2$ is not soluble in OAm, thus forming a gel-like consistency in the viscous solvent. This gel liquefies above a temperature of around 70 to 80 °C. Upon addition of OAm to $Ni(acac)_2$ a colour change from light turquoise to blue occurs, indicating a complexation or rather ligand exchange of acetyl acetonate with the amine. At elevated temperatures water settles on the glass walls, which may originate from crystal water

of the $Ni(acac)_2$ or, proposed by Kulla, from a condensation reaction of the amine with the carbonyl function of the acetylacetonate ligand in which water is released. A second colour change occurs after adding TOP to the solution at 100 °C which indicates a second ligand exchange of the Ni complex since OAm and TOP are both clear solvents. Upon heating to 220 °C a drastic colour change to black/brown occurs, indicating the nucleation process of the metals and formation of NPs.

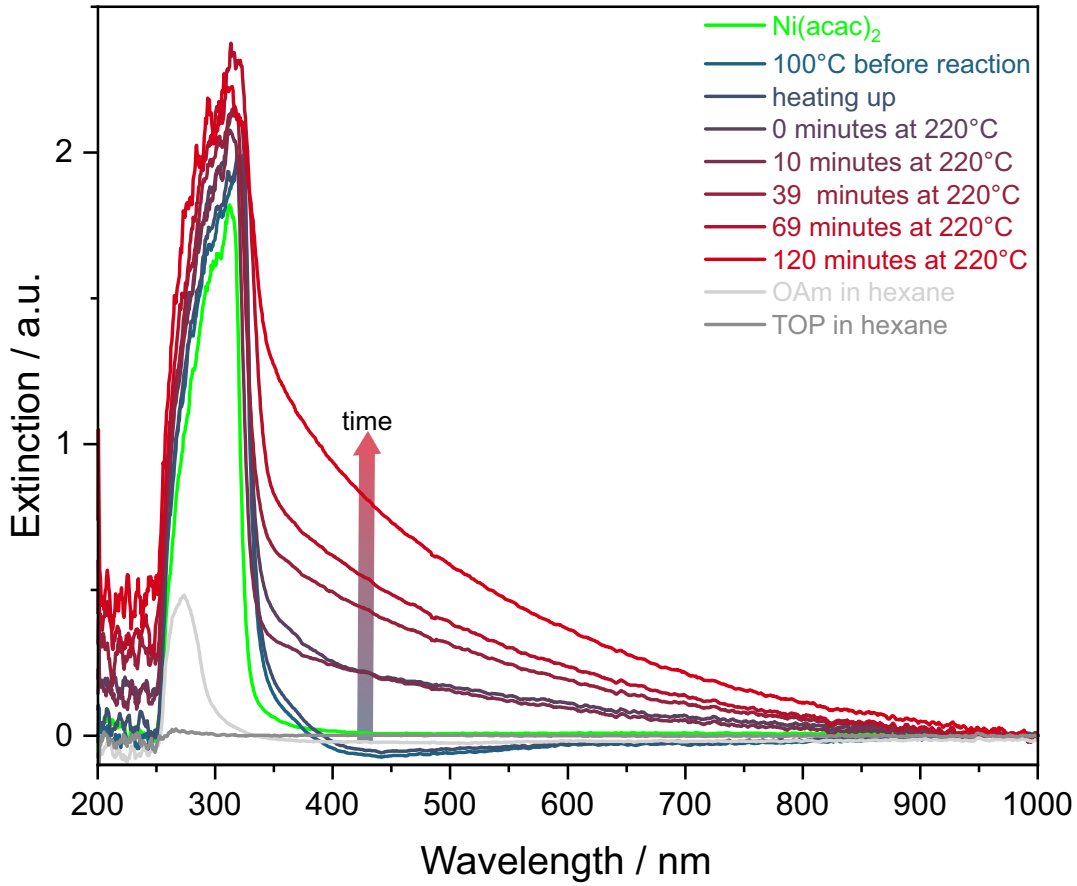

Figure 4.5: UV Vis spectra of reaction solution at different points of the synthesis. All solutions were diluted in hexane from 1:20 up to 1:80. Additional to the reaction solution after TOP addition, while heating and after 0, 10, 39, 69, and 120 minutes at reaction temperature 220 °C reference spectra of $Ni(acac)_2$, OAm, and TOP are shown.

The time dependence of the particle formation was studied with SAXS, TEM, and UV-Vis spectroscopy. The following reaction conditions were used: 25 mmol L^{-1} $Ni(acac)_2$ with 120 eq reducing agent and solvent OAm and three eq stabilizer TOP, for two hours at 220 °C. The visible colour shift was also detected by UV Vis spectroscopy, Figure 4.5. The extinction was recorded at different points throughout the synthesis. The absorption maximum of pure $Ni(acac)_2$ in ethanol is around 310 nm. The UV Vis extinction after 40 minutes shows the beginning of extinction of light over the whole spectral range

corresponding to the brown/black colour, which the NP solution exhibits. The whole spectral range extinction intensifies over the course of the reaction. This phenomenon can be described as a convolution of absorption and scattering processes of the reaction species and the formed NPs.[213]

Table 4.2: Influence of reaction time on particle size (diameter d) and polydispersity (PD) derived from TEM and SAXS. The following reaction conditions were chosen: 25 mmol/L $Ni(acac)_2$, 120 eq OAm, 3 eq TOP, 2 h at 220°C.

time / min	**size / nm**[a]	**PD / %**[a]	**size /nm**[b]	**PD /%**[b]
0	3.7	28	-	-
10	8.7	22	8.3	8
40	12.5	11	11.5	7
70	12.9	10	11.8	9
120	12.9	8	12.2	5

[a] = TEM data. [b] = SAXS data.

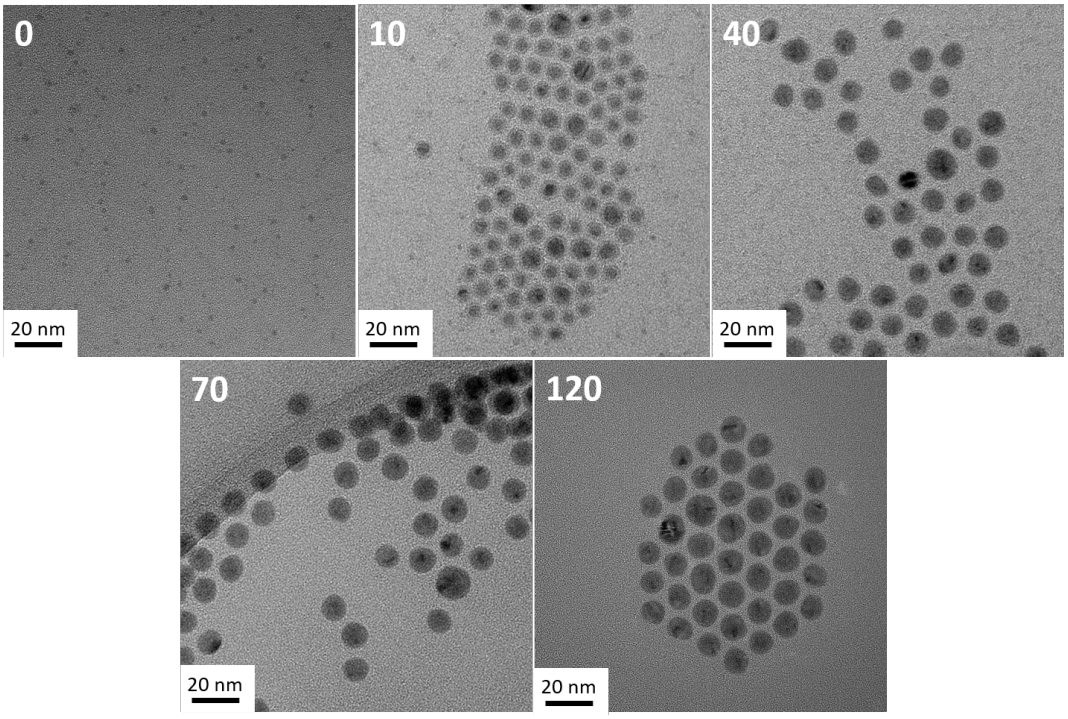

Figure 4.6: TEM images of NiNPs after 0, 10, 40, 70, and 120 minutes reaction time at the same reaction conditions noted in Table 4.2.

The reaction was stopped after several time periods at reaction temperature (220 °C, after 0, 10, 40, 70, and 100 minutes), NPs were precipitated and redispersed in n-hexane, and TEM and SAXS were measured. The particle sizes are shown in Table 4.2. The

main NP growth takes place during the first 40 minutes at reaction temperature 220 °C. Within this time the final particle size of 12-13 nm is reached. The TEM images show the increase in size from quite polydisperse spherical 4 nm NPs (PD 28 %) to much more uniform NPs after 40 minutes. At all investigated times during the reaction the NPs were spherical. After 40 minutes a relatively low polydispersity of 11 % is reached which decreases to a final minimum dispersity of 8 % after a two-hour reaction time. NPs can be considered monodisperse, when the standard deviation of their diameter is less than 10 %.[214–216] The NP sizes derived from SAXS data are in good agreement with the TEM data although they are slightly smaller, see Table 4.2.
Carenco *et al.* showed in a TEM study that particles which offered a coarse surface after one hour of reaction time ripened to spherical NPs within two hours of reaction.[49] Due to the agreement of our results with those of Carenco *et al.* showing a decreasing dispersity within the second hour at reaction temperature 220 °C, two hours reaction time was chosen for investigations concering the influence of the reaction conditions on the final NPs.

4.1.1 Studies of Reaction Conditions

The ability to tune the size of the NiNPs is critical ensuring their suitability for large-scale industrial applications. Various aspects of this new adapted synthesis method were explored to optimize the conditions for the tunability such as (1) amount of reducing agent (5–122 eq OAm), (2) amount of stabilizer (1–50 eq TOP), and (3) the reaction volume dependence (5–20 mL). The long-term stability of the NPs and their catalytic activity are discussed afterwards.

(1) Amount of reducing agent OAm:

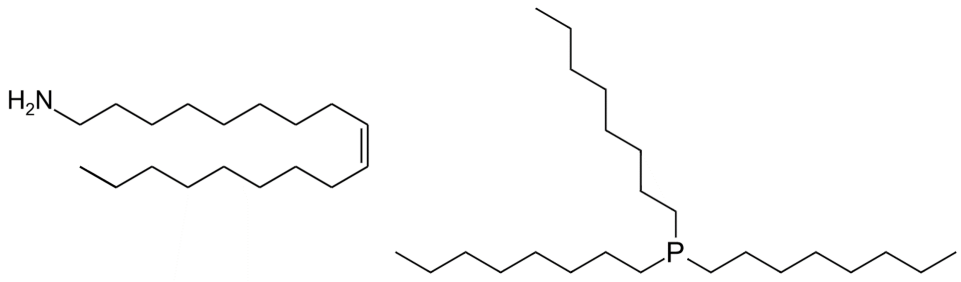

Figure 4.7: Chemical structures of the reducing agent OAm (left) and the stabilizer TOP (right).

The chemical structure of OAm is given in Figure 4.7. To investigate the influence of OAm on the particle size the TOP amount was kept stable at 1.5 eq. To keep the

volume stable the co-solvent DBE was added in various amounts. It is considered a good additional solvent to OAm since it is non-toxic, stable at high temperatures, and available in high purity. Alternatives like octadecene worked well as co-solvents, but were very difficult to separate from the NPs.[212] Based on SAXS data, the influence of the amount of OAm on the particle size was studied using 5 - 122 eq OAm (see Figure 4.8). The underlying SAXS data are shown in Figure A.3. The diameter of the particles varies between 8.0 and 15.5 nm (black squares) and a decreasing amount of reducing agent results directly in the formation of larger NPs.

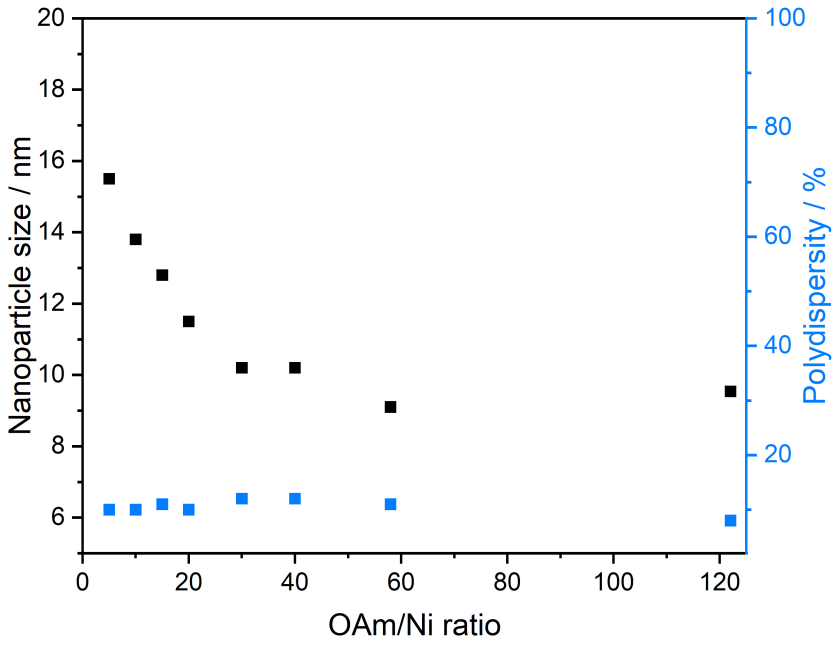

Figure 4.8: NP size relative to amount of OAm with corresponding polydispersity, based on SAXS data. T = 220 °C, t = 2 h, [Ni] = 50 mmol/L, TOP/Ni = 1.5.

The OAm amount variation induces no significant change in the polydispersity (blue squares in Figure 4.8), which varies within 8 and 12%. When no DBE was used with 58 eq OAm, 9.1 nm large NiNPs were obtained. To reach 122 eq OAm the Ni concentration was reduced to 25 mmol L^{-1} leading to 9.5 nm NiNPs, which is comparable to 60 eq OAm. By changing the amount of reducing agent OAm the size of the final NPs can be adjusted mainly within 5 - 30 eq OAm from 15.5 to 10.5.

(2) Amount of stabilizer TOP:

The influence of 1 - 50 eq TOP was studied using two different Ni precursor concentrations (50 and 25 mmol L^{-1}), one identical to the investigations concerning the OAm influence and one with the half concentration of Ni precursor to get an insight whether the stabilizing effect of TOP depends on the metal concentration. The sizes

of the synthesized NiNPs are shown in Figure 4.9, which are based on SAXS data, shown in Figure A.4. Increasing the TOP concentration results for both concentrations in decreasing NP sizes (Figure 4.9a). The decrease in particle size with an increasing amount of TOP is steeper for the 50 mmol L^{-1} $Ni(acac)_2$ concentration, which might be explained by noting that the higher number of growing seeds in the same volume increases the tendency of nuclei to coalesce. TEM images of several different syntheses demonstrate well-separated, narrowly dispersed spherical NPs that are arranged in an ordered fashion, presumably due to the effective stabilization by TOP (Figure 4.9b–d). Upon increasing the amount of TOP to 30 eq, much smaller NPs are formed, which are still well-separated but are now randomly distributed and no longer ordered compared to 10 eq TOP for example.

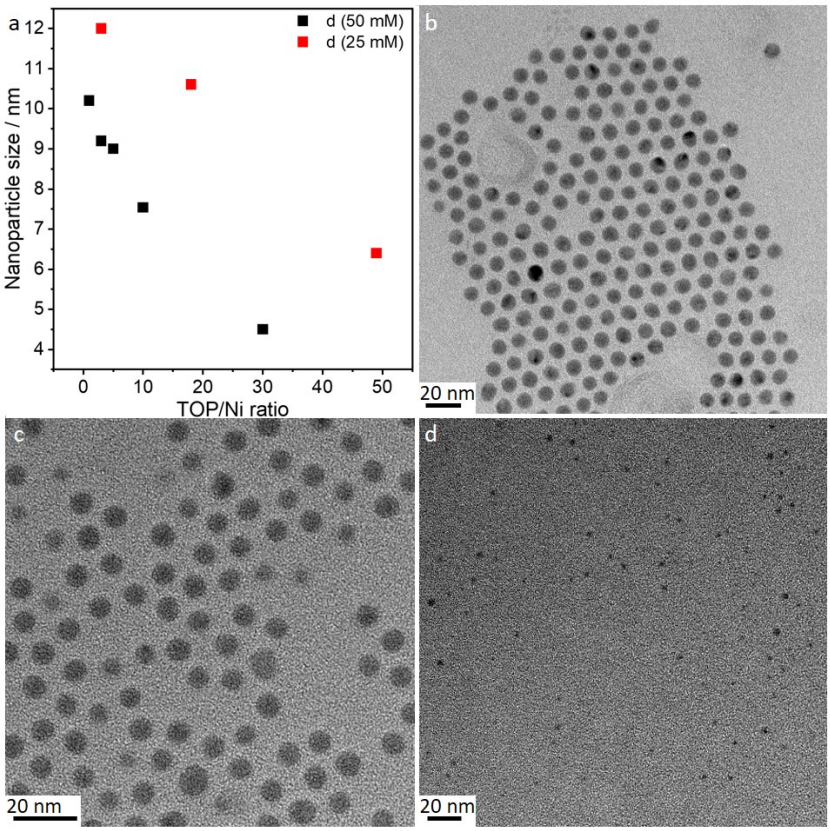

Figure 4.9: a) Influence of TOP concentration on NP size: T = 220 °C, t = 2 h; b)–d) TEM images of NiNPs formed from 50 mmol L^{-1} $Ni(acac)_2$ with 3 eq TOP b), TOP/Ni = 10 c), and TOP/Ni = 30 d).

(3) Reaction volume dependence:

Three repetition experiments were conducted using a volume of 5 mL and a concentration of 50 mmol L^{-1} Ni to test the reproducibility of the adapted synthesis method. The syntheses lead reproducibly to 9 nm NPs with a low polydispersity, as shown in Table 4.3. The respective SAXS data are shown in Figure A.5. Increasing the reaction volume twice and fourfold to 10 and 20 mL shows negligible effects on the NP size as well as on the size distribution. This finding indicates an independence of the synthesis method from the reaction volume which is a good starting point for upscaling with regard to large scale industrial catalyst production.

Table 4.3: Volume-dependent NP size in a range of 5 to 20 mL based on SAXS data. [Ni] 50 mmol L^{-1}, 3 eq TOP, 2 h at 220 °C.

volume / mL	size / nm	PD / %
5	9.2	8
5	9.4	8
5	8.8	11
10	9.4	9
20	9.6	11

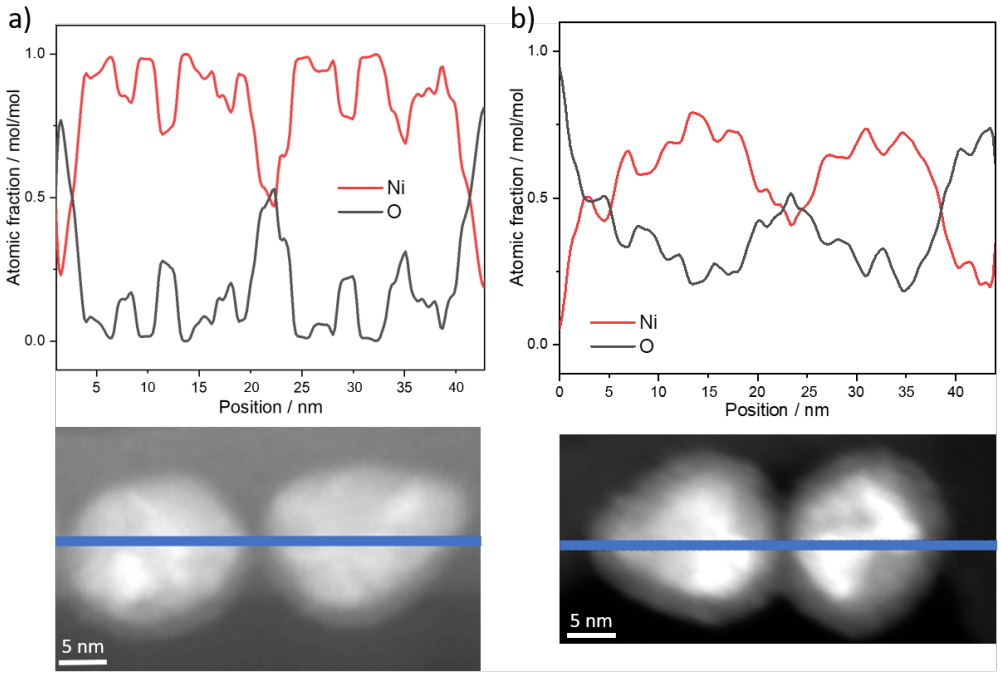

Figure 4.10: Element distribution of Ni and oxygen by EDX/STEM on NiNPs synthesized with the following conditions: 50 mmol L^{-1} $Ni(acac)_2$, three eq TOP, and 61 eq OAm. a) Two weeks after preparation; b) stored in air for nine weeks after first measurement. The full STEM image and the regions of interest are shown in Figure A.2.

Long-term stability of the NPs:

The element distribution throughout the NPs was investigated using scanning electron transmission microscopy (STEM) and energy dispersive X-ray spectroscopy (EDX) measurements. Figure 4.10 shows the element distribution of Ni and oxygen within the NiNPs (top) and the corresponding STEM images (bottom) with a blue line indicating the path of the linescan. The NPs were examined two weeks after synthesis (Figure 4.10a) and after nine weeks of storage under ambient conditions (Figure 4.10b) on the TEM grid. The element distribution of Ni within the NiNPs (depicted in the linescan) matched with the contrast differences in the STEM image (shown underneath the linescan) which are visible by the electron density difference between the Ni in the NPs and the carbon film in the background. The maximum average atomic fraction of Ni, derived from a linescan of an EDX map shown in Figure 4.10, in the NPs decreased over time. This is indicated by a maximum of 100 mol/mol Ni in the freshly prepared NPs compared to a maximum atomic fraction of 80 mol/mol Ni in the aged particles. The local oxygen concentration after synthesis indicated a small oxygen appearance around the NPs whereas most of the particle surface was not oxidized. The overall increase of the oxygen fraction over storage time indicated the partial oxidation of the particles.

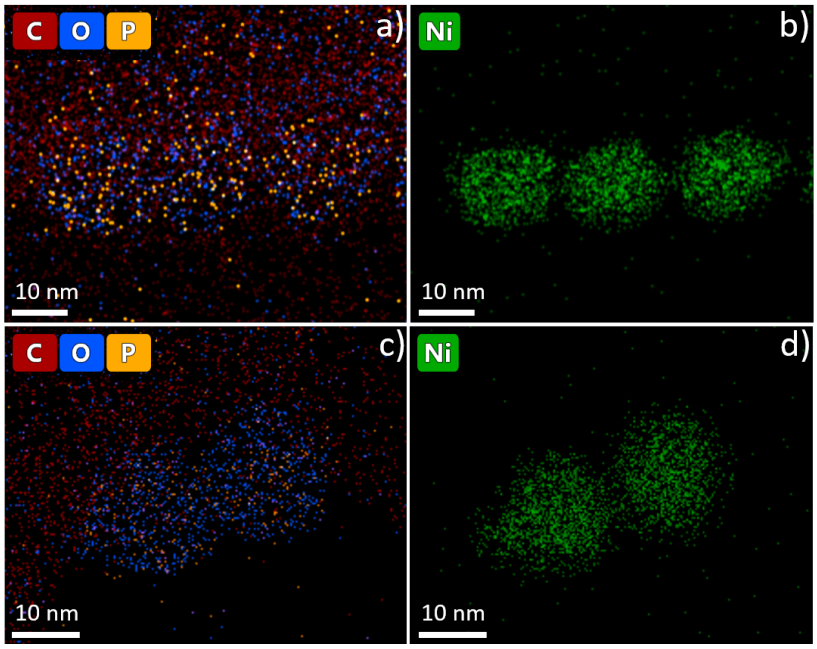

Figure 4.11: EDX mapping of NiNPs after synthesis (50 mmol L^{-1} $Ni(acac)_2$, three eq TOP, and 61 eq OAm): a) Element distribution of carbon, oxygen, phosphorus, and b) Ni. EDX mapping of these NiNPs after nine weeks storage in air: c) Element distribution of carbon, oxygen, phosphorus and d) Ni.

The NPs show a higher oxygen amount across the whole linescan thereby indicating a partial surface oxidation of the NP. The findings in the element distribution in the linescans are even more prominent in the element mapping in Figure 4.11. The Ni is evenly distributed within the particles (b and d). The oxygen, carbon and phosphorous distributions are shown in Figure 4.11a and c. The carbon distribution was not analysed in the linescan, as it showed strong intensities around the particles assignable to the lacey carbon film on the used Cu TEM grid which is visible in the top half of Figure 4.11a. The phosphorus distribution confirmed the presence of stabilizer TOP on the particle surface leading to separated and well-organized NPs. The intensity of the oxygen increased over the time of storage, which is easily seen in the differences of the mapping images by comparing the amounts of oxygen and carbon, since the amount of carbon keeps stable. The oxidation occuring over time suggest that there are open sites on the NP surface accessible for the gas phase, which are fundamentally important for catalytic applications.

The NP size prepared with the facile adapted synthesis method can be tuned within 4 and 15.5 nm by varying the amount of reducing agent OAm and stabilizer TOP, while the reaction volume does not affect the final NPs. After a reaction time of two hours at reaction temperature 220 °C spherical non-oxidized NiNPs are achieved, which oxidize over time. A next step after the characterization of the preparation method is the investigation of a possible application of the prepared NiNPs as catalysts for the RWGS reaction.

4.1.2 Catalytic activity of Nickel Nanoparticles for RWGS Reaction

The conversion of CO_2 to syngas (H_2 and CO) via the reverse water gas shift reaction (RWGS), a mixture of CO and H_2, has been recognized as one of the most promising processes for CO_2 utilization.[120] The catalytic activity of the NiNPs synthesized with the new adapted simple synthesis procedure for the reverse water gas shift reaction (RWGS) was determined at atmospheric pressure using a representative sample with a particle size of 14 nm (reaction conditions given in Table A.1). The NiNPs were supported on porous silicon dioxide (SiO_2, GRACE) via a dry impregnation method described in subsection 3.3.9 resulting in 1.05 wt% loading, as determined by mass spectrometry (ICP-MS). The NPs supported on SiO_2 as prepared are shown in Figure 4.12a-b in two magnifications. The TEM images indicate a uniform distribution of well-separated NPs on the SiO_2 surface. XAS measurements of the catalyst material were conducted before catalysis and are shown in Figure 4.12b-c.

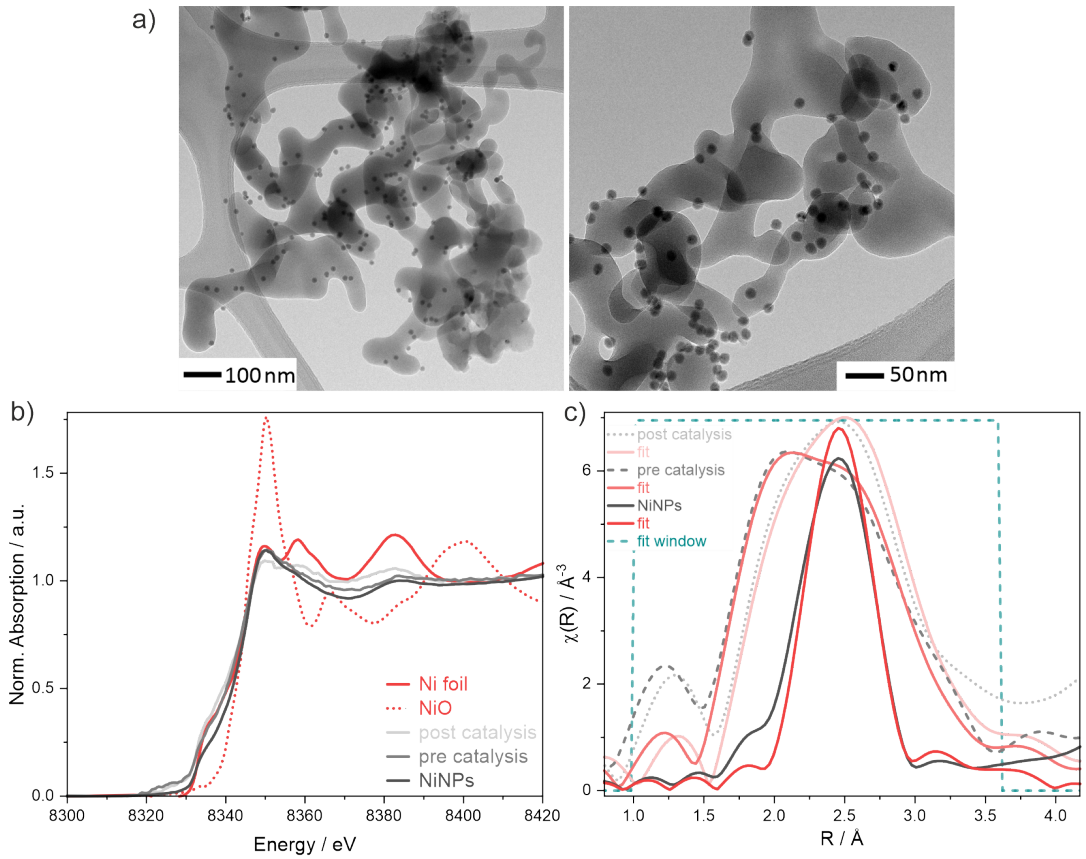

Figure 4.12: a) TEM images of 14 nm NiNPs on porous SiO_2 with a NP loading of 1.05 wt%, b) normalized Ni K-edge XANES-spectra of NiNPs (black), NiNPs@SiO_2 as prepared (dark grey), NiNPs@SiO_2 after catalysis (light grey), a Ni foil (red straight), and NiO (red dotted), and c) EXAFS oscillations as a function of the interatomic distance R in real space obtained by Fourier transformation of NiNPs (straight black), NiNPs@SiO_2 as prepared (dark grey dashed), NiNPs@SiO_2 after catalysis (light grey), and the corresponding fcc Ni bulk/NiO fits in different shades of red.

Table 4.4: Comparison of the fitted EXAFS data of unsupported NiNPs (RMSE = 0.05 Å) and the catalyst material (NiNPs@SiO_2) before catalysis (pre, RMSE = 0.11 Å) and after catalysis (post, RMSE = 0.13 Å) with the structural parameters of fcc Ni and NiO.

	coordination number				**distance R/Å**			
	Ni fcc	**exp**	**NiO**	**exp**	**Ni fcc**	**exp**	**NiO**	**exp**
NiNPs	12	6.55 ± 0.44	-	-	2.49	2.47	-	-
pre	12	1.60 ± 0.97	6	0.67 ± 0.31	2.49	2.49	2.09	1.94
post	12	1.90 ± 1.14	6	0.49 ± 0.49	2.49	2.50	2.09	1.91

Compared to the pure NiNPs (straight black line), which exhibits dominantly a Ni-Ni distance of 2.49 Å like bulk Ni fcc, the as prepared catalyst (dashed dark grey) shows the shorter Ni-O distance of 2.09 Å like NiO in addition to the Ni-Ni distance. The catalyst was prepared under ambient conditions, which made more oxidation possible. The catalyst material post catalysis (dotted light grey) shows interestingly a shift back to the longer Ni-Ni distance and slight changes in the coordination number (Table 4.4), indicating a higher amount of Ni fcc and lower amount of NiO.

The catalytic activity was tested in a fixed-bed reactor at ambient pressure (1 bar) with 25 mL/min 1:1 H_2:CO_2 from 200 to 700 °C and the resulting activity and selectivity is shown in Figure 4.13a. A near 100% selectivity for CO (S(CO)) was achieved over the whole temperature range while negligible amounts of CH_4 were formed. The catalytic activity becomes significant above 350°C and increases strongly until 430 °C reaching a CO_2 conversion (X(CO_2)) of 11 %. The activity increases constantly up to 700 °C although the steepness decreases above 430 °C. A maximum catalytic activity at 700°C of 46 % conversion of CO_2 is reached. In a second approach the catalytic activity was tested stepwise up to 500 °C and afterwards down to 300 °C shown in Figure 4.13b. The strong increase above 350 °C is reproduced in two experiments and the activity below 400 °C increases strongly after the catalyst was heated to 500 °C. This behaviour change might be connected to the reduction of NiO in the catalyst as determined by EXAFS.

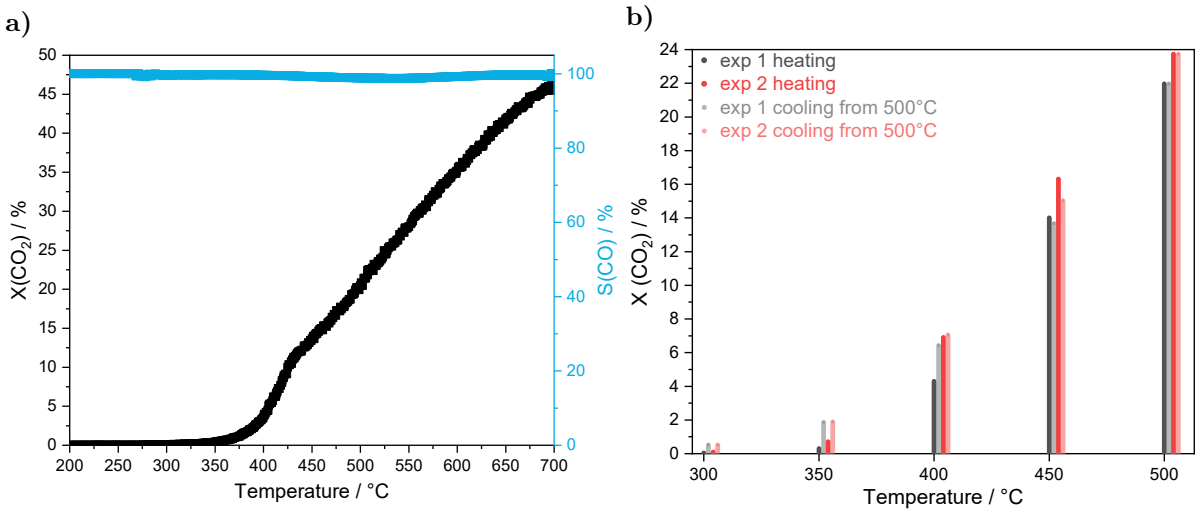

Figure 4.13: CO_2 conversion and selectivity of monometallic NiNPs@SiO_2 for the RWGS reaction with 100 mg catalyst, 1.05 wt% loading, and a gas hourly space velocity (GHSV) = 15 000 L kg^{-1} h^{-1}, CO_2:H_2 1:1 a) continuously between 200 and 700 °C and b) stepwise up to 500°C and cooling afterwards. In a) the conversion of CO_2 to CO is shown in % (black) and the CO selectivity in % (blue) and the two experiments in b) in black respectively red with transparency for cooling.

4.1.3 Findings in context of literature

The herein presented new facile adapted synthesis route leads to pure NiNPs with a narrow size distribution for which the term monodisperse is used in the field of nanomaterials. Monodispersity describes a collection of objects which have the same size, shape, or mass without a dispersity. IUPAC prefers to use the more satisfactory term uniform mainly in the field of polymers.[217] Xu *et al.* defined monodisperse samples as NPs with <10% standard deviation in diameter[216] and Wu *et al.* synthesized Co NPs with a diameter of 10 nm ± 1 nm, which they claimed monodisperse.[215] Carenco *et al.* produced monodisperse NiNPs with 9 nm and a standard deviation of $\sigma < 7.9\,\%$[49] comparable to monodisperse NiNPs synthesized by Metin *et al.* which are 3.2 nm in diameter with a standard deviation of ~7 %.[70] Metin *et al.* refer mono- respectively polydispersity to the shape of the formed NPs. Murray *et al.* define their metal NPs as monodisperse with a standard deviation of $\sigma < 5$ %.[93] Very recently Muzzio *et al.* stated that "For NPs to be defined as monodisperse, the standard deviation in their diameter (or in one dimension) should be less than ten percent."[214]

The herein described NiNPs with narrow size distribution exhibit a polycrystalline character such as syntheses reported in literature by e.g. Eluri *et al.*, Wang *et al.*, and Ishizaki *et al.*[48,218,219]

XRD measurements of the NiNPs indicate the formation of non-oxidized NPs. Although no standard air-free techniques were used, also XANES strongly suggests the formation of pure non-oxidized NiNPs, consistent with literature.[69] The XANES measurements prove the herein adapted, facile, and near-air-free synthesis procedure to be a valid alternative to the complex routes described in literature.[48,71,208] Winnischofer *et al.* concluded a disordered complex structure of their NiNPs from their XANES measurements. In this work we support this finding and give deeper insights into this disorder with EXAFS by quantifying the number of surrounding Ni atoms.

Taking a closer look at the local and surface structure of the herein prepared NiNPs, the formation of a thin and disordered NiO layer around the NiNPs is detected. This seems to be contrary to the XRD data, which only identified Ni fcc. This phenomenon was also described by Winnischofer *et al.* and Couto *et al.*[69,220] They concluded the formation of pure NiNPs from the XRD data, but found a negligible percentage of metallic Ni species on the NP surface with XPS. It was not possible to detect the NiO with XRD presumably due to low crystallinity and low occurrence.

The time frame of the particle formation found with our adapted synthesis procedure leading to particles exhibiting the near final size after 40 minutes is in accordance with the findings of Ishizaki *et al.*[219] who determined a full conversion of $Ni(acac)_2$ to NiNPs within 30 minutes using 0.5 eq TOP and OAm as reducing agent and solvent. They

used 60 mmol Ni precursor corresponding to 3.5 g Ni and utilized XRD to investigate the product composition, and the product weight to examine the turn-over of the synthesis. After 5 minutes they still saw reflections assignable to $Ni(acac)_2$ in XRD which disappeared after a 15 minute reaction time. At this time reflections corresponding to Ni were found in XRD and 2.7 g particles were recovered (corresponding to 77 % turn-over). After 30 and 60 minutes reaction duration Ishizaki *et al.* recovered 3.5 g particles (100 % turn-over) exhibiting reflections of Ni in XRD.

However, Carenco *et al.*[49] showed in a TEM study investigating NiNP formation that the particle surface after one hour reaction time was still very rough. By extending it to two hours, they found that the sphericity of the NPs increased. This process was attributed to digestive ripening, which includes an intra-particular reorganization of the Ni atoms in the outer layer of the particle.

Oleylamine plays an important role in the metal NP formation as investigated by Vivien *et al.*[221] They determined the importance of the double bond in comparison to octadecylamine leading to a much lower polydispersity which might be due to a lower stability of the capping with octadecylamine. Additionally, the bend of the OAm chain induced by the double bond disfavours the interdigitation and limits the aggregation of the NPs.[222] The chain length of the amines was found to be important in the final stabilization of the NPs since melting evolutions appeared in an electron beam after using octylamine (C_8) instead of oleylamine (C_{18}).[221] The amine function was found to be essential for controlling size, shape, and stability of NPs in solution. The replacement of oleylamine with octadecene or tetradecane led to bulk metal instead of NPs. It was found by Cheng *et al.* that at least 3 eq OAm is needed for a quantitative reduction of the Ni salt,[68] which was a key factor in choosing the investigated range of 5-122 eq OAm in this work. Compared to syntheses described in the literature using standard air-free methods, e.g., by Carenco *et al.*,[49] in this work smaller particles are observed at comparable amounts of reducing agent, which also show a higher sphericity at a comparable polydispersity.

Two main reasons are important for the dramatic particle size changes at lower OAm equivalents (5–30 eq). The first one is a kinetic effect due to the nature of oleylamine acting as a reducing agent, correlating the amount of OAm present in the reaction volume directly to the reaction rate. A slower reaction rate induced by less reducing agent also decreases the nucleation rate and increases the probability of growth of the existing Ni clusters through aggregation. The amine group plays the most important role in these reaction kinetics, which is responsible for the reduction process as demonstrated by Carenco *et al.*[71] via successful reduction with even shorter alkyl amines. The second reason is the role of OAm as a stabilizing agent. The amine part interacts with the Ni surface while the hydrophobic chain provides steric hindrance.[223] By reducing the OAm amount the number of nucleation seeds increases in solution, which are not sterically

hindered from each other, increasing the chance of growth. However, when enough OAm is present (around 30 eq OAm) in its role as stabilizer, the size of the particles changes only slightly upon increasing OAm amount from 10.2 to 8.0 nm. Using less than 5 eq OAm only agglomerates settling down to the magnetic stirring bar were observed. The ferromagnetism of Ni contributes to the agglomeration on the stirring bar since particles lager than 32 nm were found to be ferromagnetic while smaller particles exhibited superparamagnetic characteristics.[224]

Increasing the amount of stabilizer TOP (Figure 4.15) leads to the formation of smaller NPs. The steric hindrance of TOP leads to the formation of a capping layer around the particles, inducing a more effective stabilization and preventing them from continued growth through aggregation.[225] The excess of OAm used in these experiments causes the nucleation to proceed so quickly that even 1 eq TOP is sufficient to stabilize the NPs. This leads to NPs with a narrow size distribution and low polydispersity of 10 %. LaGrow *et al.* studied the effect of TOP concentration in a range of 0 - 2 eq TOP using 100 kPa hydrogen in a synthesis cell designed for in situ experiments.[56] They found final particle sizes of 14.0 nm for 0.5 eq TOP to 11.0 nm for 2 eq TOP with increasing sphericity of the NPs with increasing amount of stabilizer TOP. The herin adapted and facilitated synthesis route results in highly spherical NPs with a comparable size (10.2 nm with 1 eq TOP) to the findings of LaGrow *et al.* The region of strong effect of the stabilizing agent on the NP size is shifted to higher amounts (3-50 eq TOP) compared to former studies of Carenco *et al.*[49] In the latter study, the increase of TOP from 0.1 to 0.5 eq led to a strong change in particle size from 25 to 9 nm, whereas the size difference was negligible between 0.5 and 5 eq TOP both giving 9 nm NPs.

The herein synthesized monometallic NiNPs show a good catalytic activity within 350-700°C with a maximum conversion of 46 % CO_2 . Ranjbar *et al.* investigated the catalytic activity of Ni supported on MgO for the RWGS reaction in the temperature range of 400 to 700 °C using effectively 100 mg catalyst with a varying loading from 2 to 15 wt%, and 50 mL min^{-1} gas flow consisting of CO_2:H_2 1:1 at atmospheric pressure.[14] They reached a maximum CO_2 conversion of 43 % CO_2 with 7 wt% Ni loading at 700 °C. The CO_2 conversion increases with temperature and Ni content up to 7 wt%, at higher loadings a decrease of catalytic activity is observed. The CO selectivity at 400 °C decreases with increasing Ni loading from 100 to 53 % for 2 to 15 wt% Ni and is around 100% at 700 °C for all loadings. The in the present work synthesized and supported NiNPs show a higher CO_2 conversion at 700 °C with 1 wt% Ni than Ranjbar *et al.* reached with 7 wt% Ni loading. The CO selectivity of the herein reported catalyst is close to 100 % at all temperatures while the CO_2 conversion at 400 °C is around 4%. This significant enhancement of catalytic activity at 700 °C might result from the supporting method, since a dry impregnation method was used in this work to

prepare the catalyst via supporting the preliminary synthesized NiNPs on SiO_2 while Ranjbar *et al.* impregnated their supporting material with metal precursor which was calcined at 600 °C afterwards. The dry impregnation of NPs on the supporting material could result in a higher Ni surface available as catalytic site therefore increasing the conversion of CO_2. An other factor playing a role in the enhanced activity of the NiNPs compared to the catalysts investigated by Ranjbar *et al.* is the flow speed of the gas mixture, which is 25 mL min^{-1} in this work and 50 mL min^{-1} reported from Ranjbar *et al.* Increasing the flow speed was found to lead to slightly decreased conversions of CO_2.[23] The increase of catalytic activity at lower temperatures after heating the catalyst up to 500 °C needs further investigation involving in situ testing of the catalyst and extensive characterization after high temperature catalysis.

Table 4.5: Comparison of catalytic activities concerning conversion of CO_2 ($X(CO_2)$, %) and selectivity of CO (S(CO), %) at 1 bar and CO_2:H_2 1:1.

T /°C		**400**	**500**	**600**	**700**
$X(CO_2)$	NiNPs@SiO_2[1]	4.0	20.5	35.1	45.9
$X(CO_2)$ literature	7% Ni-M1[2,*14]	14	27	35	43
	Ni-CP[3,*25]	4	16	29	38
	Ni-P123[4,*138]			36	
S(CO)	NiNPs@SiO_2[1]	99.6	98.8	99.3	99.7
S(CO) literature	7% Ni-M1[2,*14]	79	84	92	100
	Ni-CP[3,*25]	90	97	99	100
	Ni-P123[4,*138]			100	

[1] 100 mg cat., 1.05 wt% NiNP on SiO_2, 25 mL min^{-1} gas flow.
[2] 100 mg catalyst, 7 wt% Ni on MgO, 50 mL min^{-1} gas flow.
[3] 50 mg catalyst, 1 wt% Ni on CeO_2, 100 mL min^{-1} gas flow.
[4] 20-50 mg catalyst, 1 wt% Ni on CeO_2-P123, 100 mL min^{-1}.
* values derived from graphical depictions

Wang *et al.* tested the catalytic activity of Ni supported on cerium oxide CeO_2 prepared by different supporting methods such as co-precipitation, deposition-precipitation, and impregnation.[25] For their catalytic tests they used 50 mg catalyst with 1 wt% Ni, CO_2/H_2 feed stream at 100 mL min^{-1} with a feed ratio of 1:1 under atmospheric pressure and in a temperature range of 400 to 750 °C. The overall highest CO_2 conversions were reached with the catalyst prepared by deposition-precipitation although this catalyst showed the lowest selectivity for CO. The catalyst prepared via impregnation showed the lowest CO_2 conversion while giving 100 % selectivity for CO throughout the temperature range. The catalyst material prepared by co-precipitation gave the best catalytic performance giving a relatively high CO_2 conversion with a good CO selectivity as shown in Table 4.5. The herein presented catalyst shows comparable CO_2 conversion at 400 °C but higher conversions at raised temperatures with comparable CO selectivities.

Liu *et al.* improved their catalyst preparation by involving P123 ((ethylene oxide)$_{20}$-(propylene oxide)$_{70}$-(ethylene oxide)$_{20}$) into the co-precipitation process of CeO_2 and Ni.[138] They could enhance their catalyst stability and the selectivity at 600 °C resulting in a comparable conversion as achieved with the herein presented catalyst. The hysteresis which occured at lower reaction temperatures after heating the catalyst up to 500 °C needs further investigation concerning the surface modification of the NiNPs and the influence of the supporting material.

4.2 Bimetallic Nickel Cobalt Nanoparticles

A common non-rare earth metal catalyst for the RWGS reaction is pure Ni. However there are some drawbacks which Ni exhibits during catalysis. Thermal instability and carbon deposition are common problems of Ni catalysts.[226] To solve these problems, different approaches such as changes in the preparation method, modification of the catalyst support, or the addition of a second metal to create a bimetallic catalyst were considered.[227] In this work the focus lays on the addition of close neighbour 3d-elements of Ni, including Co and Cu, to form bimetallic Ni NPs. By this approach the use of expensive and rare noble metals can be avoided.

Bimetallic Ni NPs were synthesized by co-reduction of two metal salts which are nickel acetylacetonate ($Ni(acac)_2$) and either cobalt acetylacetonate ($Co(acac)_2$) or ($Ni(acac)_2$) and copper acetylacetonate ($Cu(acac)_2$). For the size control the reaction parameters were varied according to the preparation of the monometallic NiNPs (see section 4.1).

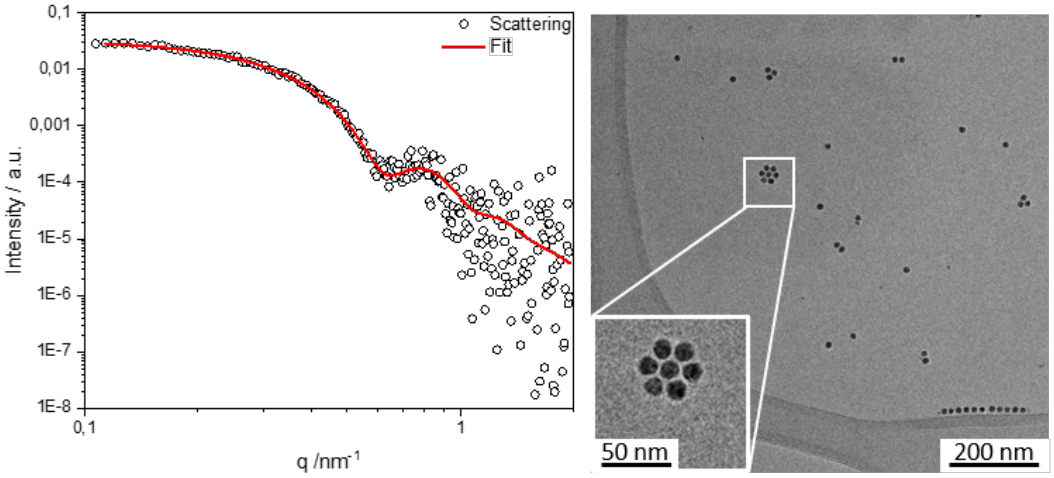

Figure 4.14: Scattering curve of bimetallic NiCo NPs with a diameter of 13.8 nm (left) and TEM image of these NPs prepared using 93 eq OAM, 3 eq TOP, a Ni/Co concentration of 30 mmol L^{-1} and a 4:1 ratio.

Standard reaction conditions of 30 mmol L^{-1} salts (4 eq $Ni(acac)_2$ and 1 eq $Co(acac)_2$) with 3 eq TOP and 93 eq OAm lead to 13.8 nm NPs with narrow size distribution of 12%. The TEM image confirms the spherical shape of the NPs and the mean size derived from that TEM image is 14.4 nm with a size distribution of 15%, which is in good agreement with the 13.8 nm derived from the SAXS measurement shown in Figure 4.14.

The impact of the amount of stabilizer on the NP size was investigated increasing the TOP amount from 1.5 to 30. The synthesized NPs were investigated using SAXS and the determined size and polydispersity of these NPs are shown in Figure 4.15. By increasing the amount of TOP the NP size decreased from 14 to 8 nm while the polydispersity kept consistently below 17%. This indicates that the size of these NPs is tunable although the size range is not very large.

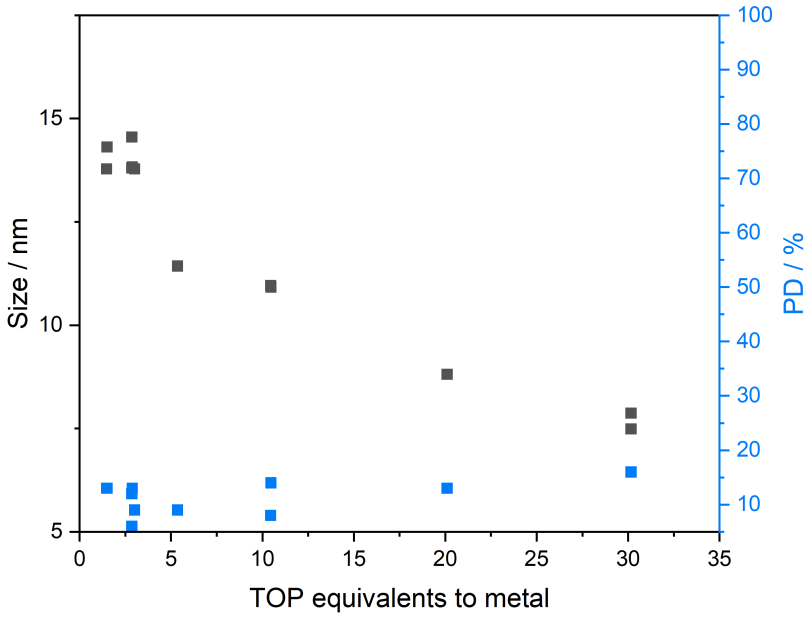

Figure 4.15: Impact of TOP on the NP size with the following reaction condition: 30 mmol/L metal salt, 0.2 eq $Co(acac)_2$, adjusted eq OAm, 5 mL, 2 h at 220°C

A rather drastic characteristic of the nanoparticle solution gets obvious by taking a closer look to the TEM image in Figure 4.16 b. Mainly spherical NPs with comparable sizes can be seen beside which some smaller irregularly shaped NPs appear. Since the pure NiNPs appeared exclusively in spherical shape the deformed NPs might be caused by the addition of the Co to the system.

To confirm this hypothesis the element distribution throughout these nanostructures was investigated by conducting an EDX mapping additional to STEM measurements represented by a linescan given in Figure 4.16 a, corresponding to the STEM image in c, which is enlarged in d. The spherical NPs consist, as expected, mainly of Ni, since it was provided in fivefold quantities in the reaction solution. Co is randomly distributed within these spherical NPs in much lower quantities. The irregularly shaped NPs however consist exclusively of Co. This shows that Ni only forms bimetallic NPs whereas Co forms also small irregular pure Co NPs. One explanation for this finding could be the standard redox potential of these two metals which indicates the energetic favourability of the reduction. The standard redox potential of Ni is $E_0(Ni^{2+}/Ni^0) = -0.23V$ and for Co $E_0(Co^{2+}/Co^0) = -0.28\,V$.

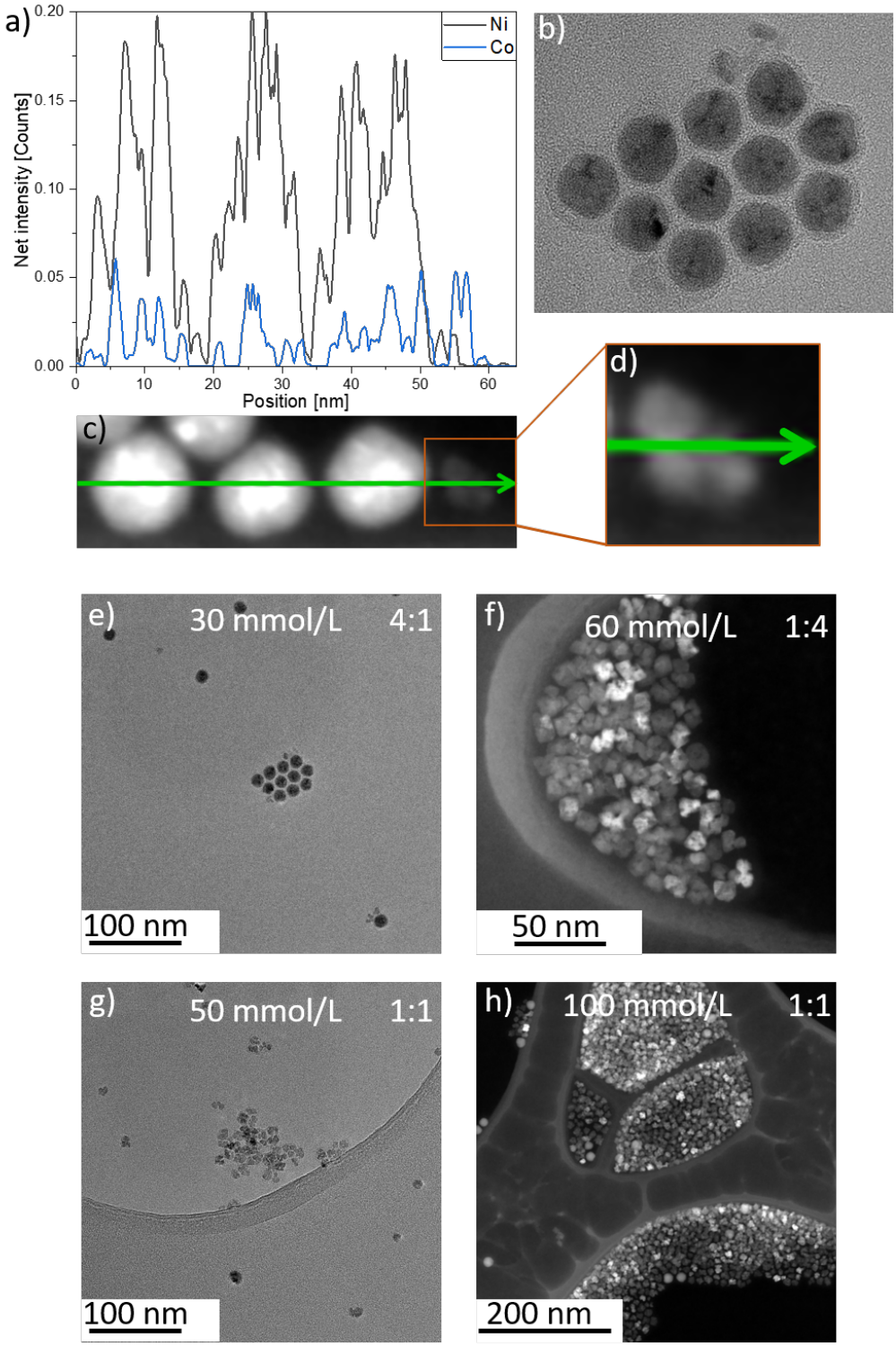

Figure 4.16: Element distribution of Ni and Co by EDXS/STEM: a) linescan of Ni and Co over four NPs, which are depicted in c), enlarged in d), and additional TEM image of the same sample b). TEM respectively STEM images of NiCo NPs prepared with 3 eq TOP, adjusted eq OAm, 5mL, 2h 220°C with different concentrations and metal ratios varying from 5:1 (Ni:Co) in e) over 1:1 in f) and g) up to 1:4 in h).

Both metals disfavour reduction while the values are very close to one another. Since $E_0(Ni^{2+}/Ni^0)$ is larger than $E_0(Co^{2+}/Co^0)$ its reduction might start earlier and with a higher reduction rate leading to the formation of spherical NiNPs. During this reduction and formation process the reduction of Co starts and Co is introduced into the spherical NPs. However, monometallic Co NPs also form. The difference in crystal structure between face centered cubic Ni and hexagonal closed packed Co could also cause the phase separation. The negative effect of Co on the sphericity of the NPs is supported by TEM/STEM images of bimetallic NPs synthesized with metal ratios varying between 5:1 and 1:4 eq $Ni(acac)_2$:$Co(acac)_2$ shown in Figure 4.16 e-h. The higher the cobalt content in the sample the rarer are spherical NPs within irregularly shaped NPs.
Due to the strong irregularity and the low size tunability Co was considered as a non-optimal co-metal for the formation of monodisperse bimetallic Ni NPs. As an alternative further investigations were conducted using Cu as co-metal in the following chapter.

4.3 Bimetallic Nickel Copper Nanoparticles

4.3.1 Physical Characterization of Nickel Copper Nanoparticles

The thermal reduction pathway adapted and simplified for the monometallic NiNPs was expanded with the addition of copper acetylacetonate ($Cu(acac)_2$) in the reaction mixture and its co-reduction with $Ni(acac)_2$. A representative synthesis with a Ni:Cu ratio of 5 leads to the formation of 15.8 nm sized NiCu NPs with a size distribution of 10 % derived by SAXS analyses using the Schulz-Zimm distribution (see Figure 4.17a). The XRD pattern of these NPs, given in Figure 4.17b, shows reflections of crystalline Ni(0) and Cu(0), indicating crystalline domains inside the NPs. TEM measurements were performed to confirm the size and resulted in spherical 16.8 nm NPs with a size distribution of 15 % as shown in Figure 4.17c-d, which is in accordance with the size derived by SAXS. STEM EDX measurements of these NPs indicate the formation of a core shell structure with Cu in the center surrounded by a Ni layer as evident from the linescan of representative NPs Figure 4.17e and in the element mapping in Figure 4.17f. The structure can be explained with the different standard potentials of Cu and Ni. The standard potential of Cu (E_0 (Cu^{2+}/Cu) = 0.34 V) is higher than Ni (E_0 (Ni^{2+}/Ni) = - 0.23 V), which means that Cu is easier to reduce while Ni requires harsher conditions thus Cu is reduced first, followed by Ni, leading to Ni@Cu core-shell NPs. To study the local structure and the oxidation state XANES/EXAFS measurements were performed. The Ni- and Cu- K-edge EXAFS spectra are shown in Figure 4.18. The Ni K-edge EXAFS spectrum of the NPs (black) shows similarities to the pure Ni fcc as well as to

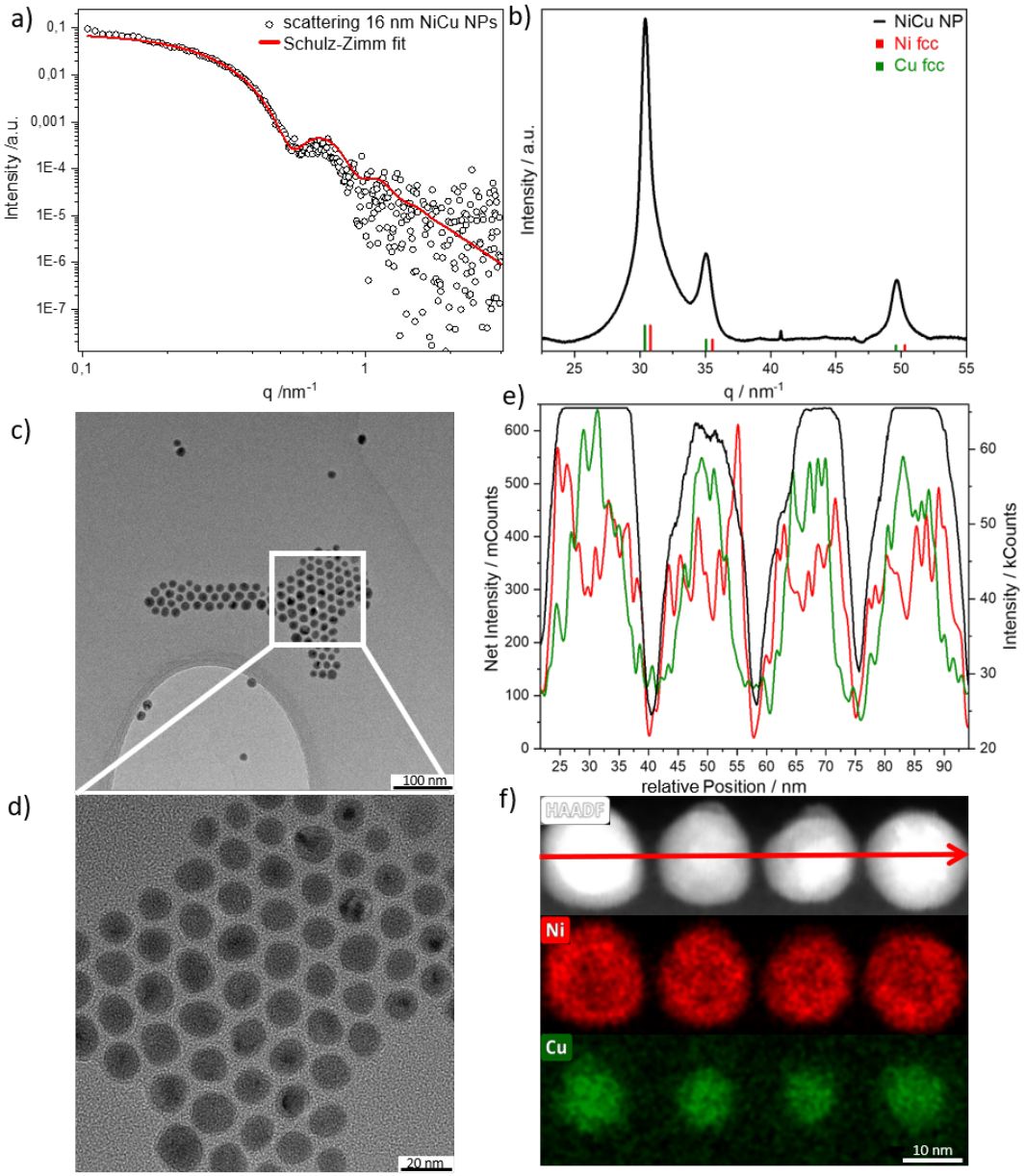

Figure 4.17: a) SAXS curve of 15.8 nm NiCu NPs (circles), prepared using 90 eq OAM, 10 eq TOP, a Ni/Cu concentration of 30 mmol L^{-1} and a 5:1 ratio, fitted with Schulz-Zimm model (red line) and b) XRD pattern of 15.8 nm NiCu NPs (black) compared to the database entries JCPDS database PDF 04-0850 for bulk Ni (black) and PDF 04-0836 for bulk Cu (red). c)-d) TEM images of monodisperse spherical NiCu NPs with a radius of 16.8 nm prepared using 90 eq OAm, 10 eq TOP, a Ni/Cu concentration of 30 mmol L^{-1} and a 5:1 ratio in two magnifications. e) Linescan of a representative bimetallic NiCu NP, f) EDX mapping with Ni (red) and Cu (green).

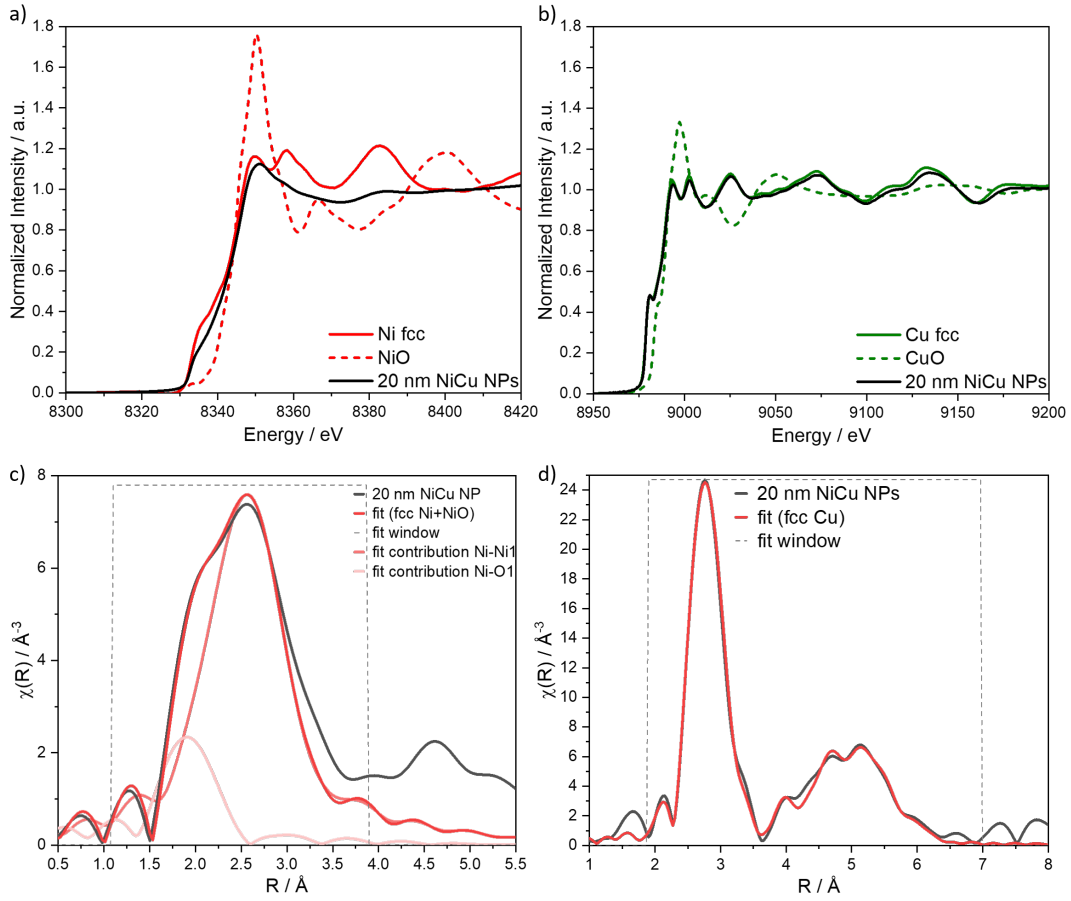

Figure 4.18: a) Normalized Ni K-edge EXAFS-spectra of bimetallic NiCu NPs (black), a Ni film (red straight), and NiO (red dotted), b) normalized Cu K-edge EXAFS-spectra of bimetallic NiCu NPs (black), a Cu foil (green), and CuO (green dotted, c) EXAFS oscillations as a function of the interatomic distance R in real space obtained by Fourier transformation of NiCu NPs (black) and fcc Ni bulk and NiO fit (red), d) EXAFS oscillations as a function of the interatomic distance R in real space obtained by Fourier transformation of NiCu NPs (black) and fcc Cu bulk fit (red).

Table 4.6: Comparison of the fitted EXAFS data of the NiCu NPs with the structural parameters of fcc Ni, NiO (RMSE = 0.11 Å), and fcc Cu (RMSE = 0.05 Å).

	coordination number		**distance R/Å**		
	ref	**NiCu NPs**	$\mathbf{R}_{model}$	$\mathbf{R}_{fit}$	$\mathbf{R}^2_{diff}$
Ni fcc	12	1.62 ± 0.60	2.49	2.54	0.023 Å^2
NiO	6	0.69 ± 0.18	2.09	1.93	0.002 Å^2
Cu fcc	12	11.29 ± 1.00	2.56	2.53	0.001 Å^2
Cu fcc	6	4.91 ± 3.44	3.62	3.57	0.003 Å^2

the NiO, although the prominent white line of NiO is not as strong for the NPs. The Cu K-edge EXAFS spectrum of the NPs (black) is nearly identical to the Cu foil, confirming the presence of metallic Cu. These similarities are supported by the coordination number N and the interatomic distance R extracted from the EXAFS data shown in Table 4.6. The number of directly coordinated Ni atoms is quite low compared to fcc Ni, which can be explained with a low crystallinity and the formation of NiO. The Cu atoms exhibit a nearly perfect first and second coordination sphere compared to fcc Cu. These findings support the location of Cu in the center of the bimetallic NPs covered by a protective passivation layer of NiO.

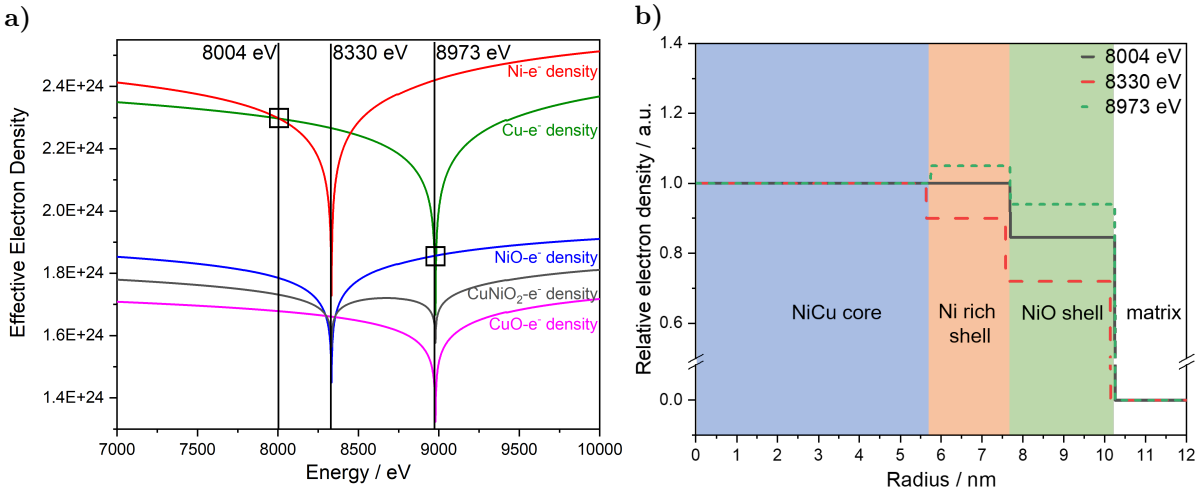

Figure 4.19: a) Effective electron density of Ni and Cu and some of their oxides calculated around the X-ray K-absorption edges of Ni (8333eV) and Cu (8979eV) and b) relative radially averaged electron density of NiCu NPs derived from scattering curves obtained at energies of 8004, 8330, and 8973 eV.

The nanochemical structure of the NiCu NPs was characterized with ASAXS measurements. ASAXS is measured at X-ray absorption edges SAXS of elements, by which the nanostructure and the elemental composition fluctuations of these elements can be determined. Ni(0) and Cu(0) have X-ray K-absorption edges at 8333 eV and 8979 eV, respectively. At 8004 eV Cu(0) and Ni(0) show the same effective electron density (EED), while being much higher than NiO and e.g. CuO as shown in Figure 4.19a. At 8330 eV the EED of Cu is significantly higher than Ni, which is still higher than NiO. The EED of Cu is not different to NiO at 8973 eV, but much less than Ni. Important is to mention that the EED of Cu is higher than that of Ni at 8330 eV. That relation is reversed at 8973 eV. This knowledge will be used to identify, where elements are enriched or diluted. The scattering curves were approximated using a sphere with a LogNorm distribution for the core and two shells surrounding the sphere, with shell 1 being the inner shell and shell 2 the outer shell. The shell and core thickness derived from the fitting model is given in Figure 4.19b. The relative effective electron densities (RED) are approximated

and given relative to the core, which is set to 1. At 8004 eV the inner shell exhibits the same RED as the core, while the RED of the outer shell 2 is much lower indicating the location of NiO in the outer shell. At 8330 eV the RED of the inner shell is lower compared to the core, suggesting the location of Cu in the core, since the EED of Cu is higher than Ni at 8330 eV. The RED of the inner shell is higher than the core at 8973 eV, supporting the assumption of a Ni rich shell 1. The RED of the outer shell is drastically lower compared to the inner shell and the core confirming the formation of a passivation NiO layer. Combining the information from the three energies, the NiCu NPs are composed of a NiCu alloy core surrounded by a Ni enriched layer, which is covered by a NiO dominated outer passivation shell.

4.3.2 Influence of Reaction Conditions

The conditions of the adapted thermal reduction synthesis method reported herein were investigated to optimize the size tunability. Reaction conditions such as (1) time dependence of the particle formation, (2) amount of reducing agent (5-90 eq OAm), (3) amount of stabilizer (1.5-50 eq TOP), and (4) concentration of metal salts were varied.

(1) time dependence of particle growth:

For this purpose, a reaction using 30 mmol L^{-1} metal salt ($Ni(acac)_2$:$Cu(acac)_2$ = 5:1) with 90 eq reducing agent OAm to the metal salt and 3 eq stabilizer TOP was heated to 220 °C and stopped after 10, 40, 70, and 120 min, precipitated, and redispersed in n-hexane. The particle sizes were determined using SAXS (see Table 4.7). The underlying SAXS-data are shown in Figure A.7.

Table 4.7: Influence of reaction time on particle size and polydispersity.The following reaction conditions were chosen: 31 mmol L^{-1} metal salt, 0.19 eq $Cu(acac)_2$, 88 eq OAm, 10 eq TOP, 2 h at 220°C.

time / min	size / nm[1]	PD / %[1]
10	15.3	20
40	19.6	15
70	19.6	10
120	19.5	24

[1] = SAXS data.

Within the first 10 minutes at 220°C a fast growth of NPs occurs. The final size is reached after 40 minutes of reaction time. The polydispersity differs within the measurements after reaching the final particle size. The UV Vis spectra of the reaction solution shown in Figure 4.20a are similar to the 5:1 $Ni(acac)_2$:$Cu(acac)_2$ reference spectrum in Figure 4.20b at the beginning of the reaction. The broad absorption maximum, which reaches up to 450 nm narrows down to 340 nm, comparable to the pure $Ni(acac)_2$ reference spectrum within the first 10 minutes. Afterwards the absorption broadens over the whole visible spectral range due to absorption and scattering contributions of the formed NPs.

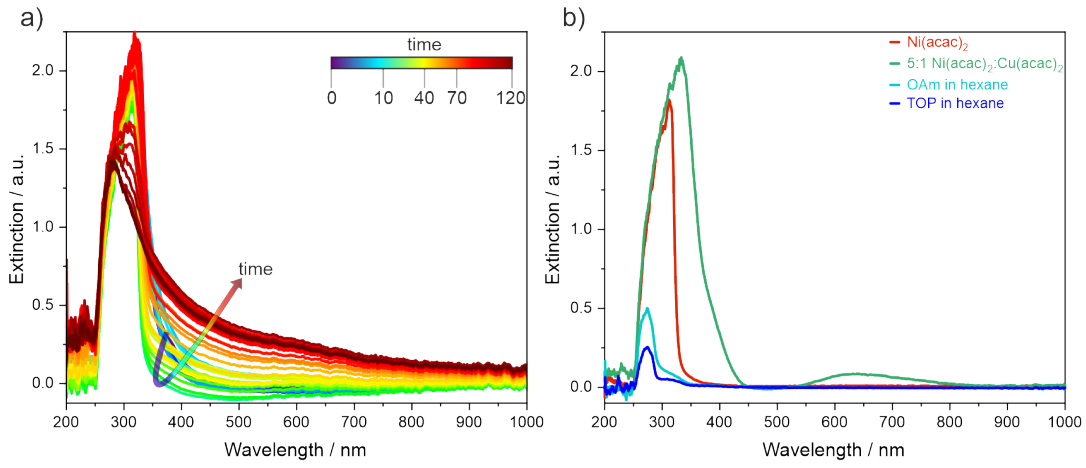

Figure 4.20: a) UV Vis spectra of the reaction solution for the formation of NiCu NPs at different points of the synthesis. All solutions were diluted in hexane from 1:20 up to 1:80. b) Reference UV Vis spectra of $Ni(acac)_2$, 5:1 $Ni(acac)_2$:$Cu(acac)_2$, OAm and TOP are shown.

(2) Amount of reducing agent OAm:

The studies concerning the impact of the amount of OAm on the particle size were conducted using 10 eq TOP and DBE as co-solvent. By increasing the amount of reducing agent from 5 to 90 eq OAm the NP size increases from 6 to 15 nm as shown in Figure 4.21 top left, based on SAXS data. The underlying SAXS data are shown in Figure A.8. 5 eq OAm lead to 6 nm NPs (PD 16 %) whereas 90 eq lead to 15 nm NPs (PD 12 %) with comparable polydispersity. TEM images of NiCu NPs shown in Figure 4.21 right indicate the formation of spherical NPs throughout the whole OAm range. Within a range of 20-50 eq OAm the polydispersity increases up to 40 % while it is below 20 % otherwise as determined by SAXS data. The increased polydispersity is visible in the TEM image of NiCu NPs prepared with 20 eq OAm compared to the other three TEM images. The increase in polydispersity with increasing amount of reducing agent can be explained by the classical nucleation theory. Herein the increase of reducing agent leads to a larger number of nuclei, which lead to a burst nucleation and offer the opportunity to grow with a larger size distribution. A possible reason might be Ostwald ripening consuming the smaller NPs and leading to a smaller size distribution. XRD pattern of NiCu NPs with increasing size due to increasing amount of OAm are shown in Figure 4.21 bottom left. Upon increasing NP diameter the reflections corresponding to Ni fcc and Cu fcc appear and get less broad.

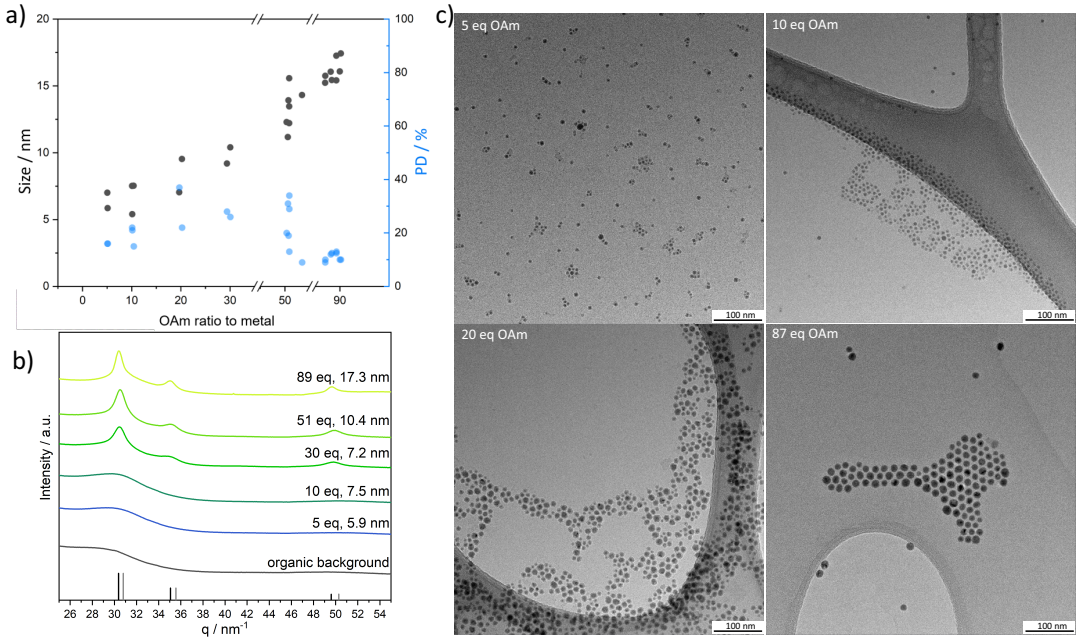

Figure 4.21: a) Size dependence of NiCu NPs on the amount of reducing agent OAm, sizes derived from SAXS measurements; b) XRD data of NiCu NPs with varying sizes prepared with varying amounts of OAm; c) TEM images of NiCu NPs prepared with varying OAm amounts.

(3) Amount of stabilizer TOP:

The influence of TOP on the final NP size was studied in a range of 1.5 to 50 eq TOP to the metal salts, while the OAm amount was adjusted according to the TOP amount without the addition of further solvent. By increasing the amount of TOP the NP size decreases proportionally from 30-40 nm to 6 nm with a stable polydispersity lower than 20 % as depicted in Figure 4.22 top left (the underlying SAXS data are given in Figure A.9). 1.5 eq TOP lead to large NPs with an average size of 33.5 nm and an average PD of 11 % down to 6.8 nm NPs with a PD of 16 % with 50 eq TOP. The TEM images given in Figure 4.22 right show the formation of spherical NPs with low polydisperisty. The NPs are quite monodisperse in all cases. Due to the steric hindrance of TOP, we hypothesize that the NPs are more effectively stabilized with an increasing amount of TOP and thus protected from continued growth via aggregation.

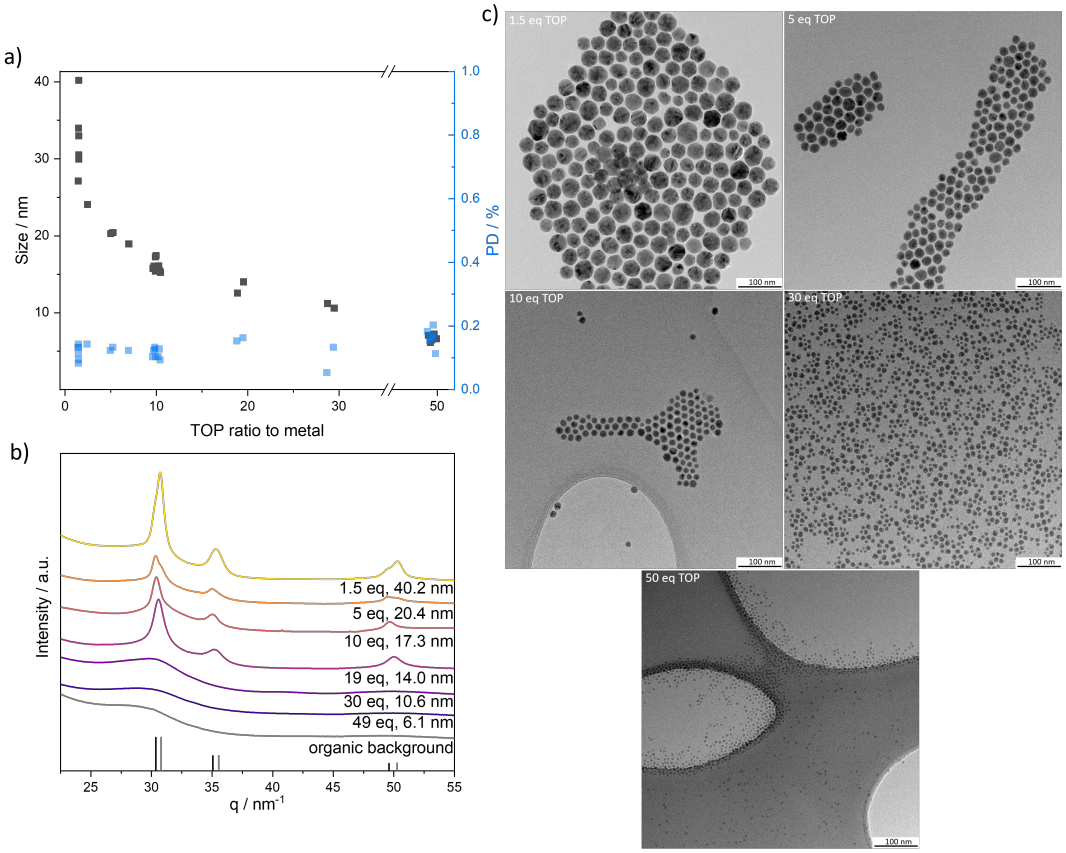

Figure 4.22: a) Size dependence of NiCu NPs on the amount of stabilizer TOP, sizes derived from SAXS measurements; b) XRD data of NiCu NPs with varying sizes prepared with varying amounts of TOP; c) TEM images of NiCu NPs prepared with varying TOP amounts.

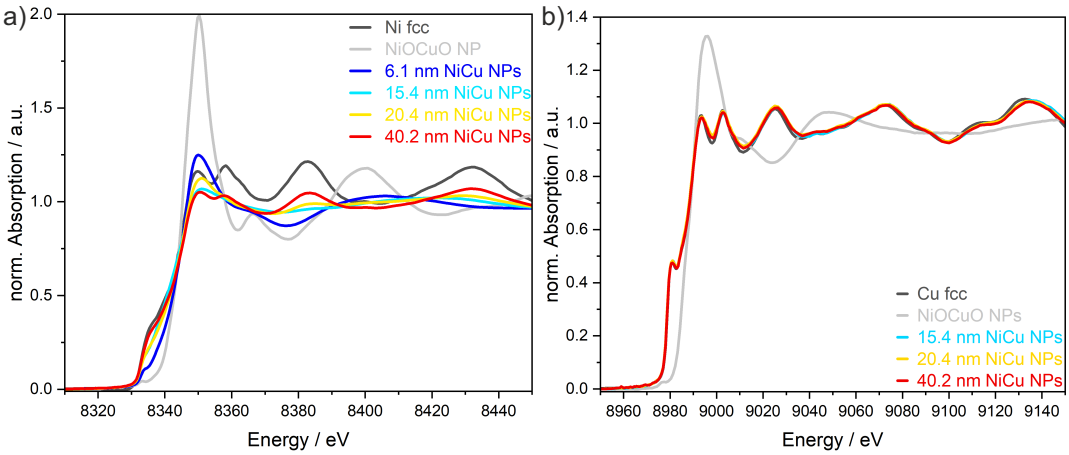

Figure 4.23: a) Normalized Ni K-edge XANES-spectra of NiCu NPs (red 40.2 nm, yellow 20.4 nm, light blue 15.4 nm, blue 6.1 nm), a Ni foil (black), and NiOCuO NPs (grey) and b) normalized Cu K-edge XANES-spectra of NiCu NPs (red 40.2 nm, yellow 20.4 nm, light blue 15.4 nm), a Cu foil (black), and NiOCuO NPs (grey).

Table 4.8: Comparison of the fitted EXAFS data of NiCu NPS (Ni:Cu = 5) with the structural parameters of fcc Ni, fcc Cu, and NiO. The NPs were prepared with 1.5 eq TOP (40.2 nm),5.3 eq TOP (20.4 nm), 10.4 eq TOP (15.4 nm), and 49.3 eq TOP (6.1 nm).

	coordination number NiCu NPs				**reference**
	40.2 nm	**20.4 nm**	**15.4 nm**	**6.1 nm**	
Ni-Ni1	6.23 ± 1.53	3.72 ± 1.81	1.62 ± 0.60	0.60 ± 1.17	Ni fcc : 12
Ni-O	-	1.05 ± 0.85	0.69 ± 0.18	2.16 ± 0.74	NiO : 6
Cu-Cu1	10.59 ± 0.83	10.91 ± 1.07	11.29 ± 1.00	-	Cu fcc : 12
Cu-Cu2	3.85 ± 2.13	5.78 ± 4.80	4.91 ± 3.44	-	Cu fcc : 6
	Distance R/Å NiCu NPs				**Reference**
	40.2 nm	**20.4 nm**	**15.4 nm**	**6.1 nm**	
Ni-Ni1	2.50	2.51	2.55	2.56	Ni fcc : 2.49
Ni-O	-	1.97	1.93	1.97	NiO : 2.09
Cu-Cu1	2.54	2.53	2.53	-	Cu fcc : 2.56
Cu-Cu2	3.59	3.57	3.57	-	Cu fcc : 3.62

EXAFS measurements of NiCu NPs of 4 different sizes (40.2, 20.4, 15.4, and 6.1 nm) were conducted to investigate the impact of the NP size on the oxidation state of the metals. In Figure 4.23 an increase of the white line at the Ni K-absorption edge appears in the XANES region with decreasing NP size. The XANES spectra at the Cu K-edge show the same features as the spectrum of Cu fcc foil, except for the 6 nm NiCu NPs, where the Cu content was to low. The EXAFS data are given in Table 4.8 and the fitted distance in the first sphere of Ni fcc and NiO, and the first and second sphere of Cu fcc are in good agreement with the reference distances of the bulk materials. The fitted

coordination number of the neighbour in the first respectively second sphere around a Ni atom vary strongly with the NP size. The largest 40 nm NiCu NPs have half of the first coordination sphere filled with Ni atoms, while statistically only 0.6 Ni atoms surround a Ni atom in the first sphere in the 6 nm NiCu NPs. The local ordering of Ni fcc decreases with decreasing NP size while the amount of NiO increases in the first sphere around a Ni atom. Surprisingly the local structure of Cu is very constant and independent of the NP size.

All NPs produced with the high purity reagents are spherical and near monodisperse. The importance of highly pure reaction compounds was shown by replacing stabilizer TOP with a high purity of 97 % with a 90 % pure TOP following the same reaction conditions otherwise. Using 10 eq TOP NPs with a diameter, determined by SAXS, of 15.4 nm (PD 12 %, 97 % pure TOP) respectively 11.3 nm (PD 21 %, 90 % pure TOP) were achieved. TEM measurements shown in Figure 4.24 revealed spherical NPs with 97 % pure TOP and a wide variety of shapes ranging from spheres, cubes, triangles, to sticks with 90 % pure TOP for 10 eq TOP respectively 1.5 eq TOP. This proves on the one hand side the importance of pure compounds on the other hand the importance of orthogonal analytical techniques like SAXS and TEM.

Guo *et al.* studied the transformation of triangular to hexagonal NiCu NPs (Ni:Cu = 5:1, 1 eq TOP) depending on the reaction

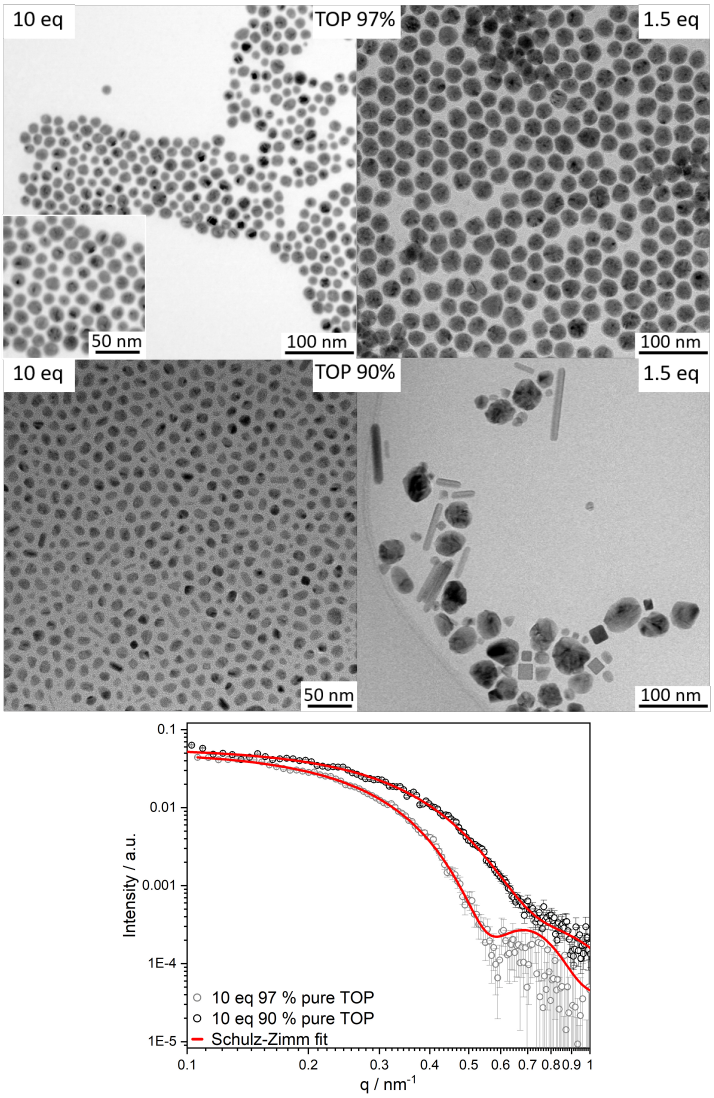

Figure 4.24: TEM images of NiCu NPs (top) prepared with 10 eq TOP (left) and 1.5 eq TOP (right) with 97% (top) and 90 % (bottom) purity resulting in spherical respectively multiform NPs. SAXS scattering of NiCu NPs (bottom) prepared with 10 eq 97% pure TOP (grey) and 90% pure TOP (black), resulting in 15.8 nm (10 % PD) respectively 11.3 nm (21 % PD).

temperature and the heating rate using 97 % pure TOP. They found a strong dependence of the NP shape on the heating rate, fast heating resulted in spherical NPs while slow heating in mostly triangular respectively mostly hexagonal nanoplates. With increasing reaction temperature the found an increasing Ni content in the NPs as well as mostly hexagonal nanoplates at 220 °C and mostly triangular plates at 210 °C.[228] In this work the diversity of shapes could be achieved at 220 °C by reducing the purity of the stabilizer from 97 to 90 %.

(4) Concentration of metal salt:

The concentration of metal salt (5:1 Ni:Cu ratio) was varied within 15 to 120 mmol L^{-1} as shown in Table 4.9 and it appears to have a negligible impact on the particle size as well as the polydispersity. Upon incresing the concentration 120 mmol L^{-1} the size decrases slightly, which might be associated with a relatively low OAm amount (11 eq), since a smaller OAm amount was found to result in smaller NPs as shown in Figure 4.21.

Table 4.9: Impact of the metal salt concentration of the size of the formed NPs. Reaction conditions: 10 eq TOP, 5:1 Ni:Cu, 5 ml, 220°C. Sizes derived from SAXS shown in Figure A.10.

metal salt concentration mmol/L	**OAm eq**	**size nm**	**PD %**
15	182.3	16.3	13
30	87.0	15.8	10
30	88.4	15.4	12
30	89.3	15.4	12
60	37.2	16.5	14
120	11.6	13.1	15

4.3.3 Catalytic Activity of Bimetallic Nickel Copper Nanoparticles

The catalytic activity of NiCu NPs for the reverse water gas shift reaction (RWGS) was determined at atmospheric pressure using a representative set of NPs varying in size and Cu content listed in Table 4.10 (reaction conditions given in Table A.2). NP sizes ranging from 7 to 31 nm with Ni/Cu ratios of >15 to 1.3 were investigated concerning the influence of NP size and Cu content on the catalytic activity. The impact of shape was taken into account with sample 12Ni5-shape, which was synthesized with the 90 % pure TOP, which led to the formation of a broad variety of sizes and shapes as described before and depicted in Figure A.12. The NPs were characterized using SAXS directly after synthesis giving size and distribution in Table 4.10, and were afterwards

supported on porous silicon dioxide (SiO_2, GRACE) via dry impregnation, described in subsection 3.3.9. The loading of the NPs on the supporting material (wt%) and the Ni/Cu ratio was determined by ICP-MS of the final catalysts and is given in Table 4.10. A loading of around 1 wt% was approached and reached with slight variations. The SiO_2 supporting material consists of particles in the micrometer range (~26 µm) shown in Figure 4.25 a, which exhibit a pore structure with a specific surface area of 23.6 $m^2\,g^{-1}$ and a most frequent pore size of 157 nm given in Table 4.11 and shown in Figure 4.25b-d in different magnifications.

Table 4.10: Samples used for catalytic testing and their characterization in size and poldisperisty using SAXS, and metal ratio and loading using ICP-MS.

sample	**size**	**PD**	**metal ratio**	**loading**
	nm	**%**	**Ni/Cu**	**wt%**
31Ni5	31.0	10	4.9	0.98
28Ni3	28.1	12	3.1	0.78
17Ni5	16.7	11	5.5	1.36
17Ni3	17.2	16	3.5	1.28
19Ni1	19.1	13	1.4	0.99
13Ni6	12.7	29	6.2	0.91
15Ni1	15.0	20	1.3	1.01
12Ni7-shape	11.5	21	6.7	1.00
7Ni34	7.1	17	33.8	1.12
8Ni15	8.0	17	15.1	1.21
8Ni2	7.5	26	2.2	1.03

TEM measurements of the catalysts after preparation and prior to catalysis were conducted and TEM images of four catalysts are shown in Figure 4.26. They indicate a uniform distribution and well separation of the NPs on the SiO_2 surface. Pore structure analysis of three representative catalysts and the pure supporting material are shown in Table 4.11. The specific surface area decreased very slightly upon supporting with the NPs from 23.6 to minimum 22.5 $m^2\,g^{-1}$. The decrease of surface area could be linked to the loading of NPs, but seems to be independent of the NP size. The specific pore volume derived from mercury intrusion porosimetry (MIP) shows a negligible decrease upon addition of NPs indicating the even distribution of the NPs on the surface of the supporting material without clogging up the pores. The most frequent pore size supports this assumption, since it shows no significant change upon supporting with NPs. The porosity of the material, however, decreases significantly during impregnation, in dependence of the NP size, where the smallest 8 nm NPs lead to the highest decrease in porosity.
The catalytic activity of the bimetallic NiCu NPs was tested at LIKAT e.V. at ambient pressure with a reactant gas mixture of 1:1 CO_2:H_2 and a flow rate of 25 mL/min.

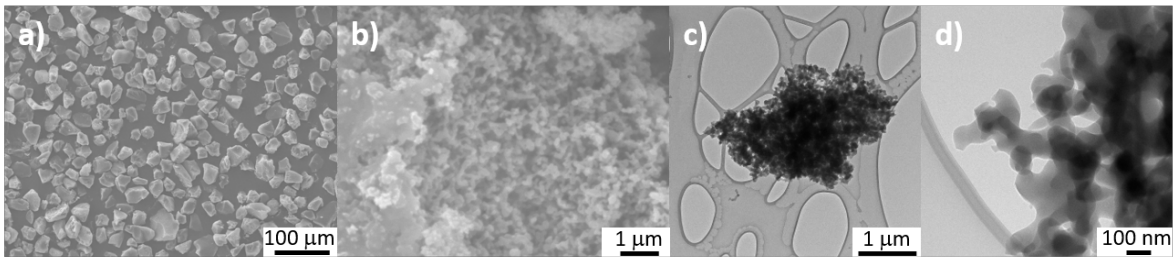

Figure 4.25: SEM images of the supporting material (a-b), as well as TEM images with higher resolution (c-d) revealing the porous structure of the silicone dioxide.

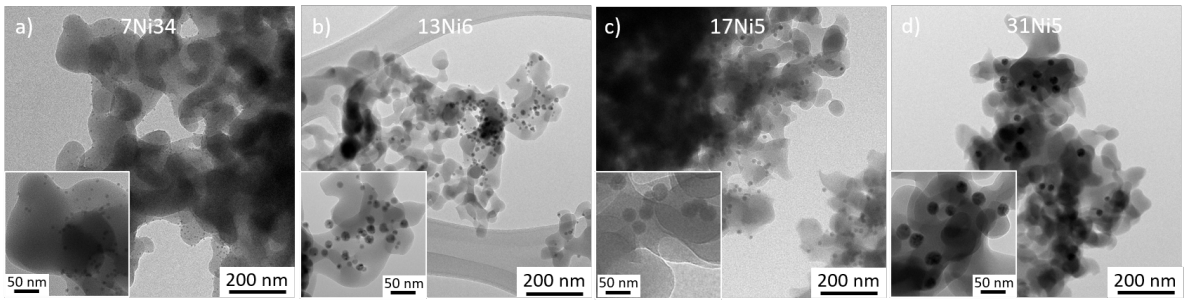

Figure 4.26: TEM images of the supported NiCu NPs on SiO_2ing material (a-b), as well as TEM images with higher resolution (c-d) revealing the porous structure of the silicone dioxide.

Table 4.11: Pore structure analysis via gas sorption and MIP resulting in the most frequent pore size, porosity, the specific pore volume, and the specific surface area (BET).

	NP loading		**MIP**			**gas sorption**
	size nm	**loading wt%**	**pore size nm**	**porosity %**	**specific pore volume mL/g**	**specific surface area m^2/g**
SiO_2	-	-	157.1	58.7	1.06	23.6
8Ni3	8.0	1.21	154.8	45.8	1.02	22.5
13Ni5	12.7	0.91	155.17	51.1	1.03	23.1
31Ni5	31.0	0.98	156.71	59.7	1.02	22.7

100 mg catalyst material was placed and fixed in a flow reactor and heated in a range of 300 to 700°C while an on-line gas analysis of the product gas was carried out. The activities of all tested catalysts at 500°C are shown in Figure 4.27 a. The conversion of CO_2 per minute per gram of NPs is shown in correlation with the size of the supported NPs. The Cu content in each catalyst is depicted by a colour code. NPs with in the size range of 17 and 30 nm show comparable activities, while an increasing amount of Cu leads to a slight decrease in activity. The smallest 8 nm NPs show the lowest activity, while the increasing Cu content has a positive effect on the activity in contrast to the bigger NPs. The 12Ni7-shape sample leads surprisingly to the lowest over all activity from all tested NPs indicating that the spherical shape of the NPs plays a

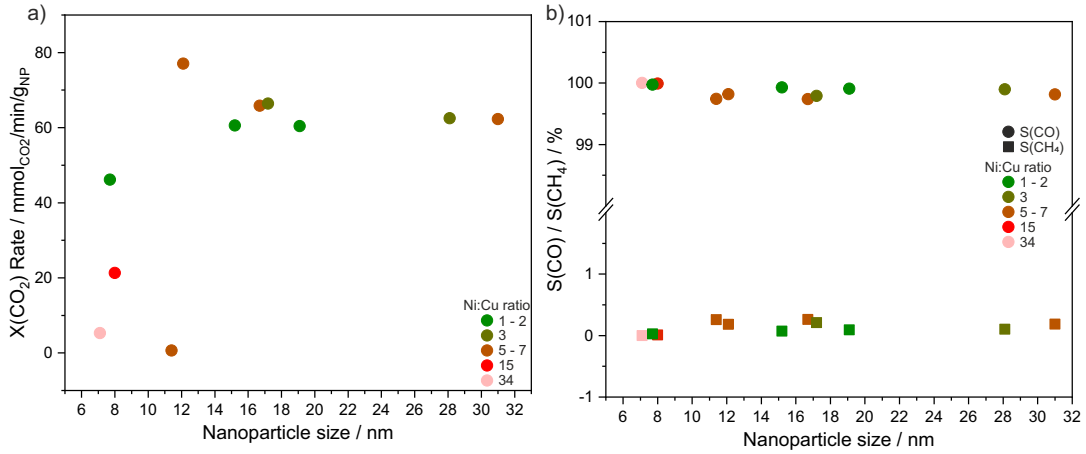

Figure 4.27: Catalytic activity of the NiCu NPs at 500°C depicted in dependence of the supported NP size. The Cu content follows the colour code green (much Cu) to red (less Cu). 100 mg catalyst, ~1 wt% NiCu NPs, GHSV = 15 000 L kg^{-1} h^{-1}, CO_2:H_2 1:1.

big role combined with the facets present on the surface. The variety of shapes might exhibit different external facets or varying ratios of these facets influencing the catalytic activity. All investigated catalysts show a selectivity of 99-100% for CO without further side products depicted in Figure 4.27b.

The catalytic activities were measured every 50°C from 300°C to 500°C while heating and cooling and the resulting activities are shown in Figure 4.28. A hysteresis appears for most of the catalysts in different intensities and forms. The 30 nm NPs showed a negative hysteresis upon cooling compared to heating as shown in Figure 4.28. The catalysts with 17 nm sized NPs showed a slight negative hysteresis above 400°C with a positive hysteresis below 400°C. The smaller the supported NPs the smaller was the hysteresis being nearly negligible for the 8 nm NP catalysts.

The catalytic activity of selected catalysts was studied up to a reaction temperature of 700°C as shown in Figure 4.29. The activity increases strongly above 400°C. A nearly continuous increase of catalytic activity can be seen for the 13Ni5 catalyst, which shows the highest CO_2 conversion at 700 °C of 222 mmol min^{-1} g^{-1} CO_2. The catalytic activity of the other catalysts was comparable at 500°C, but splits up upon temperature rise. At 700 °C the 32 nm NiCu catalyst shows the second highest activity of 171 mmol min^{-1} g^{-1} at 700°C, whilst it decreases over two hours from 192 to 171 mmol min^{-1} g^{-1}, where it stabilizes. The 17 nm NiCu catalyst reaches a maximum of 147 mmol min^{-1} g^{-1} and stabilizes within 30 minutes at 142 mmol min^{-1} g^{-1}. The 15 nm NiCu catalyst with a Ni:Cu ratio of 1.3 reaches a maximum 169 mmol min^{-1} g^{-1} and stabilizes over 90 minutes at 161 mmol min^{-1} g^{-1}. The corresponding selectivities of the tested catalysts are given in Figure 4.29 b, indicating a CO selectivity of over 99% while the lowest CO selectivities are detected below 400°C and at around 600°C.

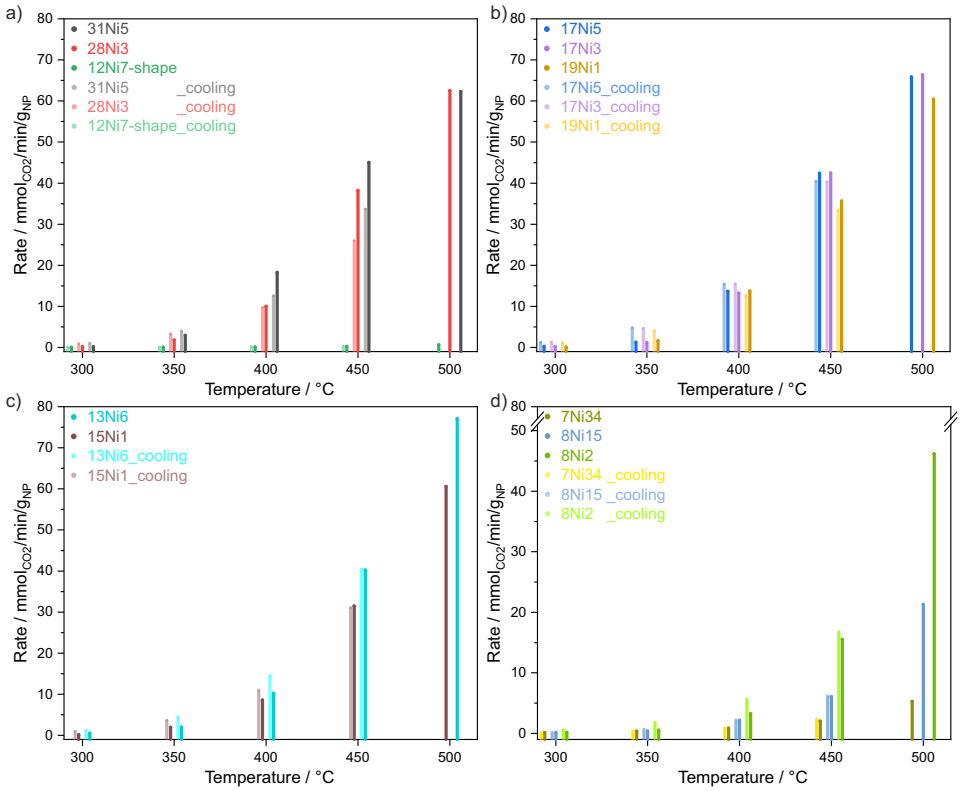

Figure 4.28: Hysterese of the catalytic activity of NiCu NPs from 300 to 500°C while heating up and cooling down (transparent) shown for the different size ranges from 30 nm a), 17 nm b), 13 nm c) to 8 nm d). 100 mg catalyst, ~1 wt% NiCu NP loading, GHSV = 15 000 L kg^{-1} h^{-1}, CO_2:H_2 1:1 stepwise to 500°C and cooling.

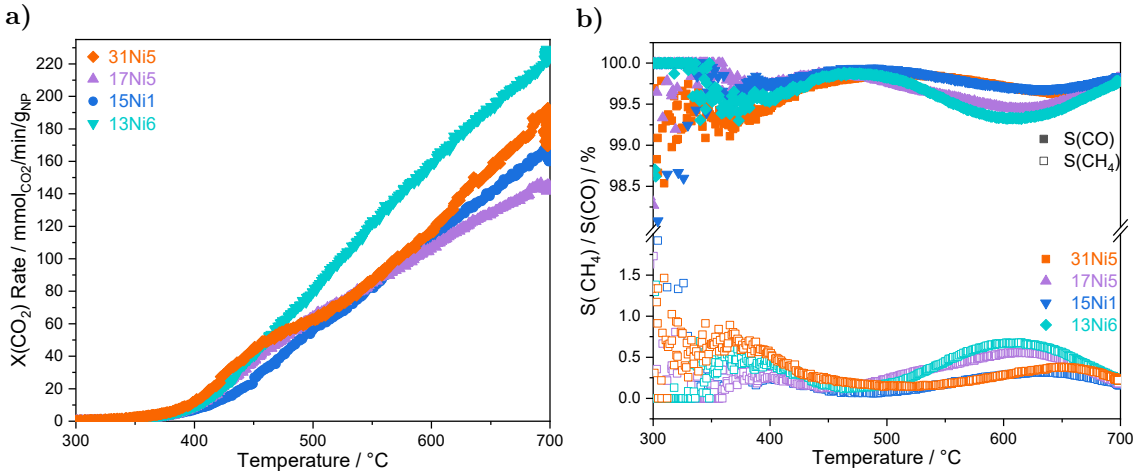

Figure 4.29: a) Catalytic activity for the conversion of CO_2 (X(CO_2)) of four NiCu catalysts with varying sizes and Ni/Cu ratios in the temperature range of 300 to 700 °C and b) corresponding selectivity for CO (S(CO), full symbols) and CH_4 (S(CH_4), open symbols); 100 mg catalyst, ~1 wt% NiCu NP loading, GHSV = 15 000 L kg^{-1} h^{-1}, CO_2:H_2 1:1.

4.3.4 Linking the Catalytic Activity to Structural Features

XANES spectra obtained before and after catalysis are given in Figure 4.30a compared to pure 13 nm NiCu NPs, Ni foil, and NiO. They show features of Ni fcc as well as NiO. The EXAFS oscillations as a function of the interatomic distance R are shown in Figure 4.30 and the EXAFS fits are given in Table 4.12. The pure 13 nm NiCu NPs and the catalyst material before catalysis show two maxima corresponding to the Ni-Ni distance in Ni fcc and the Ni-O distance in NiO in the first sphere. The NiO distance is less prominent after catalysis supported by the calculated coordination number, which decreased from 2.2 to 0.3 during catalysis. This indicates the partial reduction of the NiCu NPs during catalysis. The local coordination of the Ni with Ni atoms as in Ni fcc

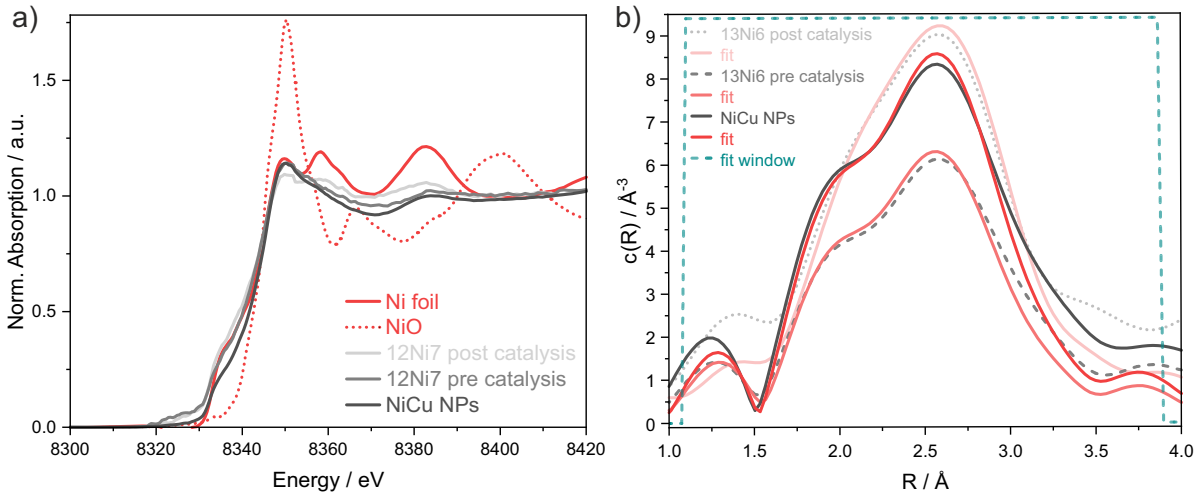

Figure 4.30: a) Normalized Ni K-edge XANES-spectra of NiCu NPs (black), 13Ni6 before catalysis (pre, dark grey), 13Ni6 after catalysis (post, light grey), a Ni foil (red straight), and NiO (red dotted); b) EXAFS oscillations as a function of the interatomic distance R in real space obtained by Fourier transformation of NiCu NPs (black), 13Ni6 before catalysis (pre, dark grey), 13Ni6 after catalysis (post, light grey), with corresponding fits in different shades of red.

Table 4.12: Comparison of the fitted EXAFS data of unsupported NiCu NPs (RMSE = 0.06 Å) and the catalyst material (13Ni6 before catalysis (pre, RMSE = 0.07 Å) and after catalysis (post, RMSE = 0.08 Å) with the structural parameters of fcc Ni and NiO.

	coordination number				**distance R/Å**			
	Ni fcc	**exp**	**NiO**	**exp**	**Ni fcc**	**exp**	**NiO**	**exp**
NiCu NPs	12	4.62 ± 2.29	6	2.02 ± 1.97	2.49	2.49	2.09	2.00
pre	12	3.56 ± 1.31	6	2.25 ± 1.65	2.49	2.49	2.09	1.99
post	12	3.37 ± 2.11	6	0.29 ± 0.67	2.49	2.50	2.09	1.97

does not change during the catalysis. The catalytic activity determined could not be easily linked to either the NP size nor the Cu content throughout all catalysts. To gain insights into the inner structure and the surface composition of the NPs, anomalous SAXS (ASAXS) and X-ray photon spectroscopy (XPS) measurements were conducted. ASAXS measurements were performed between 7000 and 10000 eV with a main focus on the energies 8004, 8330, and 8973 eV, since the effective electron density (EED) of the interesting elements Ni and Cu and their possible oxidized states cross or change their difference. As mentioned above, Cu(0) and Ni(0) show the same EED at 8004 eV, while being much higher than NiO and CuO as shown in Figure 4.31a. At 8330 eV the EED of Cu is significantly higher than Ni, which is still higher than NiO. The relation of Cu and Ni is reversed at 8973 eV and the EED of Cu is not different to NiO at 8973 eV. The variation of EED of the elements and their oxides will be used to identify, where elements are enriched or diluted.

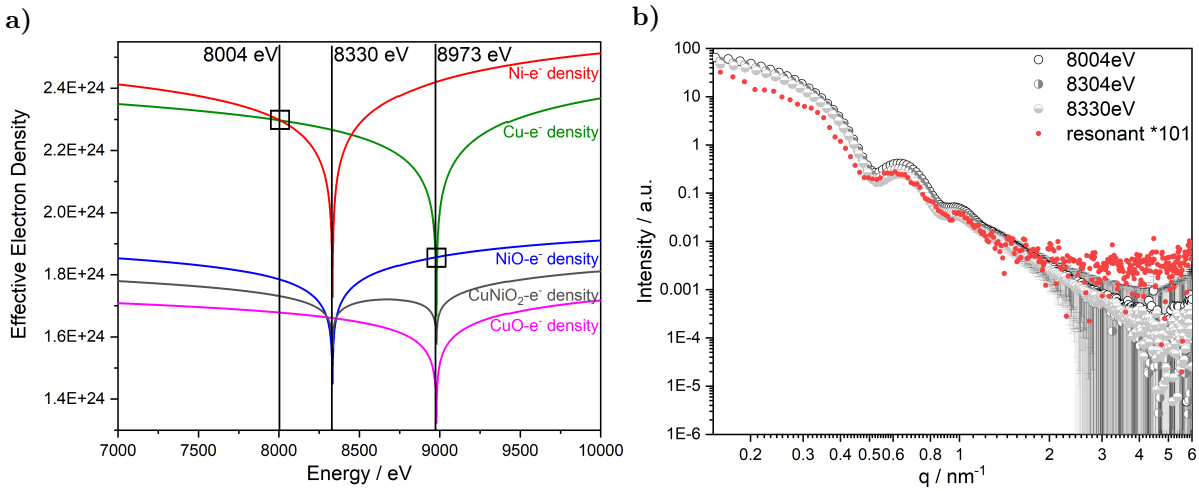

Figure 4.31: a) Effective electron density of Ni and Cu and some of their oxides calculated around the X-ray K-absorption edges of Ni (8333eV) and Cu (8979eV) and b) scattering curves of 17Ni5 NPs obtained at 8004, 8304 and 8330 eV compared to the resonant curve (red).

The scattering curves of NiCu NPs (17Ni5) obtained near the K-edge of Ni at 8004, 8304, and 8330 eV are given in Figure 4.31b. Via the Stuhrmann equation (Equation 3.11) the resonant scattering curve I_r of Ni (red dots) can be calculated with these three scattering curves. The shape of the scattering curves does not change with changing incident energy and the calculated Ni resonant. The similarities indicate the distribution of Ni in all nanostructural parts of the NP. The absorption edges of Ni and Cu are close together, so that the anomalous, energy dependent behaviour of the elements is overlapping, contradicting the Stuhrmann equation. Therefore the total scattering curves are used for further interpretation after background subtraction.

A common structural model needs to be identified, which is able to approximate the scattering curves at all three incident energies. Any modelling with a size distribution of homogeneous spherical NPs found no conclusive solution. Since this simple model failed, a homogeneous sphere could be ruled out. A common form-factor model including a core with a size distribution and a fixed shell thickness was applied. The scattering curve at 8004 eV could be successful approximated with a reduced relative electron density in the shell compared to the core. The scattering curves measured at 8330eV and 8973eV were impossible to approximate with this model, leading to the addition of a second shell with an electron density difference and a constant thickness to the model. This model with a core with a LogNorm size distribution and two shells was able to fit the scattering curves at 8330eV and 8973eV. For all three energies the outer shell (shell 2) thickness remained constant with a decreased RED, while the sum of core and the inner shell (shell 1) equals the core size at 8004eV. The shell and core thicknesses are given in Figure 4.32 and Figure 4.33, and are summarized in Table A.4. The relative effective electron densities (RED) are given relative to the core, which is set to 1. At 8004 eV the inner shell exhibits the same RED as the core, while the RED of the outer shell 2 is lower. For the 8Ni15 NiCu NPs a RED ratio between core and shell 2 of 0.64 was achieved, which is comparable to the theoretical ratio of NiO/Ni EEDs of 0.78 at 8004 eV, indicating the formation of a NiO outer shell.

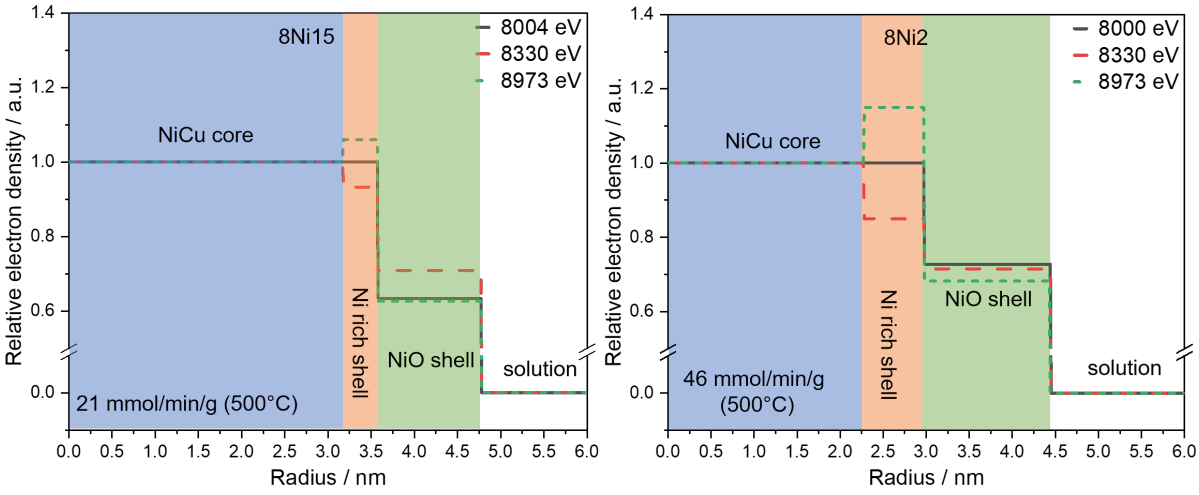

Figure 4.32: Relative radially averaged electron density of small NiCu NPs, derived from ASAXS measurements at energies of 8004, 8330, and 8973 eV.

The scattering curve obtained at 8330 eV resulted in the same core and shell thicknesses, but alternating REDs: The inner shell exhibits a lower RED of 0.93, indicating the location of Cu in the core, since the EED of Cu is higher than Ni at this energy (see Figure 4.31 a). The RED of the outer shell is even lower at 0.71, which is slightly higher

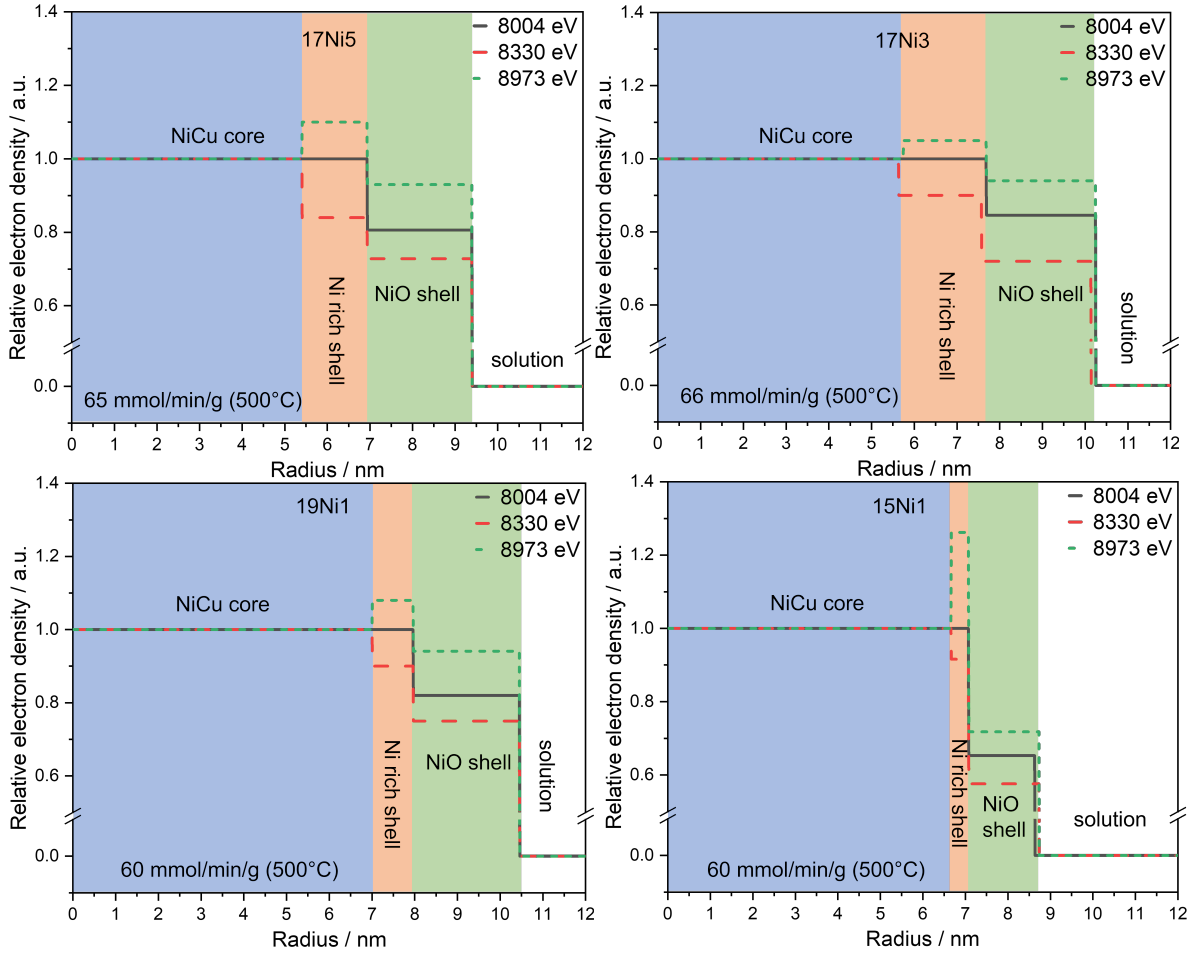

Figure 4.33: Relative radially averaged electron density of 15-19 nm NiCu NPs, derived from ASAXS measurements at energies of 8004, 8330, and 8973 eV.

than the NiO/Ni ratio of 0.67, but lower than NiO/Cu of 0.81. The REDs at 8973 eV invert, resulting in 1.06 for shell 1 and 0.63 for shell 2. The calculated RED of Ni and NiO to a 5:1 Ni:Cu mixture at 8973 eV is 1.04 respectively 0.80.

Combining the information gathered from the SAXS data at the three energies, the NiCu NPs are composed of a NiCu alloy core with varying diameter surrounded by a Ni enriched layer, which is covered by a NiO dominated outer passivation shell. The core-shell-fits for 15-19 nm "bigger" NiCu NPs are shown in Figure 4.33. With increasing Cu content the core radius increases and the Ni enriched shell decreases accordingly. The thickness of the NiO outer shell seems to be independent of the Cu content, but influenced by the average NP size as visualized comparing 19Ni1 and 15Ni1. The NP sizes derived by SAXS measurements at the synchrotron are larger compared to the sizes derived from the lab-scale Kratky-type instrument. For the smaller around 8 nm NiCu NPs the core size is inversely proportional to the Cu content, the Ni enriched inner shell seems to be unaffected, and the NiO outer shell increases with increasing

Cu content in the NP. The RED of shell 2 should have an expected value of 0.78 for NiO/Ni respectively NiO/Cu at 8004 eV, but shows smaller values of 0.73 respectively 0.63. The RED of the outer shell was fitted as 0.68 respectively 0.63 at 8973 eV. The calculated RED for NiO relative to different mixtures of Ni:Cu is depicted in Figure 4.34 as outer shell. The lowest expected RED for a potential pure Ni core would be 0.80 vs the highest expected for a pure Cu core of 1. The decreased RED of the NiO shell 2 might be explained with porosity, which would reduce the EED and thus the RED to the NP core.

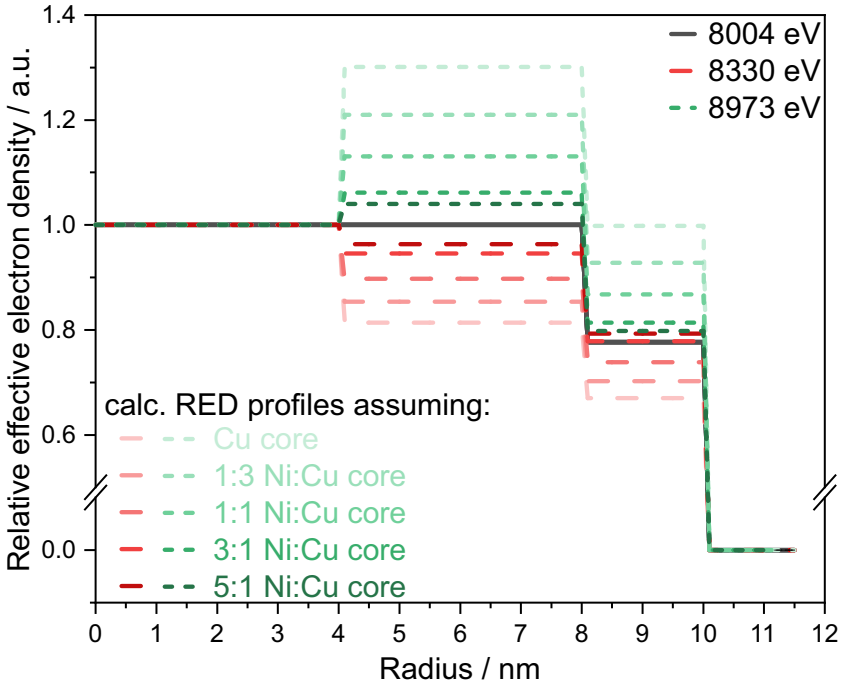

Figure 4.34: Relative effective electron density profiles calculated for the energies of 8004, 8330, and 8973 eV between a core having different ratios of Ni and Cu (set to 1) with respect to the solution are shown. Two typical shells surrounding the core are shown. The inner shell is assumed as pure Ni and the outer shell as pure NiO.

Since catalysis often takes place on the surface of material, the element distribution on the surface of the NPs was investigated by XPS. The information depth of XPS for this system is around 3 to 4 nm, which is why XPS can be treated as bulk analysis for the small NPs. A representative spectrum of 15.0 nm NiCu NPs in the region of of the Ni2p$_{3/2}$ states is shown in Figure 4.35. Ni(0), Ni(II), and Cu(0) / monovalent Cu were detected. Due to the weakness of the Cu LMM Auger signal it was not possible to distinguish between both valence states without doubt. In a semiquantitative approach the Cu/Ni ratio was determined using Cu 2p and Ni 2p peaks, and the Ni(0)/Ni(II) ratio considering the Ni2$p_{3/2}$ peak, which was fitted according to Biesinger *et al.*[229] The determined Ni and Cu ratios are given in Table 4.13. The Cu/Ni ratio observed for the

larger NPs within 15 to 20 nm is drastically lower than determined via MS, but increases with increasing Cu content in the NPs. The location of Cu in the core of the NP as determined by ASAXS is an explanation for the low Cu signal, since the radius of the NPs is around 4 times the information depth of XPS for these NPs.

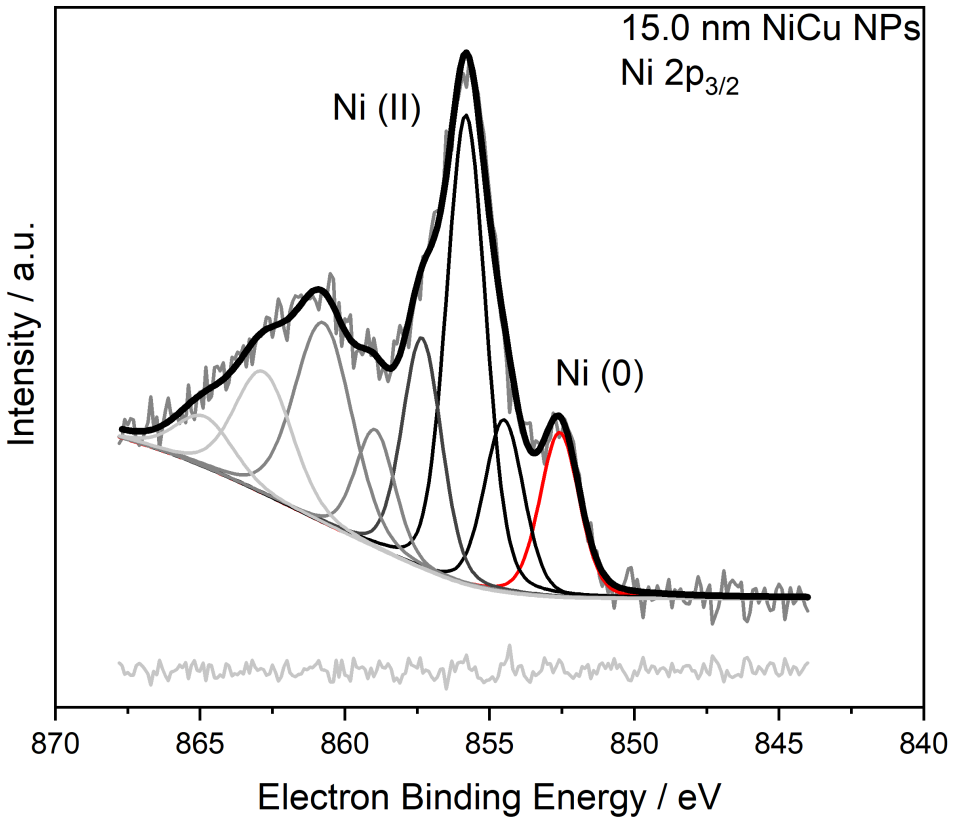

Figure 4.35: XPS spectrum of 15.0 nm NiCu NPs in the region of of the Ni$2p_{3/2}$ states.

Table 4.13: Cu/Ni ratios and the Ni(0)/Ni(II) ratios of selected core shell NiCu NPs obtained with XPS. Uncertainties were calculated with a triangular distribution based on three measurement points at three different locations on the sample.

sample	**size nm**	**Cu/Ni ratio**[1]	**X(CO_2)** [2]	**Cu/Ni ratio**[3]	**Ni(0)/Ni(II) ratio**[3]	**(Ni(0)+Cu)/ Ni(II) ratio**[3]
17Ni5	16.7	0.18	65.8	0.02 ± 0.01	0.06 ± 0.01	0.08 ± 0.01
17Ni3	17.2	0.28	66.4	0.06 ± 0.05	0.06 ± 0.02	0.14 ± 0.09
19Ni1	19.1	0.70	60.4	0.15 ± 0.03	0.06 ± 0.02	0.27 ± 0.04
15Ni1	15.0	0.78	60.6	0.18 ± 0.02	0.12 ± 0.02	0.40 ± 0.04
8Ni15	8.0	0.07	21.3	0.05 ± 0.01	0.21 ± 0.02	0.30 ± 0.03
8Ni2	7.5	0.47	46.2	0.42 ± 0.12	0.37 ± 0.04	1.01 ± 0.10

[1] = MS data, [2] = catalytic testing in mmol min^{-1} g^{-1}(NP), [3] = XPS data.

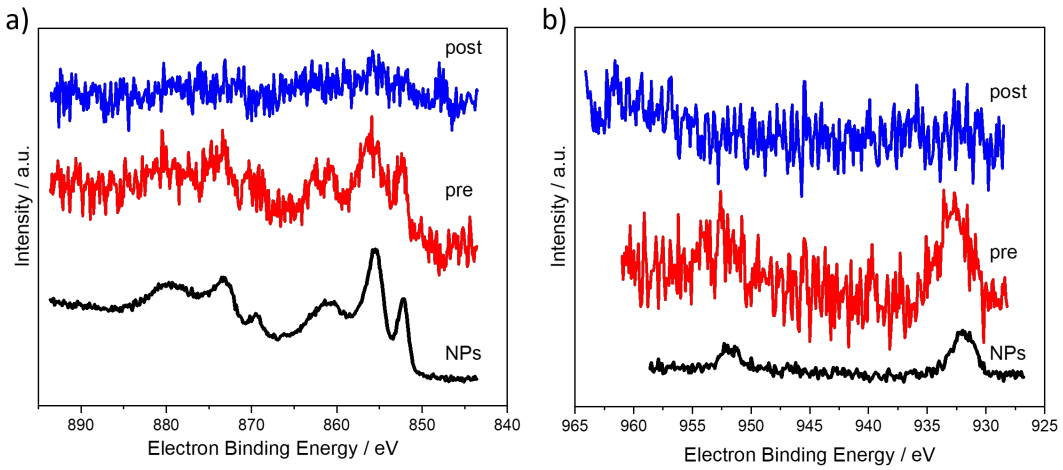

Figure 4.36: XPS spectra of 8.0 nm NiCu NPs (black), supported on SiO_2 before catalysis (pre, red) and after catalysis (post, blue) in the region of of the Ni2p states a) and of the Cu2p states b).

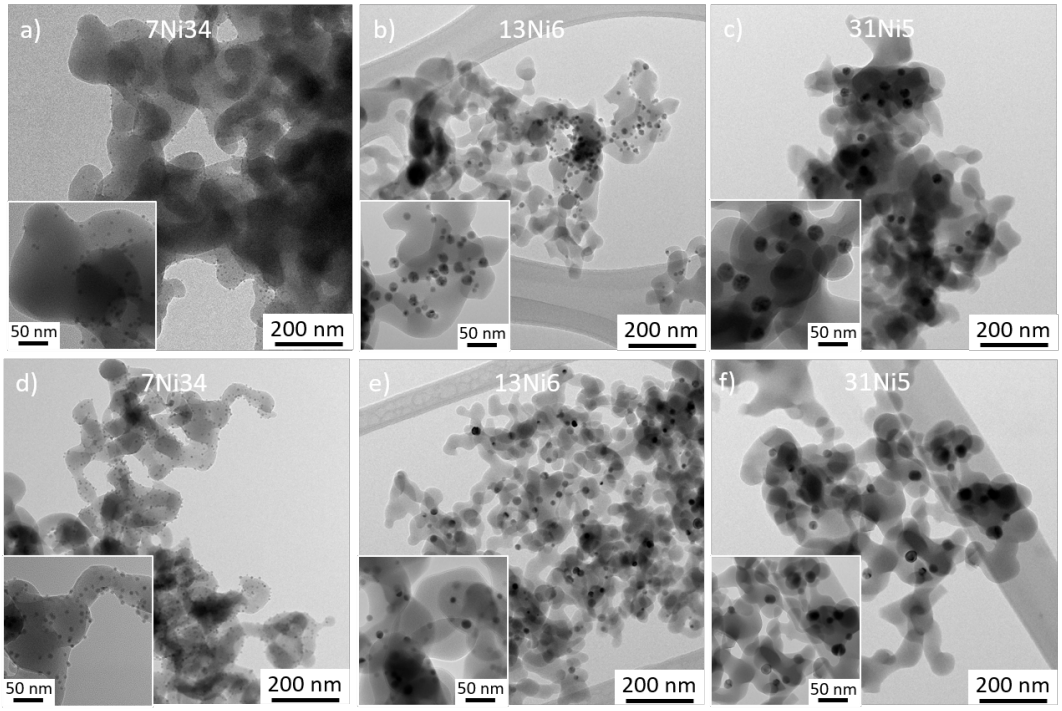

Figure 4.37: TEM images of the supported NiCu NPs on SiO_2 before catalysis a)-c), and after catalysis c)-d).

For the around 8 nm NPs a slightly lower but comparable Cu/Ni ratio was observed compared to the analysis performed with MS. Due to the exponential decrease of intensity with increasing information depth, a lower Cu content would be expected. A porous NiO shell, indicated by ASAXS could be an explanation and lead to stronger signals from the Cu core. With decreasing Ni/Cu ratio the amount of metallic Ni compared to

Ni(II) increased, indicating a thinner NiO shell, which is contrary to the findings from ASAXS. The amount of metallic Ni compared to Ni(II) in the bigger NPs is much lower compared to the smaller NPs, indicating a thicker NiO shell, which is in accordance with the ASAXS analyses. The samples were measured at three different positions to detect heterogeneities in the samples. For 8Ni1 and 17Ni3 in particular a higher degree of heterogeneity was observed, resulting in a higher uncertainty for the Cu/Ni ratio. The Ni(0)/Ni(II) ratio is, however, not affected, suggesting, that the heterogeneity appears mainly in the Cu content rather than the Ni content.
XPS analyses of the supported NPs on SiO_2 were performed as shown in Figure 4.36. XPS spectra of 8Ni5 pre and post catalysis show the same features as the unsupported NPs confirming the similarity of the final catalyst material and the NPs. Due to the low concentration of the NPs (1 wt%), it was not possible to perform as extensive evaluations as for the NPs. The further decrease in intensity for the post catalysis measurement could be explained by the possible mixing with quartz wool and slight changes in sample preparation. Qualitatively no change in Cu/Ni ratio occurred during catalysis, but possible contaminations through the catalysis can not be ruled out.
TEM measurements after performed catalysis in Figure 4.37d-f show the intact NPs separated on the supporting material compared to pre catalysis in Figure 4.37a-c, confirming the absence of coarsening or other effects affecting the NPs during the catalysis.

4.3.5 Discussion

With the herein adapted thermal reduction synthesis route monometallic NiNPs and bimetallic NiCo and NiCu NPs were prepared by co-reduction of two metal salts. Cu and Co are close neighbours to Ni in the periodic table with standard redox potentials in the order $E_0(Cu^{2+}/Cu^0) = 0.34V > E_0(Ni^{2+}/Ni^0) = -0.23V > E_0(Co^{2+}/Co^0) = -0.28V$. The co-reduction of Ni and Co led to spherical NiNPs with low Co content and smaller irregularly shaped CoNPs. The size of the spherical NPs could be adjusted within 8 to 14 nm by changing the amount of stabilizer TOP from 30 to 3 equivalents. Carenco *et al.* successfully synthesized bimetallic CoNi NPs via thermal reduction, but a two-step reduction was necessary. A Ni core was formed in a first step and a Co shell was added in afterwards.[76] Similarly Yamauchi *et al.* prepared CoNi core-shell NPs via microwave assisted synthesis.[75] López *et al.* prepared NiCo alloy NPs by heating up presynthesized pure Ni and Co NPs,[230] but a co-reduction of Co and Ni was to the best of my knowledge not reported for bimetallic NiCo NPs.

By co-reduction of Ni and Cu monodisperse spherical bimetallic NPs were achieved. Few bimetallic NiCu NPs were prepared via thermal reduction adaptations using standard air-free methods,[81] with borane tributylamine as reducing agent in OAm under Argon,[82] utilizing space-consuming lab-ware,[231] and pure OAm as solvent.[83]
The NiCu NPs could be adjusted in a size range of 6 to 33 nm and with a Ni/Cu ratio of ∞ to 1.3 by adjusting the reaction conditions. Increasing the TOP amount from 1.5 to 50 eq, the NP size decreased from 33 to 7 nm. In a direct comparison to the NiCo NPs, larger NiCu NPs were achieved using the same amount of stabilizer. Using 10 eq TOP 8 nm NiNPs, 11 nm NiCo NPs, and 16 nm NiCu NPs were formed. By increasing the TOP amount to 30 eq the NPs shrunk to 5 nm, 8 nm, and 11 nm and increased to 9 nm, 14 nm, and 20 nm by decreasing the TOP to 3 eq. The smaller size of the NiCo compared to NiCu NPs might be explained with the formation of the smaller irregularly shaped Co NPs, which are not visible in the Kratky type SAXS measurements due to the limited well resolved q-range. Starting with the same amount of metal salts, less metal atoms are available for the formation of the spherical NPs. The NiCu NPs reach twice the size as compared to pure NiNPs applying comparable reaction conditions. The stabilizing abilities of TOP seem to be diminished as soon as a second metal is involved in the reduction process, most obvious in the formation of the irregularly shaped CoNPs. The impact of TOP on the final NP size and shape was exemplarily demonstrated by using a chemical with decreased purity (90 % instead of normally used 97 %), which allowed the NiCu NPs to grow in various shapes and sizes. The influence of OAm on the final NP size inverted from the NiNPs, where the NP size decreased with increasing amount of OAm, to the NiCu NPs, which increased in size with increasing OAm amount. The

investigation for the NiNPs were conducted keeping the TOP amount constantly at 1.5 eq, while it was kept at 10 eq for the NiCu NPs. The OAm dependent final NP size might thus be different at varying TOP amounts.

The final NiCo NPs resemble the pure NiNPs with the addition of pure Co NPs, whereas the co-reduction of Ni and Cu results in bimetallic NPs. STEM EDX measurements indicate a Cu enrichment in the core and a Ni enrichment in the shell, which was confirmed by XPS measurements, which detected almost exclusively Ni on the NiCu NPs surface, and ASAXS measurements, which revealed a NiCu alloy core encircled by an Ni enriched shell, covered by a NiO shell. The core-shell-shell model developed from the ASAXS measurements confirmed the STEM analyses, which suggested a Cu enrichment in the core and a Ni rich shell surrounding it. The location of Cu in the NP core could be caused by the higher standard redox potential of Cu compared to Ni. This leads to a faster/easier reduction of Cu. Following this relationship, the formation of separated CoNPs while co-reduction of Co with Ni could be explained. Co should be more difficult to reduce, which might lead to the formation of a Ni core, which seems not to favour the addition of Co.
The standard SAXS measurements for the determination of the NP size and distribution after synthesis were conducted on a lab-scale Kratky-type instrument (SAXSess). The scattering curves were approximated with a homogeneous sphere and a Schulz-Zimm distribution. In contrast are the ASAXS measurements performed at the synchrotron at varying energies allowing a much higher resolution and the characterization of nano-objects in the size range from 1 to 100 nm. The ASAXS measurements resulted unambiguously in inhomogeneous spheres. The scattering curve of 17 nm NiCu NPs obtained on the SAXSess is shown in Figure 4.38 compared to the data recorded at the beamline.

The short measuring time and the necessary desmearing of the data leads to a rapid decrease in signal to noise, so only the total NP size could be detected with the SAXSess and was thus approximated with a homogeneous sphere. But to support that, the SAXSess scattering data are given once fitted with a Schulz-Zimm distribution of a homogeneous sphere and once with a core-shell model with a core with Schulz-Zimm distribution and a shell with reduced RED. Both fitting approaches approximate the scattering curve equally, so the simpler approach was used. The increase of resolution and beam brilliance lead to a deeper insight into the structure of the bimetallic NiCu NPs, enhancing the knowledge gained with the lab-scale measurement. The total NP sizes determined by the complex model from the scattering curves obtained at the synchrotron are systematically larger compared to the total sizes determined with the Schulz-Zimm fit of the lab-scale scattering curves. The drastically lower effective electron density in the NiO core might be the reason. It is taken into account in the complex model assuming an inhomogeneous NP, while being neglected in the assumption made utilizing the

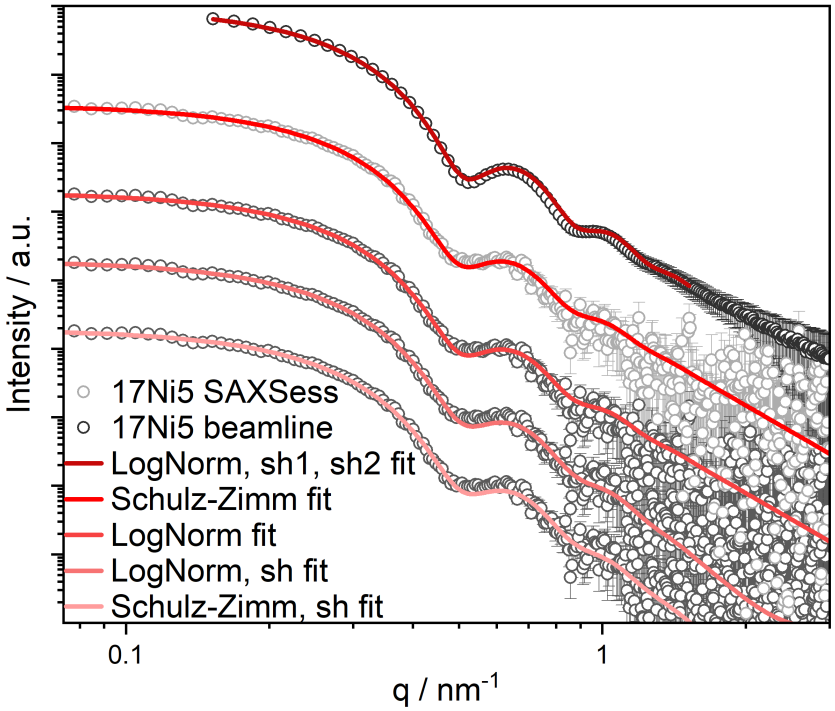

Figure 4.38: Scattering curves of NiCu NPs used for the catalyst 17Ni5 obtained at the lab-scale instrument (grey) and the synchrotron (black) and different fitting approaches marked in different shades of red. The following reaction conditions were used: 29 mmol/L metals, 0.2 eq $Cu(acac)_2$, 90 eq OAm, 10 eq TOP, 2 h at 220°C.

homogeneous sphere with Schulz-Zimm distribution. More important is the calculation of a number-weighted radius with the Schulz-Zimm fit vs. a volume-weighted radius with the LogNorm fit of the scattering data obtained at the synchrotron. Taking the volume-weighted radius of the Schulz-Zimm fit into account, the difference of the radii decreases by half the amount.

All tested NiCu NPs showed near 100 % selectivity for CO by the RWGS reaction. The alternative reaction converting CO_2 to CH_4 (Sabatier reaction) was nearly negligible over the whole investigated temperature range. Which is interesting compared to literature, where Ni is also utilized as catalyst for the Sabatier reaction. Mostly the selectivity for methane was higher at lower temperatures and decreased with increasing reaction temperature.[14,25] Zhang *et al.* found a preference for the RWGS reaction at low catalyst loadings, which shifted to preferred Sabatier reaction with higher loadings.[232] The loading of NiCu NPs investigated herein was around 1 wt%, which might explain the strong preference for the RWGS reaction. The catalytic activity of NiCu NPs compared to literature is given in Table 4.14 as CO_2 conversion in % and CO selectivity in %. The activity of the NiCu catalysts prepared in this work is comparable to t he literature known catalysts throughout the given temperature range. Ranjbar *et al.* reached the

Table 4.14: Comparison of catalytic activity of the in this work tested NiCu catalysts concerning conversion of CO_2 ($X(CO_2)$, %) and selectivity of CO (S(CO), %) at 1 bar compared to literature known catalysts (lit.).

T /°C		**400**	**500**	**600**	**700**
$X(CO_2)$	31Ni5[a]	1.6	12.1	22.5	33.5
	17Ni5[b]	3.7	17.7	28.5	38.6
	13Ni6[c]	1.8	13.9	28.5	40.8
	15Ni1[d]	1.7	12.1	22.4	31.1
	8Ni2[e]	0.7	9.4		
$X(CO_2)$ lit.	7% Ni-M1[f,*14]	14	27	35	43
	Ni-CP[g,*25]	4	16	29	38
	Ni-P123[h,*138]			36	
	CuCe(rod)[i,*23]	27	-	-	-
S(CO)	31Ni5[a]	99.5	99.8	99.7	99.8
	17Ni5[b]	99.8	99.7	98.5	99.8
	13Ni6[c]	99.7	99.8	99.3	99.8
	15Ni1[d]	99.8	99.9	99.7	99.8
	8Ni2[e]	99.9	99.9		
S(CO) lit.	7% Ni-M1[f,*14]	79	84	92	100
	Ni-CP[g,*25]	90	97	99	100
	Ni-P123[h,*138]			100	
	CuCe(rod)[i,*23]	100	-	-	-

[a] 100 mg cat, 0.98 wt% NiCu NP on SiO_2, 25 mL min^{-1} gas flow, CO_2:H_2 1:1.
[b] 1.36 wt%, [c] 0.91 wt%, [d] 1.01 wt%, [e] 1.03 wt% NiCu NP.
[f] 100 mg cat, 7 wt% Ni on MgO, 50 mL min^{-1} gas flow, CO_2:H_2 1:1.
[g] 50 mg cat, 1 wt% Ni on CeO_2, 100 mL min^{-1} gas flow, CO_2:H_2 1:1.
[h] 20-50 mg cat, 1 wt% Ni on CeO_2-P123, 100 mL min^{-1} gas flow, CO_2:H_2 1:1.
[i] 50 mg cat, 1 wt% Cu on Cerod, 50 mL min^{-1} gas flow, CO_2:H_2:Ar 1:4:95.
* values derived from published graphical depictions.

best CO_2 conversion with 7 wt% Ni loading on MgO. The activity of the 7% Ni-M1 catalyst at lower temperatures is higher compared to the catalysts prepared in this work, but becomes comparable at 700 °C.[14] Wang *et al.* and Lui *et al.* supported Ni on cerium oxide with varying supporting techniques and surfactants resulting slightly lower but comparable catalytic activities as Ranjbar *et al.*[25,138] The 17Ni5 catalyst prepared in the present work shows similar activities to the Ni-CP catalyst prepared by Wang *et al.* Lu *et al.* supported Cu on cerium oxide reaching a conversion of 27 % CO_2 at 400 °C, which is drastically more efficient compared to the other catalysts. But they applied

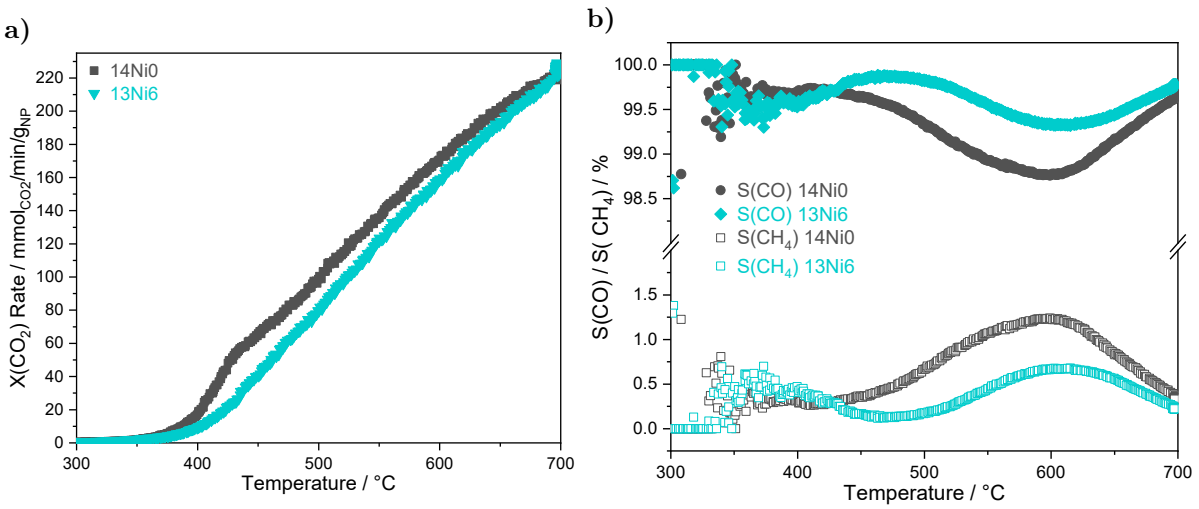

Figure 4.39: a) Catalytic activity of catalysts 14Ni0 and 13Ni6 in the temperature range of 300 to 700 °C; b) corresponding selectivity for CO (full symbols) and CH_4 (open symbols);100 mg catalyst, ~1 wt% NiCu NP loading, GHSV = 15 000 L kg^{-1} h^{-1}, CO_2:H_2 1:1.

only 5 % reactant gas with 95 % inert gas, compared to a 1:1 mixture of CO_2:H_2 in all the other cases. The low amount of reactant enables a much higher conversion.
With the catalytic testing of the NiCu NP catalysts prepared in this work while heating and cooling a deactivation of the catalyst could be ruled out, instead an increase in catalytic activity was detected for all catalysts below 400 °C after heating up to 500 °C. This might be due to reduction of NiO to elemental Ni as detected with EXAFS. The largest NiCu NPs exhibit a strong negative hysteresis above 400 °C which is less prominent with decreasing NP size. The 8 nm NiCu catalysts show drastic differences in their hysteresis. The Cu rich 8Ni2 catalyst has a positive hysteresis at all temperatures, while the 8Ni15 catalyst exhibits only negligible changes in catalytic activity upon cooling. The ASAXS measurements suggest a thicker NiO layer on the 8Ni2 NPs, which might result in higher CO yields after partial reduction to Ni(0) at elevated temperatures.
For 8Ni15 (21 mmol min^{-1} g^{-1}) the ratio core radius:shell thickness (inner + outer shell) is 2.0 and for 8Ni2 (46 mmol min^{-1} g^{-1}) 1.0, indicating that the catalytic performance of the NiCu NPs could be linked to the thickness of the Ni rich shells, which is also visible for the larger NiCu NPs. The NiO shell of the 8Ni15 NPs is indicated to be more porous compared to the 8Ni2 NPs according to the low relative effective electron density compared to the NiCu core. The XPS measurements resulted in a higher amount of Ni(0) on the surface of the NPs of 8Ni2 compared to 8Ni15, which might explain the drastically increased catalytic activity.
The catalytic activity of the NiCu NPs was comprised compared to the pure 14 nm NiNPs, although equivalent activity was found at 700 °C as depicted in Figure 4.39. The selectivity for the formation of CO is, however, increased for the bimetallic NiCu NP catalyst although the activity is slightly smaller.

4.4 Crystallization of Simvastatin

The ex situ investigation of nucleation of inorganic material which is interrupted leading to NPs is taken to the macroscopic scale by investigating the crystallization behaviour of the active pharmaceutical ingredient (API) simvastatin in situ. An acoustic levitator was used to avoid the influence of vessel walls on the crystallization potentially leading to heterogeneous nucleation.[233]

4.4.1 Simvastatin as API

Simvastatin is one of the most widely used active pharmaceutical ingredients (API) for the treatment of hyperlipidemias. It is a prominent member of the statin family, a class of drugs that are very effective in reducing the level of low density lipoprotein cholesterol (LDL) ("bad cholesterol") in human blood plasma.[234–236] A high LDL level is a primary risk factor for cardiovascular diseases and statin therapy is a prevention benchmark for such diseases.[236,237] Simvastatin ($C_{25}H_{38}O_5$), was approved for marketing by the U.S. Food and Drug Administration in 1991 and is widely prescribed to control hypercholesterolemia.[234–236,238,239] The pharmaceutical form of simvastatin is normally a

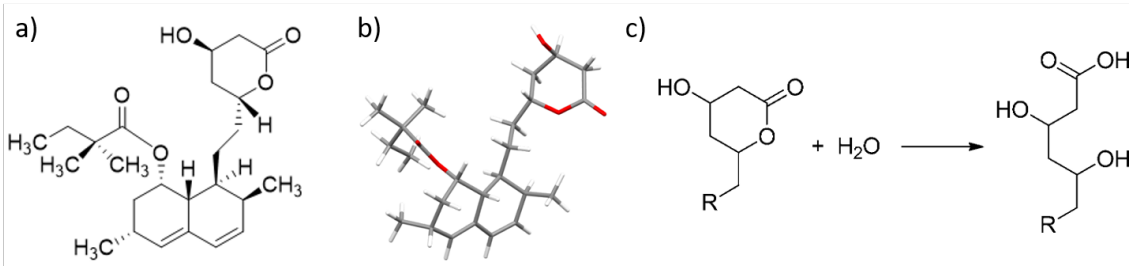

Figure 4.40: a) Molecular structure of simvastatin and b) a capped sticks representation of polymorph I,[240] and c) hydrolysis of predrug lactone to biologically active β-hydroxy acid.

solid lactone predrug (Figure 4.40), which undergoes hydrolysis to the corresponding biologically active β-hydroxy acid upon dissolution at physiological pH (Figure 4.40 bottom).[241,242] The simvastatin metabolite acts as reversible, competitive inhibitor of 3-hydroxy-3-methylglutaryl coenzyme A (HMG-CoA) reductase, an early and rate limiting enzyme in the biosynthesis of cholesterol. Through the reduction of LDL synthesis the number of LDL receptors expressed in cells are increased, resulting in greater uptake and degradation of LDL, thus reducing the LDL blood level even more.[243] Simvastatin is very insoluble in water ($30\,\mu g\,mL^{-1}$).[244] The pharmaceutical form of an API is very important concerning the bioavailability and manufacturability. Many organic compounds used as pharmaceuticals tend to form different polymorphs with varying physico-chemical characteristics.[245] Polymorphism is the ability of materials to form different crystalline structures of the same compound. Polymorphism has been long known

and has been relevant for many industrial sectors which handle crystalline materials such as minerals, metals, polymers, or organic compounds. First observations concerning polymorphism in organics were made by Woehler and Liebig who studied benzamid transforming from crystal needles into orthorhombic crystals.[246] Polymorphism drew attention when it was discovered in pharmaceutical substances[247–250] with ritonavir as dramatic example.[251] Ritonavir is a protease inhibitor for the treatment of Acquired Immunodeficiency Syndrome (AIDS).[252] Two years after release in 1996 as Norvir a new unknown and more stable polymorph appeared, exhibiting a four times lower solubility and thus lowered bioavailability, which led to a temporary removal from the market until new formulation was obtained.[253] Further examples for the impact of polymorphism on the physico-chemical characteristics are paracetamol and theophylline. Paracetamol is used to treat pain and fever and exhibits three polymorphic forms, of which form I is the thermodynamic stable form, which is commercially available. Form I is a powdery solid with a poor compression affinity leading to a costly production process of tablets. The layered structure of paracetamol form II allows a facilitated press procedure without additives.[254] It was found that the stable anhydrous theophylline used for asthma, bronchitis, emphysema, etc. shows a faster dissolution compared to the hydrate form as well as a metastable anhydrous polymorph of theophylline.[255,256]

The herein investigated simvastatin exhibits three reported polymorphic forms (see Figure 4.41). The corresponding XRD pattern are shown in Figure 4.41. Polymorph II and III were investigated by Hušák *et al.* and it was found that a phase transition from form III $\rightarrow$ II occurs at 232 K and from form II $\rightarrow$ I at 272 K.[257] The thermodynamic stable crystalline form of simvastatin under ambient conditions is polymorph I.[240,257,258] Besides the crystalline appearance, simvastatin also exhibits a literature known amorphous phase, which was accessed by melting and quench-cooling or cryo-milling.[259,260]

Simvastatin is due to its polymorphism and amorphism an interesting model to investigate how key experimental conditions such as temperature, solvent properties (e.g. polarity, hygroscopicity), and dynamics of the evaporation process influence the outcome of evaporative crystallization in the contactless environment of an acoustically levitated droplet.

Controlling the crystallization of APIs from solution is important issue to ensure the manufacture of formulations with highly reproducible pharmaceutical properties. External parameters like solvents, temperature, and surface need to be well-defined during the crystallization to guide the process to the requested form of an API. Previous studies investigated the influence of pure solvents on the selective crystallization of organic compounds starting from diluted solution.[261,262] A surface-free environment with defined temperature and humidity was provided by using an acoustic levitator and an enveloping gas stream. Under these conditions the solvent is the main influencing factor for the crys-

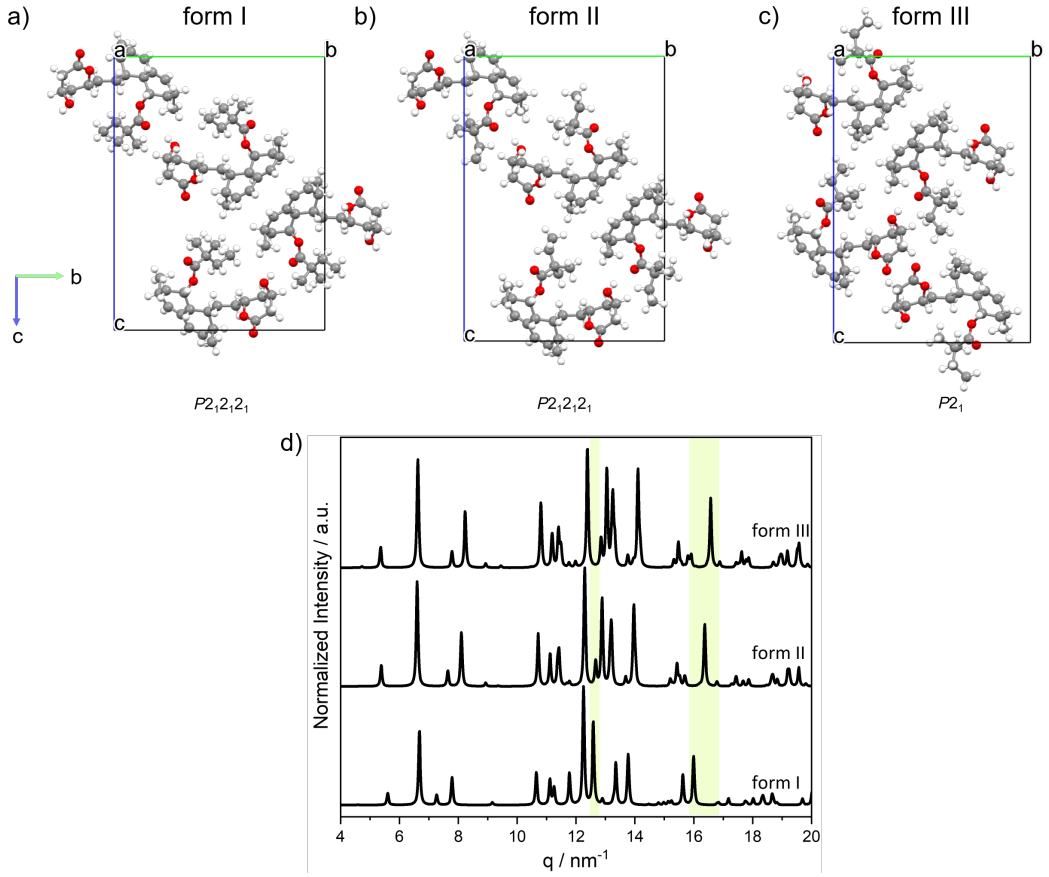

Figure 4.41: Unit cell of simvastatin a) form I, b) form II, and c) form III along the crystallographic a axis. d) XRD pattern of the three different polymorphs of simvastatin derived from literature.[250] Areas which exhibit the strongest differences are marked in green.

tallization. Thi *et al.* could selectively crystallize paracetamol form I from 1-propanol and form II from methanol[262] and Gnutzmann *et al.* selectively crystallized ROY ((5-methyl-2-[(2-nitrophenyl)amino]-3-thiophenecarbonitrile) based on solvent and concentration choice. They concluded that the crystallization of a specific polymorph could be attributed to nearest neighbour interactions and intermolecular attractive forces between solvent and analyte.[261] Further in situ investigations utilizing the acoustic levitator were performed of cement hydration,[263,264] nanoparticle formation,[114,201,265] crystallization of organic compounds,[174,266–268] and polymorphism.[262,269,270]

In this work the crystallization behaviour of simvastatin and the influence of the solvent is investigated in three solvents, which differ in polarity and protic character, including polar aprotic acetone, less polar aprotic ethyl acetate, and polar protic ethanol.

In a first step the temperature dependent saturation concentration of simvastatin in the three solvents was investigated since there are few systematic studies on the temperature dependent solubility of simvastatin in pure solvents. In a second step the crystallization behaviour was investigated in situ by using simultaneous synchrotron X-ray diffraction,

Raman spectroscopy, thermography, and imaging analysis. The influence of the solvent and its nature concerning volatility, hygroycopicity, polarity, and protic character on the crystallization behaviour from acoustically levitated droplets was studied.

4.4.2 Solubility of Simvastatin

Surprisingly very few systematic studies on the temperature dependent solubility of simvastatin in pure solvents can be found. The reported studies include several alcohols from ethanol to octanol in the temperature range 6 to 43 °C (279 to 316 K)[271,272] and acetates from methyl acetate to isobutyl acetate for temperatures of 5 to 45 °C (278 to 318 K).[272,273]

The reliability of these data is difficult to assess, since there are not negligible discrepancies between the solubilities determined in different studies. To resolve the large discrepancies in ethanol and ethyl acetate and to identify the solubility in acetone the solubility of simvastatin in the three solvents was investigated in dependence of the temperature. The saturation concentration was determined in a temperature range from 10 to 30 °C (283 to 303 K) by the gravimetric and UV Vis methods (described in subsection 3.3.11).[206]

The temperature dependent mole fraction solubilities of simvastatin in acetone, ethyl acetate, and ethanol are show in Figure 4.42 compared to the previously reported data. In the top left graph the solubility order acetone (grey) > ethyl acetate (red) > ethanol (blue) throughout the temperature range is shown. The top right graph shows the solubilities derived from the different methods in acetone. The solubilities derived from gravimetric method are given with open symbols and the solubility derived from UV Vis measurements in full symbols. The solubility derived from UV Vis results in lower concentrations compared to the gravimetric method. This might be due to the volatility of the solvents which makes it hard to get good measurements of the masses and thus leads to errors in the calculation of the dilutions which where necessary for the measurements, as mentioned in subsection 3.3.11. Although the values are lower they are still in accordance with the trend which can be seen in data from the gravimetric method and thus support them. The mole fraction solubility of simvastatin in ethyl acetate is shown bottom left derived from gravimetric (orange and yellow) and from UV Vis measurements (light grey and blue) compared to the previously reported data from Nti *et al.* (black) and Yan *et al.* (dark grey). Our data are in good agreement with the values determined by Yan *et al.* whereas the data from Nti *et al.* could not be reproduced. Yan *et al.* determined the solubility by the gravimetrical method and Nti *et al.* via reversed-phase analytical HPLC with UV detection.

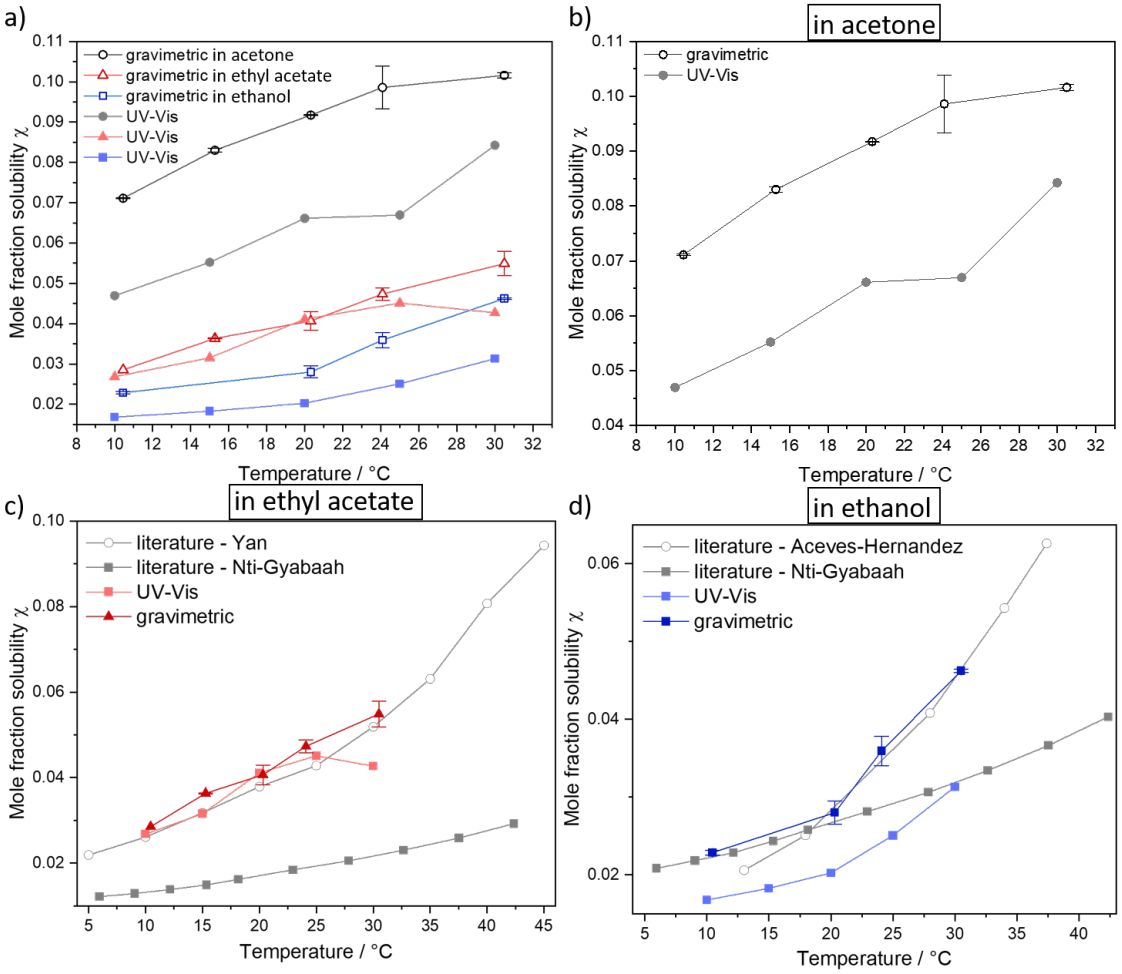

Figure 4.42: Solubility of simvastatin a) in all solvents and split up in acetone b), ethyl acetate c), and ethanol d) depending on temperature. Depicted is the molar fraction solubility χ derived from gravimetric method (darker colour), and derived from UV Vis measurements (lighter colour). Solubilities reported in the literature are shown from Nti *et al.*[272] (grey full squares) for ethanol and ethyl acetate, from Yan *et al.*[273] in ethyl acetate (grey open circles), and from Aceves-Hernandez *et al.*[271] in ethanol (grey open circles).

The mole fraction solubility of simvastatin in ethanol shown in bottom right are in good agreement with the data published by Aceves-Hernandez *et al.* (dark grey) whereas also here the data of Nti *et al.* could not be reproduced. Aceves-Hernandez *et al.* used similar to Nti *et al.* the reversed phase method for the measurement of the saturation concentrations. It was impossible to assess the origin of the discrepancy between the herein determined saturation concentrations in ethyl acetate and ethanol compared to the results from Nti *et al.* All measurements were performed above 275 K, so only the thermodynamically stable form I should exist in solutions, suggesting that polymorphism is unlikely as origin as well as gel formation during the evaporation of the solvent since Aceves-Hernandez *et al.* performed HPLC measurements of the saturated solutions such

as Nti *et al.* did. The discrepancies between the solubilities derived from gravimetric and UV Vis measurements are the highest for acetone followed by ethanol and ethyl acetate. This might be due to the volatility of these solvents which reflect the order of the discrepancy decrease: acetone 233 hPa (20 °C) > ethanol 59 hPa (20 °C) ~ ethyl acetate 59 hPa (20 °C). The order of the solubilities in the three solvents follows the obtained activity coefficients of simvastatin which describes the discrepancy between the real and an ideal mixture.[206] In acetone simvastatin follows an ideal behaviour implying full solvation of the simvastatin molecules. This result supports the highest solubility of simvastatin found in acetone. The lipophilic character of simvastatin and the aprotic character coupled with low polarity of acetone might increase the possible supramolecular interactions between the molecules. In ethyl acetate and ethanol positive deviations from the ideal solution behaviour are found. Ethanol is the solvent with the highest polarity investigated being close to the polarity of water, in which simvastatin is barely soluble. The poor solubility in ethanol can be explained by unfavourable intermolecular interactions between simvastatin and solvent molecules, which was confirmed by molecular dynamics simulations examined by Carlos Bernardes.[206] These simulations showed a high amount of large aggregates of simvastatin molecules which lead to segregation from the solution in ethanol resulting in a low solubility. In ethyl acetate as aprotic and less polar solvent than ethanol the solubility of simvastatin is slightly increased although not as high as in acetone. The molecular dynamics simulations resulted in the formation of few simvastatin aggregates comparable with the amount found in acetone. In acetone, however, more effective solute-solvent-interactions by means of alternating simvastatin and solvent molecules in the networks were found. These molecular dynamics simulations suggest that the solubility of simvastatin depends on an interplay of intermolecular interactions and its cluster-forming tendency.

Considering the simvastatin solubility in the three solvents the in situ investigation of the crystallization behaviour is investigated starting with an initial concentration approximately 10 times lower than the saturation concentration at room temperature.

4.4.3 In Situ Crystallization of Simvastatin

In the following chapter the crystallization of simvastatin in three solvents, which differ in polarity, protic, and hygroscopic character, was investigated in situ by using simultaneous synchrotron X-ray diffraction, Raman spectroscopy, thermography, and imaging analysis to study solvent evaporation from acoustically levitated droplets. It was studied how key experimental conditions such as solvent properties and temperature influence the crystallization behaviour of simvastatin.

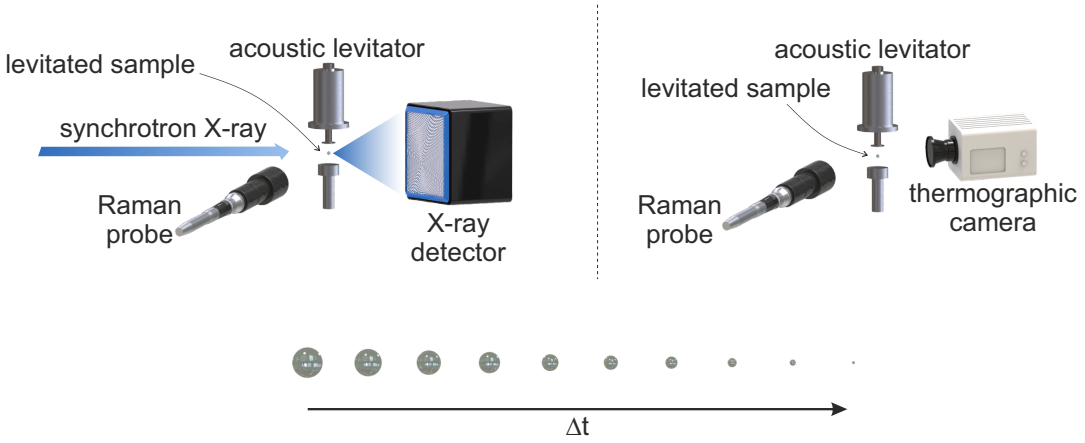

Figure 4.43: Experimental in situ setup for the crystallization of simvastatin using a combination of XRD, Raman and volume detection at the synchrotron (left) and thermographic, Raman and volume detection in the lab (right).

For the crystallization experiments undersaturated simvastatin solutions were used, with concentrations of around 4×10^{-2} mol kg^{-1} for the simvastatin to reach saturation during evaporation. The used concentrations are around ten times lower than the literature known saturation concentration of simvastatin in ethyl acetate and ethanol.[271–273] The simvastatin solutions were inserted into the acoustic levitator and the crystallization was monitored during the evaporation of the levitated droplets in a set up shown in Figure 4.43 described in detail in subsubsection 3.3.10 for 30 to 90 minutes. The in situ XRD and Raman spectroscopy data for the simvastatin crystallization from levitated droplet of ethanol solution are shown in Figure 4.44.

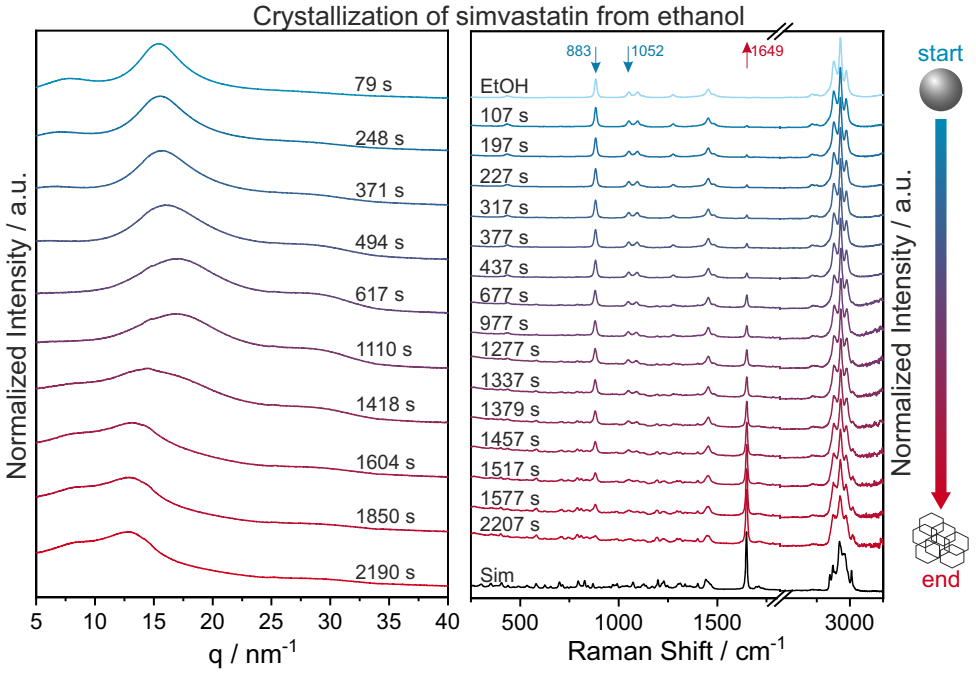

Figure 4.44: In situ simultaneously recorded synchrotron XRD and Raman spectroscopy of simvastatin from ethanol in the acoustic levitator.

The presence of solvent molecules ethanol during the solvent evaporation can be identified by the symmetric and the asymmetric stretch vibration ν_s(CCO) at 883 cm^{-1} and ν_{as}(CCO) at 1052 cm^{-1} in the Raman spectra. The evaporation of ethanol correlates with the decrease of these Raman bands accompanied by an increase of characteristic Raman signals of simvastatin, which are the C=O vibration at 1649 cm^{-1} and the C-H stretch vibrations around 3000 cm^{-1}.[259] The region between 2800 and 3200 cm^{-1} shows broader signals compared to the crystalline simvastatin at room temperature (black), indicating the formation of amorphous simvastatin as described by Graeser *et al.*[259] The ethanol related vibration band intensities vanish completely after 1600 seconds (~26 minutes), when ethanol is completely evaporated. The ethanol evaporation is also evident in the XRD patterns. The two broad amorphous scattering halos of the droplet at q = 15.4 and 7.6 nm^{-1} in the first XRD pattern after 79 seconds (s) shift to q = 19.1, and 29.4 nm^{-1} within 1100 s and then to q = 8.2, 12.8, and 29.4 nm^{-1} within 1604 s. Until the end of the experiment no crystallization indicated by sharp reflections appear in the XRD pattern, suggesting the formation of a persistent amorphous simvastatin phase from ethanol. A comparable XRD pattern with an amorphous halo q = 12.5 was published by Graeser *et al.* and given in Figure A.14 identifying the persistent amorphous simvastatin manufactured by different methods such as cryo milling and quench-cooling.[259] The halos detected at 1100 s can be assigned to water as depicted in Figure 4.45.

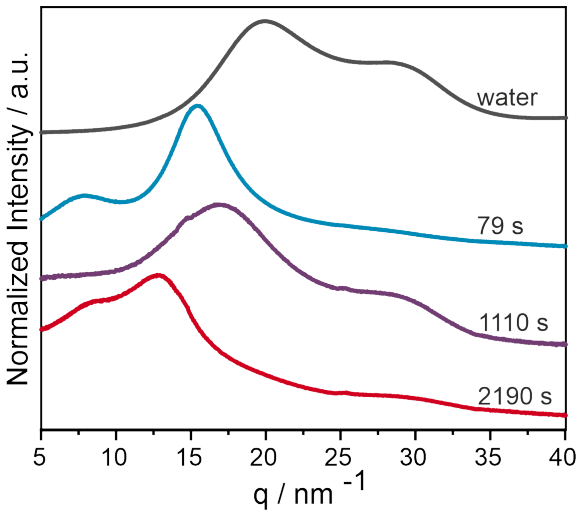

Figure 4.45: Scattering curve of water compared to the scattering obtained at different times during the evaporation of ethanol, which can be correlated to the initial solvent (79 s), intermediate state (1110 s), and the final amorphous simvastatin (2190 s).

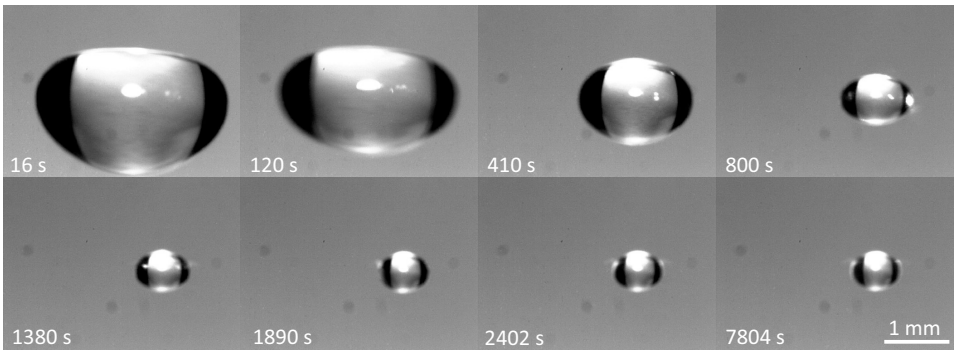

Figure 4.46: In situ recorded images of the evaporating droplet of simvastatin from ethanol in the acoustic levitator.

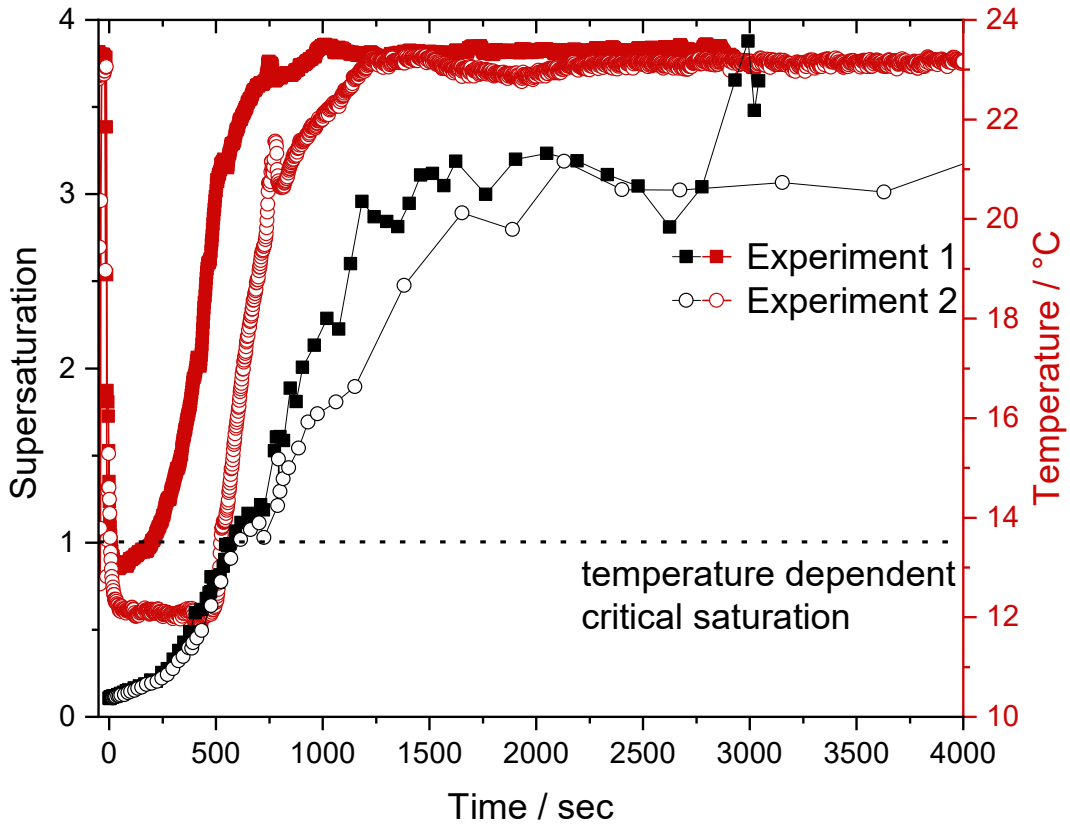

Figure 4.47: Temperature-saturation curve of the simvastatin-ethanol droplet during the levitation.

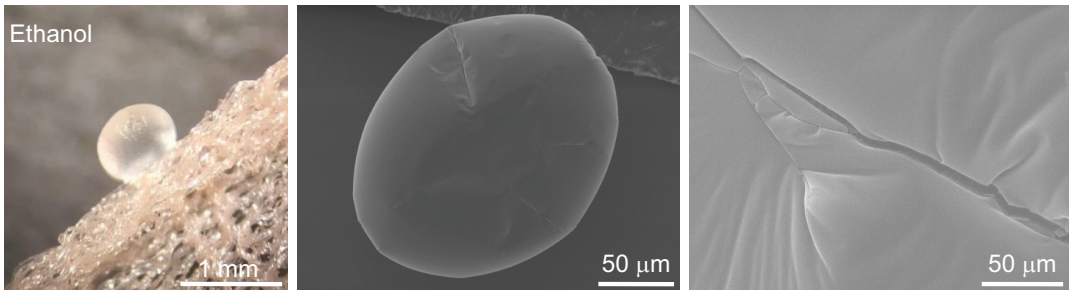

Figure 4.48: Microscope and SEM images of simvastatin crystallized from ethanol.

The thermographic measurements of the evaporating droplet in Figure 4.47 show significant temperature changes during the course of solvent evaporation and are assembled with the calculated saturation of simvastatin in the droplet based on the saturation concentrations mentioned above. Two curves from two independent experiments are plotted as function of levitation time. At the beginning the temperature of the empty acoustic levitator forms a plateau at ambient temperature. After injecting the droplet into the acoustic levitator at t = 0 into a stable position the temperature drops drastically due to the gradual evaporation of the solvent. Within the first 20 s the temperature decreases by around 11 °C and increases after 200-500 s reaching ambient temperatures after around 1200 s. This is in accordance with the evaporation of ethanol evident in

the Raman and XRD data as well as in the images of the levitated droplet shown in Figure 4.46. The concentration of simvastatin in the droplet increases during the evaporation of ethanol until the saturation is reached after around 600 s and a supersaturation level of 3 is reached, when the droplet is at ambient temperatures. The supersaturation is calculated by dividing the actual concentration in the droplet by the temperature dependent saturation concentration determined previously. The concentration reached a plateau after around 1500 s confirming the complete evaporation of ethanol leaving a clear sphere of amorphous simvastatin. The microscope image of the resulting sphere in Figure 4.48 shows a gel-like consistence, which is supported by SEM images confirming the smooth surface.

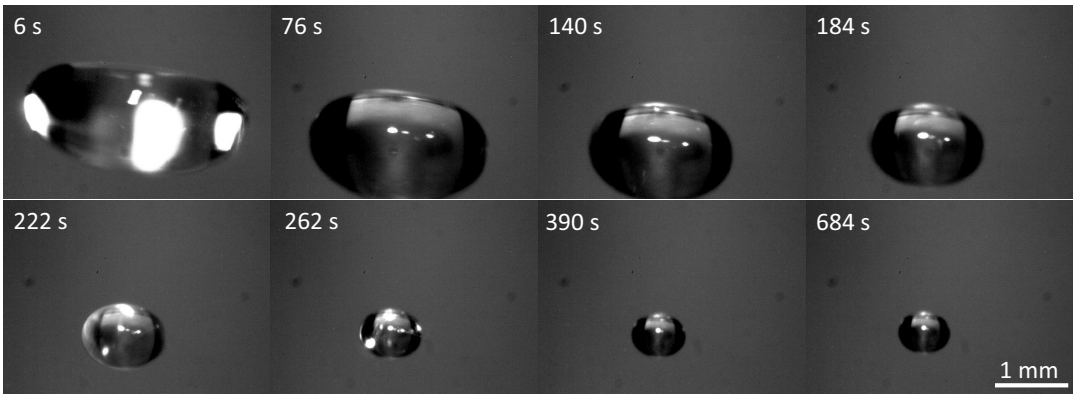

Figure 4.49: In situ recorded images of the evaporating droplet of simvastatin from ethyl acetate in the acoustic levitator.

The in situ measurements of the crystallization of simvastatin in ethyl acetate are shown in Figure 4.50a. The characteristic vibration bands of ethyl acetate at 378 cm^{-1} (C-C bending) and 2940 cm^{-1} (C-H stretching),[274] are present in the Raman spectra during the first 500 s after which they vanish indicating the complete evaporation of the solvent. The characteristic Raman signals of simvastatin at 1649 cm^{-1} and around 3000 cm^{-1} increase simultaneously, with the 2800 to 3200 cm^{-1} region showing broader signals compared to the crystalline simvastatin at room temperature (black), indicating the formation of amorphous simvastatin. The first XRD pattern exhibits a prominent solvent halo at q = 14.7 nm^{-1} which shifts to q = 12.5 nm^{-1} within the first 250 s. This shift indicates the evaporation of ethyl acetate and formation of amorphous simvastatin. Also in ethyl acetate no crystallization occurs until the end of the experiment resulting in amorphous simvastatin. Similar to the ethanol solution the temperature profile of the crystallization from ethyl acetate in Figure 4.50b shows a fast temperature decrease within the first 20 s of 13 °C. The temperature drops further 2 °C within the following 200 s while the concentration of simvastatin increases to the saturation point after 200 s. When evaporation passes through its final phase, temperature and concentration undergo a steep rise and the final amorphous simvastatin sample reaches the initial temperature

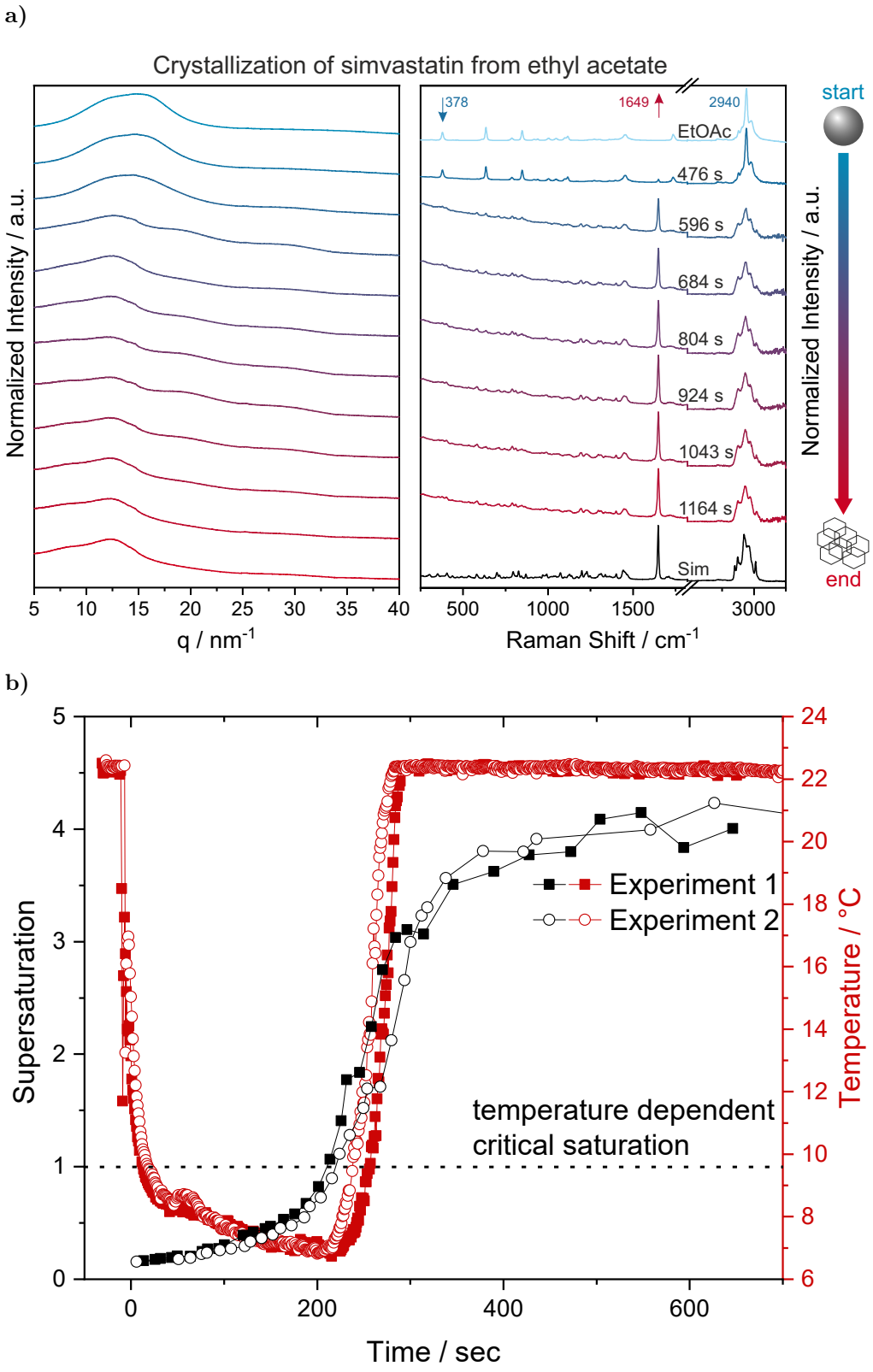

Figure 4.50: a) In situ simultaneously recorded synchrotron XRD and Raman spectroscopy of simvastatin from ethyl acetate in the acoustic levitator recorded at the synchrotron and b) in situ thermography and concentration measurements of the simvastatin-ethyl acetate droplet during the levitation achieved in the lab.

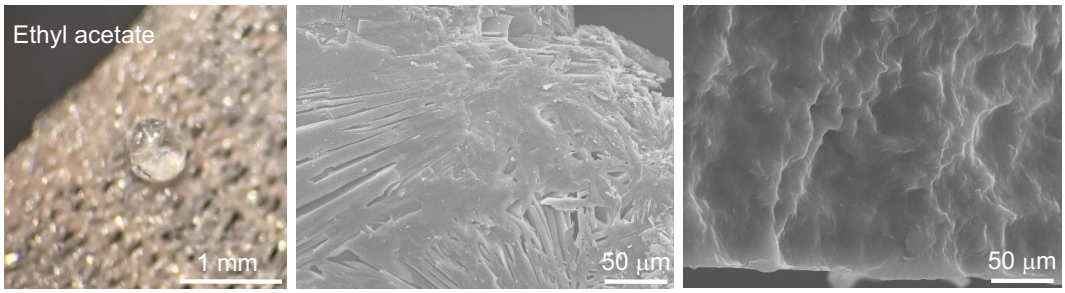

Figure 4.51: Microscope and SEM images of simvastatin crystallized from ethyl acetate.

after 300 s and a maximum supersaturation of 4 after 500 s. The time-dependent course of the concentration fits the in situ XRD results and is evident in the images of the shrinking droplet shown in Figure 4.49 which reached its final minimal size after around 400 s while an enormous shrinking happened until 260 s. Microscopic images of the final amorphous simvastatin are shown in Figure 4.51 indicating a spherical clear glassy solid which is not stable but crystallized over a period of two weeks. The surface as depicted in SEM images is not as smooth as the simvastatin sphere received from ethanol solution, but shows roughness and incipient needle like domains.

The in situ measurement data of the simvastatin crystallization in droplet from an acetone solution is shown in Figure 4.52a. Characteristic Raman bands of C-H and C-C stretch vibrations of the acetone solvent molecules are positioned at 2923 cm^{-1} and 790 cm^{-1}.[275] After 300 s, these characteristic bands of acetone disappear and the characteristic Raman spectrum of simvastatin is detected dominated by the vibration bands at 1649 and around 3000 cm^{-1}. The 2800 to 3200 cm^{-1} region shows some broad but also sharper signal comparable with the Raman spectrum of crystalline simvastatin at room temperature (black), indicating the formation of crystalline simvastatin. The first XRD pattern shows a broad scattering halo with a maximum at q = 14.6 nm^{-1}, which shifts to higher q values in the first 140 s. After 200 s, three distinguishable scattering contributions develop at around q = 12.9 and 19.4 nm^{-1}.
These halos can be assigned to amorphous simvastatin and water as depicted in Figure 4.45. First reflections of simvastatin at q = 6.7, 12.3, and 12.6 nm^{-1} appear after around 320 s in the XRD pattern indication the formation of crystalline simvastatin, where the reflex at q = 12.6 nm^{-1} is characteristic for polymorph I (see Figure 4.41). The intensity of these reflections increases over time and the scattering halos disappear due to solvent evaporation and transformation of amorphous to crystalline simvastatin. This observation is in agreement with the images of the shrinking droplet in Figure 4.53 (grey square and circle). The clear droplet directly after injection shrinks due to evaporation and appears turbid after around 110 s due to supersaturation of simvastatin in the droplet.

a)

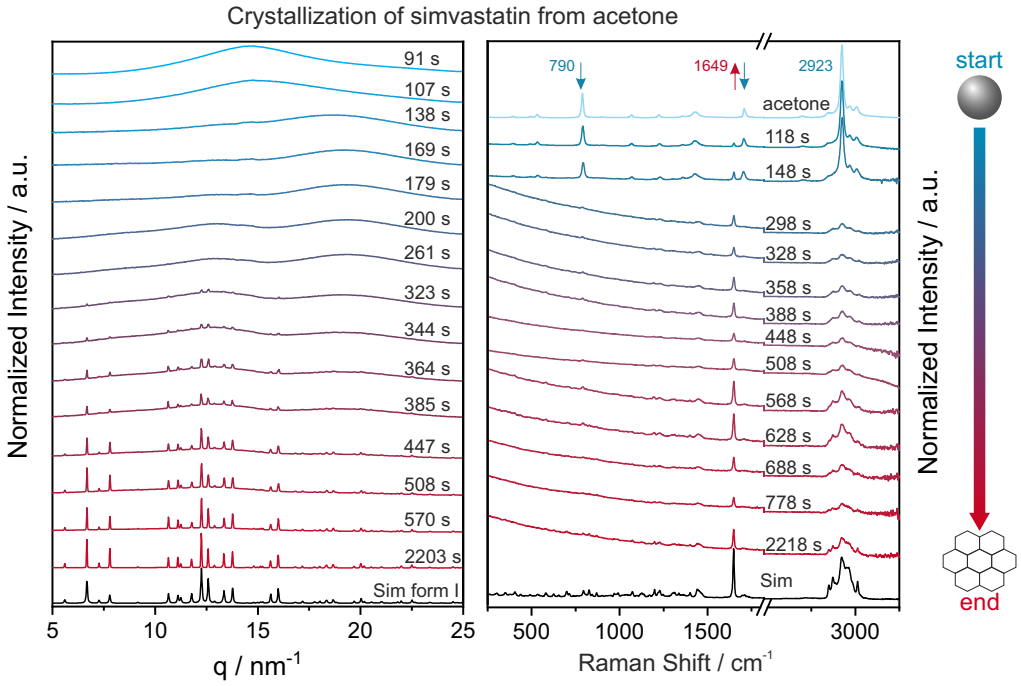

b)

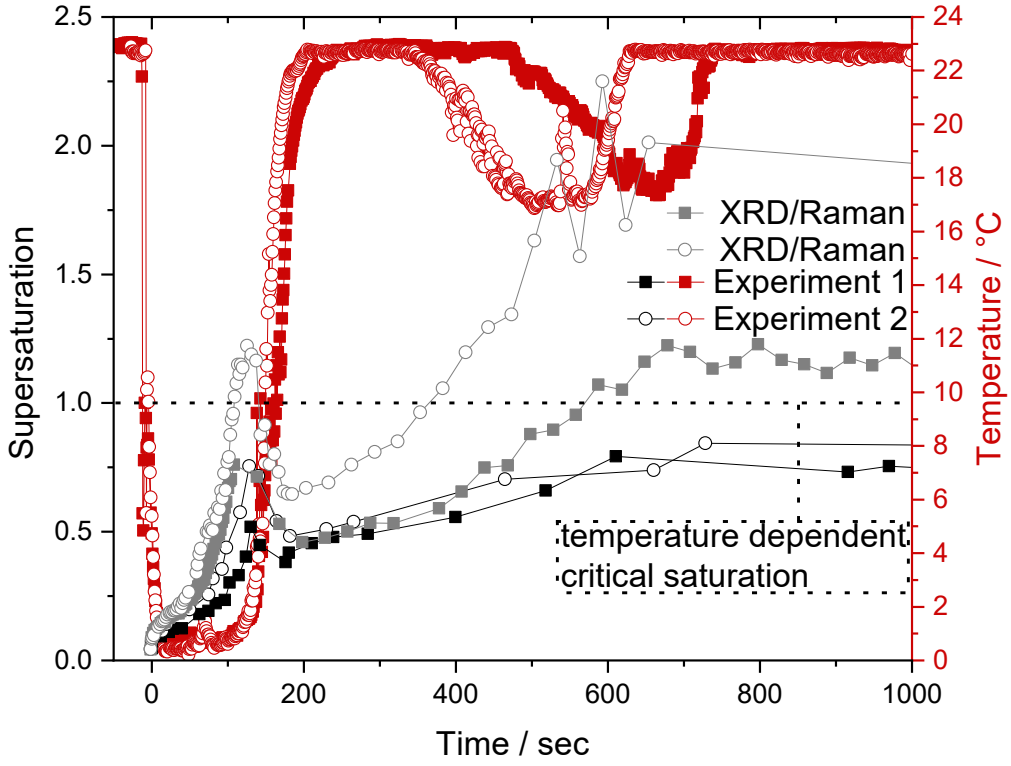

Figure 4.52: a) In situ simultaneously recorded synchrotron XRD and Raman spectroscopy of simvastatin from acetone in the acoustic levitator and b) temperature-concentration curve of the simvastatin-acetone droplet during the levitation.

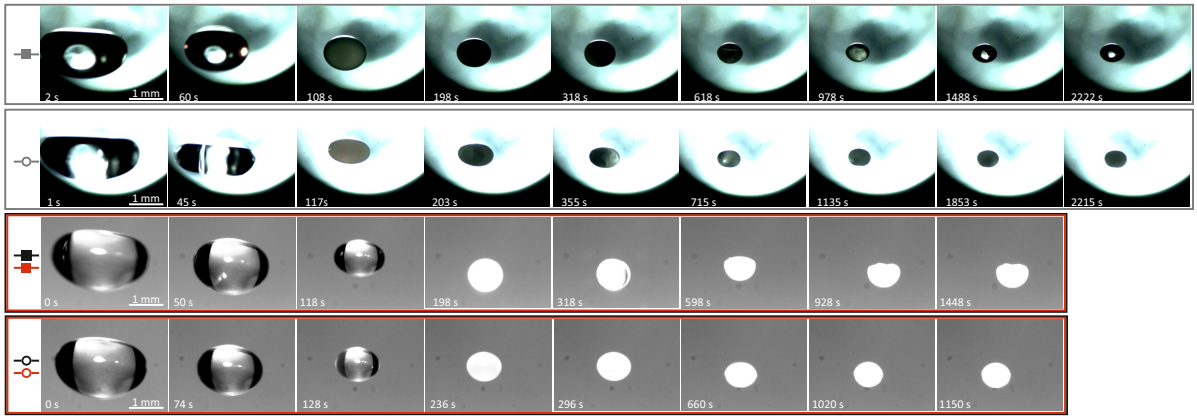

Figure 4.53: Images taken of the simvastatin in acetone droplets over time. Compared are the images of the four experiments analysed in Figure 4.52b. The black and red marked courses are the thermography experiments and the grey marked images are the XRD and Raman experiments. The final droplet size of the XRD and Raman experiments (marked in grey) is smaller than the final droplets in the thermography experiments (red and black) and results in higher supersaturation for the grey courses of supersaturation depicted in Figure 4.52b.

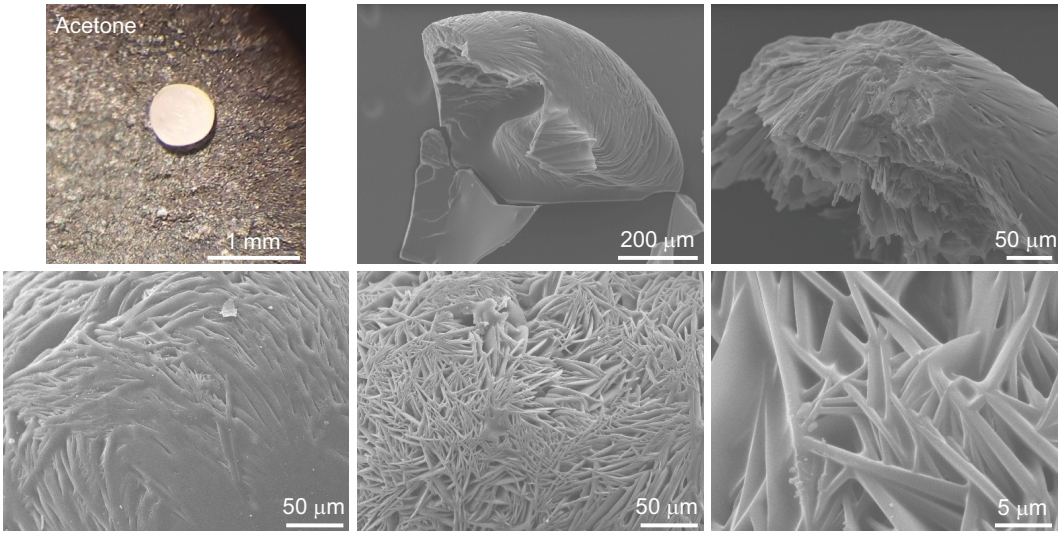

Figure 4.54: Microscope and SEM images of simvastatin crystallized from acetone.

The supersaturation of simvastatin in the droplet is depicted in Figure 4.52b (grey and black squares and circles) together with the thermographic measurements (red square and circle). The depicted temperature pathways are directly linked to the saturation curves depicted with black square and circle and the two lower rows in Figure 4.53, resulting from the same two experiments. Within the first 20 s of solvent evaporation the temperature drops drastically by 22 °C and increases after 100 s reaching ambient temperatures after 200 s. The reproducible low temperature leads to the condensation of water from the surrounding air as indicated in the XRD pattern. Shortly after the initial temperature of the empty levitator is reached a second temperature drop occurs, which

can be referred to the evaporation of water. The initial temperature plateau is finally reached after the adsorbed water molecules completely left the sample. After around 600 s a non circular shape of the droplet (Figure 4.53 black square) indicates the final solidification of simvastatin which supports the assumption of completed evaporation of the water from the droplet. The droplets are shrinking due to solvent evaporation and after around 200 s, when the droplet is again at ambient temperature, the droplet gets turbid. The saturation curves corresponding to these experiments (black square and circle) suggest that depending on the droplet temperature saturation of the acetone solution is never reached. But this finding can be explained with the formation of a crystalline simvastatin shell forming on the surface of the droplet circumventing the further shrinking of the droplet size during evaporation. This gets evident, when comparing the final size of the droplets shown in Figure 4.53 derived from the thermography experiments (two bottom rows) and the XRD and Raman experiments (two top rows). The saturation curve representing the XRD and Raman experiments depicted as grey square and circle curves correspond to the two top rows in Figure 4.53. The saturation concentrations at each point were calculated using the averaged temperature profiles determined. After around 100 s the concentration in the droplet increased to saturation or near-saturation. This temporary very high concentration leads to the clouding of the droplet, as depicted in Figure 4.53. The concentration drops afterwards due to the increase of the droplet temperature and resulting improved solubility of simvastatin in acetone. But after 400 respectively 600 s the supersaturation is finally reached. Microscopic images of the crystalline simvastatin show a white sphere under light microscope in Figure 4.54. The top right SEM images depict a broken simvastatin shell, which formed during the solvent evaporation. The inner part shows a sheet like structure, which appears like intergrown needles on the surface. The bottom images confirm the fibrous surface consisting of intergrown needles.

Crystallization of simvastatin was only detected in acetone while amorphous simvastatin was formed in ethanol and ethyl acetate. The polarity of the solvent showed no significant impact on the crystallization behaviour of simvastatin. It crystallized from polar acetone, but not from polar ethanol. The protic character however showed a tendency to crystallization, since acetone and ethyl acetate are aprotic, while ethanol is protic. The initial water contents in the solvents as given by supplier are 200 ppm in ethyl acetate and 50 ppm in acetone and ethanol, while these two are hygroscopic solvents. The tendency towards crystallization seems to be strongly influenced by the dynamics of the evaporation process. The higher volatility of acetone (acetone > ethyl acetate > ethanol) leads to a faster evaporation and a larger temperature drop during evaporation. The low temperature reached during acetone evaporation seems to promote the uptake

of water from the atmosphere, which acts as antisolvent, triggering the crystallization of simvastatin. Finally, the present results show the importance of controlling experimental conditions such as surface cooling and hygroscopicity for experiments in levitated droplets.

5 Conclusion

The adapted, facile thermal reduction approach was successfully implemented for pure Ni, and spherical monodisperse NiNPs could be achieved. These NiNPs were investigated thoroughly resulting in metallic NiNPs with crystalline Ni fcc domains visible for XRD, XAFS, and TEM and a thin NiO passivation layer, which was only visible for XPS and ASAXS. With ASAXS it was possible to reveal a core-shell structure of elemental Ni in the core covered by a NiO shell. The size of the NPs could be tuned by changing the amount of reducing agent and stabilizer within 5 and 16 nm with a spherical shape at all sizes. The main growth occurs within the first 40 minutes of reaction time and the reaction volume had no significant influence on the NP size in a range of 5 to 20 mL. NiNPs with a size of 14 nm were supported on porous SiO_2 and showed good catalytic activity for the conversion of CO_2 to syngas (CO and H_2) via the reverse water gas shift reaction (RWGS). The activity increased with increasing temperature, and also at lower temperatures after heating up to 500 °C.

The crystallization of the active pharmaceutical ingredient simvastatin in a levitated droplet was studied in acetone, ethyl acetate, and ethanol and a solvent dependent behaviour was found. The saturation concentration of simvastatin was determined in the temperature range of 10 to 20 °C in the three solvents, resolving the discrepancies in for ethanol and ethyl acetate, and identifying the not before published saturation concentration in acetone. Simvastatin crystallized from acetone reproducibly, triggered by a strong temperature drop of 22 °C during evaporation, resulting in supersaturation and the condensation of water, which acts as antisolvent. From ethanol simvastatin formed a persistent gel-like amorphous phase after solvent evaporation. A glassy amorphous simvastatin was achieved by evaporation of ethyl acetate, which shows microscopic similarities to the crystalline form and tends to crystallization after a short period of time.

The adapted facile, and straight-forward synthesis method was successfully transferred from monometallic NiNPs to bimetallic Ni systems. Bimetallic NiCo NPs were prepared in varying sizes and metal compositions by co-reduction. With increasing amount of Co, spherical NPs containing mainly Ni beside irregularly shaped NPs consisting of mainly Co were formed. With varying amounts of stabilizer TOP from 2-30 eq an NP size range of 14 to 8 nm was accessible. Due to the irregularity of the final NPs, Co was substituted by Cu as second metal beside Ni. Bimetallic NiCu NPs ranging from 7 to

40 nm could be prepared by the adapted thermal reduction synthesis route. Spherical NPs with crystalline domains of fcc Ni and fcc Cu were formed, as determined by TEM and XRD. STEM-EDX measurements indicated the formation of core-shell NPs with a Cu enriched core and a Ni shell. EXAFS suggested the formation of NiO, which is enriched on the surface of the NP, as determined by XPS measurements.
ASAXS measurements were conducted at three defined energies (8004 eV, 8330 eV, and 8973 eV) and confirmed the formation of a core-shell NP with NiO on its surface, revealing an even more complex structure: A CuNi alloy core is surrounded by an Ni enriched shell, which is covered by a NiO shell. The core and shell thicknesses are correlated to the NP size and the Cu content. In combination with XPS a porous NiO shell is very probable, explaining, why it is not visible in XRD. Such an explicit usage of the total scattering curves to derive the nanostructure as well as the elemental composition at three outstanding X-ray energies was rarely used up to now.
The NP size could be adjusted by adjusting the amount of reducing agent OAm and stabilizer TOP, while the amount of stabilizer showed stronger impact on the NP size. With 1.5 eq TOP 30-40 nm NiCu NPs were achieved, while 50 eq TOP led to the formation of 6 nm NiCu NPs. All sizes of NiCu NPs had a spherical shape, except when prepared with a stabilizer TOP with lower purity, which led to the formation of NiCu NPs with sizes ranging from sticks, triangles, cubes, to spheres.
A set of eleven NiCu NPs with varying sizes, Cu contents and shapes was supported on porous SiO_2 via dry impregnation in an evenly distributed fashion. The NPs were tested for their catalytic activity for the RWGS reaction in dependence of the structural composition. A strong dependency on the Cu content was found for small NiCu NPs resulting in an increasing activity with increasing Cu content. In larger NiCu NPs the Cu content played a minor role. TEM measurements of catalyst material before and after catalysis indicated no sintering, aggregation, or coarsening of the NPs during catalysis and XPS measurement pre and post catalysis resulted in comparable Ni/Cu ratios, which supports the reusability and the sustainability of these catalysts for real life applications.
Further insights into the catalytic process and the impact of Cu on the catalytic activity could be gained by in situ investigations and the comparison to the catalytic activity of pure Cu NPs. Long-term stability and the desactivation of the catalysts over several cycles might give more insights into the applicability of these NiCu NPs in future catalytic applications. Bimetallic Ni NPs could be tested in future studies concerning the size, shape, shape and metal ratio as well as improvements in catalytic activity.

Bibliography

[1] ISO, *ISO/TS 19590:2017(en), Nanotechnologies — Size distribution and concentration of inorganic nanoparticles in aqueous media via single particle inductively coupled plasma mass spectrometry*.

[2] Gleiter, H. Nanocrystalline Materials. *Prog. Mater. Sci.* **1989**, *33*, 223–315.

[3] Kawi, S.; Kathiraser, Y.; Ni, J.; Oemar, U.; Li, Z. W.; Saw, E. T. Progress in Synthesis of Highly Active and Stable Nickel-Based Catalysts for Carbon Dioxide Reforming of Methane. *Chemsuschem* **2015**, *8*, 3556–3575.

[4] Bedwell, T. S.; Whitcombe, M. J. Analytical applications of MIPs in diagnostic assays: future perspectives. *Anal. Bioanal. Chem.* **2016**, *408*, 1735–1751.

[5] Deshmukh, S. P.; Patil, S. M.; Mullani, S. B.; Delekar, S. D. Silver nanoparticles as an effective disinfectant: A review. *Mat. Sci. Eng. C-Mater.* **2019**, *97*, 954–965.

[6] Kalimuthu, K.; Cha, B. S.; Kim, S.; Park, K. S. Eco-friendly synthesis and biomedical applications of gold nanoparticles: A review. *Microchem. J.* **2020**, *152*, 9.

[7] Rai, M.; Yadav, A.; Gade, A. Silver nanoparticles as a new generation of antimicrobials. *Biotechnol. Adv.* **2009**, *27*, 76–83.

[8] Naseem, K.; Begum, R.; Farooqi, Z. H. Platinum nanoparticles fabricated multiresponsive microgel composites: Synthesis, characterization, and applications. *Polym. Compos.* **2018**, *39*, 2167–2180.

[9] Yu, L.; Li, N. Noble Metal Nanoparticles-Based Colorimetric Biosensor for Visual Quantification: A Mini Review. *Chemosensors* **2019**, *7*, 23.

[10] Ndolomingo, M. J.; Bingwa, N.; Meijboom, R. Review of supported metal nanoparticles: synthesis methodologies, advantages and application as catalysts. *J. Mater. Sci.* **2020**, *55*, 6195–6241.

[11] Zhang, G.; Liu, J.; Xu, Y.; Sun, Y. A review of CH_4-CO_2 reforming to synthesis gas over Ni-based catalysts in recent years (2010–2017). *Int. J. Hydrog. Energy* **2018**, *43*, 15030–15054.

[12] Bae, S. Y.; Mahmood, J.; Jeon, I. Y.; Baek, J. B. Recent advances in ruthenium-based electrocatalysts for the hydrogen evolution reaction. *Nanoscale Horiz.* **2020**, *5*, 43–56.

[13] Guo, H. Y.; Fang, Z. W.; Li, H.; Fernandez, D.; Henkelman, G.; Humphrey, S. M.; Yu, G. H. Rational Design of Rhodium-Iridium Alloy Nanoparticles as Highly Active Catalysts for Acidic Oxygen Evolution. *ACS Nano* **2019**, *13*, 13225–13234.

[14] Ranjbar, A.; Irankhah, A.; Aghamiri, S. F. Reverse water gas shift reaction and CO_2 mitigation: nanocrystalline MgO as a support for nickel based catalysts. *J. of Environ. Chem. Eng.* **2018**, *6*, 4945–4952.

[15] Dhakshinamoorthy, A.; Pitchumani, K. Clay entrapped nickel nanoparticles as efficient and recyclable catalysts for hydrogenation of olefins. *Tetrahedron Lett.* **2008**, *49*, 1818–1823.

[16] Saxena, A.; Kumar, A.; Mozumdar, S. Ni-nanoparticles: An efficient green catalyst for chemo-selective oxidative coupling of thiols. *J. Mol. Catal. A Chem.* **2007**, *269*, 35–40.

[17] Gong, M.; Wang, D.-Y.; Chen, C.-C.; Hwang, B.-J.; Dai, H. A mini review on nickel-based electrocatalysts for alkaline hydrogen evolution reaction. *Nano Res.* **2016**, *9*, 28–46.

[18] Ahmed, R.; Liu, G.; Yousaf, B.; Abbas, Q.; Ullah, H.; Ali, M. U. Recent advances in carbon-based renewable adsorbent for selective carbon dioxide capture and separation-A review. *J. Clean. Prod.* **2020**, *242*, 118409.

[19] *WMO GREENHOUSE GASBULLETIN - The State of Greenhouse Gases in the AtmosphereBased on Global Observations through 2018*; resreport, Accessed: 25.11.2019.

[20] Centi, G.; Perathoner, S. CO_2-based energy vectors for the storage of solar energy. **2011**, *1*, 21–35.

[21] Goguet, A.; Meunier, F. C.; Tibiletti, D.; Breen, J. P.; Burch, R. Spectrokinetic Investigation of Reverse Water-Gas-Shift Reaction Intermediates over a Pt/CeO2 Catalyst. *J. Phys. Chem. B* **2004**, *108*, 20240–20246.

[22] Lalinde, J. A. H.; Roongruangsree, P.; Ilsemann, J.; Baeumer, M.; Kopyscinski, J. CO_2 methanation and reverse water gas shift reaction. Kinetic study based on in situ spatially-resolved measurements. *ChemE.* **2020**, *390*.

[23] Lu, B.; Zhang, Z.; Li, X.; Luo, C.; Xu, Y.; Zhang, L. High-efficiency CuCe(rod) catalysts for CO_2 hydrogenation with high Cu content. *Fuel* **2020**, *276*.

[24] Chamnankid, B.; Fottinger, K.; Rupprechter, G.; Kongkachuichay, P. Cu/Ni-Loaded CeO_2-ZrO_2 Catalyst for the Water-Gas Shift Reaction: Effects of Loaded Metals and CeO_2 Addition. *Chem. Eng. & Technol.* **2014**, *37*, 2129–2134.

[25] Wang, L.; Liu, H.; Liu, Y.; Chen, Y.; Yang, S. Influence of preparation method on performance of Ni-CeO_2 catalysts for reverse water-gas shift reaction. *J. Rare Earths* **2013**, *31*, 559–564.

[26] Daza, Y. A.; Kuhn, J. N. CO_2 conversion by reverse water gas shift catalysis: comparison of catalysts, mechanisms and their consequences for CO_2 conversion to liquid fuels. *RSC Adv.* **2016**, *6*, 49675–49691.

[27] Feynman, R. P. There's Plenty of Room at the Bottom. *Engineering and Science 23 (5)*, 22–36.

[28] Klabunde, K. J. *Nanoscale Materials in Chemistry*; John Wiley & Sons, Ltd, 2001.

[29] Burda, C.; Chen, X.; Narayanan, R.; El-Sayed, M. A. Chemistry and Properties of Nanocrystals of Different Shapes. *Chem. Rev.* **2005**, *105*, 1025–1102.

[30] Imran Din, M.; Rani, A. Recent advances in the synthesis and stabilization of nickel and nickel oxide nanoparticles: a green adeptness. *Int. J. Anal. Chem.* **2016**, *2016*.

[31] Xia, Y.; Yang, H.; Campbell, C. T. Nanoparticles for catalysis. *Accounts of Chemical Research* **2013**, *46*, 1671–1672.

[32] Alonso, F.; Riente, P.; Yus, M. Hydrogen-transfer reduction of carbonyl compounds promoted by nickel nanoparticles. *Tetrahedron* **2008**, *64*, 1847–1852.

[33] Alonso, F.; Riente, P.; Yus, M. Alcohols for the alpha-Alkylation of Methyl Ketones and Indirect Aza-Wittig Reaction Promoted by Nickel Nanoparticles. *Eur. J. Org. Chem.* **2008**, *2008*, 4908–4914.

[34] Zhuang, Z.; Giles, S. A.; Zheng, J.; Jenness, G. R.; Caratzoulas, S.; Vlachos, D. G.; Yan, Y. Nickel supported on nitrogen-doped carbon nanotubes as hydrogen oxidation reaction catalyst in alkaline electrolyte. *Nat. Commun.* **2016**, *7*, 1–8.

[35] Li, Y.; Zhang, B.; Xie, X.; Liu, J.; Xu, Y.; Shen, W. Novel Ni catalysts for methane decomposition to hydrogen and carbon nanofibers. *J. Catal.* **2006**, *238*, 412–424.

[36] Sudhasree, S.; Shakila Banu, A.; Brindha, P.; Kurian, G. A. Synthesis of nickel nanoparticles by chemical and green route and their comparison in respect to biological effect and toxicity. *Toxicol. Environ. Chem.* **2014**, *96*, 743–754.

[37] Angajala, G.; Radhakrishnan, S. A review on nickel nanoparticles as effective therapeutic agents for inflammation. *Inflammation and Cell Signaling* **2014**, *1*, 1–8.

[38] Mariam, A. A.; Kashif, M.; Arokiyaraj, S.; Bououdina, M.; Sankaracharyulu, M.; Jayachandran, M.; Hashim, U. Bio-synthesis of NiO and Ni nanoparticles and their characterization. *Digest J. Nanomater. Biostruct.* **2014**, *9*, 1007–1019.

[39] Chen, M.; Zhang, Y.; Huang, B.; Yang, X.; Wu, Y.; Liu, B.; Yuan, Y.; Zhang, G. Evaluation of the antitumor activity by Ni nanoparticles with verbascoside. *J. Nanomater.* **2013**, *2013*.

[40] Kim, T.-S.; Song, H. J.; Dar, M. A.; Lee, H.-J.; Kim, D.-W. Fast adsorption kinetics of highly dispersed ultrafine nickel/carbon nanoparticles for organic dye removal. *Appl. Surf. Sci.* **2018**, *439*, 364–370.

[41] Odobel, F.; Le Pleux, L.; Pellegrin, Y.; Blart, E. New Photovoltaic Devices Based on the Sensitization of p-type Semiconductors: Challenges and Opportunities. *Acc. Chem. Res.* **2010**, *43*, 1063–1071, PMID: 20455541.

[42] Granqvist, C. G. Electrochromics for smart windows: Oxide-based thin films and devices. *Thin Solid Films* **2014**, *564*, 1–38.

[43] Verrelli, E.; Tsoukalas, D.; Giannakopoulos, K.; Kouvatsos, D.; Normand, P.; Ioannou, D. Nickel nanoparticle deposition at room temperature for memory applications. *Microelectron. Eng.* **2007**, *84*, 1994–1997, INFOS 2007.

[44] Kudr, J.; Haddad, Y.; Richtera, L.; Heger, Z.; Cernak, M.; Adam, V.; Zitka, O. Magnetic Nanoparticles: From Design and Synthesis to Real World Applications. *J. Nanomater.* **2017**, *7*.

[45] Raab, C.; Simkó, M.; Fiedeler, U.; Nentwich, M.; Gazsó, A. Herstellungsverfahren von Nanopartikeln und Nanomaterialien. *Nanotrust Dossiers 6*, 1–4.

[46] Jamkhande, P. G.; Ghule, N. W.; Bamer, A. H.; Kalaskar, M. G. Metal nanoparticles synthesis: An overview on methods of preparation, advantages and disadvantages, and applications. *J. Drug. Deliv. Sci. Technol.* **2019**, *53*, 101174.

[47] Nikam, A.; Prasad, B.; Kulkarni, A. Wet chemical synthesis of metal oxide nanoparticles: a review. *CrystEngComm* **2018**, *20*, 5091–5107.

[48] Wang, Z. C.; Chen, Y. Z.; Zeng, D. Q.; Zhang, Q. F.; Peng, D. L. Solution synthesis of triangular and hexagonal nickel nanosheets with the aid of tungsten hexacarbonyl. *CrystEngComm* **2016**, *18*, 1295–1301.

[49] Carenco, S.; Boissière, C.; Nicole, L.; Sanchez, C.; Le Floch, P.; Mézailles, N. Controlled Design of Size-Tunable Monodisperse Nickel Nanoparticles. *Chem. Mater.* **2010**, *22*, 1340–1349.

[50] Eremin, A.; Gurentsov, E.; Musikhin, S. Synthesis of binary iron–carbon nanoparticles by UV laser photolysis of $Fe(CO)_5$ with various hydrocarbons. *Mater. Res. Express* **2016**, *3*, 105041.

[51] Grand, J.; Ferreira, S. R.; de Waele, V.; Mintova, S.; Nenoff, T. M. Nanoparticle alloy formation by radiolysis. *J. Phys. Chem. C* **2018**, *122*, 12573–12588.

[52] Kristl, M.; Dojer, B.; Gyergyek, S.; Kristl, J. Synthesis of nickel and cobalt sulfide nanoparticles using a low cost sonochemical method. *Heliyon* **2017**, *3*, e00273.

[53] Khoshooei, M. A.; Scott, C. E.; Carbognani, L.; Pereira-Almao, P. Ultrasound-assisted bimetallic NiMo nanocatalyst preparation using microemulsions for in-situ upgrading application: Impact on particle size. *Catal. Today* **2020**,

[54] Brust, M.; Walker, M.; Bethell, D.; Schiffrin, D. J.; Whyman, R. Synthesis of thiol-derivatised gold nanoparticles in a two-phase liquid–liquid system. *J. Chem. Soc., ChemComm* **1994**, 801–802.

[55] Carroll, K. J.; Reveles, J. U.; Shultz, M. D.; Khanna, S. N.; Carpenter, E. E. Preparation of elemental Cu and Ni nanoparticles by the polyol method: an experimental and theoretical approach. *J. Phys. Chem. C* **2011**, *115*, 2656–2664.

[56] LaGrow, A. P.; Ingham, B.; Toney, M. F.; Tilley, R. D. Effect of Surfactant Concentration and Aggregation on the Growth Kinetics of Nickel Nanoparticles. *J. Phys. Chem. C* **2013**, *117*, 16709–16718.

[57] Park, J.; Kang, E.; Son, S. U.; Park, H. M.; Lee, M. K.; Kim, J.; Kim, K. W.; Noh, H. J.; Park, J. H.; Bae, C. J.; Park, J. G.; Hyeon, T. Monodisperse Nanoparticles of Ni and NiO: Synthesis, Characterization, Self-Assembled Superlattices, and Catalytic Applications in the Suzuki Coupling Reaction. *J. Adv. Mater.* **2005**, *17*, 429–434.

[58] Heilmann, M.; Kulla, H.; Prinz, C.; Bienert, R.; Reinholz, U.; Guilherme Buzanich, A.; Emmerling, F. Advances in Nickel Nanoparticle Synthesis via Oleylamine Route. *J. Nanomater.* **2020**, *10*, 713.

[59] Chen, D.-H.; Hsieh, C.-H. Synthesis of nickel nanoparticles in aqueous cationic surfactant solutions. *J. Mater. Chem.* **2002**, *12*, 2412–2415.

[60] Wu, Z. G.; Munoz, M.; Montero, O. The synthesis of nickel nanoparticles by hydrazine reduction. *Adv. Powder Technol.* **2010**, *21*, 165–168.

[61] Yan, S.; Sun, D.; Tan, Y.; Xing, X.; Yu, H.; Wu, Z. Synthesis and formation mechanism of Ag–Ni alloy nanoparticles at room temperature. *J. Phys. Chem. Solids* **2016**, *98*, 107–114.

[62] Sidhaye, D. S.; Bala, T.; Srinath, S.; Srikanth, H.; Poddar, P.; Sastry, M.; Prasad, B. Preparation of nearly monodisperse nickel nanoparticles by a facile solution based methodology and their ordered assemblies. *J. Phys. Chem. C* **2009**, *113*, 3426–3429.

[63] Kumar, A.; Saxena, A.; De, A.; Shankar, R.; Mozumdar, S. Controlled synthesis of size-tunable nickel and nickel oxide nanoparticles using water-in-oil microemulsions. *Adv. Nat. Sci.: Nanosci. Nanotechnol.* **2013**, *4*, 025009.

[64] Logutenko, O.; Titkov, A.; Vorob'ev, A.; Shundrina, I.; Yukhin, Y. M.; Lyakhov, N. Synthesis of nickel nanoparticles by the reduction of its salts using the modified polyol method in the presence of sodium polyacrylates with various molecular weights. *Russ. J. Gen. Chem.* **2018**, *88*, 288–294.

[65] Song, H.-J.; Jia, X.-H.; Yang, X.-F.; Tang, H.; Li, Y.; Su, Y.-T. Controllable synthesis of monodisperse polyhedral nickel nanocrystals. *CrystEngComm* **2012**, *14*, 405–410.

[66] Chen, D.-H.; Wang, S.-R. Protective agent-free synthesis of Ni–Ag core–shell nanoparticles. *Mater. Chem. Phys.* **2006**, *100*, 468–471.

[67] Fu, X.-Z.; Liang, Y.; Chen, S.-P.; Lin, J.-D.; Liao, D.-W. Pt-rich shell coated Ni nanoparticles as catalysts for methanol electro-oxidation in alkaline media. *Catal. Commun.* **2009**, *10*, 1893–1897.

[68] Cheng, G.; Puntes, V. F.; Guo, T. Synthesis and self-assembled ring structures of Ni nanocrystals. *J. Colloid Interface Sci.* **2006**, *293*, 430–436.

[69] Winnischofer, H.; Rocha, T. C. R.; Nunes, W. C.; Socolovsky, L. M.; Knobel, M.; Zanchet, D. Chemical Synthesis and Structural Characterization of Highly Disordered Ni Colloidal Nanoparticles. *ACS Nano* **2008**, *2*, 1313–1319.

[70] Metin, Ö.; Özkar, S.; Sun, S. Monodisperse nickel nanoparticles supported on SiO 2 as an effective catalyst for the hydrolysis of ammonia-borane. *Nano Res.* **2010**, *3*, 676–684.

[71] Carenco, S.; Labouille, S.; Bouchonnet, S.; Boissière, C.; Le Goff, X.-F.; Sanchez, C.; Mezailles, N. Revisiting the molecular roots of a ubiquitously successful synthesis: Nickel (0) nanoparticles by reduction of [Ni (acetylacetonate) 2]. *Chem. Eur. J.* **2012**, *18*, 14165–14173.

[72] Xiang, J.; Li, P.; Chong, H.; Feng, L.; Fu, F.; Wang, Z.; Zhang, S.; Zhu, M. Bimetallic Pd-Ni core-shell nanoparticles as effective catalysts for the Suzuki reaction. *Nano Research* **2014**, *7*, 1337–1343.

[73] Guo, H.; Chen, Y.; Chen, X.; Wen, R.; Yue, G.-H.; Peng, D.-L. Facile synthesis of near-monodisperse Ag@ Ni core–shell nanoparticles and their application for catalytic generation of hydrogen. *Nanotechnology* **2011**, *22*, 195604.

[74] Gao, X.; Du, X.; Liu, D.; Gao, H.; Wang, P.; Yang, J. Core-shell gold-nickel nanostructures as highly selective and stable nonenzymatic glucose sensor for fermentation process. *Scientific reports* **2020**, *10*, 1–10.

[75] Yamauchi, T.; Tsukahara, Y.; Yamada, K.; Sakata, T.; Wada, Y. Nucleation and Growth of Magnetic Ni- Co (Core- Shell) Nanoparticles in a One-Pot Reaction under Microwave Irradiation. *Chem. Mater.* **2011**, *23*, 75–84.

[76] Carenco, S.; Wu, C.-H.; Shavorskiy, A.; Alayoglu, S.; Somorjai, G. A.; Bluhm, H.; Salmeron, M. Synthesis and structural evolution of nickel–cobalt nanoparticles under H_2 and CO_2. *Small* **2015**, *11*, 3045–3053.

[77] Horlyck, J.; Lawrey, C.; Lovell, E. C.; Amal, R.; Scott, J. Elucidating the impact of Ni and Co loading on the selectivity of bimetallic NiCo catalysts for dry reforming of methane. *ChemE.* **2018**, *352*, 572–580.

[78] Wu, Z.; Yang, B.; Miao, S.; Liu, W.; Xie, J.; Lee, S.; Pellin, M. J.; Xiao, D.; Su, D.; Ma, D. Lattice strained Ni-Co alloy as a high-performance catalyst for catalytic dry reforming of methane. *ACS Catal.* **2019**, *9*, 2693–2700.

[79] Hernández Mejía, C.; van der Hoeven, J. E. S.; de Jongh, P. E.; de Jong, K. P. Cobalt–Nickel Nanoparticles Supported on Reducible Oxides as Fischer–Tropsch Catalysts. *ACS Catal.* **2020**, *10*, 7343–7354.

[80] Hashemizadeh, S. A.; Biglari, M. Cu: Ni bimetallic nanoparticles: facile synthesis, characterization and its application in photodegradation of organic dyes. *Journal of Materials Science: Materials in Electronics* **2018**, *29*, 13025–13031.

[81] Beaumont, S. K.; Alayoglu, S.; Pushkarev, V. V.; Liu, Z.; Kruse, N.; Somorjai, G. A. Exploring surface science and restructuring in reactive atmospheres of colloidally prepared bimetallic CuNi and CuCo nanoparticles on SiO 2 in situ using ambient pressure X-ray photoelectron spectroscopy. *Faraday discussions* **2013**, *162*, 31–44.

[82] Li, S.-J.; Wang, H.-L.; Yan, J.-M.; Jiang, Q. Oleylamine-stabilized Cu0. 9Ni0. 1 nanoparticles as efficient catalyst for ammonia borane dehydrogenation. *International Journal of Hydrogen Energy* **2017**, *42*, 25251–25257.

[83] He, W.; Ding, Y.; Ji, L.; Zhang, X.; Yang, F. A high performance sensor based on bimetallic NiCu nanoparticles for the simultaneous determination of five species of biomolecules. *Sensors and Actuators B: Chemical* **2017**, *241*, 949–956.

[84] Becker, R.; Döring, W. Kinetische Behandlung der Keimbildung in übersättigten Dämpfen. *Ann. Phys.* **1935**, *416*, 719–752.

[85] Zeng, X. C.; Oxtoby, D. W. Gas–liquid nucleation in Lennard-Jones fluids. *J. Chem. Phys.* **1991**, *94*, 4472–4478.

[86] Dickens, D.; Sloan, J. The nucleation and freezing of dilute nitric acid aerosols. *J. Chem. Phys. A* **2002**, *106*, 10543–10549.

[87] Turner, G. W.; Bartell, L. S. On the probability of nucleation at the surface of freezing drops. *J. Chem. Phys. A* **2005**, *109*, 6877–6879.

[88] Polte, J. Fundamental growth principles of colloidal metal nanoparticles–a new perspective. *CrystEngComm* **2015**, *17*, 6809–6830.

[89] Sugimoto, T. *Monodispersed Particles*; Elsevier Science, 2001.

[90] Bøjesen, E.; Iversen, B. The chemistry of nucleation. *CrystEngComm* **2016**, *18*, 8332–8353.

[91] LaMer, V. K.; Dinegar, R. H. Theory, production and mechanism of formation of monodispersed hydrosols. *J. Am. Chem. Soc.* **1950**, *72*, 4847–4854.

[92] Mer, V. K. L. Nucleation in phase transitions. *Ind. Eng. Chem. Res.* **1952**, *44*, 1270–1277.

[93] Murray, C.; Sun, S.; Doyle, H.; Betley, T. Monodisperse 3d Transition-Metal (Co,Ni,Fe) Nanoparticles and Their Assembly intoNanoparticle Superlattices. *MRS Bull.* **2001**, *26*, 985–991.

[94] Ise, N.; Sogami, I. *Structure formation in solution: ionic polymers and colloidal particles*; Springer Science & Business Media, 2005.

[95] ISO, *ISO/TS 80004-2:2015 Nanotechnologies — Vocabulary — Part 2: Nano-objects*.

[96] IUPAC, *Compendium of Chemical Terminology*; 2010.

[97] Ostwald, W. Über die vermeintliche Isomerie des roten und gelben Quecksilberoxyds und die Oberflächenspannung fester Körper. *Z. Phys. Chem.* **1900**, *34*, 495–503.

[98] Shevchenko, E. V.; Talapin, D. V.; Schnablegger, H.; Kornowski, A.; Festin, Ö.; Svedlindh, P.; Haase, M.; Weller, H. Study of nucleation and growth in the organometallic synthesis of magnetic alloy nanocrystals: the role of nucleation rate in size control of CoPt3 nanocrystals. *J. Am. Chem. Soc.* **2003**, *125*, 9090–9101.

[99] Lin, P.-C.; Lin, S.; Wang, P. C.; Sridhar, R. Techniques for physicochemical characterization of nanomaterials. *Biotechnol. Adv.* **2014**, *32*, 711–726.

[100] Leopold, K.; Philippe, A.; Wörle, K.; Schaumann, G. E. Analytical strategies to the determination of metal-containing nanoparticles in environmental waters. *Trac-Trend. Anal. Chem.* **2016**, *84*, 107–120.

[101] Sötebier, C. A.; Weidner, S. M.; Jakubowski, N.; Panne, U.; Bettmer, J. Separation and quantification of silver nanoparticles and silver ions using reversed phase high performance liquid chromatography coupled to inductively coupled plasma mass spectrometry in combination with isotope dilution analysis. *J. Chromatogr. A* **2016**, *1468*, 102–108.

[102] Costo, R.; Heinke, D.; Grüttner, C.; Westphal, F.; Morales, M. P.; Veintemillas-Verdaguer, S.; Gehrke, N. Improving the reliability of the iron concentration quantification for iron oxide nanoparticle suspensions: a two-institutions study. *Anal. Bioanal. Chem.* **2019**, *411*, 1895–1903.

[103] Menéndez-Miranda, M.; Encinar, J. R.; Costa-Fernández, J. M.; Sanz-Medel, A. Asymmetric flow field-flow fractionation coupled to inductively coupled plasma mass spectrometry for the quantification of quantum dots bioconjugation efficiency. *J. Chromatogr. A* **2015**, *1422*, 247–252.

[104] Marbella, L. E.; Millstone, J. E. NMR techniques for noble metal nanoparticles. *Chem. Mater.* **2015**, *27*, 2721–2739.

[105] You, Z.; Nirmalananthan-Budau, N.; Resch-Genger, U.; Panne, U.; Weidner, S. M. Separation of polystyrene nanoparticles bearing different carboxyl group densities and functional groups quantification with capillary electrophoresis and asymmetrical flow field flow fractionation. *J. Chromatogr. A* **2020**, *1626*, 461392.

[106] Chakraborty, S.; Roy, M.; Saha, R. Cost-effective synthesis method of facile environment friendly SnO_2 nanoparticle for efficient photocatalytic degradation of water contaminating compound. *Water Sci. Technol.* **2020**, *81*, 508–517.

[107] Sapsford, K. E.; Tyner, K. M.; Dair, B. J.; Deschamps, J. R.; Medintz, I. L. Analyzing Nanomaterial Bioconjugates: A Review of Current and Emerging Purification and Characterization Techniques. *Anal. Chem.* **2011**, *83*, 4453–4488, PMID: 21545140.

[108] Müller, A.; Krahl, T.; Radnik, J.; Wagner, A.; Kreyenschulte, C.; Werner, W. S.; Ritter, B.; Kemnitz, E.; Unger, W. E. Chemical in-depth analysis of (Ca/Sr) F_2 core–shell like nanoparticles by X-ray photoelectron spectroscopy with tunable excitation energy. *Surf. Interface Anal.* **2021**,

[109] Ridolfi, A.; Caselli, L.; Montis, C.; Mangiapia, G.; Berti, D.; Brucale, M.; Valle, F. Gold nanoparticles interacting with synthetic lipid rafts: an AFM investigation. *J. Microsc.* **2020**, *280*, 194–203.

[110] Smith, M. C.; Crist, R. M.; Clogston, J. D.; McNeil, S. E. Zeta potential: a case study of cationic, anionic, and neutral liposomes. *Anal. Bioanal. Chem.* **2017**, *409*, 5779–5787.

[111] Liu, S.; Mei, J.; Zhang, C.; Zhang, J.; Shi, R. Synthesis and magnetic properties of shuriken-like nickel nanoparticles. *J. Mater. Sci. Technol.* **2018**, *34*, 836–841.

[112] Rosalie, J. M.; Pauw, B. R. Form-free size distributions from complementary stereological TEM/SAXS on precipitates in a Mg–Zn alloy. *Acta Mater.* **2014**, *66*, 150–162.

[113] Pauw, B. R. Everything SAXS: small-angle scattering pattern collection and correction. *J. Condens. Matter Phys.* **2013**, *25*, 383201.

[114] Kabelitz, A.; Guilherme, A.; Joester, M.; Reinholz, U.; Radtke, M.; Bienert, R.; Schulz, K.; Schmack, R.; Kraehnert, R.; Emmerling, F. Time-resolved in situ studies on the formation mechanism of iron oxide nanoparticles using combined fast-XANES and SAXS. *CrystEngComm* **2015**, *17*, 8463–8470.

[115] Woodard, D. L.; Davis, S. J.; Randerson, J. T. Economic carbon cycle feedbacks may offset additional warming from natural feedbacks. *PNAS* **2019**, *116*, 759–764.

[116] Wang, W.; Wang, S.; Ma, X.; Gong, J. Recent advances in catalytic hydrogenation of carbon dioxide. *Chem. Soc. Rev.* **2011**, *40*, 3703–3727.

[117] Zhang, Z.; Huisingh, D. Carbon dioxide storage schemes: Technology, assessment and deployment. *J. Clean. Prod.* **2017**, *142*, 1055–1064, Special Volume on Improving natural resource management and human health to ensure sustainable societal development based upon insights gained from working within 'Big Data Environments'.

[118] Hansson, A.; Bryngelsson, M. Expert opinions on carbon dioxide capture and storage—a framing of uncertainties and possibilities. *Energy Policy* **2009**, *37*, 2273–2282.

[119] Das, S.; Pérez-Ramírez, J.; Gong, J.; Dewangan, N.; Hidajat, K.; Gates, B. C.; Kawi, S. Core–shell structured catalysts for thermocatalytic, photocatalytic, and electrocatalytic conversion of CO_2. *Chem. Soc. Rev.* **2020**, *49*, 2937–3004.

[120] Xiaoding, X.; Moulijn, J. Mitigation of CO_2 by chemical conversion: plausible chemical reactions and promising products. *Energy & Fuels* **1996**, *10*, 305–325.

[121] Centi, G.; Quadrelli, E. A.; Perathoner, S. Catalysis for CO_2 conversion: a key technology for rapid introduction of renewable energy in the value chain of chemical industries. *Energy Environ. Sci.* **2013**, *6*, 1711–1731.

[122] Liu, K.; Song, C.; Subramani, V. *Hydrogen and syngas production and purification technologies*; John Wiley & Sons, 2010.

[123] Wilhelm, D.; Simbeck, D.; Karp, A.; Dickenson, R. Syngas production for gas-to-liquids applications: Technologies, issues and outlook. *Fuel Process. Technol.* **2001**, *71*, 139–148.

[124] Rennard, D.; French, R.; Czernik, S.; Josephson, T.; Schmidt, L. Production of synthesis gas by partial oxidation and steam reforming of biomass pyrolysis oils. *Int. J. Hydrog. Energy* **2010**, *35*, 4048–4059.

[125] Schwab, E.; Milanov, A.; Schunk, S. A.; Behrens, A.; Schodel, N. Dry Reforming and Reverse Water Gas Shift: Alternatives for Syngas Production? *Chem. Ing. Tech.* **2015**, *87*, 347–353.

[126] Maschio, G.; Lucchesi, A.; Stoppato, G. Production of syngas from biomass. *Bioresour. Technol.* **1994**, *48*, 119–126.

[127] Rostrup-Nielsen, J. R. New aspects of syngas production and use. *Catal. Today* **2000**, *63*, 159–164.

[128] Bosch, C.; Wild, W. Producing hydrogen.

[129] Fishman, Z. S.; He, Y.; Yang, K. R.; Lounsbury, A. W.; Zhu, J.; Tran, T. M.; Zimmerman, J. B.; Batista, V. S.; Pfefferle, L. D. Hard templating ultrathin polycrystalline hematite nanosheets: effect of nano-dimension on CO 2 to CO conversion via the reverse water-gas shift reaction. *Nanoscale* **2017**, *9*, 12984–12995.

[130] Mallapragada, D. S.; Singh, N. R.; Curteanu, V.; Agrawal, R. Sun-to-fuel assessment of routes for fixing CO_2 as liquid fuel. *Ind. Eng. Chem. Res.* **2013**, *52*, 5136–5144.

[131] Mathew, T.; Saju, S.; Raveendran, S. In *Engineering Solutions for CO_2 Conversion*; Dr. Reina, T. R., Ed.; John Wiley & Sons, 2021; p 281.

[132] Sakurai, H.; Tsubota, S.; Haruta, M. Hydrogenation of CO_2 over gold supported on metal oxides. *APPL Catal. A-Gen.* **1993**, *102*, 125–136.

[133] Xu, H.; Li, Y.; Luo, X.; Xu, Z.; Ge, J. Monodispersed gold nanoparticles supported on a zirconium-based porous metal–organic framework and their high catalytic ability for the reverse water–gas shift reaction. *ChemComm* **2017**, *53*, 7953–7956.

[134] Ye, J.; Ge, Q.; Liu, C.-j. Effect of PdIn bimetallic particle formation on CO_2 reduction over the Pd–In/SiO_2 catalyst. *Chem. Eng. Sci.* **2015**, *135*, 193–201.

[135] Chen, X.; Su, X.; Duan, H.; Liang, B.; Huang, Y.; Zhang, T. Catalytic performance of the Pt/TiO_2 catalysts in reverse water gas shift reaction: Controlled product selectivity and a mechanism study. *Catal. Today* **2017**, *281*, 312–318.

[136] Yan, B.; Wu, Q.; Cen, J.; Timoshenko, J.; Frenkel, A. I.; Su, D.; Chen, X.; Parise, J. B.; Stach, E.; Orlov, A., et al. Highly active subnanometer Rh clusters derived from Rh-doped $SrTiO_3$ for CO_2 reduction. *Appl. Catal.* **2018**, *237*, 1003–1011.

[137] Aitbekova, A.; Wu, L.; Wrasman, C. J.; Boubnov, A.; Hoffman, A. S.; Goodman, E. D.; Bare, S. R.; Cargnello, M. Low-temperature restructuring of CeO_2-supported Ru nanoparticles determines selectivity in CO_2 catalytic reduction. *J. Am. Chem. Soc.* **2018**, *140*, 13736–13745.

[138] Liu, H.; Zhao, C.; Wang, L. Mesoporous Ni–CeO_2 Catalyst with Enhanced Selectivity and Stability for Reverse Water–Gas Shift Reaction. *J. Chem. Eng. Japan* **2016**, *49*, 161–165.

[139] Zhu, J.; Zhang, G.; Li, W.; Zhang, X.; Ding, F.; Song, C.; Guo, X. Deconvolution of the Particle Size Effect on CO_2 Hydrogenation over Iron-Based Catalysts. *ACS Cata.* **2020**, *10*, 7424–7433.

[140] Zagoraios, D.; Tsatsos, S.; Kennou, S.; Vayenas, C. G.; Kyriakou, G.; Katsaounis, A. Tuning the RWGS Reaction via EPOC and In Situ Electro-oxidation of Cobalt Nanoparticles. *ACS Cata.* **2020**, *10*, 14916–14927.

[141] Daily Metal Spot Prices. `https://www.dailymetalprice.com/metalprices.php?c=ru&u=kg&d=1`, Accessed: 19.06.2021.

[142] Haynes, W. M., Ed. *CRC Handbook of Chemistry and Physics*, 97th ed.; CRC Press., Chapter ABUNDANCE OF ELEMENTS IN THE EARTH'S CRUST AND IN THE SEA, p 14–17.

[143] Roiaz, M.; Monachino, E.; Dri, C.; Greiner, M.; Knop-Gericke, A.; Schlögl, R.; Comelli, G.; Vesselli, E. Reverse Water–Gas Shift or Sabatier Methanation on Ni(110)? Stable Surface Species at Near-Ambient Pressure. *J. Am. Chem. Soc.* **2016**, *138*, 4146–4154.

[144] Yang, Y.; Liu, J.; Liu, F.; Wu, D. Reaction mechanism of CO_2 methanation over Rh/TiO2 catalyst. *Fuel* **2020**, *276*.

[145] Rodriguez, J. A.; Evans, J.; Feria, L.; Vidal, A. B.; Liu, P.; Nakamura, K.; Illas, F. CO_2 hydrogenation on Au/TiC, Cu/TiC, and Ni/TiC catalysts: Production of CO, methanol, and methane. *J. Catal.* **2013**, *307*, 162–169.

[146] Dziadyk, E.; Trawczyński, J.; Szyja, B. M. The pathways of the CO_2 hydrogenation by NiCu/ZnO from DFT molecular dynamics simulations. *J. Mol. Graph. Model.* **2020**, *100*, 107677.

[147] Foit, S. R.; Vinke, I. C.; de Haart, L. G.; Eichel, R.-A. Power-to-Syngas: An Enabling Technology for the Transition of the Energy System? *Angew. Chem. Int. Ed.* **2017**, *56*, 5402–5411.

[148] Rueter, G. Energiewende: Ist Power-to-Gas die Lösung? `https://www.dw.com/de/energiewende-ist-power-to-gas-die-lösung/a-18677372`, 01.09.2015, Accessed: 16.07.2021.

[149] Dutta, S. A review on production, storage of hydrogen and its utilization as an energy resource. *J. Ind. Eng. Chem.* **2014**, *20*, 1148 – 1156.

[150] Gahleitner, G. Hydrogen from renewable electricity: An international review of power-to-gas pilot plants for stationary applications. *Int. J. Hydrog. Energy* **2013**, *38*, 2039–2061.

[151] The National Hydrogen Strategy, Federal Ministry for Economic Affairs and EnergyPublic Relations Division. Berlin, 2020.

[152] Chatterjee, A. *Sponge iron production by direct reduction of iron oxide*; PHI Learning Pvt. Ltd., 2010.

[153] Fischer, F.; Tropsch, H. Über die direkte Synthese von Erdöl-Kohlenwasserstoffen bei gewöhnlichem Druck.(Erste Mitteilung). *Ber. Dtsch. Chem. Ges.(A and B)* **1926**, *59*, 830–831.

[154] Davies, P.; Snowdon, F. F.; Bridger, G. W.; Hughes, D. O.; Young, P. W. Water-Gas Conversion and Catalysts Therefor. patentuk GB1010871A, 1965.

[155] Cockcroft, J. K.; Fitch, A. N. *Powder diffraction: Theory and practice*; The Royal Society of Chemistry, 2008; pp 20–57.

[156] Spieß, L.; Behnken, H.; Genzel, C.; Schwarzer, R.; Teichert, G. *Moderne Röntgenbeugung*; Springer, 2009; Vol. 2.

[157] Borchert, H.; Shevchenko, E. V.; Robert, A.; Mekis, I.; Kornowski, A.; Grübel, G.; Weller, H. Determination of Nanocrystal Sizes: A Comparison of TEM, SAXS, and XRD Studies of Highly Monodisperse $CoPt_3$ Particles. *Langmuir* **2005**, *21*, 1931–1936, PMID: 15723491.

[158] Glatter, O.; Kratky, O. *Small angle X-ray scattering*; Academic press, 1982.

[159] Breßler, I.; Kohlbrecher, J.; Thünemann, A. F. SASfit: a tool for small-angle scattering data analysis using a library of analytical expressions. *J. Appl. Crystallogr.* **2015**, *48*, 1587–1598.

[160] Kohlbrecher, J. *SASfit: A program for fitting simple structural models to small angle scattering data*; 2018.

[161] Bressler, I.; Pauw, B. R.; Thünemann, A. F. *McSAS*: software for the retrieval of model parameter distributions from scattering patterns. *J. Appl. Crystallogr.* **2015**, *48*, 962–969.

[162] Pauw, B. R.; Pedersen, J. S.; Tardif, S.; Takata, M.; Iversen, B. B. Improvements and considerations for size distribution retrieval from small-angle scattering data by Monte Carlo methods. *J. Appl. Crystallogr.* **2013**, *46*, 365–371.

[163] Haas, S.; Hoell, A.; Wurth, R.; Rüssel, C.; Boesecke, P.; Vainio, U. Analysis of nanostructure and nanochemistry by ASAXS: Accessing phase composition of oxyfluoride glass ceramics doped with Er^{3+}/Yb^{3+}. *Phys. Rev. B* **2010**, *81*, 184207.

[164] Kronig, R. d. L. On the theory of dispersion of x-rays. *Josa* **1926**, *12*, 547–557.

[165] Cromer, D. T.; Liberman, D. Relativistic calculation of anomalous scattering factors for X rays. *J. Chem. Phys* **1970**, *53*, 1891–1898.

[166] Stuhrmann, H. B. In *Resonance Scattering in MacromolecularStructure Research, Advances in Polymer Science*; Kausch, H., Zachmann, H., Eds.; Springer-Verlag, Vol. 67; p 123–163.

[167] Hoell, A.; Tatchev, D.; Haas, S.; Haug, J.; Boesecke, P. On the determination of partial structure functions in small-angle scattering exemplified by Al89Ni6La5 alloy. *Journal of Applied Crystallography* **2009**, *42*, 323–325.

[168] Krumrey, M.; Ulm, G. High-accuracy detector calibration at the PTB four-crystal monochromator beamline. *Nucl. Instrum. Methods. Phys. Res. A* **2001**, *467*, 1175–1178.

[169] Krumrey, M.; Gerlach, M.; Hoffmann, M.; Müller, P. Thin Transmission Photodiodes as Monitor Detectors in the X-ray Range. *AIP Conf. Proc.* **2007**, *879*, 1145–1147.

[170] Friedrich, W.; Knipping, P.; Laue, M. v. Interferenzerscheinungen bei Röntgenstrahlen. *Ann. Phys.(Berl.)* **1913**, *436*, 971–988.

[171] Bragg, W. H.; Bragg, W. L. The reflection of X-rays by crystals. *Proc. R. Soc. Lond. A* **1913**, *88*, 428–438.

[172] Laue, M.; Friedrich, W.; Knipping, P. Interferenz-Erscheinungen bei Röntgenstrahlen. **1912**, 363–373.

[173] Paris, O.; Li, C.; Siegel, S.; Weseloh, G.; Emmerling, F.; Riesemeier, H.; Erko, A.; Fratzl, P. A new experimental station for simultaneous X-ray microbeam scanning for small-and wide-angle scattering and fluorescence at BESSY II. *J. Appl. Crystallogr.* **2007**, *40*, s466–s470.

[174] Leiterer, J.; Leitenberger, W.; Emmerling, F.; Thünemann, A. F.; Panne, U. The use of an acoustic levitator to follow crystallization in small droplets by energy-dispersive X-ray diffraction. *J. Appl. Crystallogr.* **2006**, *39*, 771–773.

[175] Benecke, G.; Wagermaier, W.; Li, C.; Schwartzkopf, M.; Flucke, G.; Hoerth, R.; Zizak, I.; Burghammer, M.; Metwalli, E.; Muller-Buschbaum, P.; Trebbin, M.; Forster, S.; Paris, O.; Roth, S. V.; Fratzl, P. A customizable software for fast reduction and analysis of large X-ray scattering data sets: applications of the new DPDAK package to small-angle X-ray scattering and grazing-incidence small-angle X-ray scattering. *J. Appl. Crystallogr.* **2014**, *47*, 1797–1803.

[176] Gražulis, S.; Merkys, A.; Vaitkus, A. Crystallography Open Database (COD). *Mat. Model. MTM* **2020**, 1863–1881.

[177] Joint Committee on Powder Diffraction Standard (JCPDS), International Center for Diffraction Data (ICDD), Swarthmore, Pa, USA.

[178] Einstein, A. Über einen die Erzeugung und Verwandlung des Lichtes betreffenden heuristischen Gesichtspunkt. *Ann. Phys.* **1905**, *322*, 132–148.

[179] Auger, P. On the Secondary P-Radiation Produced in a Gas by X-rays. *Comptes Rendus* **1925**, *180*, 65–68.

[180] Jablonski, A.; Powell, C. *NIST Electron Effective-Attenuation-Length Database*; National Institute of Standards and Technology Gaithersburg, MD, 2011; Vol. Version 1.3.

[181] ISO, *ISO 15472:2010, Surface chemical analysis – X-ray photoelectron spectrometers – Calibration of energy scales. International Organization for Standardization:.*

[182] Hesse, R.; Denecke, R. Improved Tougaard background calculation by introduction of fittable parameters for the inelastic electron scattering cross-section in the peak fit of photoelectron spectra with UNIFIT 2011. *Surf. Interface Anal.* **2011**, *43*, 1514–1526.

[183] Scofield, J. H. Hartree-Slater subshell photoionization cross-sections at 1254 and 1487 eV. *J. Electron Spectrosc.* **1976**, *8*, 129–137.

[184] Tanuma, S.; Powell, C. J.; Penn, D. R. Calculations of electron inelastic mean free paths (IMFPS). IV. Evaluation of calculated IMFPs and of the predictive IMFP formula TPP-2 for electron energies between 50 and 2000 eV. *Surf. Interface Anal.* **1993**, *20*, 77–89.

[185] Shard, A. G.; Spencer, S. J. Intensity calibration for monochromated Al Kα XPS instruments using polyethylene. *Surf. Interface Anal.* **2019**, *51*, 618–626.

[186] Powell, C. J.; Werner, W.; Kalbe, H.; Shard, A.; Castner, D. G. Comparisons of analytical approaches for determining shell thicknesses of core–shell nanoparticles by X-ray photoelectron spectroscopy. *J. Phys. Chem. C* **2018**, *122*, 4073–4082.

[187] Evans, J. *X-Ray Absorption Spectroscopy for the Chemical and Materials Sciences*; John Wiley & Sons, Ltd, 2018; Chapter 1, pp 1–8.

[188] Westre, T. E.; Kennepohl, P.; DeWitt, J. G.; Hedman, B.; Hodgson, K. O.; Solomon, E. I. A multiplet analysis of Fe K-edge 1s $\rightarrow$ 3d pre-edge features of iron complexes. *J. Am. Chem. Soc.* **1997**, *119*, 6297–6314.

[189] Görner, W.; Hentschel, M. P.; Müller, B. R.; Riesemeier, H.; Krumrey, M.; Ulm, G.; Diete, W.; Klein, U.; Frahm, R. BAMline: the first hard X-ray beamline at BESSY II. *Nucl. Instrum. Meth A* **2001**, *467-468*, 703 – 706, 7th Int.Conf. on Synchrotron Radiation Instrumentation.

[190] Ravel, B.; Newville, M. ATHENA, ARTEMIS, HEPHAESTUS: data analysis for X-ray absorption spectroscopy using IFEFFIT. *J. Synchrotron Radiat.* **2005**, *12*, 537–541.

[191] Knoll, M.; Ruska, E. Das Elektronenmikroskop. *Z. Phys.* **1932**, *78*, 318–339.

[192] Williams, D. B.; Carter, C. B. *The Transmission Electron Microscope*; Springer-Verlag US: Boston, MA, 2009.

[193] de Broglie, L. Recherches sur la théorie des quanta. *Ann. Phys. (Paris)* **1925**, *3*, 22–128.

[194] Kurz, C.-A.; Lorenz, A. Das Elektronen-Mikroskop (Raster- und Transmissionsmikroskopie). 2020; `http://daten.didaktikchemie.uni-bayreuth.de/umat/elektronenmikroskop/Elektronenmikroskop.pdf`, Accessed 09.12.2020.

[195] Brunauer, S.; Emmett, P. H.; Teller, E. Adsorption of Gases in Multimolecular Layers. *Journal of the American Chemical Society* **1938**, *60*, 309–319.

[196] Washburn, E. W. The Dynamics of Capillary Flow. *Phys. Rev.* **1921**, *17*, 273–283.

[197] Bücks, K.; Müller, H. Über einige Beobachtungen an schwingenden Piezoquarzen und ihrem Schallfeld. *Z. Phys.* **1933**, *84*, 75–86.

[198] Santesson, S.; Nilsson, S. Airborne chemistry: acoustic levitation in chemical analysis. *Anal. Bioanal. Chem.* **2004**, *378*, 1704–1709.

[199] Priego-Capote, F.; de Castro, L. Ultrasound-assisted levitation: Lab-on-a-drop. *TRAC-Trend Anal. Chem.* **2006**, *25*, 856–867.

[200] Scheeline, A.; Behrens, R. L. Potential of levitated drops to serve as microreactors for biophysical measurements. *Biophys. Chem.* **2012**, *165*, 1–12.

[201] Shi, Q.; Di, W.; Dong, D.; Yap, L. W.; Li, L.; Zang, D.; Cheng, W. A general approach to free-standing nanoassemblies via acoustic levitation self-assembly. *ACS nano* **2019**, *13*, 5243–5250.

[202] Stindt, A.; Andrade, M.; Albrecht, M.; Adamowski, J.; Panne, U.; Riedel, J. Experimental and numerical characterization of the sound pressure in standing wave acoustic levitators. *Rev. Sci. Instrum.* **2014**, *85*, 015110.

[203] Raman, C. V. The Raman effect. Investigation of molecular structure by light scattering. *Trans. Faraday Soc.* **1929**, *25*, 781–792.

[204] Schmidt, W. *Optische Spektroskopie*; VHC: Weinheim, 1994; pp 310–311.

[205] Gonçalves, E. M.; da Piedade, M. E. M. Solubility of nicotinic acid in water, ethanol, acetone, diethyl ether, acetonitrile, and dimethyl sulfoxide. *J. Chem. Thermodyn.* **2012**, *47*, 362–371.

[206] Simões, R. G.; Melo, P. L. T.; Bernardes, C. E. S.; Heilmann, M. T.; Emmerling, F.; Minas da Piedade, M. E. Linking Aggregation in Solution, Solvation, and Solubility of Simvastatin: An Experimental and MD Simulation Study. *Cryst. Growth Des.* **2021**, *21*, 544–551.

[207] Heilmann, M.; Simões, R.; Bernardes, C.; Ramish, Y.; Bienert, R.; Röllig, M.; Emmerling, F.; Minas da Piedade, M. Real-time In situ XRD Study of Simvastatin Crystallization in Levitated Droplets. *Cryst. Growth Des.* **2021**, accepted.

[208] Donegan, K. P.; Godsell, J. F.; Otway, D. J.; Morris, M. A.; Roy, S.; Holmes, J. D. Size-tuneable synthesis of nickel nanoparticles. *Journal of Nanoparticle Research* **2012**, *14*.

[209] Chen, G.; Desinan, S.; Rosei, R.; Rosei, F.; Ma, D. Synthesis of Ni-Ru Alloy Nanoparticles and Their High Catalytic Activity in Dehydrogenation of Ammonia Borane. *Chem. Eur. J* **2012**, *18*, 7925–7930.

[210] Joint Committee on Powder Diffraction Standard (JCPDS), PDF 00-004-0850, International Center for Diffraction Data (ICDD), Swarthmore, Pa, USA.

[211] Sakamoto, T.; Kishi, H.; Yamaguchi, S.; Matsumura, D.; Tamura, K.; Hori, A.; Horiuchi, Y.; Serov, A.; Artyushkova, K.; Atanassov, P.; Tanaka, H. Mechanism Study of Hydrazine Electrooxidation Reaction on Nickel Oxide Surface in Alkaline Electrolyte by In Situ XAFS. *J. Electrochem. Soc.* **2016**, *163*, H951–H957.

[212] Kulla, H. Nickelnanopartikel für die Reformierung von CO_2 zu Synthesegas: Synthese und Charakterisierung. mathesis, 2014.

[213] Evanoff, D. D.; Chumanov, G. Size-Controlled Synthesis of Nanoparticles. 2. Measurement of Extinction, Scattering, and Absorption Cross Sections. *The Journal of Physical Chemistry B* **2004**, *108*, 13957–13962.

[214] Muzzio, M.; Li, J.; Yin, Z.; Delahunty, I. M.; Xie, J.; Sun, S. Monodisperse nanoparticles for catalysis and nanomedicine. *Nanoscale* **2019**, *11*, 18946–18967.

[215] Wu, L.; Li, Q.; Wu, C. H.; Zhu, H.; Mendoza-Garcia, A.; Shen, B.; Guo, J.; Sun, S. Stable Cobalt Nanoparticles and Their Monolayer Array as an Efficient Electrocatalyst for Oxygen Evolution Reaction. *J. Am. Chem. Soc.* **2015**, *137*, 7071–7074, PMID: 26018822.

[216] Xu, C.; Sun, S. Monodisperse magnetic nanoparticles for biomedical applications. *Polym. Int.* **2007**, *56*, 821–826.

[217] McNaught, A. D.; Wilkinson, A. *IUPAC. Compendium of Chemical Terminology*, 2nd ed.; Blackwell Scientific Publications, Oxford, 1997; Vol. 1669.

[218] Eluri, R.; Paul, B. Microwave assisted greener synthesis of nickel nanoparticles using sodium hypophosphite. *Mater. Lett.* **2012**, *76*, 36–39.

[219] Ishizaki, T.; Yatsugi, K.; Akedo, K. Effect of particle size on the magnetic properties of Ni nanoparticles synthesized with trioctylphosphine as the capping agent. *J. Nanomater.* **2016**, *6*, 172.

[220] Couto, G. G.; Klein, J. J.; Schreiner, W. H.; Mosca, D. H.; de Oliveira, A. J.; Zarbin, A. J. Nickel nanoparticles obtained by a modified polyol process: synthesis, characterization, and magnetic properties. *J. Colloid Interface Sci.* **2007**, *311*, 461–468.

[221] Vivien, A.; Guillaumont, M.; Meziane, L.; Salzemann, C.; Aubert, C.; Halbert, S.; Gérard, H.; Petit, M.; Petit, C. Role of Oleylamine Revisited: An Original Disproportionation Route to Monodispersed Cobalt and Nickel Nanocrystals. *Chem. Mater.* **2019**, *31*, 960–968.

[222] Yamamoto, M.; Kashiwagi, Y.; Nakamoto, M. Size-controlled synthesis of monodispersed silver nanoparticles capped by long-chain alkyl carboxylates from silver carboxylate and tertiary amine. *Langmuir* **2006**, *22*, 8581–8586.

[223] Mourdikoudis, S.; Liz-Marzán, L. M. Oleylamine in nanoparticle synthesis. *Chem. Mater.* **2013**, *25*, 1465–1476.

[224] Gong, W.; Li, H.; Zhao, Z.; Chen, J. Ultrafine particles of Fe, Co, and Ni ferromagnetic metals. *Int. J. Appl. Phys.* **1991**, *69*, 5119–5121.

[225] Hens, Z.; Moreels, I.; Martins, J. In situ H-1 NMR study on the trioctylphosphine oxide capping of colloidal InP nanocrystals. *Chemphyschem* **2005**, *6*, 2578–2584.

[226] Bizkarra, K.; Bermudez, J.; Arcelus-Arrillaga, P.; Barrio, V.; Cambra, J.; Millan, M. Nickel based monometallic and bimetallic catalysts for synthetic and real bio-oil steam reforming. *Int. J. Hydrog. Energy* **2018**, *43*, 11706–11718, HYdrogen POwer THeoretical and Engineering Solutions –International Symposium (Hypothesis XII).

[227] Zhu, M.; Ge, Q.; Zhu, X. Catalytic reduction of CO 2 to CO via reverse water gas shift reaction: Recent advances in the design of active and selective supported metal catalysts. *rans. Tianjin Univ.* **2020**, *26*, 172–187.

[228] Guo, H.; Chen, Y.; Ping, H.; Wang, L.; Peng, D.-L. One-pot synthesis of hexagonal and triangular nickel–copper alloy nanoplates and their magnetic and catalytic properties. *J. Mater. Chem.* **2012**, *22*, 8336–8344.

[229] Biesinger, M. C.; Payne, B. P.; Lau, L. W.; Gerson, A.; Smart, R. S. C. X-ray photoelectron spectroscopic chemical state quantification of mixed nickel metal, oxide and hydroxide systems. *Surface and Interface Analysis: An International Journal devoted to the development and application of techniques for the analysis of surfaces, interfaces and thin films* **2009**, *41*, 324–332.

[230] López-Tinoco, J.; Mendoza-Cruz, R.; Bazán-Díaz, L.; Karuturi, S. C.; Martinelli, M.; Cronauer, D. C.; Kropf, A. J.; Marshall, C. L.; Jacobs, G. The Preparation and Characterization of Co–Ni Nanoparticles and the Testing of a Heterogenized Co–Ni/Alumina Catalyst for CO Hydrogenation. *Catalysts* **2020**, *10*.

[231] Guo, K.; Ding, Y.; Luo, J.; Gu, M.; Yu, Z. NiCu Bimetallic Nanoparticles on silica support for catalytic hydrolysis of ammonia borane: Composition-dependent activity and support size effect. *ACS Applied Energy Materials* **2019**, *2*, 5851–5861.

[232] Zhang, Z.; Tian, Y.; Zhang, L.; Hu, S.; Xiang, J.; Wang, Y.; Xu, L.; Liu, Q.; Zhang, S.; Hu, X. Impacts of nickel loading on properties, catalytic behaviors of Ni//*gamma*-Al_2O_3 catalysts and the reaction intermediates formed in methanation of CO_2. *international journal of hydrogen energy* **2019**, *44*, 9291–9306.

[233] McGinty, J.; Yazdanpanah, N.; Price, C.; ter Horst, J. H.; Sefcik, J. *The Handbook of Continuous Crystallization*; RSC, 2020; pp 1–50.

[234] Li, J. J. *Triumph of the heart: the story of statins*; Oxford University Press, 2009.

[235] Tiwari, R.; Pathak, K. Statins therapy: a review on conventional and novel formulation approaches. *J. Pharm. Pharmacol.* **2011**, *63*, 983–998.

[236] Taylor, F.; Ward, K.; Moore, T. H.; Burke, M.; Smith, G. D.; Casas, J. P.; Ebrahim, S. Statins for the primary prevention of cardiovascular disease. *Cochrane Database Syst. Rev.* **2011**,

[237] Virani, S. S. et al. Heart Disease and Stroke Statistics—2020 Update: A Report From the American Heart Association. *Circulation* **2020**, *141*, e139–e596.

[238] Mortensen, M. B.; Falk, E.; Schmidt, M. Twenty-Year Nationwide Trends in Statin Utilization and Expenditure in Denmark. *Circ Cardiovasc Qual Outcomes* **2017**, *10*, e003811.

[239] Baxendale, I. R.; Hayward, J. J.; Ley, S. V.; Tranmer, G. K. Pharmaceutical strategy and innovation: An academics perspective. *ChemMedChem: Chemistry Enabling Drug Discovery* **2007**, *2*, 768–788.

[240] Cejka, J.; Kratochvil, B.; Císařová, I.; Jegorov, A. Simvastatin. *Acta Crystallogr. C* **2003**, *59*, 428–430.

[241] Ellison, D. K.; Moore, W. D.; Petts, C. R. *Analytical profiles of drug substances and excipients*; Elsevier, 1993; Vol. 22; pp 359–388.

[242] Geboers, S.; Stappaerts, J.; Tack, J.; Annaert, P.; Augustijns, P. In vitro and in vivo investigation of the gastrointestinal behavior of simvastatin. *Int. J. Pharm.* **2016**, *510*, 296–303.

[243] Todd, P. A.; Goa, K. L. Simvastatin. *Drugs* **1990**, *40*, 583–607.

[244] Murtaza, G. Solubility enhancement of simvastatin: A review. *Acta Pol. Pharm.* **2012**, *69*, 581–90.

[245] Bhatia, A.; Chopra, S.; Nagpal, K.; Deb, P. K.; Tekade, M.; Tekade, R. K. In *Dosage Form Design Parameters*; Tekade, R. K., Ed.; Advances in Pharmaceutical Product Development and Research; Academic Press, 2018; pp 31 – 65.

[246] Wöhler, F.; von Liebig, J. F. *Untersuchungen über das Radikal der Benzoesäure*; W. Engelmann, 1891.

[247] Haleblian, J.; McCrone, W. Pharmaceutical applications of polymorphism. *J. Pharm. Sci.* **1969**, *58*, 911–929.

[248] Dunitz, J. D.; Bernstein, J. Disappearing polymorphs. *Acc. Chem. Res* **1995**, *28*, 193–200.

[249] Li, R.; Mayer, P. T.; Trivedi, J. S.; Fort, J. J. Polymorphism and crystallization behavior of Abbott-79175, a second-generation 5-lipoxygenase inhibitor. *J. Pharm. Sci.* **1996**, *85*, 773–780.

[250] Simões, R. G.; Bernardes, C. E.; Joseph, A.; Minas da Piedade, F.; Kraus, W.; Emmerling, F.; Diogo, H. P.; Minas da Piedade, M. E. Polymorphism in Simvastatin: Twinning, Disorder, and Enantiotropic Phase Transitions. *Mol.* **2018**, *15*, 5349–5360, PMID: 30230340.

[251] Bauer, J.; Spanton, S.; Henry, R.; Quick, J.; Dziki, W.; Porter, W.; Morris, J. Ritonavir: an extraordinary example of conformational polymorphism. *Pharm. Res.* **2001**, *18*, 859–866.

[252] Kempf, D. J.; Marsh, K. C.; Denissen, J. F.; McDonald, E.; Vasavanonda, S.; Flentge, C. A.; Green, B. E.; Fino, L.; Park, C. H.; Kong, X.-P. ABT-538 is a potent inhibitor of human immunodeficiency virus protease and has high oral bioavailability in humans. *PNAS* **1995**, *92*, 2484–2488.

[253] Morissette, S. L.; Soukasene, S.; Levinson, D.; Cima, M. J.; Almarsson, Ö. Elucidation of crystal form diversity of the HIV protease inhibitor ritonavir by high-throughput crystallization. *PNAS* **2003**, *100*, 2180–2184.

[254] Di Martino, P.; Guyot-Hermann, A.-M.; Conflant, P.; Drache, M.; Guyot, J.-C. A new pure paracetamol for direct compression: The orthorhombic form. *Int. J. Pharm.* **1996**, *128*, 1 – 8.

[255] Zhu, H.; Yuen, C.; Grant, D. J. Influence of water activity in organic solvent + water mixtures on the nature of the crystallizing drug phase. 1. Theophylline. *Int. J. Pharm.* **1996**, *135*, 151 – 160.

[256] Phadnis, N. V.; Suryanarayanan, R. Polymorphism in anhydrous theophylline—implications on the dissolution rate of theophylline tablets. *J. Pharm. Sci.* **1997**, *86*, 1256–1263.

[257] Hušák, M.; Kratochvíl, B.; Jegorov, A.; Brus, J.; Maixner, J.; Rohlíček, J. Simvastatin: structure solution of two new low-temperature phases from synchrotron powder diffraction and ss-NMR. *J. Struct. Chem.* **2010**, *21*, 511–518.

[258] Simões, R. G.; Bernardes, C. E.; Diogo, H. P.; Agapito, F.; Minas da Piedade, M. E. Energetics and structure of simvastatin. *Mol. Pharm.* **2013**, *10*, 2713–2722.

[259] Graeser, K. A.; Strachan, C. J.; Patterson, J. E.; Gordon, K. C.; Rades, T. Physicochemical properties and stability of two differently prepared amorphous forms of simvastatin. *Cryst. Growth Des.* **2008**, *8*, 128–135.

[260] Zhang, F.; Aaltonen, J.; Tian, F.; Saville, D. J.; Rades, T. Influence of particle size and preparation methods on the physical and chemical stability of amorphous simvastatin. *Eur. J. Pharm. Biopharm.* **2009**, *71*, 64–70.

[261] Gnutzmann, T.; Nguyen Thi, Y.; Rademann, K.; Emmerling, F. Solvent-triggered crystallization of polymorphs studied in situ. *Cryst. Growth Des.* **2014**, *14*, 6445–6450.

[262] Thi, Y. N.; Rademann, K.; Emmerling, F. Direct evidence of polyamorphism in paracetamol. *CrystEngComm* **2015**, *17*, 9029–9036.

[263] Schlegel, M.-C.; Sarfraz, A.; Müller, U.; Panne, U.; Emmerling, F. First Seconds in a Building's Life—In Situ Synchrotron X-Ray Diffraction Study of Cement Hydration on the Millisecond Timescale. *Angew. Chem. Int. Ed.* **2012**, *51*, 4993–4996.

[264] Stroh, J.; Schlegel, M.-C.; Schmidt, W.; Thi, Y. N.; Meng, B.; Emmerling, F. Time-resolved in situ investigation of Portland cement hydration influenced by chemical admixtures. *Constr. Build Mater.* **2016**, *106*, 18–26.

[265] Polte, J.; Ahner, T. T.; Delissen, F.; Sokolov, S.; Emmerling, F.; Thünemann, A. F.; Kraehnert, R. Mechanism of gold nanoparticle formation in the classical citrate synthesis method derived from coupled in situ XANES and SAXS evaluation. *J. Am. Chem. Soc.* **2010**, *132*, 1296–1301.

[266] Cao, H.-L.; Yin, D.-C.; Guo, Y.-Z.; Ma, X.-L.; He, J.; Guo, W.-H.; Xie, X.-Z.; Zhou, B.-R. Rapid crystallization from acoustically levitated droplets. *J. Acoust. Soc. Am.* **2012**, *131*, 3164–3172.

[267] Tröbs, L.; Thi, Y. N.; Rump, D.; Emmerling, F. Crystallization behavior of carbamazepine. *Z. Phys. Chem.* **2014**, *228*, 493–501.

[268] Nguyen, T. Y.; Roessler, E. A.; Rademann, K.; Emmerling, F. Control of organic polymorph formation: crystallization pathways in acoustically levitated droplets. *Z. Kristallogr. – Cryst. Mater.* **2017**, *232*, 15–24.

[269] Klimakow, M.; Leiterer, J.; Kneipp, J.; Rössler, E.; Panne, U.; Rademann, K.; Emmerling, F. Combined synchrotron XRD/Raman measurements: In situ identification of polymorphic transitions during crystallization processes. *Langmuir* **2010**, *26*, 11233–11237.

[270] Alieva, A.; Boyes, M.; Vetter, T.; Casiraghi, C. Selective polymorphism of α-glycine by acoustic levitation. *CrystEngComm* **2020**, *22*, 7075–7081.

[271] Aceves-Hernández, J. M.; Hinojosa-Torres, J.; Nicolás-Vázquez, I.; Ruvalcaba, R. M.; García, R. M. L. Solubility of simvastatin: A theoretical and experimental study. *J. Mol. Struct.* **2011**, *995*, 41–50.

[272] Nti-Gyabaah, J.; Chan, V.; Chiew, Y. Solubility and limiting activity coefficient of simvastatin in different organic solvents. *Fluid Ph. Equilibria* **2009**, *280*, 35–41.

[273] Yan, J.; Yin, Q.; Jiang, C.; Gong, J.; Zhang, M.; Wang, Y.; Hou, B.; Hao, H. Solution thermodynamics of simvastatin in pure solvents and binary solvent mixtures. *Fluid Ph. Equilibria* **2015**, *406*, 77–90.

[274] Neelakantan, P. Raman spectra of liquid mixtures (cyclohexanol and ethyl acetate). Proceedings of the Indian Academy of Sciences-Section A. 1963; pp 330–336.

[275] Dellepiane, G.; Overend, J. Vibrational spectra and assignment of acetone, $\alpha\alpha\alpha$ acetone-d3 and acetone-d6. *Spectrochim. Acta* **1966**, *22*, 593–614.

Appendix

Table A.1: Synthesis parameters used for the formation of monometallic NiNPs. Listed are the amount and concentration (c) of metal precursor $Ni(acac)_2$ in mmol respectively mmol/L, the equivalents (eq) of oleylamine (OAm), trioctylphosphin (TOP) to the amount of metal precursor, and the volume of additional solvent dibenzylether (DBE). The resulting NP diameter (size) and dispersity (PD) derived from SAXS measurements are listed in addition.

parameter	**precursor mmol**	**OAm eq**	**TOP eq**	**DBE eq**	**c mmol/L**	**size nm**	**PD %**
standard	0.264	54.1	2.9	-	52		
catalysis	0.251	56.8	3.1	-	49.8	14.2	
time	0.122	119.8	3.1	-	24.5		
OAm	0.249	5.0	1.5	4.42	49.8	15.5	10
	0.249	10.0	1.5	4.01	49.8	13.8	13
	0.249	15.0	1.5	3.6	49.9	15.4	10
	0.249	20.1	1.5	3.2	49.8	11.5	10
	0.249	30.1	1.5	2.37	49.8	10.2	12
	0.249	40.1	1.5	1.5	49.9	10.2	12
	0.249	58.9	1.5	-	49.9	9.1	11
	0.124	122.4	1.1	-	24.5	9.5	8
TOP	0.249	59.5	1.0	-	50.0	10.2	10
	0.249	56.9	3.0	-	49.9	9.2	8
	0.249	54.2	5.0	-	49.8	9.0	10
	0.249	47.4	10.0	-	49.8	7.5	13
	0.249	20.2	30.1	-	49.8	4.5	15
	0.128	116.3	3.0	-	25.3	12	8
	0.125	97.0	17.9	-	25.1	10.6	6
	0.128	119.0	49.2	-	16.4	7.6	10
volume	0.249	57.0	3.0	-	49.8	8.8	12
	0.249	56,9	3.0	-	49.9	9.2	8
	0.249	57.0	3.0	-	49.9	9.3	16
	0.498	57.0	3.0	-	49.8	9.5	9
	1.000	56.7	3.0	-	50.0	9.5	11

Table A.2: Representative synthesis parameters used for the formation of bimetallic NiCo and NiCu NPs. Listed are the amount of Ni precursor $Ni(acac)_2$ in mmol, the equivalents (eq) of the metal precursors $Co(acac)_2$ or $Cu(acac)_2$ to the Ni precursor, the equivalents of oleylamine (OAm), trioctylphosphin (TOP) to the amount of total metal precursor, the concentration (c) of total metals in mmol/L and the volume of additional solvent dibenzylether (DBE). The resulting NP diameter (size) and dispersity (PD) derived from SAXS data are listed in addition.

	$Ni(acac)_2$ mmol	**$Co(acac)_2$ eq**	**OAm eq**	**TOP eq**	**DBE mL**	**c mmol/L**	**size nm**	**PD %**
standard	0.127	0.24	93.0	2.9	-	31.4	13.8	12
TOP	0.124	0.20	99.9	1.5	-	29.8	14.3	13
	0.124	0.20	97.9	3.0	-	29.8	13.8	9
	0.125	0.21	94.9	5.4	-	29.8	11.4	9
	0.123	0.22	87.0	10.5	-	30.0	11.0	8
	0.125	0.21	74.7	20.1	-	29.8	8.8	13
	0.123	0.21	61.3	30.2	-	29.7	7.5	16
	$Ni(acac)_2$ mmol	**$Cu(acac)_2$ eq**	**OAm eq**	**TOP eq**	**DBE mL**	**c mmol/L**	**size nm**	**PD %**
standard	0.127	0.19	88.4	10.4	-	29.7	15.4	12
time	0.252	0.24	93.3	2.9	-	31.3	19.5	24
TOP	0.125	0.20	100.0	1.5	-	29.8	30.5**	9
	0.125	0.20	99.4	1.6*	-	29.9	-	-
	0.130	0.19	93.8	2.5	-	31.3	24.1	14
	0.125	0.19	93.6	5.3	-	30.2	20.4	13
	0.125	0.21	90.6	7.0	-	30.4	18.9	12
	0.127	0.19	88.4	10.4	-	29.7	15.4	12
	0.125	0.20	75.5	19.6	-	29.8	14.0	16
	0.127	0.20	59.9	29.5	-	30.4	10.6	13
	0.126	0.19	38.5	49.3	-	28.9	6.1	15
OAm	0.124	0.20	5.1	10.2	4.0	30.2	5.9	16
	0.126	0.20	10.1	10.1	3.8	30.2	7.5	22
	0.125	0.21	20.2	10.0	3.3	30.2	9.5	22
	0.123	0.23	30.1	10.1	2.8	30.5	10.4	26
	0.124	0.20	50.9	10.2	2.2	27.8	15.6	13
	0.127	0.19	88.4	10.4	-	29.7	15.4	12
catalysts								
31Ni5	0.125	0.20	99.9	1.5	-	29.8	31.0**	10

Table A.2: continued from previous page.

	$Ni(acac)_2$ mmol	**$Cu(acac)_2$ eq**	**OAm eq**	**TOP eq**	**DBE mL**	**c mmol/L**	**size nm**	**PD %**
28Ni3	0.113	0.32	99.3	1.5	-	30.0	28.1**	12
17Ni5	0.124	0.20	90.0	10.3	-	29.3	16.7	11
17Ni3	0.113	0.33	89.2	9.9	-	29.6	17.2	16
19Ni1	0.077	0.97	88.5	9.8	-	29.9	19.1	13
13Ni6	0.126	0.21	49.7	10.0	2.2	28.4	12.7	29
15Ni1	0.076	0.98	50.5	10.6	2.2	27.8	15.0	20
12Ni7 -shape	0.125	0.20	89.1	9.9*	-	29.7	11.5	21
7Ni34	0.126	0.20	36.2	49.0	-	29.6	7.1	17
8Ni15	0.113	0.33	34.6	49.6	-	29.8	8.0	17
8Ni2	0.076	1.01	33.7	48.2	-	30.7	7.5	26
	* = 90% purity TOP used, ** = size derived from TEM data							

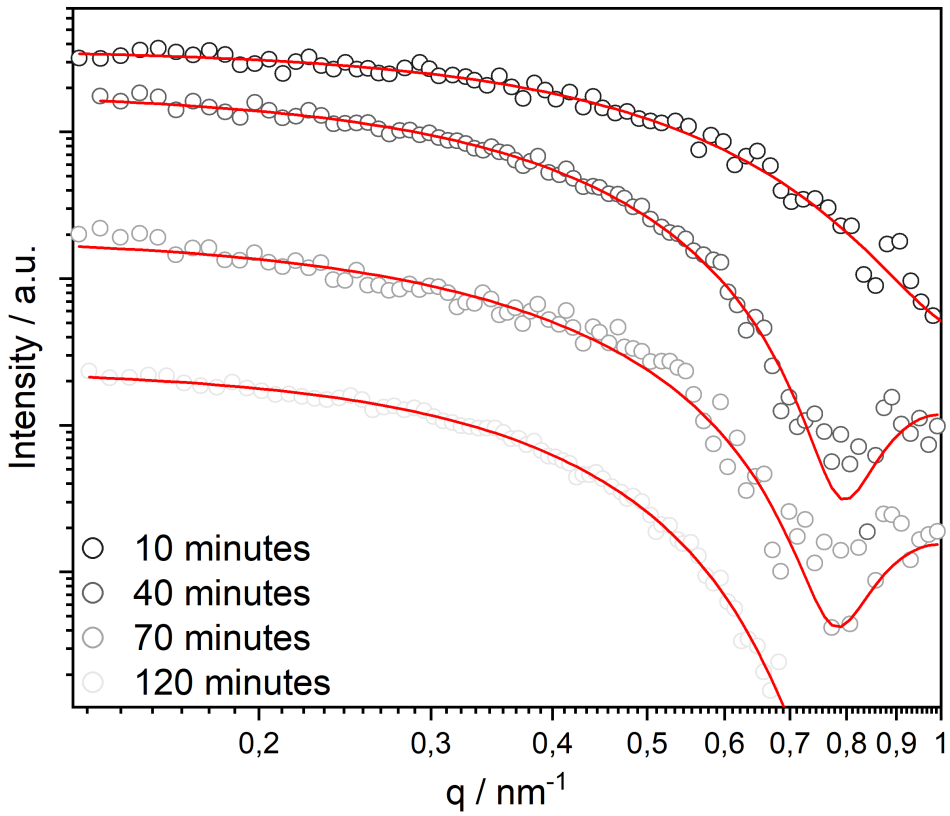

Figure A.1: SAXS data of NiNPs after 0, 10, 40, 70, and 120 minutes reaction time used for the given size determination.

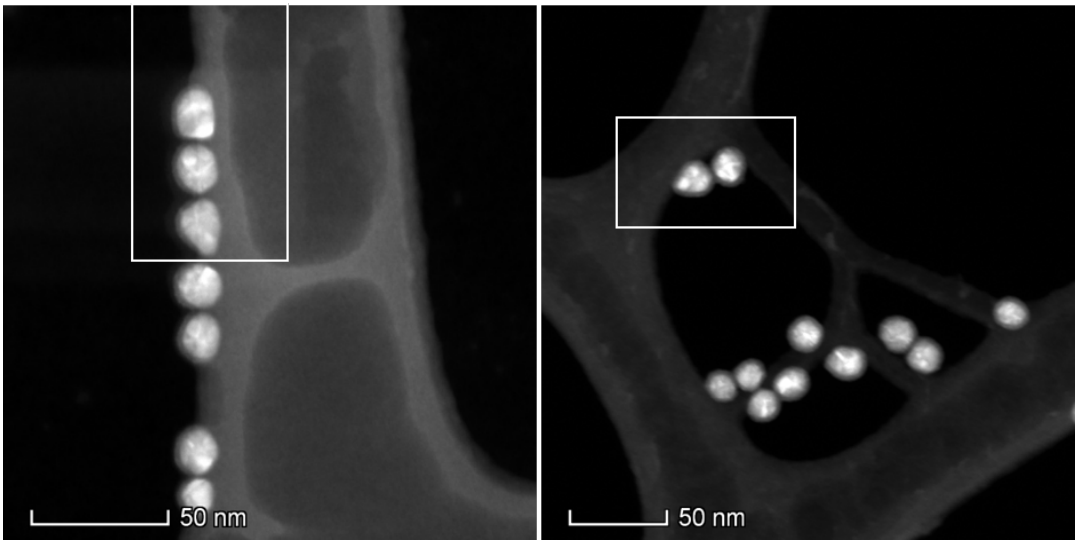

Figure A.2: STEM images of NiNPs after synthesis (left) and after nine weeks of storage in air (right), with selected regions (white rectangle) used for EDX mappings.

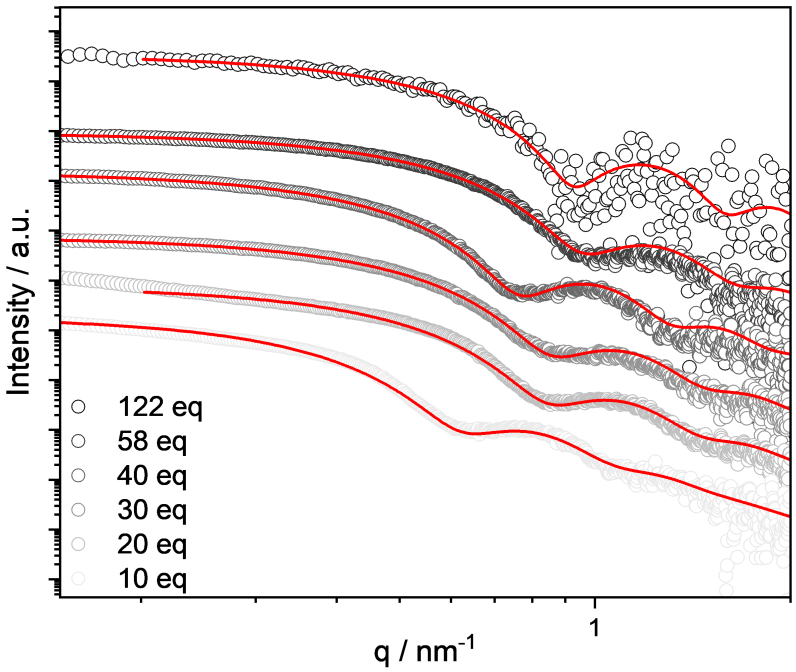

Figure A.3: SAXS data of Ni NPs synthesized using different amounts of OAm with corresponding Schulz–Zimm fit (red lines). T = 220 °C, t = 2 h, [Ni] = 50 mmol/L, TOP = 1.5 eq.

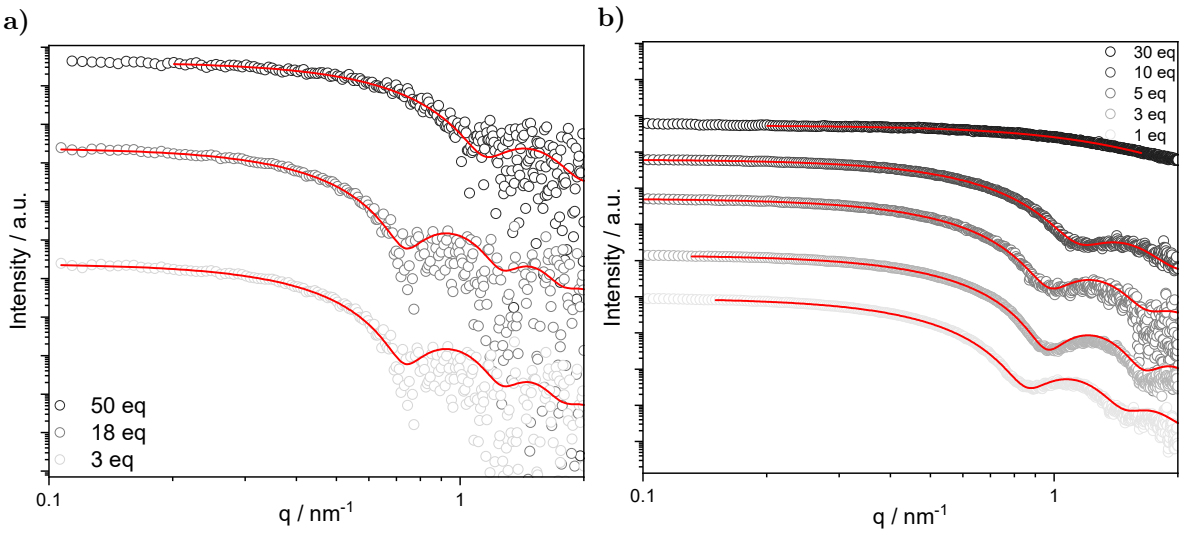

Figure A.4: a) Ni = 25 mmol/L, b) Ni = 50 mmol/L.SAXS data of Ni NPs synthesized using different amounts of TOP with corresponding Schulz–Zimm fit (red lines). T= 220 °C, t = 2 h, pure Oam.

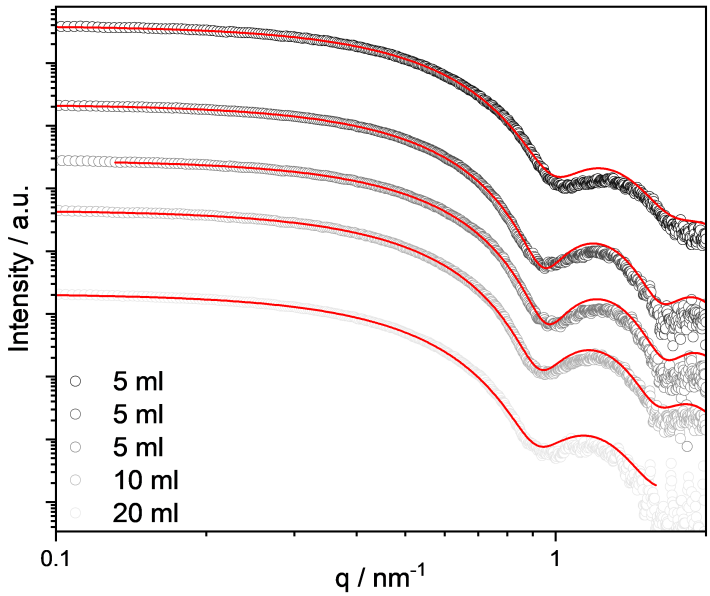

Figure A.5: SAXS data with corresponding Schulz–Zimm fit (red lines). Volume-independent NP size. T = 220 °C, t = 2 h, [Ni] = 50 mmol/L, TOP = 1.5 eq, pure OAm.

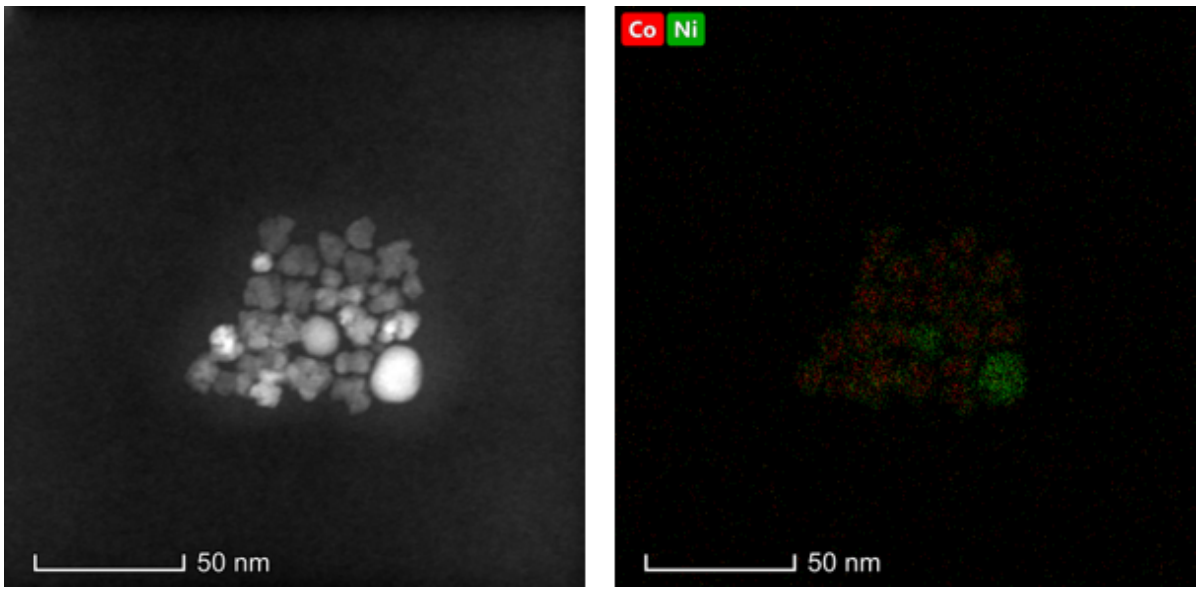

Figure A.6: STEM images of bimetallic NiCo NPs with a metal ratio of 1:1 (left) and after synthesis (left) and an associated element mapping of Ni (green) and Co (red) (right).

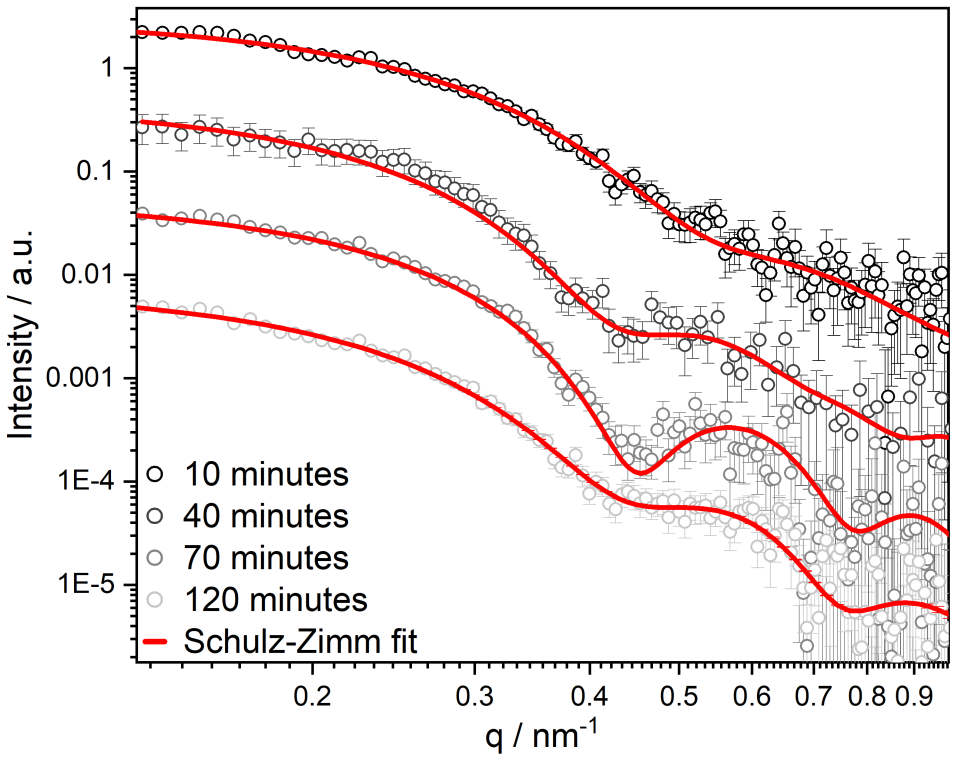

Figure A.7: SAXS data of NiCu NPs after 10, 40, 70, and 120 minutes reaction time used for the given size determination in chapter 5TabtimeNiCu.

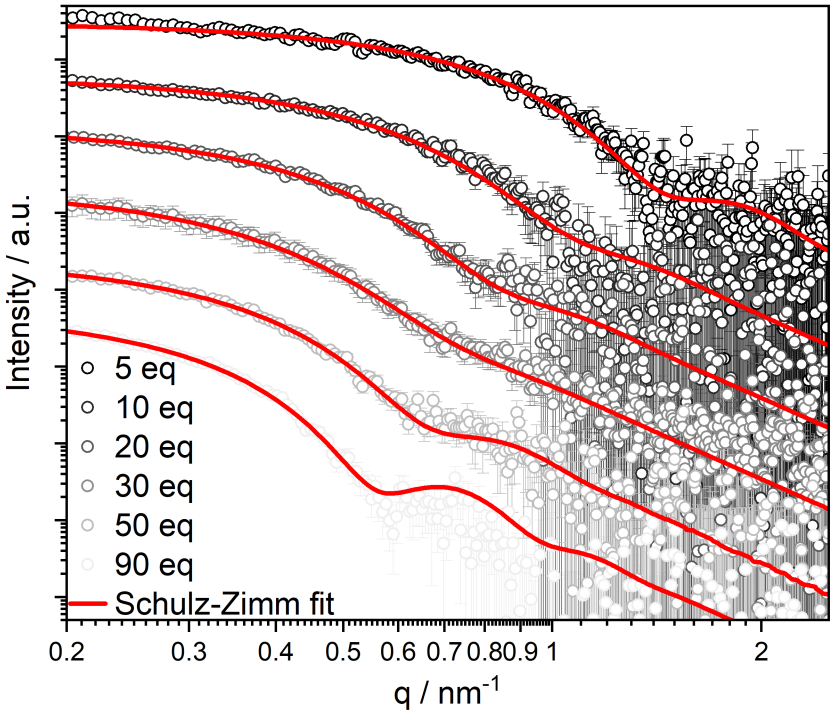

Figure A.8: SAXS data with corresponding Schulz-Zimm fit (red lines) of NiCu NPs prepared with 5-90 eq OAm and 10 eq TOP, 5 mL, 2h at 220 °C.

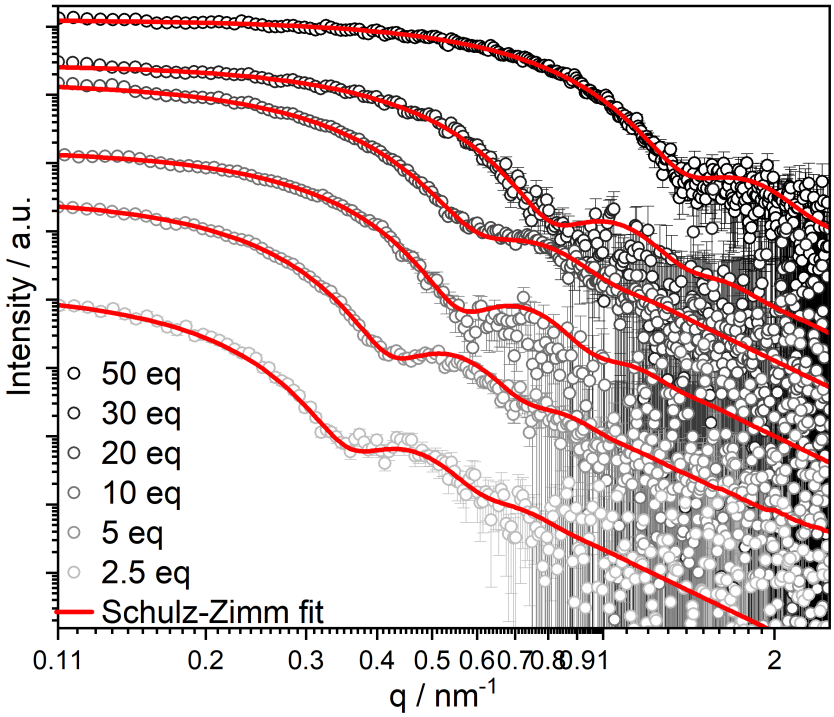

Figure A.9: SAXS data with corresponding Schulz-Zimm fit (red lines) of NiCu NPs prepared with 50 to 2.5 eq TOP and adjusted OAm content, 5 mL, 2h at 220 °C.

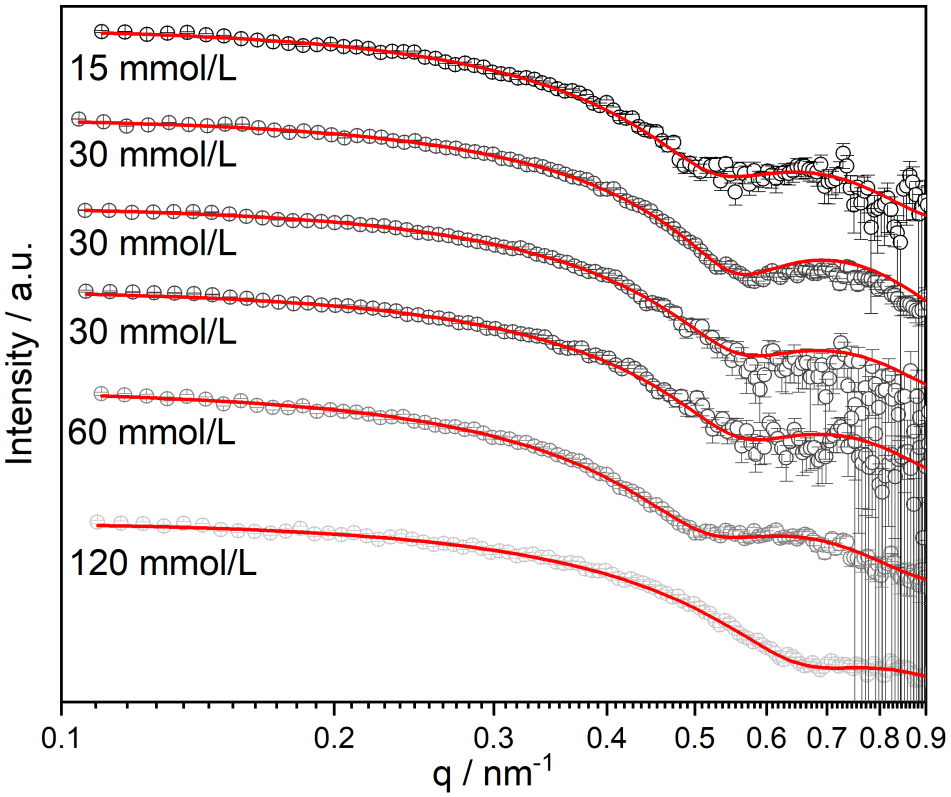

Figure A.10: SAXS data of NiCu NPs prepared with 15, 30, 60, and 120 mmol/L metal salt concentration (5:1 Ni:Cu) with 10 eq TOP and adjusted OAm content, 5 mL, 220°C.

Table A.3: Fitted EXAFS data of NiNPs, catalysts, and NiCu NPs with varying sizes.

		coordination number		**distance R/Å**			
		ref	**NiNPs**	$\mathbf{R}_{model}$	$\mathbf{R}_{fit}$	$\mathbf{R}^2_{diff}$	RMSE
NiNPs	**Ni1.1**	12	6.55 ± 0.44	2.49	2.47	0.0007	0.05
	Ni1.2	6	2.85 ± 2.69	3.52	3.46	0.004	
pre	**Ni-Ni1**	12	1.60 ± 0.97	2.49	2.49	0.0001	0.105
	NiO	6	0.67 ± 0.31	2.09	1.94	0.02	
post	**Ni-Ni1**	12	1.90 ± 1.14	2.49	2.50	0.0001	0.127
	NiO	6	0.49 ± 0.49	2.09	1.91	0.03	
		ref	**NiCu NPs**	$\mathbf{R}_{model}$	$\mathbf{R}_{fit}$	$\mathbf{R}^2_{diff}$	RMSE
40.2 nm	**Ni-Ni1**	12	6.23 ± 1.53	2.49	2.50	0.0002	0.013
	Cu-Cu1	12	10.59 ± 0.83	2.56	2.54	0.0007	0.049
	Cu-Cu2	6	3.58 ± 2.13	3.62	3.59	0.0013	
20.4 nm	**Ni-Ni1**	12	3.72 ± 1.81	2.49	2.51	0.0004	0.080
	NiO	6	1.05 ± 0.85	2.09	1.97	0.012	
	Cu-Cu1	12	10.91 ± 1.07	2.56	2.53	0.0009	0.06
	Cu-Cu2	6	5.78 ± 4.80	3.62	3.57	0.0025	
15.4 nm	**Ni-Ni1**	12	1.62 ± 0.60	2.49	2.54	0.002	0.114
	NiO	6	0.69 ± 0.18	2.09	1.93	0.024	
	Cu-Cu1	12	11.29 ± 1.00	2.56	2.53	0.0013	0.053
	Cu-Cu2	6	4.91 ± 3.44	3.62	3.57	0.003	
6.1 nm	**Ni-Ni1**	12	0.6 ± 1.17	2.49	2.56	0.013	0.097
	NiO	6	2.16 ± 0.74	2.09	1.97	0.013	
NiCu NPs	**Ni-Ni1**	12	4.62 ± 2.29	2.49	2.49	0.00001	0.06
	NiO	6	2.02 ± 1.97	2.09	2.00	0.007	
pre	**Ni-Ni1**	12	3.56 ± 1.31	2.49	2.49	0.00001	0.07
	NiO	6	2.25 ± 1.65	2.09	1.99	0.009	
post	**Ni-Ni1**	12	3.37 ± 2.11	2.49	2.50	0.00005	0.08
	NiO	6	0.29 ± 0.67	2.09	1.97	0.013	

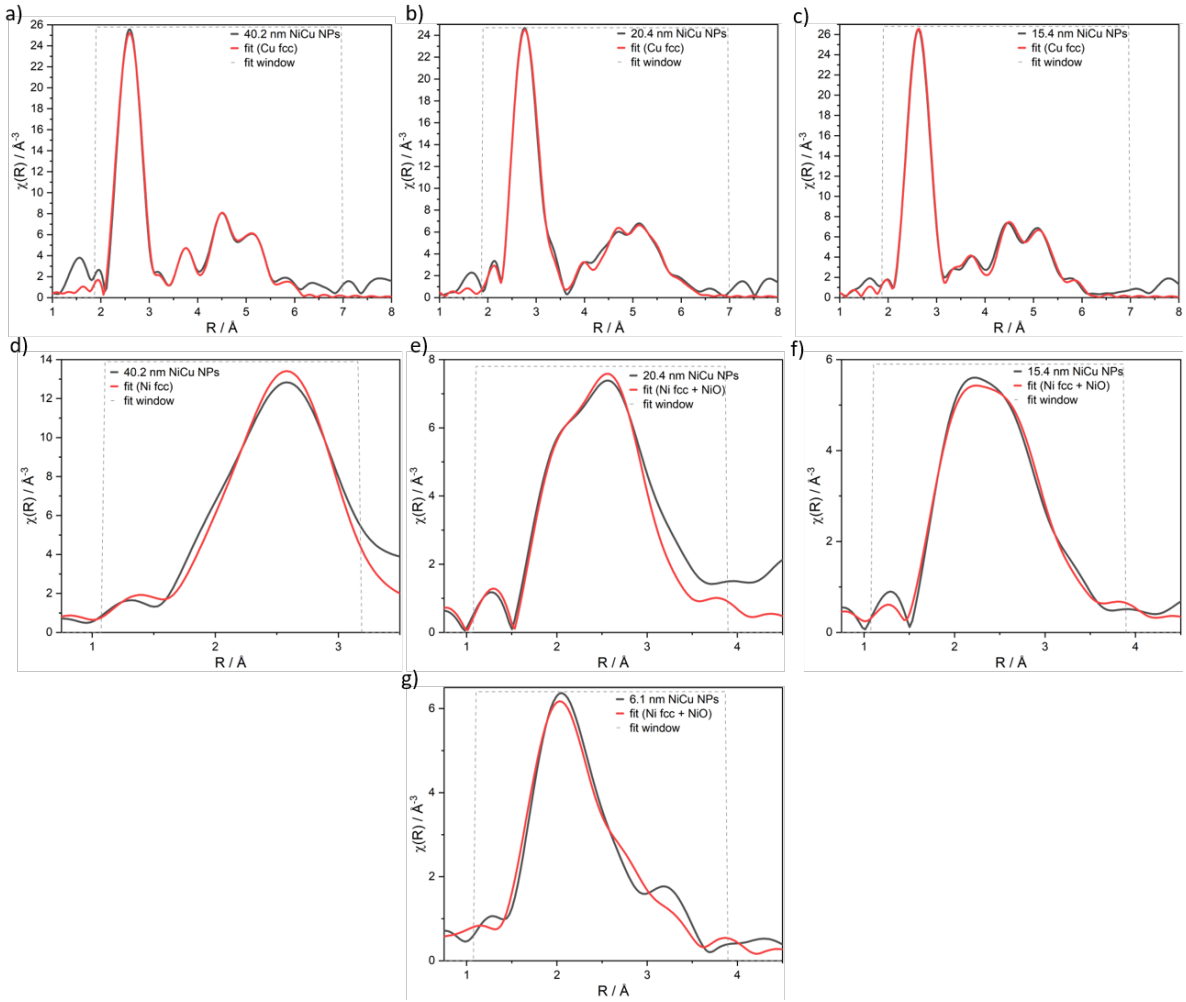

Figure A.11: EXAFS oscillations as function of the interatomic distance R in real space obtained by Fourier transformation of NiCu NPs (black) and fcc Cu bulk fit (red) in the fit window (grey) for a) 40.2 nm, b) 20.4 nm, and c) 15.4 nm. EXAFS oscillations as function of the interatomic distance R in real space obtained by Fourier transformation of NiCu NPs (black) and fcc Ni bulk and NiO fit (red) in the fit window (grey) for d) 40.2 nm, e) 20.4 nm, f) 15.4, and g) 6.1 nm.

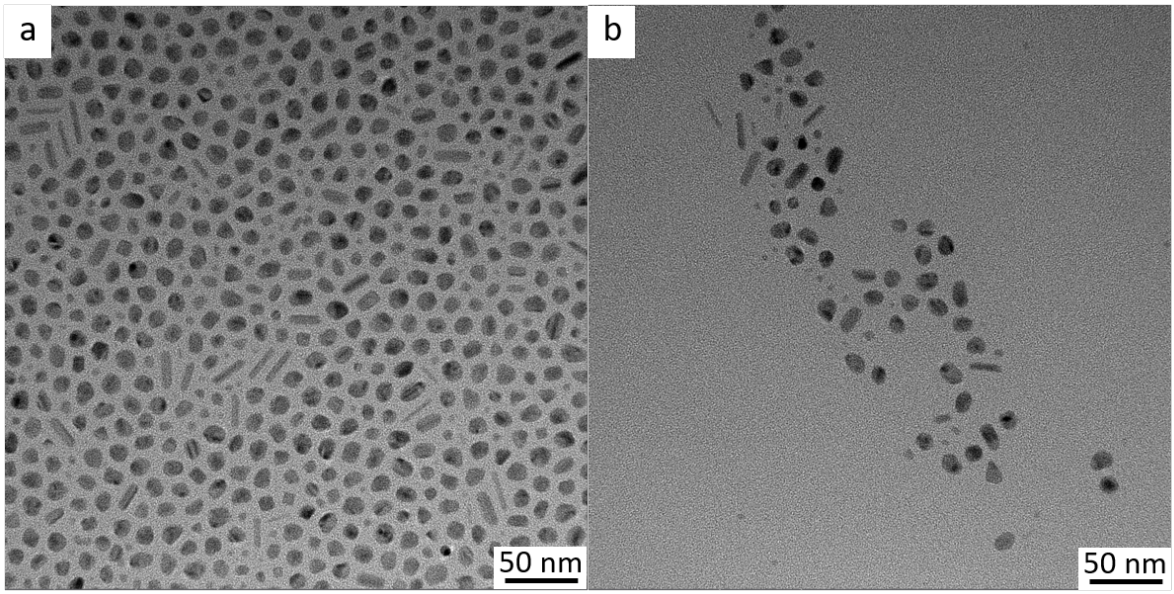

Figure A.12: TEM images of NiCu NPs (12Ni7-shape) with an average size of 11.5 nm derived from SAXS, prepared with 90 % pure TOP appearing in various sizes and shapes.

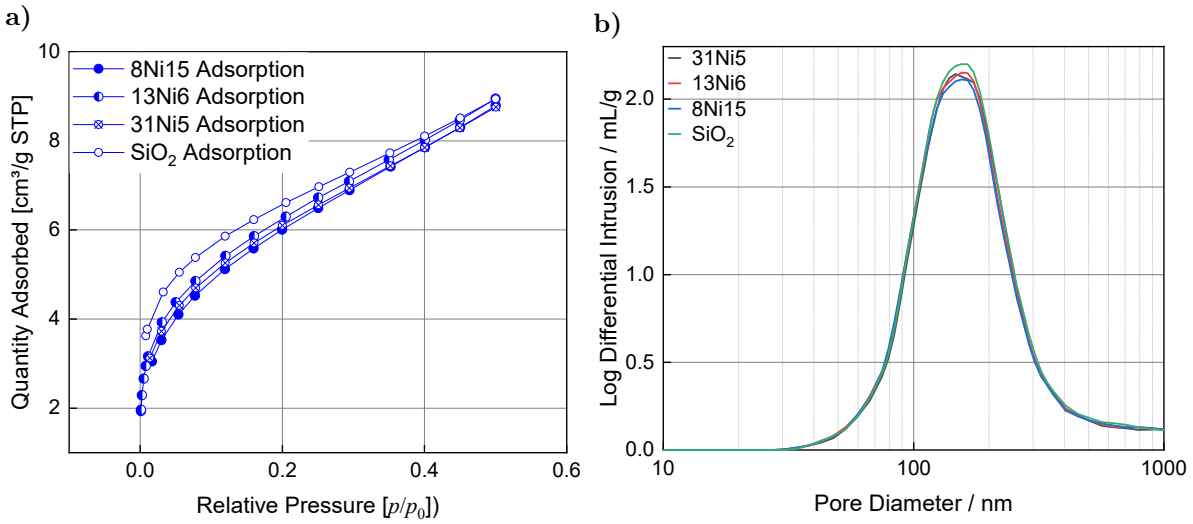

Figure A.13: a) Isotherm from N_2 Adsorption b) Pore diameter from Hg porosity. Pore structure analysis data of the supporting material SiO_2 (GRACE) and three representative catalysts 31Ni5, 13Ni6, and 8Ni15.

Table A.4: Core and shell thickness of NiCu NPs derived from ASAXS measurements, applying a core with a volumeweighted radius and a LogNorm distribution and an inner shell 1 and an outer shell 2 without distribution.

	size nm[1]	**Cu/Ni ratio**[2]	**R core nm**	**th sh1 nm**	**th sh2 nm**	**RED core**	**RED sh1**	**RED sh2**	**s**
				8000 eV					
14Ni0	14.2	-	5.44	3.05	-	1	0.82	-	0.14
8Ni2	7.5	2.2	2.27	0.70	1.47	1	1.0	0.73	0.35
				8004 eV					
17Ni5	16.7	5.5	5.50	2.89	1.06	1	0.94	0.67	0.18
17Ni3	17.2	3.5	5.74	1.94	2.56	1	1.0	0.85	0.30
19Ni1	19.1	1.4	7.00	0.96	2.49	1	1.0	0.82	0.18
15Ni1	15.0	1.3	6.66	0.41	1.56	1	1.0	0.65	-
8Ni15	8.0	15.1	3.17	0.40	1.20	1	1.0	0.63	0.25
				8304 eV					
14Ni0	14.2	-	5.44	3.05	-	0.90	0.76	-	0.14
				8330 eV					
17Ni5	16.7	5.5	5.50	2.89	1.06	1	0.86	0.73	0.18
17Ni3	17.2	3.5	5.63	1.94	2.56	1	0.82	0.72	0.29
19Ni1	19.1	1.4	7.00	0.96	2.49	1	0.90	0.75	0.18
14Ni0	14.2	-	5.44	3.05	-	0.82	0.71	-	0.14
15Ni1	15.0	1.3	6.66	0.41	1.66	1	0.92	0.58	-
8Ni15	8.0	15.1	3.17	0.40	1.20	1	0.93	0.71	0.25
8Ni2	7.5	2.2	2.27	0.70	1.47	1	0.85	0.71	0.35
				8397 eV					
17Ni5	16.7	5.5	5.50	2.89	1.06	1	1.05	0.78	0.18
17Ni3	17.2	3.5	5.74	1.94	2.56	1	1.05	0.94	0.30
19Ni1	19.1	1.4	7.00	0.96	2.49	1	1.08	0.94	0.18
15Ni1	15.0	1.3	6.66	0.41	1.66	1	1.26	0.72	
8Ni15	8.0	15.1	3.17	0.40	1.20	1	1.06	0.63	0.25
8Ni2	7.5	2.2	2.27	0.70	1.46	1	1.15	0.68	0.68

[1] = SAXSess number weighted size, [2] = MS data.

Table A.5: Absorbance (A) of simvastatin solutions in acetone (1:100 diluted in ethanol), ethyl acetate (1:200 diluted in ethanol), and ethanol at 238 nm as a function of concentration (c, $g\,kg^{-1}$).

acetone		**ethyl acetate**		**ethanol**	
c	**A**	**c**	**A**	**c**	**A**
0	0	0	0	0	0
0,0027	0,122	0,001911	0,115	0,003135	0,178
0,003944	0,202	0,007475	0,282	0,004227	0,237
0,004769	0,209	0,011230	0,407	0,004928	0,252
0,005062	0,236	0,014866	0,541	0,005244	0,252
0,005306	0,238	0,018610	0,746	0,007989	0,384
0,006459	0,31			0,008394	0,415
0,006758	0,323			0,009048	0,449
0,006885	0,307			0,011817	0,568
0,007968	0,374			0,013416	0,654
0,010454	0,501			0,015396	0,804
0,010929	0,559			0,016799	0,809
0,012656	0,614			0,020345	0,989
0,009324	0,482			0,013578	0,65
0,009382	0,511			0,015963	0,792
0,011662	0,576			0,0161	0,777
0,012864	0,606			0,01624	0,835
0,013612	0,732			0,01927	0,941
				0,014151	0,706
				0,015624	0,768
				0,015779	0,86
				0,015828	0,804
				0,016243	0,825

Table A.6: Saturation concentrations of simvastatin in three solvents ($g\,kg^{-1}$) determined by gravimetric method and UV Vis spectroscopy.

temperature	**acetone**		**ethyl acetate**		**ethanol**	
	1	**2**	**1**	**2**	**1**	**2**
K	$g\,kg^{-1}$		$g\,kg^{-1}$		$g\,kg^{-1}$	
283	355.6	274.2	122.5	123.7	175.3	200.5
288	394.9	319.6	151.9	146.2	177.9	159.2
293	421.3	343.3	167.5	191.6	207.4	127.6
298	440.2	404.5	190.9	210.6	252.7	114.9
303	449.1	493.3	216.1	199.1	305.8	105.5

1: gravimetric; 2: UV Vis

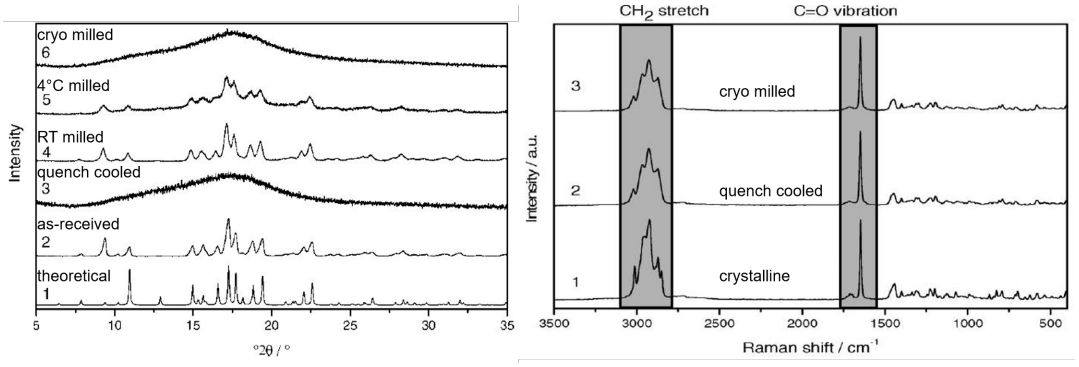

Figure A.14: Literature XRD and Raman data from crystalline and amorphous simvastatin as published by Graeser *et al.*[259] Reprinted (adapted) with permission from Graeser, K. A.; Strachan, C. J.; Patterson, J. E.; Gordon, K. C. & Rades, T. Physicochemical properties and stability of two differently prepared amorphous forms of simvastatin *Cryst. Growth Des.*, **2008**, 8, 128-135. Copyright 2021 American Chemical Society.

Danksagung

Diese Arbeit wurde an der Bundesanstalt für Materialforschung und -prüfung im Fachbereich 6.3 ‘Strukturanalytik’ erarbeitet, wo mich Frau Dr. habil. Franziska Emmerling als Doktormutter betreute. Ihr gilt zunächst ganz besonderer Dank für die Bereitstellung des Themas, darüber hinaus aber auch für ihre unermüdliche Unterstützung, ein stets offenes Ohr, ihren Zuspruch und all die Dinge, die ich von ihr lernen durfte.
Für die Erstellung Ihrer Gutachten danke ich ausdrücklich Prof. Klaus Rademann und Prof. Wolfgang Tremel.
Mein besonderer Dank gilt Ralf Bienert für seine umfassende fachliche Unterstützung bei SAXS Messungen und Auswertungen sowie diversen Strahlzeiten als auch Carsten Prinz für die Durchführung von TEM Messungen. Ihr Beistand ging oft über das Fachliche hinaus. Genauso danke ich meinen Kollegen aus dem FB 6.3 für die gute Atmosphäre, viele spannende Strahlzeiten und ergebnisorientierte Zusammenarbeit. Hier erwähne ich insbesondere Paulo Filho Marques de Oliveira, Adam Michalchuk und Anke Kabelitz.
Herrn Jörg Radnik danke ich für die Durchführung und Auswertung der XPS Messungen sowie die intensiven und weiterführenden wissenschaftlichen Diskussionen. Diese Arbeit wäre ohne externe Messungen nicht möglich gewesen, weswegen ich mich an dieser Stelle ausdrücklich bedanke bei Ines Feldmann für SEM Messungen, Antje Cossmer für ICP-MS Messungen, Annett Zimathies für Gassorption/Hg-Porosimetrie Messungen und Ana Buzanich für XAS-Messungen sowie die anteilige Messauswertung von Yen Ramisch. Armin Hoell und Robert Wendt zeichnen für die Durchführung und Auswertung der ASAXS Daten verantwortlich, Sebastian Wohlrab und Benny Kunkel für die Bereitstellung des katalytischen Messaufbaus und wissenschaftlichen Inputs. Ihnen gebührt mein Dank dafür! Ich hatte tatkräftige Unterstützung durch die beiden Auszubildenden Jonathan Olbeter und Paul Andrle. Vielen Dank! Erwähnt sei hier auch Hannes Kulla für die Vorversuche im Rahmen seiner Diplomarbeit.
Ein besonderes Highlight im Rahmen dieser Arbeit war mein STSM in Lissabon, das durch die finanzielle Unterstützung der COST Action CM1402 möglich war. Die Zusammenarbeit mit Prof. Manuel Minas da Piedade, Carlos Bernardes und Ricardo Simões war ein Meilenstein in meiner wissenschaftlichen Entwicklung. Bei Ihnen allen bedanke ich mich ausdrücklich!
Abschließend bedanke ich mich für den unerschütterlichen Rückhalt meiner Familie, der mich motivierte, wo es nötig war.

Publications

Advances in Nickel Nanoparticle Synthesis via Oleylamine Route
M. Heilmann, H. Kulla, C. Prinz, R. Bienert, U. Reinholz, A. Guilherme Buzanich, F. Emmerling, *nanomaterials*, **2020**, *10*, 4, 713-726.

Linking Aggregation in Solution, Solvation, and Solubility of Simvastatin: An Experimental and MD Simulation Study
R.G. Simões, P.L.T. Melo, C.E.S. Bernardes, M.T. Heilmann, F. Emmerling, M.E. Minas da Piedade, *Crystal Growth & Design*, **2021**, *21*, 1, 544–551.

Real-time In situ XRD Study of Simvastatin Crystallization in Levitated Droplets
M. T. Heilmann, R.G. Simões, C.E.S. Bernardes, Y. Ramisch, R. Bienert, M. Röllig, F. Emmerling, M.E. Minas da Piedade, *Crystal Growth & Design*, **2021**, *21*,8, 4665-4673.

Size-tunable Ni-Cu-Core-Shell Nanoparticles - Linking the Catalytic Activity for RWGS Reaction to Nanochemical Structure
M. Heilmann, C. Prinz, R. Bienert, R. Wendt, B. Kunkel, J. Radnik, A. Hoell, S. Wohlrab, A. Kabelitz, A. Buzanich, F. Emmerling, *Adv. Eng. Mater.*, **2022**, 2101308. 10.1002/adem.202101308

Too much water? Not enough? In situ monitoring of the mechanochemical reaction of copper salts with dicyandiamide
L. Casali, T. Feiler, M. Heilmann, D. Braga, F. Emmerling, F. Grepioni, *CrystEngComm*, **2022**, *24*, 1292-1298.

Conference Contributions

Real-time In-situ Synchrotron Study of Simvastatin Crystallization on Levitated Droplets
M. Heilmann, C.E.S. Bernardes, F. Emmerling, M.E. Minas da Piedade;
BACG, **2018**, Limerick, Ireland.

Solution for dirty water sources – "clean water is a fundamental right, not a priviledge"
M. Heilmann, Z. You, T. Bewersdorff;
1. International Nanotechnology Olympiade, **2018**, Teheran, Iran.

Selbstständigkeitserklärung

Ich erkläre, dass ich die Dissertation selbständig und nur unter Verwendung der von mir gemäß § 7 Abs. 3 der Promotionsordnung der Mathematisch-Naturwissenschaftlichen Fakultät, veröffentlicht im Amtlichen Mitteilungsblatt der Humboldt-Universität zu Berlin Nr. 42/2018 am 11.07.2018 angegebenen Hilfsmittel angefertigt habe.

Berlin, den